energies

MDPI

Article

Pyrolysis of Grape Marc from Tunisian Wine Industry: Feedstock Characterization, Thermal Degradation and Kinetic Analysis

Besma Khiari [1] and Mejdi Jeguirim [2,*]

[1] Laboratoire des Sciences et Technologies de l'Environnement, University of Carthage, BP 50 Borj Cedria Technopark, 2050 Hammam-Lif, Tunisia; besmakhiari@yahoo.com

[2] Institut de Sciences des Matériaux de Mulhouse, UMR 7661 CNRS, 15 rue Jean Starcky, 68057 Mulhouse, France

* Correspondance: mejdi.jeguirim@uha.fr; Tel.: +33-389-608-661

Received: 7 March 2018; Accepted: 22 March 2018; Published: 23 March 2018

Abstract: Despite the huge amounts of grape marc generated in Tunisia from the wine industry, very few efforts have been exerted to manage this harmful waste. Therefore, thermal processes may contribute to an environmental friendly management and also help winemakers to create new economic profitable circuits in an increasingly competitive context. Among the various thermochemical conversion process, pyrolysis is suitable for the recovery of food processing residues, due to their high minerals content and ability to create high added values of the derived products (biochar, bio-oil and syngas). In this context, the aim of this work is to optimize the pyrolysis process in order to benefit from the grape marc potential for achieving highest product yields. Therefore, physico-chemical and energy characteristics of grape marc issued from a Tunisian wine cooperative were determined according to international standards. Thermogravimetric analyzes were also performed to predict the grape marc behavior during degradation under an inert atmosphere. The profile of the mass loss rate shows two decomposition peaks corresponding to the cellulose and lignin decomposition. These peaks are shifted to lower temperatures comparing to several lignocellulosic biomass feedstocks due to high content of minerals that may play a catalytic role in the thermal degradation process. The biochar yield was about 40%, which was never met in literature for agricultural biomass in slow pyrolysis. Such behavior may be attributed to high lignin content in grape marc. Activation energies were calculated using integral Flynn-Wall-Ozawa and Kissinger-Akahira-Sunose methods and differential Friedman method. The obtained values were 226.8, 224.2 and 229.5 kJ/mol, respectively. Such kinetics data are crucial in the design of the pyrolyzer for Tunisian grape marc recovery.

Keywords: grape marc; kinetic models; characterization; pyrolysis

1. Introduction

Grape is one of the most important fruit crops in the world with over 74 million tons produced annually [1]. Pressing grapes give juice, which is mostly for fermentation, and marc, which is also called pomace (solid product) [2], containing skins, seeds and stalks [3]. Although the pressing grape method depends strongly on the type of wine (white or red), Toscano et al. [3] described a general process giving the following proportions of grape products: 73% of juice and 27% of grape marc. The grape marc is distributed as follows: 19.5% of skins, 4.5% of seeds and 3% of stalks [3]. Grape marc may be processed further in distilleries in order to extract alcohol and the generated waste is called the exhausted grape marc residues. Wine cave (fresh grape marc) and alcohol distilleries (exhausted grape marc) produce large amounts of wastes, which are estimated at 7 million tons worldwide per year [4].

Grape marc characteristics depend strongly on the climatic conditions [5]. In general, grape marc is a wet (60% of moisture content) and heterogeneous waste [2]. Fresh grape marc are considered as a non-contaminated material with harmful characteristics, such as low pH and high organic matter (90%), including phytotoxic and antibacterial phenolic substances [6]. The most common methods to recover these residues include production of alcohol, tartar, pharmaceuticals, cosmetics [6], feedstuff [7], yeast [8], extraction of phenolic compounds [9], production of oil [10] or energy [11], decontamination of effluents containing metals, such as copper and nickel [12], composting [13] and direct use as an organic fertilizer [14]. According to the European Council Regulation EC1493/1999 involving the common organization of wine market, fresh grape marc (except stalks) must be transferred to alcohol distilleries [6]. In Spain, several studies showed that exhausted grape marcs have a high content of lignin and tannin and are not easily digested. Therefore, they are not appropriate as nutritional supplements for animals. Besides, their high C/N ratio limits their potential as soil fertilizers [14]. In this way, Italian laws (2010) require wine producers to send their wastes to distilleries [3]. Thus, some recovery methods are no longer permitted. In the same context, composting was also declared to not be economically viable in France and is gradually disappearing. Therefore, 60% of distilleries in France are using grape marc as combustible [4]. In fact, grape marc has interesting physical and thermal properties and energy contents [2,15]. However, a particular attention should be paid to the ash accumulation and pollutants emissions factors during grape marc combustion.

Similar to other Mediterranean countries, Tunisia is committed to finding a solution for environmental and economical disposal of their wastes and to participate further to reduce the global greenhouse effect. The wine industry in Tunisia generates annually about 25,000 tons of grape marc issued from internationally-known varieties, such as Grenache, Syrah, Cinsaut, Muscat of Alexandria, and from 54 aboriginal varieties, such as Razzegui, Tebourbi, Asli, Bazzoul Khaddem, Sakalsi, Garrat, Hamri, Chetoui and Chaouch. The grape plantations and the wine extraction processes are spread almost all over the country, although they are mainly located in the North East [16]. The discharge of the generated grape marc is usually centralized and seasonal in a short period of the year (August–October) [16]. Furthermore, only 10% from the generated grape marc are used as nutritional ferment. A small part is used for compost production or dried and used as fertilizer [5]. The rest is either dumped or used as a traditional combustible in an uncontrolled manner, leading to the release of hazardous pollutants.

Currently, there is no sustainable strategy for the grape marc recovery in Tunisia. Recently, Kraiem et al. [17,18] showed that despite suitable lower heating, high mineral contents and low bulk densities limit their direct use as biofuels in a combustion appliance for the residential heating sector. Authors had then resort to the densification and the blend of grape marc with woody biomass, which has low ash content [17,18]. However, combustion tests showed the high particular matter emissions, which limit the recovery of grape marc in domestic heating [17,18]. Therefore, the pyrolysis process could be a promising issue for the grape marc valorization since their mineral contents may be blocked in the residual char. This pyrolysis process could be interesting for wine, juice or jam-making industries [19,20]. However, as far as we know, a similar survey was never conducted in Tunisia, despite big potential gains. In fact, storage, handling and transport costs may be reduced with nearby, decentralized pretreatment establishments. Moreover, the pyrolytic gases can provide the power required for the endothermic pyrolysis process, ensuring self-sufficient operating system. In addition, the bio-oil and the biochar obtained from the pyrolysis process could be recuperated by winemakers for biofuels or soil amendments applications.

Consequently, the aim of this experimental work is to contribute to the understanding of the Tunisian grape marc behavior within an industrial processed pyrolysis. In particular, characteristics, including proximate and ultimate analyses, are determined. Thermogravimetric analyzes are also performed to predict the behavior of this waste during thermal degradation under different inert types of atmosphere. The obtained data are used for determining kinetic parameters that are subsequently used for determining the optimum pyrolysis process parameters.

2. Materials and Methods

Grape marc used in this study was collected from a wine cooperative located in the north of Tunisia (Bou Argoub, Nabeul). The sample was fresh with 60% (wb) of moisture, which was reduced to 10%. The sample was characterized through moisture content (EN 14774-1), ash content (EN 14775) and Low Heating Value, LHV (EN 14918) determination. Volatile matters and fixed carbon were determined using the Thermogravimetric analysis method [21]. Furthermore, elemental analysis was performed using a CHNOS analyzer (ThermoFisher Scientific, Villebon, France).

Thermogravimetric analyses (TGA) were carried out using a Mettler-Toledo TGA/DSC3+ (Mettler-Toledo, Columbus, OH, USA) thermobalance apparatus and repeated at least three times, with good reproducibility. The experiments were performed under nitrogen with flows of 12 Nl·h^{-1} according to different linear heating programs (5, 10, 20 and 30 °C/min) in the range of 20–950 °C.

3. Kinetic Approach

Many works have focused on the data analysis method for extracting reliable kinetic data from TGA experiments. There are three types of kinetic methods used for the analysis of biomass pyrolysis kinetics: differential, isoconversional, model-fitting and pseudo-components kinetics methods [22–25].

The fundamental rate equation used in all kinetic studies is generally described as:

$$\frac{dX}{dt} = k(T)f(X), \tag{1}$$

where k is the rate constant and $f(X)$ is the reaction model that describes the reaction mechanism. The conversion rate X is given by Equation (2):

$$X = \frac{W_0 - W_t}{W_0 - W_f}, \tag{2}$$

where W_t, W_0, and W_f are time t, initial and final weights of the sample, respectively.

The Arrhenius equation (Equation (3)) expresses the rate constant k:

$$k = Aexp\left(\frac{-Ea}{RT}\right), \tag{3}$$

where Ea is the activation energy (kJ/mol), R is the universal gas constant (8.314 J/K mol), A is the pre-exponential factor (s^{-1}) and T is the absolute temperature (K).

Energy activation is defined as the minimum energy requirement that must be overcome before molecules can get close enough to react and form products. Accordingly, the reactions with a high Ea need a high temperature or a long reaction time.

By combining Equations (1) and (3), we obtain:

$$\frac{dX}{dt} = Aexp\left(\frac{-Ea}{RT}\right)f(X). \tag{4}$$

If the temperature is varied by a constant designed by β, which is the heating rate ($\beta = \frac{dT}{dt}$), the introducing of β in the Equation (4) gives:

$$\frac{dX}{dT} = \frac{A}{\beta}exp\left(\frac{-Ea}{RT}\right)f(X). \tag{5}$$

By taking the logarithms of both sides of Equation (5), the first proposed differential Friedman method (Equation (6)) is obtained [26]:

$$Ln\frac{dX}{dt} = Ln\left(\beta\frac{dX}{dT}\right) = Ln[Af(X)] - \frac{Ea}{RT}. \quad (6)$$

If we rearrange Equation (6), we can obtain:

$$L\frac{dX}{f(X)} = \frac{A}{\beta}exp\left(\frac{-Ea}{RT}\right)dT. \quad (7)$$

After integrating Equation (7), it can be obtained:

$$g(X) = \int_0^X \frac{dX}{f(X)} = \frac{A}{\beta}\int_0^T exp\left(\frac{-Ea}{RT}\right)dT \quad (8)$$

By taking logarithms and using the Doyle approximation, Equation (8) can be rewritten as Equation (9). This equation is known as the Flynn-Wall-Ozawa method (FWO) [27]:

$$Ln\beta = Ln\frac{AEa}{g(X)R} - 2.315 - \left(\frac{1.0516Ea}{RT}\right). \quad (9)$$

By using the derivation of Equation (3), and applying the logarithmic scale with the temperature data for each conversion rate (X) at different heating rates ($\beta_j = \frac{dT}{dt}$), the Kissinger method (KAS) calculates activation energy by plotting Equation (9) [28]:

$$Ln\frac{\beta}{T^2} = Ln\frac{AR}{Eag(X)} - \frac{Ea}{RT}. \quad (10)$$

The kinetic methods used in this study are Friedman, Flynn-Wall-Ozawa (FWO) and Kissinger-Akahira-Sunose (KAS) and their principles are listed in Table 1.

Table 1. Isoconversional Kinetic methods used in evaluating activation energy in this study.

Method	Expression	Plots	Reference
Friedman	$Ln\frac{dX}{dt} = Ln\left(\beta\frac{dX}{dT}\right) = Ln[Af(X)] - \frac{Ea}{RT}$	$Ln\left(\beta\frac{dX}{dT}\right)$ vs. $\frac{1}{T}$	[26]
FWO	$Ln\beta = Ln\frac{AEa}{g(X)R} - 2.315 - (\frac{1.0516Ea}{RT})$	$Ln\beta$ vs. $\frac{1}{T}$	[27]
KAS	$Ln\frac{\beta}{T^2} = Ln\frac{AR}{Eag(X)} - \frac{Ea}{RT}$	$Ln\frac{\beta}{T^2}$ vs. $\frac{1}{T}$	[28]

4. Results and Discussions

4.1. Grape Marc Characterization

Table 2 shows the proximate and ultimate analyses of the Tunisian grape marc. Moisture is reduced to 10%, since it was very high after the wine extraction process (60 wt %). Furthermore, the direct use of the grape marc has a negative effect on the thermochemical process efficiency and temperature [29].

Table 2. Proximate and ultimate analyses of grape marc.

	This Study	Miranda et al. [15]	Gonzalez-Vazquez et al. [30]	Makela et al. [31]
Proximate Analysis	%			
Moisture ^{wb}	10	7.49	-	1.4
Fixed Carbon ^{db}	31.1	24.73	19.7	-
Volatile matter ^{db}	55.6	67.80	67.6	-
Ash ^{db}	13.3	7.47	12.7	8.23
LHV ^{db} ($MJ \cdot kg^{-1}$)	18.02	19.54	18.7	19.6
Elemental Analysis ^{db}	%			
C	42.2	42.97	45.5	48.7
H	3.5	9.28	5.1	5.57
O	37.7	-	34.7	35.9
N	3.0	2.05	1.8	1.66
S	0.3	0.17	0.17	-

^{wb} Wet basis, ^{db} dry basis.

The ash content is 13.3%, which is higher than wood chips, at the same level as the grape marc was found by other authors, although this was lower than wheat straw [3]. The fixed carbon (31.1%) is higher than the value obtained by Miranda et al. (25%) for grape marc and higher than several biomass resources, such as olive husk (19%) and pine sawdust (17%). However, as expected, the volatile matter (55.6%) is lower than the grape marc of Miranda et al. (67.8%), olive husk (76%) and pine sawdust (69%) [15,32–34]. The high ash and fixed carbon contents confirm that slow pyrolysis is the suitable thermochemical conversion process for the grape marc recovery. In particular, the char yield (fixed carbon fix and ash contents) was about 44.4%, which was never met in literature for agricultural biomass under slow pyrolysis conditions. This feature distinguishes Tunisian grape marc from European ones and even from Chinese and American pomace. Many factors can explain these differences, such as local wine making practices and Tunisian grapevine specificity. The pyrolytic char derived from the Tunisian grape marc may have several applications, including soil amendment, adsorbents, biocoal, etc.

Elemental analysis also shows some differences with values met in literature, although this is consistent with the wide range of biomass composition that would undergo efficient pyrolysis. Carbon, hydrogen and oxygen are lower than the mean reported values, while N and S are quite high. This repartition is close to the composition of grape skins, although it is quite different from that of its seeds or stalks [32–34]. If nitrogen remains in char, this would be a supplementary argument in favor of pyrolysis against combustion, as biochar can be used as nutrients for soils.

4.2. Thermal Degradation of Grape Marc under Inert Atmosphere

The thermal degradation of biomass feedstocks was well described in the literature, which serves the main purpose of ensuring that from an energy standpoint, the pyrolysis process is self-sufficient [24–28,33,35]. Many factors affect the kinetic parameters based on the processing of TGA data, including processing conditions; heat and mass transfer limitations; physical and chemical heterogeneity of the sample; and systematic errors.

Figure 1 shows the mass loss (X) and the derivative (DTG) of mass loss (dX/dt) curves obtained during the pyrolysis of Tunisian grape marc. Thermogravimetric analysis could evaluate the thermal behavior of fuels under an inert atmosphere. The results are helpful in the fundamental understanding of biomass fuels when developing biomass utilization for the pyrolysis plant.

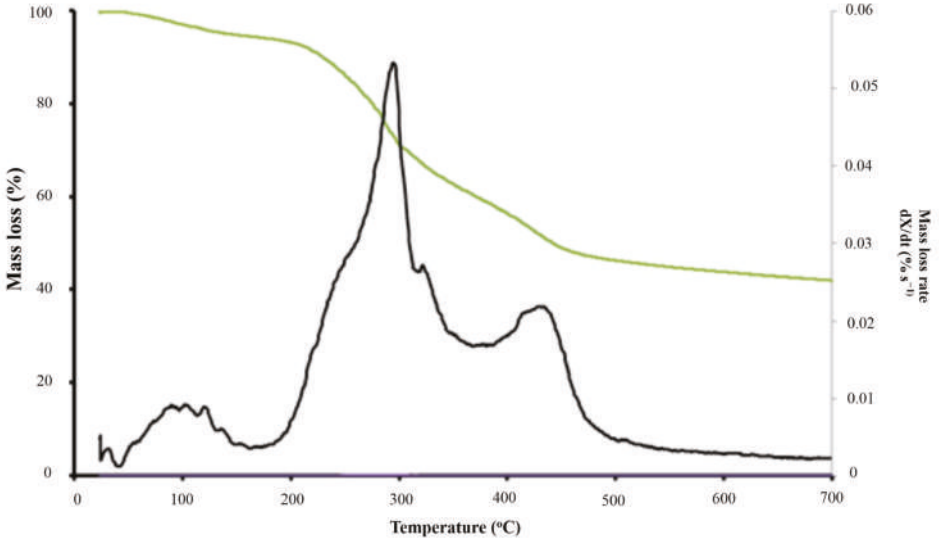

Figure 1. TG and DTG curves of Grape Marc under an inert atmosphere at 5 °C/min.

The shape of Derivative Thermo-Gravimetric (DTG) curve includes three regions in ascending order of temperature variation, corresponding to three degradation steps. The first region occurred between 23 and 166 °C, which corresponds to the biomass drying by moisture loss and the departure of light volatiles. The second region corresponds to the devolatilization step, which occurs between 166 °C and 500 °C. This step was called in the literature as the active pyrolysis includes two zones. The first one occurs between 166 and 362 °C, which corresponds to the decomposition of cellulose and hemicellulose. A clear peak at 288 °C is attributed to the decomposition of cellulose with an overall maximum rate of 0.055 %·s^{-1}. A second zone occurs between 362 °C and 500 °C, which corresponds to the lignin degradation. After the devolatilization step, a third step of passive pyrolysis is observed. This step characterized by a low and a continuous mass loss rate corresponds to the end of lignin degradation as well as char formation and rearrangement.

Several phenomena occur within grape marc pyrolysis and to varying extents: cracking, reforming, dehydration, condensation, polymerization and even oxidation and gasification reactions, which take place after the release of the oxygen and the vapors present in the product.

The obtained TG data, T (temperature), X (mass loss), T_{peak} (peak temperature), dX/dt (mass loss rate) and R_M (mean reactivity) are shown in Table 3. One may remind that reactivity is calculated as follows:

$$R_M = 100 \sum \left(\frac{R_{peak}}{T_{peak}} \right). \quad (11)$$

The comparison of the obtained values with those found in literature for various lignocellulosic biomass feedstocks shows several differences. First, the peak temperature obtained at 288 °C is lower than the reported peak temperatures for cellulose decomposition, which is between 310 and 320 °C. Furthermore, this is lower than the peak temperature of 332 °C for pure cellulose [36] and for various lignocellulosic biomass in the literature [22,35,37]. However, this peak was at 261 °C for palm kernel shells for example [38]. The high content of minerals initially present in the Tunisian grape marc [20,21] is thought to be responsible for the shift to lower levels of temperatures as they may play a catalyzing role in the process. The impact of these minerals, especially Na, K and Mg, were evidenced in previous investigations [39].

Table 3. TG under inert atmosphere (5 °C/min).

	Pyrolysis Zone		
		T (°C)	166–750
		X (%)	94.5–41.3
Active Pyrolsis	**Zone 1**	T (°C)	166–362
		X (%)	94.5–61.2
		$T_{peak\ 1}$ (°C)	288
		R_1 (%·s^{-1})	0.032
	Zone 2	T (°C)	362–500
		X (%)	64.81–46.4
		$T_{peak\ 2}$ (°C)	423
		R_2 (%·s^{-1})	0.021
		$R_M \times 10^3$ (%·s^{-1}·°C^{-1})	0.14
Passive Pyrolysis		T (°C)	500–750
		X (%)	46.4–41.3

Hemicellulose decomposition is identified through the shoulder between 238 and 257 °C, which is in the interval of 195–306 °C. Such behavior is well-known in the literature and the hemicellulose decomposition step appears usually as a more or less pronounced shoulder instead of a well-defined peak [38]. Similar to cellulose decomposition, during the grape marc thermal degradation, hemicellulose decomposition occurs at a lower temperature due to the catalytic effect of alkali and alkali-earth metals [39].

The lignin degradation step also shows a clear difference compared to the usual shape of the DTG curve of lignocellulosic biomasses. In particular, the DTG curve of the Tunisian grape marc shows a specific region occurring between 362 and 500 °C, with a peak at 425 °C that yields an overall rate around 0.021 %·s^{-1}. This peak is attributed to the high contents of lignin. Otherwise, the zone corresponding to the cracking of the polymeric structure of C–C or C–O–C bonds in lignin would result in only a flat tailing section. Generally, the thermal degradation of lignocellulosic biomass is not characterized by a sharp peak for lignin decomposition.

The reactivity value (0.14×10^{-3} %·s^{-1}·°C^{-1}) is in the same magnitude as those of various biomasses, such as the coffee husk around 0.19×10^{-3} %·s^{-1}·°C^{-1} [38] or palm residues (0.23×10^{-3} %·s^{-1}·°C^{-1}) [40] for the same heating rate.

The char yield of 39.68% is expected in view of the proximate analysis, although this is higher than any agricultural waste. The char resulting from the first stages also probably contributed to the secondary reactions, which mainly occurred by catalyzing cracking and polymerization reactions that promoted recombination reactions among the volatile species to yield more condensed char structures [39].

In order to extract the kinetic parameters of the thermal degradation of Tunisian grape marc under pyrolysis conditions, the impact of different heating rates was investigated. Figure 2 showed that increasing the heating rate leads to a shift in the peak temperature towards higher values together with higher mass loss rates. Indeed, when heating rate is increased from 5 to 30 °C/min, the maximum peak temperature moves from 288 to 322 °C. The explanation is that the material reaches the cracking temperature in a shorter time when higher heating rates are considered. Due to the heat and mass transfer limitations inside the particle, these higher heating rates are a consequence of inner temperature gradients. In fact, increasing the reactor temperature ramp does not allow good temperature stabilization within the grape marc, which causes a delay in the volatile matter departure. The same behavior has been reported in the literature for numerous biomasses [40–42].

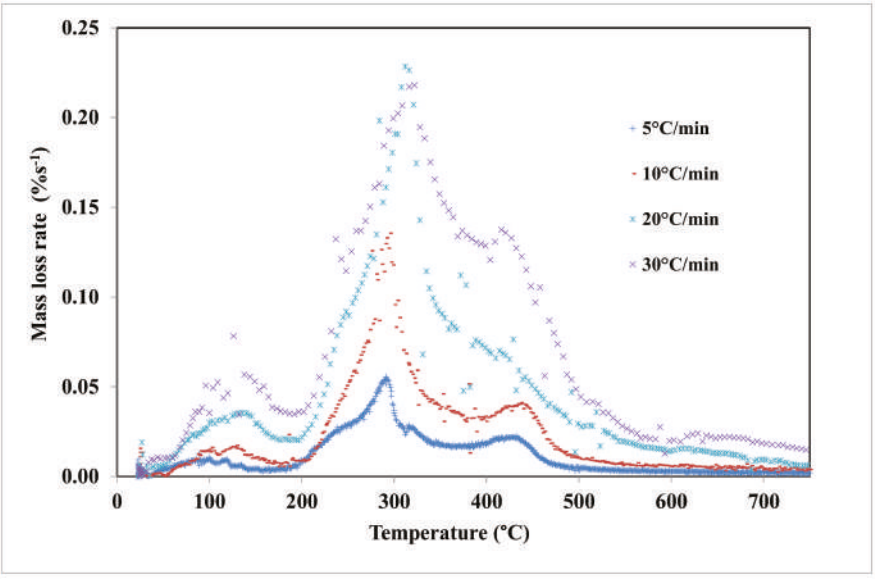

Figure 2. Mass loss rate for different heating rates.

4.3. Kinetic Study

The linear plots of KAS, FWO and Friedman are shown in Figure 3. As the initial mass loss is attributed to the moisture loss, the first conversion rate selected to determine the kinetic parameters is 0.2, while the final point is taken at 0.65. Above this value, no good determination coefficients were obtained, which may be attributed to the complexity of the char production and rearrangement.

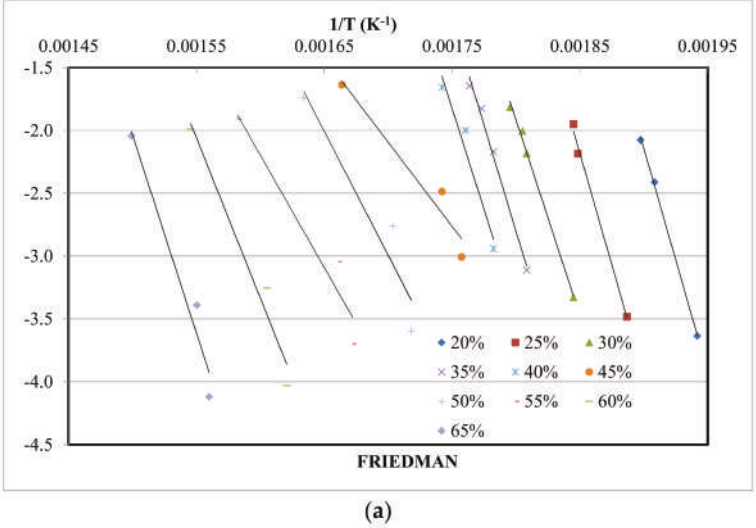

(a)

Figure 3. *Cont.*

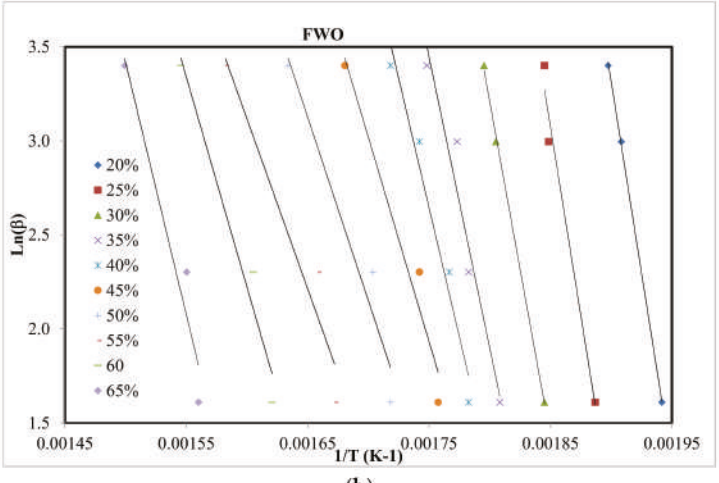

(b)

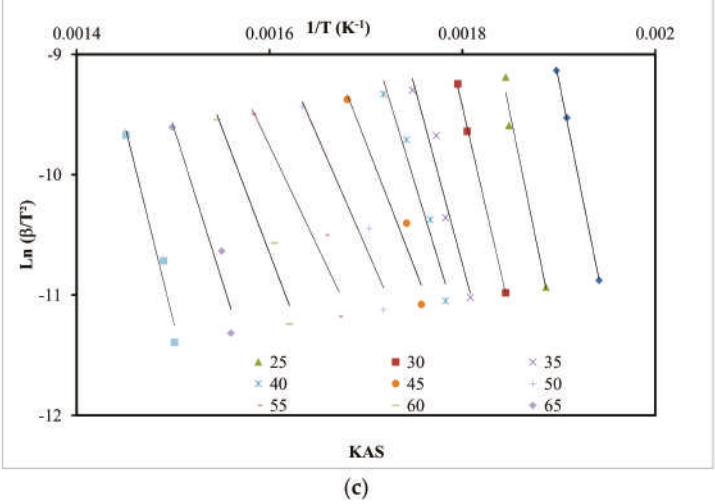

(c)

Figure 3. Plots for kinetic models. (**a**) Friedman; (**b**) FWO; (**c**) KAS.

The calculated corresponding values are presented for each conversion ratio in Table 4. The mean activation energy values for GM with the use of the KAS, FWO and Friedman methods were 224.2, 226.8 and 229.5 kJ/mol, respectively. Table 4 depicts that the activation energy decreases when the conversion increases. It is assumed that a good biomass thermal degradation meets low activation energy values. In the initial stages and for KAS, FWO and Friedman methods, the *Ea* values were high (333.3, 323.3 and 295.9 kJ/mol, respectively, at $X = 0.2$). However, these values gradually decrease as the conversion rate X goes up until it reaches 55%, before increasing again (an exception point around 45% is probably due to an experimental error). This phenomenon was not reported in other works, where *Ea* was decreasing continuously, for several cellulosic biomasses [43,44]. This is explained by the quick and first scission of the weakly bonded amorphous cellulose and hemicelluloses. Once all-crystalline cellulose has decomposed, lignin accounted for a further decrease in activation energy [44].

Table 4. Calculated Energy activation with R^2 values from Friedman, FWO and KAS models (E, kJ/mol).

X	Friedman		FWO		KAS	
	Ea	R^2	*Ea*	R^2	*Ea*	R^2
0.20	295.9	0.999	323.3	0.999	333.3	0.999
0.25	295.0	0.995	316.9	0.979	324.4	0.978
0.30	259.2	0.995	282.0	0.999	287.4	0.999
0.35	280.5	0.991	244.4	0.947	247.7	0.943
0.40	267.5	0.955	217.0	0.964	218.8	0.961
0.45	111.4	0.947	172.1	0.959	171.3	0.954
0.50	163.8	0.911	154.5	0.948	157.6	0.941
0.55	148.5	0.936	142.9	0.939	140.0	0.930
0.60	212.3	0.965	176.9	0.962	175.3	0.958
0.65	262.2	0.959	212.1	0.941	212.1	0.935
Mean	229.5		226.8		224.2	

In our case and according to previous studies [2–5,14,31,41], lignin content in grape marc is much higher than cellulose. Consequently, the whole pyrolysis is thought to be mainly controlled by the lignin and its intermediate products.

In another hand, it is noticed that the activation energy for grape marc is greater than the values obtained for the pyrolysis of lignin [45,46] and other biomass [32,47–50]. These activation energies are high even when compared to other grape marc that originated from Italy. Fiori et al. found values between 171 and 178 kJ/mol for heating rates between 3 and 30 °C/min [51].

The isoconversional methods were applied to four different experimental data sets (5, 10, 20 and 30 °C/min). The results are presented in Figure 4. KAS and FWO are very close. The calculated *Ea* at the different conversion levels can be attributed to a different macro-component decomposition. At low conversion levels (0.2–0.3), the activation energies between 250 and 340 kJ/mol can be regarded as being related to hemicelluloses degradation. The lower *Ea* in the range of 140–240 kJ/mol are obtained for the conversion levels of 0.25 and 0.50, which can be attributed to cellulose cracking. The activation energy increases to 212 kJ/mol for KAS and OFW models and to 262 for the Friedman model at higher conversion levels, for which lignin is thought to be responsible. At higher temperatures, activation energies decrease, which may be explained by an overlapping of cellulose and lignin continuing degradation as well as by char rearrangement through secondary and more complex reactions, which was found in literature [52–55].

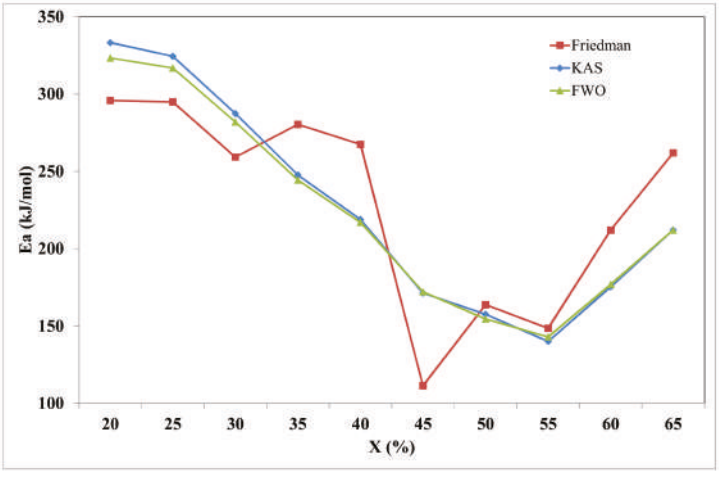

Figure 4. Activated Energies for Friedman, FWO and KAS method for conversion from 20 to 65%.

5. Conclusions

In these times, where the circular economy is at the service of the economic actors, the slow pyrolysis of grape marc can be an advantage in the wine industry and distilleries on more than one level, especially in the Tunisian context. Furthermore, as better environmental management of grape marc is increasingly necessary, this study is required to achieve a better understanding of the economics of grape marc pyrolysis for bio-fuel production and for resolving issues related to the capabilities of this technology in practical applications. Indeed, the pyrolysis process applied to these residues provides a high biochar yield of around 40%, which was never reached by any other agricultural waste. This fact is explained by the inhibition of hemicellulose and cellulose decomposition on one hand and by high lignin content on the other hand. With the same aim to improve some characteristics of grape marc by increasing its bulk density and reducing its ash content, densification and blending with woody biomass can help to solve the problem. The biochar is interesting as it may be used as nutritional ferment for soils or may undergo direct and efficient gasification. Minerals, which were an obstacle in combustion operations, become a major asset in pyrolysis. Furthermore, their presence played a catalytic role and shifted the cracking temperatures to lower values, thus reducing the operation cost.

To optimize this and to achieve high energy recovery from grape marc, kinetics data were calculated and helped in the design of pyrolysis reactors for grape marc. Integral and differential methods used in the frame of this work showed very close and reliable kinetic parameters.

Author Contributions: All authors contributed equally to the work done.

Conflicts of Interest: The authors declare no conflict of interest.

Nomenclature

A	pre-exponential factor (s^{-1})
Ea	activation energy (kJ/mol)
k	rate constant (s^{-1})
R	universal gas constant (J/K mol)
R_M	mean reactivity (%·s^{-1}·°C^{-1})
t	time (s)
T	absolute temperature (K)
T_{peak}	peak temperature (K)
W_0	initial weight of the sample (mg)
W_f	final weight of the sample (mg)
W_t	time t weight of the sample (mg)
X	mass loss (%)
β	heating rate (K/s)

References

1. Moncayo, J.R.; Aurand, J.M. *Table and Dried Grapes*; Food and Agriculture Organisation (FAO): Rome, Italy, 2016; ISBN 978-92-5-109708-3.
2. Celma, A.R.; Rojas, S.; Lopez-Rodriguez, F. Waste-to-energy possibilities for industrial olive and grape by-products in Extremadura. *Biomass Bioenergy* **2007**, *31*, 522–534. [CrossRef]
3. Toscano, G.; Riva, G.; Duca, D.; Pedretti, E.F.; Corinaldesi, F.; Rossini, G. Analysis of the characteristics of the residues of the wine production chain finalized to their industrial and energy recovery. *Biomass Bioenergy* **2013**, *55*, 260–267. [CrossRef]
4. Dwyer, K.; Hosseinian, F.; Rod, M. The Market Potential of Grape Waste Alternatives. *J. Food Res.* **2014**, *3*, 91–106. [CrossRef]
5. Souza, E.C.; Uchoa-Thomaz, A.M.A.; Carioca, J.O.B.; Lima, A.; Martin, C.G.; Alexandrino, C.D.; Ferreira, P.A.T.; Rodrigues, A.L.M.; Rodrigues, S.P.; Silva, J.N.; et al. Chemical composition and bioactive compounds of grape pomace (*Vitis vinifera*, L.), Benitaka variety, grown in the semiarid region of Northeast Brazil. *Food Sci. Technol, Campinas* **2014**, *34*, 135–142. [CrossRef]

6. Bustamante, M.A.; Moral, R.; Paredes, C.; Perez-Espinosa, A.; Moreno-Caselles, J.; Pérez-Murcia, M.D. Agrochemical characterisation of the solid by-products and residues from the winery and distillery industry. *Waste Manag.* **2008**, *28*, 372–380. [CrossRef] [PubMed]
7. Vaccarino, C.; Tripodo, M.M.; Lo Curto, R.B.; Cimino, G. The effects of NaOH treatments of grape-marc, vinasse, and wheat-straw mixtures on their degradability in vitro. *Bioresour. Technol.* **1993**, *44*, 197–202. [CrossRef]
8. Lo Curto, R.B.; Tripodo, M.M. Yeast production from virgin grape marc. *Bioresour. Technol.* **2001**, *78*, 5–9. [CrossRef]
9. Louli, V.; Ragoussis, N.; Magoulas, K. Recovery of phenolic antioxidants from wine industry by-products. *Bioresour. Technol.* **2004**, *92*, 201–208. [CrossRef] [PubMed]
10. Xu, C.; Zhang, Y.; Wang, J.; Lu, J. Extraction, distribution and characterisation of phenolic compounds and oil in grapeseeds. *Food Chem.* **2010**, *122*, 688–694. [CrossRef]
11. Kabir, M.J.; Chowdhury, A.A.; Rasul, M.G. Pyrolysis of Municipal Green Waste: A Modelling, Simulation and Experimental Analysis. *Energies* **2015**, *8*, 7522–7541. [CrossRef]
12. Villaescusa, I.; Fiol, N.; Martinez, M.; Miralles, N.; Poch, J.; Serarols, J. Removal of copper and nickel ions from aqueous solutions by grape stalks wastes. *Water Res.* **2004**, *38*, 992–1002. [CrossRef] [PubMed]
13. Bertran, E.; Sort, X.; Soliva, M.; Trillas, I. Composting winery waste: Sludges and grape stalks. *Bioresour. Technol.* **2004**, *95*, 203–208. [CrossRef] [PubMed]
14. Bustamante, M.A.; Pérez-Murcia, M.D.; Paredes, C.; Moral, R.; Pérez-Espinosa, A.; Moreno-Caselles, J. Short-term carbon and nitrogen mineralisation in soil amended with winery and distillery organic wastes. *Biores. Technol.* **2007**, *98*, 3269–3277. [CrossRef] [PubMed]
15. Miranda, M.T.; Arranz, J.I.; Román, S.; Rojas, S.; Montero, I.; López, M. Characterization of grape pomace and pyrenean oak pellets. *Fuel Process Technol.* **2011**, *92*, 278–283. [CrossRef]
16. Agence Nationale de Gestion des Déchets—ANGED. *Strategic Options for the Promotion of Value of Organic Waste VDO Tunisia*; Agence Nationale de Gestion des Déchets: Tunis, Tunisie, 2009.
17. Kraiem, N.; Lajili, M.; Limousy, L.; Said, R.; Jeguirim, M. Energy recovery from Tunisian agri-food wastes: Evaluation of combustion performance and emissions characteristics of green pellets prepared from tomato residues and grape marc. *Energy* **2016**, *107*, 409–418. [CrossRef]
18. Jeguirim, M.; Kraiem, N.; Lajili, M.; Guizani, C.; Zorpas, A.; Leva, Y.; Michelin, L.; Josien, L.; Limousy, L. The relationship between mineral contents, particle matter and bottom ash distribution during pellet combustion: Molar balance and chemometric analysis. *Environ. Sci. Pollut. Res. Int.* **2017**, *24*, 9927–9939. [CrossRef] [PubMed]
19. Brassard, P.; Godbout, S.; Raghavan, V.; Palacios, J.H.; Grenier, M.; Zegan, D. The Production of Engineered Biochars in a Vertical Auger Pyrolysis Reactor for Carbon Sequestration. *Energies* **2017**, *10*, 288. [CrossRef]
20. Yang, X.; Wang, H.; Strong, P.J.; Xu, S.; Liu, S.; Lu, K.; Sheng, K.; Guo, J.; Che, L.; He, L.; et al. Thermal Properties of Biochars Derived from Waste Biomass Generated by Agricultural and Forestry Sectors. *Energies* **2017**, *10*, 469. [CrossRef]
21. Jeguirim, M.; Elmay, Y.; Limousy, L.; Lajili, M.; Said, R. Devolatilization behavior and pyrolysis kinetics of potential Tunisian biomass fuels. *Environ. Prog. Sustain. Energy* **2014**, *33*, 1452–1458. [CrossRef]
22. Mishra, R.K.; Mohanty, K. Pyrolysis kinetics and thermal behavior of waste sawdust biomassusing thermogravimetric analysis. *Biores. Tech.* **2018**, *25*, 63–74. [CrossRef] [PubMed]
23. White, J.E.; Catallo, W.J.; Legendre, B.L. Biomass pyrolysis kinetics: A comparative critical review with relevant agricultural residue case studies. *J. Anal. Appl. Pyrol.* **2011**, *9*, 11–33. [CrossRef]
24. Cepeliogullar, O.; Haykiri Acma, H.; Yaman, S. Kinetic modelling of RDF pyrolysis: Model-fitting and model-free approaches. *Waste Manag.* **2016**, *48*, 275–284. [CrossRef] [PubMed]
25. Bartocci, P.; Anca Couce, A.; Slopiecka, K.; Nefkens, S.; Evic, N.; Retschitzegger, S.; Barbanera, M.; Buratti, C.; Cotana, F.; Bidini, G.; et al. Pyrolysis of pellets made with biomass and glycerol: Kinetic analysis and evolved gas analysis. *Biomass Bioenergy* **2017**, *97*, 11–19. [CrossRef]
26. Friedman, H.L. Kinetics of thermal degradation of char-forming plastics from thermogravimetry. Application to a phenolic plastic. *J. Polym. Sci. Polym. Symp.* **1964**, *6*, 183–195. [CrossRef]
27. Flynn, J.H.; Wall, L.A. General treatment of thermogravimetry of polymers. *J. Res. NBS A Phys. Chem.* **1966**, *70*, 487–523. [CrossRef]

28. Kissinger, H.E. Variation of peak temperature with heating rate in differential thermal analysis. *J. Res. Natl. Bur. Stand.* **1956**, *57*, 217–221. [CrossRef]
29. Guizani, C.; Jeguirim, M.; Valin, S.; Limousy, L.; Salvador, S. Biomass Chars: The Effects of Pyrolysis Conditions on Their Morphology, Structure, Chemical Properties and Reactivity. *Energies* **2017**, *10*, 796. [CrossRef]
30. González-Vázquez, M.P.; Garcia, R.; Pevida, C. Optimization of a Bubbling Fluidized Bed Plant for Low-Temperature Gasification of Biomass. *Energies* **2017**, *10*, 306. [CrossRef]
31. Makela, M.; Kwong, C.W.; Bostrom, M.; Yoshikawa, K. Hydrothermal treatment of grape marc for solid fuel applications. *Energy Convers. Manag.* **2017**, *145*, 371–377. [CrossRef]
32. Arvelakis, S.; Koukios, E.G. Physicochemical upgrading of agroresidues as feedstocks for energy production via thermochemical conversion methods. *Biomass Bioenergy* **2002**, *22*, 331–348. [CrossRef]
33. Limousy, L.; Jeguirim, M.; Dutournié, P.; Kraiem, N.; Lajili, M.; Said, R. Gaseous products and particulate matter emissions of biomass residential boiler fired with spent coffee grounds pellets. *Fuel* **2013**, *107*, 323–329. [CrossRef]
34. Gamzenur, O.; Ayse Eren, P. Kinetics and evolved gas analysis for pyrolysis of food processing wastes using TGA/MS/FT-IR. *Waste Manag.* **2017**. [CrossRef]
35. ElSayed, S.A.; Khairy, M. Effect of heating rate on the chemical kinetics of different biomass pyrolysis materials. *Biofuels* **2015**, *6*, 157–170. [CrossRef]
36. Orfao, J.J.M.; Antunes, F.J.A.; Figueiredo, J.L. Pyrolysis kinetics of lignocellulosic materials of three independent reactions model. *Fuel* **1999**, *78*, 349–358. [CrossRef]
37. ElSayed, S.A.; Mostafa, M.E. Kinetic Parameters Determination of Biomass Pyrolysis Fuels Using TGA and DTA Techniques. *Waste Biomass Valoriz.* **2015**, *6*, 401–415. [CrossRef]
38. Jeguirim, M.; Bikai, J.; Elmay, Y.; Limousy, L.; Njeugna, E. Thermal characterization and pyrolysis kinetics of tropical biomass feedstocks for energy recovery. *Energy Sustain. Dev.* **2014**, *23*, 188–193. [CrossRef]
39. Haddad, K.; Jeguirim, M.; Jellali, S.; Guizani, C.; Delmottea, L.; Bennicia, S.; Limousy, L. Combined NMR structural characterization and thermogravimetric analyses for the assessment of the AAEM effect during lignocellulosic biomass pyrolysis. *Energy* **2017**, *134*, 10–23. [CrossRef]
40. El may, Y.; Jeguirim, M.; Dorge, S.; Trouvé, G.; Said, R. Study on the thermal behavior of different date palm residues: Characterization and devolatilization kinetics under inert and oxidative atmospheres. *Energy* **2012**, *44*, 702–709. [CrossRef]
41. Yuan, H.; Xing, S.; Huhetaoli, L.T.; Chen, Y. Influences of copper on the pyrolysis process of demineralized wood dust through thermogravimetric and PyeGC/ MS analysis. *J. Anal. Appl. Pyrolysis* **2015**, *112*, 325–332. [CrossRef]
42. Jeguirim, M.; Dorge, S.; Trouvé, G. Thermogravimetric analysis and emission characteristics of two energy crops in air atmosphere: Arundo donax and Miscanthus giganthus. *Bioresour. Technol.* **2010**, *101*, 788–793. [CrossRef] [PubMed]
43. Skreiberg, A.; Skreiberg, O.; Sandquist, J.; Sorum, L. TGA and macro-TGA characterisation of biomass fuels and fuel mixtures. *Fuel* **2011**, *90*, 2182–2197. [CrossRef]
44. Chouchene, A.; Jeguirim, M.; Khiari, B.; Zagrouba, F.; Trouvé, G. Thermal degradation of olive solid waste: Influence of particle size and oxygen concentration. *Resour. Conserv. Recycl.* **2010**, *54*, 271–277. [CrossRef]
45. Rhén, C.; Ohman, M.; Gref, R.; Wasterlund, I. Effect of raw material composition in woody biomass pellets on combustion characteristics. *Biomass Bioenergy* **2007**, *1*, 66–72. [CrossRef]
46. Chouchene, A.; Jeguirim, M.; Trouvé, G.; Favre-Reguillon, A.; Le Buzit, G. Combined process for the treatment of olive oil mill wastewater: Absorption on sawdust and combustion of the impregnated sawdust. *Bioresour. Technol.* **2010**, *101*, 6962–6971. [CrossRef] [PubMed]
47. Jahirul, M.I.; Rasul, M.G.; Chowdhury, A.A.; Ashwath, N. Biofuels Production through Biomass Pyrolysis—A Technological Review. *Energies* **2012**, *5*, 4952–5001. [CrossRef]
48. Ghouma, I.; Jeguirim, M.; Guizani, C.; Ouederni, A.; Limousy, L. Pyrolysis of Olive Pomace: Degradation Kinetics, Gaseous Analysis and Char Characterization. *Waste Biom. Valoriz.* **2017**, *8*, 1689–1697. [CrossRef]
49. Jun-Ho, J.; Seung-Soo, K.; Ye-Eun, L.; Yeong-Seok, Y. Pyrolysis Characteristics and Kinetics of Food Wastes. *Energies* **2017**, *10*, 1191. [CrossRef]
50. McKendry, P. Energy production from biomass (part 1): Overview of biomass. *Bioresour. Technol.* **2002**, *83*, 37–46. [CrossRef]

51. Ghetti, P.; Ricca, L.; Angelini, L. Thermal analysis of biomass and corresponding pyrolysis products. *Fuel* **1996**, *75*, 565–573. [CrossRef]
52. Fiori, L.; Valbusa, M.; Lorenzi, D.; Fambri, L. Modeling of the devolatilization kinetics during pyrolysis of grape residues. *Biores. Tech.* **2012**, *103*, 389–397. [CrossRef] [PubMed]
53. Marculescu, C.; Ciuta, S. Wine industry waste thermal processing for derived fuel properties improvement. *Renew. Energy* **2013**, *57*, 645–652. [CrossRef]
54. Di Blasi, C. Modeling chemical and physical processes of wood and biomass pyrolysis. *Prog. Energy Combust. Sci.* **2008**, *34*, 47–90. [CrossRef]
55. Wang, P.; Bret, H.; Howard, B.H. Impact of Thermal Pretreatment Temperatures on Woody Biomass Chemical Composition, Physical Properties and Microstructure. *Energies* **2018**, *11*, 25. [CrossRef]

© 2018 by the authors. Licensee MDPI, Basel, Switzerland. This article is an open access article distributed under the terms and conditions of the Creative Commons Attribution (CC BY) license (http://creativecommons.org/licenses/by/4.0/).

energies

MDPI

Article

Release Mechanism of Fuel-N into NO_x and N_2O Precursors during Pyrolysis of Rice Straw

Xiaorui Liu, Zhongyang Luo *, Chunjiang Yu, Bitao Jin and Hanchao Tu

State Key Laboratory of Clean Energy Utilization, Zhejiang University, Hangzhou 310027, China; liuxiaorui214@zju.edu.cn (X.L.); chunjiang@zju.edu.cn (C.Y.); 21627061@zju.edu.cn (B.J.); 21527068@zju.edu.cn (H.T.)

* Correspondence: zyluo@zju.edu.cn; Tel.: +86-571-8795-2440

Received: 25 January 2018; Accepted: 24 February 2018; Published: 28 February 2018

Abstract: Rice straw, which is a typical agricultural residue in China, was pyrolyzed in a horizontal tube reactor connected with a Fourier transform infrared (FTIR) analyzer at temperatures ranging from 500 to 900 °C to research the release mechanism of fuel-N into NO_x and N_2O precursors. The concentrations of gaseous nitrogen components were monitored online. NH_3, HCN, HNCO, as well as NO were identified components. A high dependency between the gaseous products and temperature was found. NH_3 and HNCO preferred to be formed at lower temperatures and HCN tended to form at higher temperatures. It is worth noting that NO was also an important product. X-ray photoelectron spectroscopy (XPS) was performed to analyze the nitrogen species in rice straw. The result showed that amino-N (N-A) was the main form of nitrogen which accounted for 88.85%. Pyrrolic-N (N-5) was also identified and occupied the rest. Then nitrogen modeling compounds, glycine and pyrrole, were appropriately selected based on the results of XPS to well understand the nitrogen release mechanism during pyrolysis of rice straw. The formation routes of all the nitrogen gaseous components were confirmed. NH_3, HNCO and NO were originated from the decomposition of amino-N. While both amino-N and pyrrolic-N produced HCN. NO was not detected during the pyrolysis of pyrrole and a little NO was found during the pyrolysis of glycine. Hence, it can be deduced that the large amount of NO formed during the pyrolysis of rice straw was due to the direct oxidization reaction of –NH and –OH, the latter is abundant in the raw material. In order to provide evidence for this deduction, cellulose was added to increase the amount of –OH and co-pyrolysis of cellulose and glycine was conducted. The effect of –OH on the formation of NO was confirmed. Then, the release mechanism of fuel-N into NO_x and N_2O precursors during rice straw pyrolysis was concluded based on the experimental results.

Keywords: nitrogen; biomass; amino acid; pyrrole; NO_x; pyrolysis

1. Introduction

Biomass is considered as one of the most promising alternative energy because of its renewability and carbon-neutrality [1–8]. About 300 million tons of straw wastes, as well as the same amount of forestry wastes, are generated in China [9]. Direct combustion power generation is the major technology for large scale utilization of biomass [10]. Rice straw, which is abundant in southern China, dominates the amount of straw wastes, and is widely used as a fuel for biomass power plants. NO_x and N_2O, which can lead to environmental pollution [11], are the main gaseous pollutants during biomass combustion although the nitrogen content in most biomass is lower than that of coal. It is well known that pyrolysis is the first step of combustion, during which, part of the nitrogen in biomass is converted into NO_x and N_2O precursors (that is, NH_3, HCN, HNCO, et al.). These precursors will produce NO_x and N_2O via subsequent combustion. It was reported that about 80% of the nitrogen in biomass is released into gaseous precursors during pyrolysis at temperatures above 850–900 K [12].

It means that most of NO_x and N_2O originate from the combustion of volatile-N. Hence, it is necessary to understand the release mechanism of nitrogen during pyrolysis well, so that the emission of NO_x can be reduced by appropriate in-furnace low-nitrogen combustion measures.

Researches have been conducted to investigate the nitrogen release during biomass pyrolysis. It was reported that the gaseous components generally contain NH_3, HCN, HNCO, and NO [13–15]. Two approaches, chemical method and thermogravimetry infrared spectrum (TG-FTIR) method, were frequently used to research the conversion of fuel-N into gaseous nitrogen components.

Chemical method was carried out by many researches [13,14,16–22]. In those studies, NH_3 and HCN were absorbed by acid and alkaline solutions to form NH_4^+ and CN^-, respectively. The total yields of NH_3 and HCN could be confirmed based on the ion concentrations of NH_4^+ and CN^- in the solutions. However, the yield of NH_3 was actually the sum of NH_3 and HNCO. HNCO, the precursor of N_2O [23], could not be investigated due to the reaction HNCO + $H_2O \rightarrow NH_3$ + CO_2 [10,15–17]. The yield of NO was also not measured. Additionally, only the yields of NH_3 and HCN could be measured by chemical method, rather than the dynamic variation of concentrations for the precursors.

The nitrogen release was also studied by TG-FTIR [15,24–27], during which, the temperature of the sample was heated from ambient temperature to a higher temperature at a certain heating rate. However, the temperature of the sample was instantly heated up in an industrial combustor. For this reason, the results obtained from those researches could not accurately represent the nitrogen conversion in industrial combustors.

Rice straw is a typical agricultural residue and contains a higher nitrogen content, therefore, it was employed to investigate the release of fuel-N into NO_x and N_2O precursors during pyrolysis. The conversion of fuel-N into gaseous components during rice straw pyrolysis was researched in a few previous studies [17,28]. Yuan et al. [14] investigated the fuel-N conversion characteristic during rapid pyrolysis of rice straw at temperatures ranging from 600 to 1200 °C using a high frequency furnace. The yields of NH_3 and HCN were measured by chemical method. The results showed that HCN was the main nitrogen product while little NH_3 was found. Ren et al. [28] researched the formation of NO_x precursors during rice straw pyrolysis using TG-FTIR. They found that HCN and HNCO were the main nitrogen products. However, the results obtained from previous studies were based on TG-FTIR or chemical method, the shortcomings of which were discussed above.

A review of literatures shows that researches on nitrogen release during the pyrolysis of rice straw are rare and the release mechanism is still not well understood. Therefore, pyrolysis experiments of rice straw were conducted in a horizontal tube furnace in this study, and the concentrations of NH_3, HCN, HNCO, and NO were accurately and dynamically monitored by a FTIR gas analyzer (Gasmet DX4000, Gasmet Technologies Inc., Helsinki, Finland) during the whole reaction process at temperatures ranging from 500 to 900 °C. Compared with previous studies, in which chemical method was employed, the concentrations of gaseous nitrogen products were on-line monitored, not only the yields. HNCO was also measured in current work. Besides, different from TG, the temperature of the sample could be heated up to the set value instantly so that the pyrolysis process could be more similar to that of an industrial combustor.

It was reported that the nitrogen conversion mechanism of biomass could be explained by nitrogen modeling compounds to some extent [23,29–33], while X-ray photoelectron spectroscopy (XPS) was reliable to investigate the nitrogen occurrence form in biomass [12,34–36]. Therefore, in order to further understand the fuel-N release mechanism during pyrolysis, XPS was performed to analyze the occurrence form in rice straw, and the appropriate nitrogen modeling compounds were selected according to the XPS result.

2. Materials and Methods

2.1. Materials

Rice straw, a widely available biomass raw material in China, was employed. The samples were first dried for 2 h at 105 °C and then pulverized. The particle size was between 0.15 and

0.25 mm. Proximate analysis of the sample was performed using an Automatic Industrial Analyzer (5E-MAG6700, Kaiyuan Instruments Co., Changsha, China). Ultimate analysis was conducted with an elemental analyzer (LECO-CHNS932, LECO Co., St. Joseph, MI, USA). The results are shown in Table 1.

Table 1. Proximate (ar, wt. %) and ultimate analysis (ad, wt. %) of rice straw.

Proximate Analysis				Ultimate Analysis				
M [a]	A [a]	V [a]	FC [a]	C	H	N	S	O
1.51	11.31	69.09	18.09	42.66	5.68	0.64	0.44	39.10

[a] M, A, V, FC represent moisture, ash, volatile and fixed carbon, respectively.

The occurrence form of nitrogen in rice straw was characterized using XPS (Escalab 250Xi, Thermo Fisher Scientific, Waltham, MA, USA), equipped with Al Kα radiation source. The constant analyzer energy (CAE) mode with 30 eV pass energy was used for survey spectra and 20 eV was used for high resolution spectra. To calibrate the binding energy, the C1s peak was set to 284.8 eV and the Shirley background was subtracted from the spectra. The N1s peaks were fitted using Gaussian (80%)−Lorentzian (20%) and established with XPSpeak. According to the result of XPS, as shown in Figure 1, the main peak at 399.9 eV was assigned to amino-A and the other peak at 400.5 eV was assigned to pyrrolic-N. Thus, the nitrogen in rice straw was composed of 11.15% pyrrolic-N (N-5) and 88.85% amino-N (N-A). Therefore, Pyrrole and glycine, commercial reagents with high purity of 98% or more, were chosen as the modeling compounds for mechanism research. Cellulose, with a purity of 99%, was also purchased as an additive to research the effect of –OH on NO formation. All of the modeling compounds were purchased from Sigma-Aldrich (St. Louis, MO, USA).

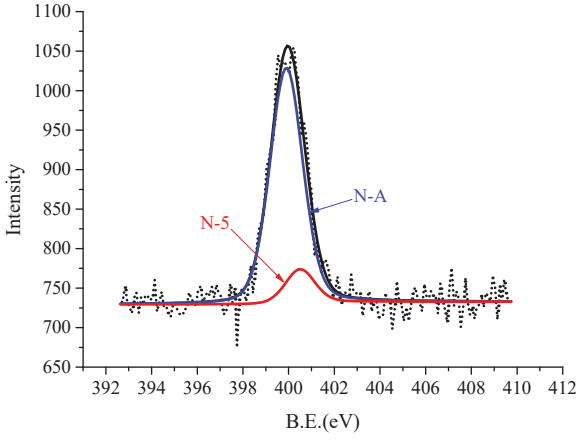

Figure 1. Nitrogen species in rice straw.

2.2. Experimental Methods

Experiments were conducted in a horizontal tube furnace reactor system, as shown in Figure 2. The furnace was 800 mm long and the inner diameter was 60 mm. The quartz tube was 1000 mm long and the inner diameter was 36 mm. The temperature of the reaction zone was controlled by a thermocouple connected to a temperature controller. The monitoring point of the thermocouple was set inside the quartz tube where the solid materials were placed to ensure an accurate temperature control. During experiments, 20 mg samples (rice straw or modeling compounds) were employed and were placed in a quartz boat (with length of 100 mm, width of 25 mm, and thickness of 1 mm). The reactor was heated by an electric furnace up to the given temperature ranging from 500 to 900 °C and maintained for 15 min. Then, the quartz boat that contained the sample was quickly pushed into the reaction zone. The carrier gas was argon (Ar) with a high purity of 99.999%. The gas flow rate was controlled at 4 L/min by mass flow meters. The volatiles released during pyrolysis were removed out from the reactor immediately by the carrier gas to keep a short residence time (less than 1.5 s) and to avoid the secondary reactions. Gasmet DX4000 (Gasmet DX 4000, Gasmet Technologies Inc., Helsinki, Finland), a kind of Fourier transform infrared gas analyzer, was employed to measure the concentrations of nitrogen containing components (NH_3, HCN, HNCO, and NO) on line. A sampling line was connected between the reactor and the gas analyzer, the temperature of which was maintained at 180 °C to avoid secondary pyrolysis and components condensing. The measurement time interval of the analyzer was set to be 3 s. Each test was repeated for three times to make sure that the relative standard deviations were less than 5%.

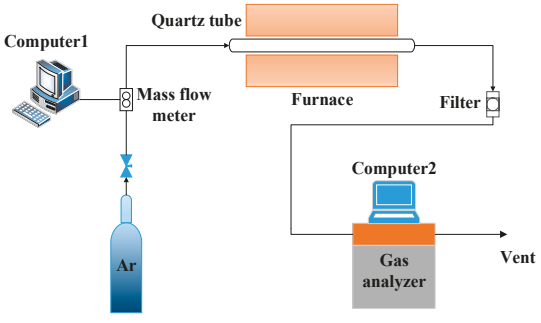

Figure 2. Schematic diagram of the horizontal tube furnace reactor system.

The convert ratios of fuel-N to gaseous nitrogen containing products (NH_3, HCN, HNCO, and NO) were calculated by Equation (1):

$$R_{\text{gas-N}} = \frac{\int c dt \times Q}{22.4 \times 10^6 \times 60} \times \frac{M_{\text{N}}}{m \times \text{N}_{\text{pc}}} \times 100\% \quad (1)$$

where $R_{\text{gas-N}}$ is the convert ratio of fuel-N to gaseous nitrogen components (%), c is the concentration of gaseous species (mg/Nm^3), t is the measuring time (s), Q is the flow rate of flue gas (L/min), M_{N} is the molar mass of nitrogen (g/mol), and m is the weight of initial rice straw sample (g).

3. Results and Discussion

3.1. Nitrogen Release during Pyrolysis of Rice Straw

NH_3, HCN, HNCO, and NO were all found during the pyrolysis experiments of rice straw. Their concentrations were measured by a FTIR gas analyzer and recorded online. Figure 3 shows the release behavior of these gaseous products at temperatures ranging from 500 to 900 °C.

As shown in Figure 3, the peaks of the concentration curves of all the species appeared earlier as the temperature increased. This means that the chemical bond was broken more easily and that the reaction was more drastic at higher temperatures. NH_3 was detected at lower temperatures. Its concentration decreased with increasing temperature and totally disappeared at temperatures higher than 700 °C. HNCO also decreased with rising temperature, and was disappeared at 800 °C. On the contrary, HCN was first detected at 600 °C and the concentration increased with an increasing temperature. It should be noted that NO was also a very important product, the concentration of which firstly increased with temperature and reached its maximum at 800 °C and then decreased.

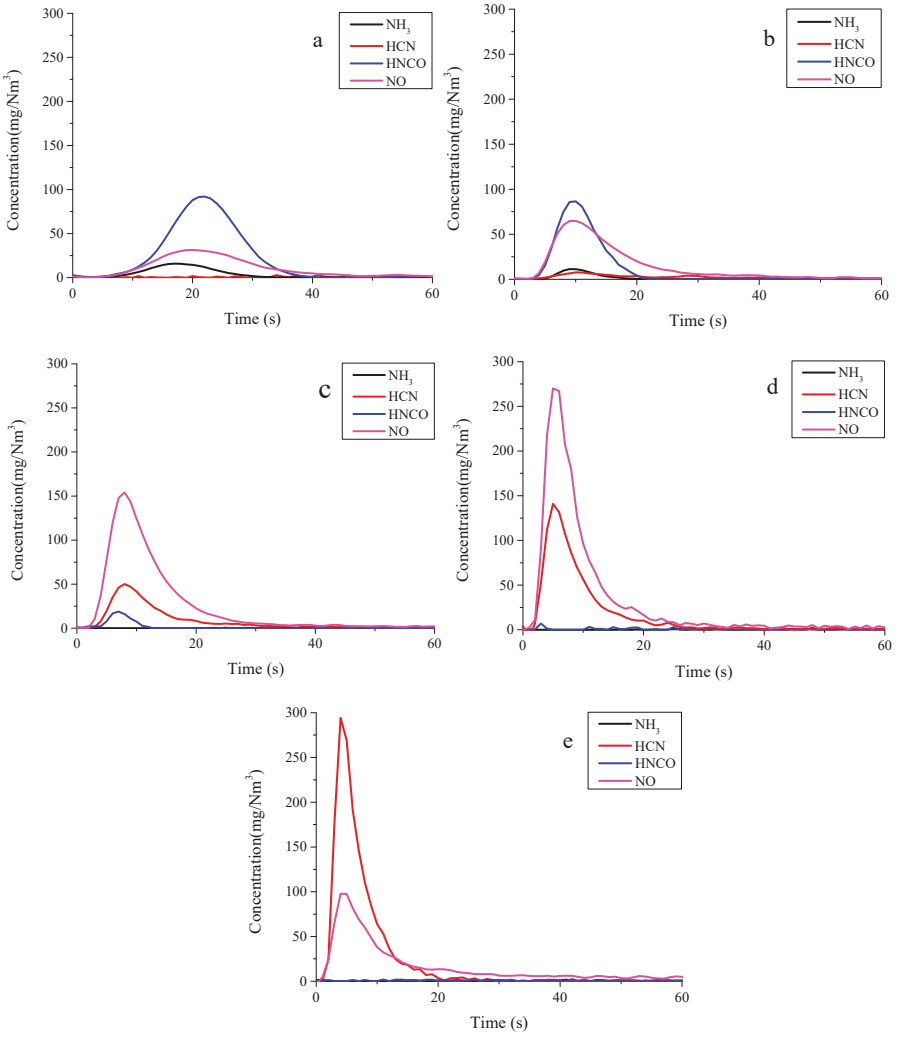

Figure 3. Release behaviors of nitrogen gaseous products during rice straw pyrolysis. (**a**) 500 °C, (**b**) 600 °C, (**c**) 700 °C, (**d**) 800 °C, (**e**) 900 °C.

The convert ratios of fuel-N to gaseous products are shown in Figure 4. The convert ratios of fuel-N to NH_3 and HNCO decreased, while that of HCN increased with the increasing temperature.

Previous researchers also reported that HCN is preferentially formed at a higher temperature or at a higher heating rate, and that NH_3 is formed at a lower temperature or a lower heating rate [4,17,23,24]. Nitrogen release during rice straw pyrolysis was also studied by other researchers [17,28]. They also reported that HCN was the main product and little NH_3 was found. These results are in accordance with the result of the current study. The convert ratio of fuel-N to NO, a very important product, firstly increased and reached its maximum yield at 800 °C, and then decreased.

It is well known that the nitrogen species in biomass is mostly composed of amino acids [2,10,23,28]. The primary decomposition step of amino acid during pyrolysis contains decarboxylation, dehydration and deamination [32,33,37]. In present experiments, NH_3 was produced at temperatures lower than 700 °C, while at higher temperatures, NH_3 thoroughly disappeared. It was reported that amino acid could be converted into heterocyclic nitrogen compounds during thermal treatment [2], which would then lead to the decrease of amino acid. Due to this, the convert ratio of fuel-N to NH_3 decreased with the increase of temperature.

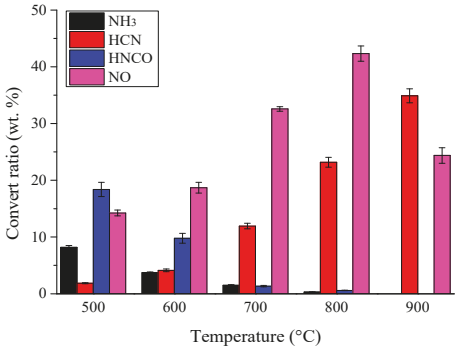

Figure 4. Convert ratios of fuel-N to gaseous products during pyrolysis of rice straw.

Cyclic amide, which was produced by dehydration, could be decomposed into HNCO and HCN further [15,23,32]. The convert ratio of fuel-N to HNCO decreased with the increase of temperature, while the reverse of HCN was observed. This corresponded with a previous study [38]. Therefore, the decomposition of cyclic amide has a high selectivity [15,23]. At lower temperatures, the convert ratio of fuel-N to HNCO was larger than that of HCN, while HCN was the main product at the higher temperatures. Hansson [38] pointed out that the activation energy for the formation of HNCO was lower than that of HCN during the decomposition of all cyclic amides. Besides, HNCO could be decomposed into HCN at high temperatures via the following reaction [24,32]:

$$\mathrm{HNCO} \rightarrow \mathrm{HCN} + \mathrm{CO}, \quad (2)$$

which also led to the decrease of HNCO.

The peaks of NO concentration curves appeared simultaneously with that of other products at the same temperature, even a little earlier at lower temperatures. Hence, NO was definitely attributed to the direct oxidization reaction of N-sites with –OH, which is abundant in rice straw. The convert ratio of fuel-N to NO firstly increased with the increase of temperature and decreased at 900 °C. It was probably caused by the reduction reaction of NO and CO, which was catalyzed by inorganic impurities and even the chars at high temperatures [12,39]. CO was largely generated during pyrolysis and the reduction reaction easily occurred at higher temperatures. The concentration of CO was also tested by the gas analyzer in the experiments, as shown in Figure 5, which was powerful evidence for this explanation.

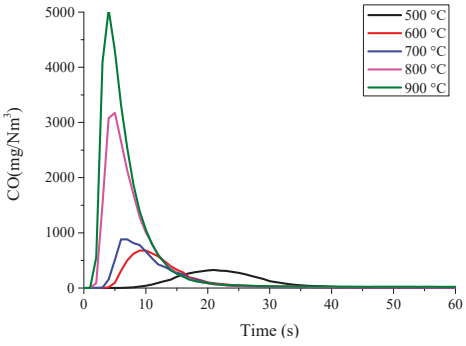

Figure 5. Variation of CO concentration with temperature.

3.2. Nitrogen Release during Pyrolysis of Nitrogen Modeling Compounds

Nitrogen in rice straw consisted of N-5 and N-A, as shown in Figure 1. It was reported that glycine is one of the major amino acids in agricultural straw [40]. Therefore, glycine and pyrrole were employed as modeling compounds to provide evidence for the release mechanism of fuel-N into gaseous components proposed above.

3.2.1. Pyrolysis of Glycine

Figure 6 shows the nitrogen release behavior during glycine pyrolysis at different temperatures. The concentrations of gaseous nitrogen containing products were much higher than that of rice straw. This was attributed to the high purity of glycine as well as its higher nitrogen content of 18.7%. The peaks of the concentration curves also appeared much earlier with the increasing temperature. The concentrations of HCN and NH_3 increased with the rising temperature, while the concentrations of other products firstly increased, and reached their maximum at 800 °C, then decreased.

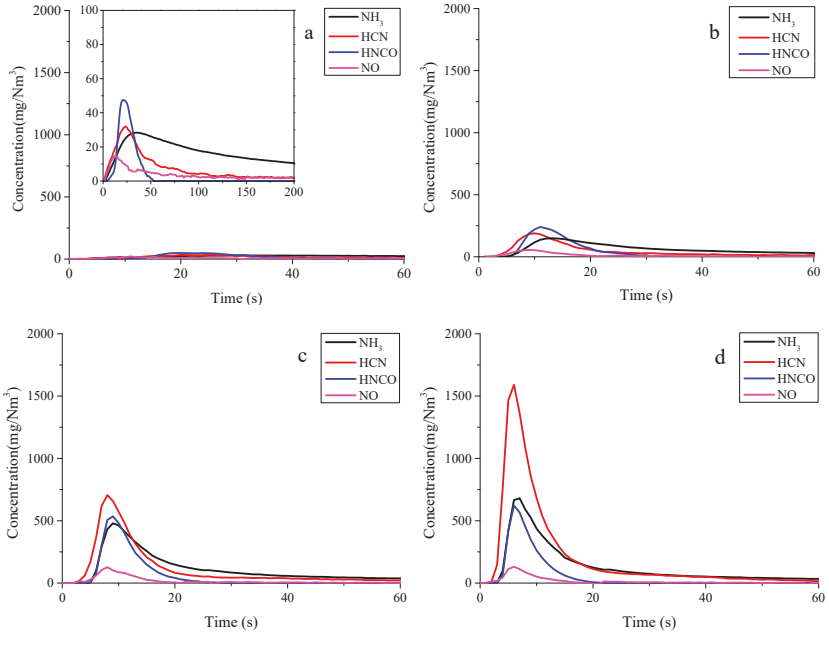

Figure 6. *Cont.*

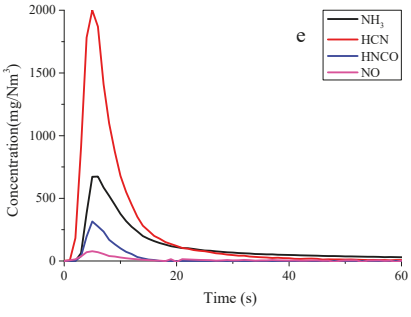

Figure 6. Release behavior of nitrogen gaseous products during glycine pyrolysis. (**a**) 500 °C, (**b**) 600 °C, (**c**) 700 °C, (**d**) 800 °C, (**e**) 900 °C.

The convert ratios of fuel-N into gaseous nitrogen containing products are shown in Figure 7. Different from the pyrolysis of rice straw, the convert ratios of fuel-N to NH_3 and HNCO firstly increased, and reached their maximum at 800 °C, then decreased. In particular, the proportion of NO was much smaller than that of rice straw.

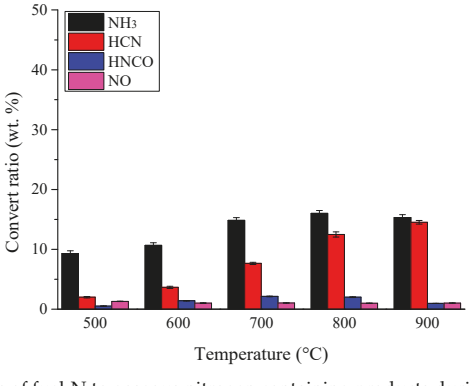

Figure 7. Convert ratios of fuel-N to gaseous nitrogen containing products during pyrolysis of glycine.

It was reported that during the pyrolysis of glycine, the main primary decomposition reactions are deamination and dehydration [33]. NH_3 and HNCO were formed via Equations (3) and (4). Additionally, the decomposition reaction of primary amines, as well as the bimolecular reactions between imine and amine, could also produce NH_3 [41].

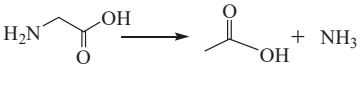

(3)

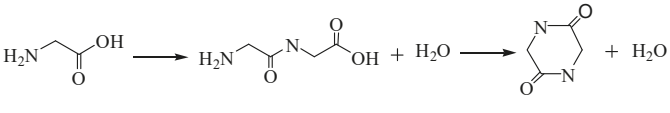

(4)

HNCO was produced by the decomposition of cyclic amino, which was formed by the dehydration reaction, as shown in Equation (5). Meanwhile, the cracking of cyclic amino also produced HCN (see Equation (6)). HNCO could be further decomposed into HCN and CO at higher temperatures, and then the reduction of HNCO could be explained.

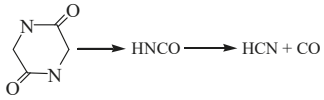

(5)

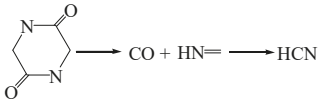

(6)

The peaks of NO concentration curves appeared a little earlier than that of other products at the same temperature. Hence, it is undoubted that NO was formed by the direct oxidization reaction of –NH with –OH. The less convert ratio of NO might be caused by the lack of –OH in glycine when compared to that rice straw.

3.2.2. Pyrolysis of Pyrrole

HCN was found to be the only product and was detected at temperatures higher than 700 °C during the pyrolysis of pyrrole, as shown in Figure 8. The concentration of HCN at higher temperatures was much higher than that of rice straw. It was caused by the high purity of pyrrole and the high nitrogen content of 20.90%.

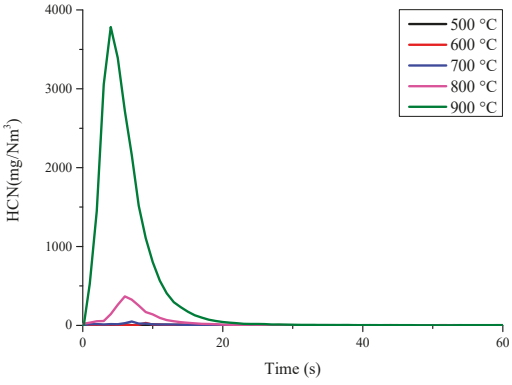

Figure 8. Variation of HCN concentration with temperature during pyrrole pyrolysis.

As it was reported in previous researches in regard to pyrrole pyrolysis [41–43], C–N was broken to generate an intermediate that decomposed into HCN and $\dot{C}H_2$–CH=$\dot{C}$H subsequently, as shown in Equation (7). The formation of HCN tended to occur at temperatures higher than 700 °C [17,44]. This highly corresponded with the current study.

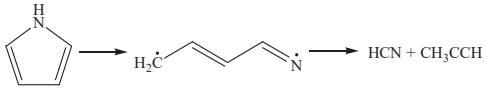

(7)

3.2.3. Effect of –OH on the Formation of NO

NO was a major product during rice straw pyrolysis, however, it was not detected during the pyrolysis of pyrrole and little was formed during the pyrolysis of glycine. Therefore, it can be deduced that the large amount of NO formed during pyrolysis of rice straw was due the direct oxidization reaction of –NH and –OH, which is abundant in rice straw.

Cellulose is the major component in lignocellulosic biomass, which accounts for 32–47% [45,46]. The percentage of cellulose in rice straw is 35% [46]. In order to prove the deduction of NO formation, cellulose was mixed into glycine to increase the amount of –OH and co-pyrolysis of glycine and cellulose was conducted. The mass ratio of cellulose to glycine was 1:4. The convert ratios of fuel-N to NO are shown in Figure 9. It is obvious that the convert ratio of NO increased with the addition of –OH. Furthermore, the ratio of –OH to amino acid in rice straw is much higher than in the mixed samples. Therefore, the larger amount of NO that is produced during pyrolysis of rice straw than model amino acid could be explained.

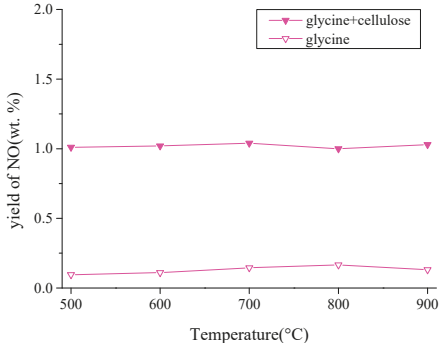

Figure 9. Convert ratios of fuel-N to NO during pyrolysis of glycine and co-pyrolysis of glycine and cellulose.

3.3. Mechanism of Nitrogen Release during Rice Straw Pyrolysis

As discussed above, NH_3 and HNCO were derived from the pyrolysis of amino acid. HCN was produced by pyrolysis of both amino acid and pyrrole. NO was an important product during rice straw pyrolysis, while a small amount of NO was found during amino acid pyrolysis, and it was not detected during pyrrole pyrolysis. Therefore, the formation of NO was attributed to the oxidization reaction of –NH and –OH, which is abundant in rice straw. This was proved by the co-pyrolysis of glycine and cellulose.

The nitrogen in rice straw was more complex than the model compounds of glycine and pyrrole. The transformation of nitrogen was reported to be affected by mineral matters [28,29,47] and the three major components of raw material, that is, cellulose, hemicellulose, and lignin [10,30,40] during pyrolysis of biomass. However, the research on modeling compounds could explain the nitrogen release route during pyrolysis due to the definite nitrogen occurrence forms in rice straw analyzed by XPS. Thus, the release mechanism of fuel-N into NO_x and N_2O precursors during rice straw pyrolysis was concluded in Figure 10.

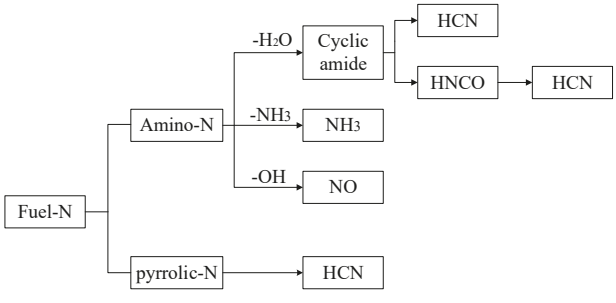

Figure 10. Release mechanism of fuel-N during rice straw pyrolysis.

4. Conclusions

Pyrolysis of rice straw was conducted to research the release mechanism of fuel-N into NO_x and N_2O precursors. The concentration variations of gaseous nitrogen components, i.e., NH_3, HCN, HNCO, and NO were dynamically monitored. The formation of gaseous nitrogen components was found to be highly dependent on temperature. NH_3 and HNCO preferred to be formed at lower temperatures and HCN tended to form at higher temperatures. It is worth noting that NO was also an important product.

The nitrogen occurrence form in rice straw was analyzed by XPS. Amino-N and pyrrolic-N were identified. Therefore, glycine, as well as pyrrole, were chosen as the nitrogen modeling compounds based on the results of XPS to understand the release mechanism of nitrogen during rice straw pyrolysis well. The formation routes of all nitrogen gaseous components were confirmed. NH_3, HNCO, and NO originated from the decomposition of amino acid. HCN was formed by the decomposition of both amino acid and pyrrole. NO was not detected during pyrolysis of pyrrole, and a little NO was found during amino acid pyrolysis. Therefore, a considerable proportion of NO formed during the pyrolysis of rice straw was due to the direct oxidization reaction of –NH and –OH in the raw material. To provide evidence for this proposal, cellulose was selected as an additive to increase the amount of –OH and co-pyrolysis of glycine and cellulose was conducted. Then, the release mechanism of fuel-N into NO_x and N_2O precursors during rice straw pyrolysis was proposed based on the experimental results. In future research, various biomass materials with different nitrogen occurrence forms would be employed to investigate the effect of fuel type on nitrogen release.

Acknowledgments: This work is supported by the National Natural Science Foundation of China (NO. 51336008).

Author Contributions: Zhongyang Luo and Chunjiang Yu conceived and designed the experiments; Xiaorui Liu performed the experiments; Xiaorui Liu analyzed the data; Hanchao Tu and Bitao Jin contributed reagents/materials/analysis tools; Xiaorui Liu wrote the paper.

Conflicts of Interest: The authors declare no conflict of interest.

References

1. Tripathi, M.; Sahu, J.N.; Ganesan, P. Effect of process parameters on production of biochar from biomass waste through pyrolysis. *Renew. Sustain. Energy Rev.* **2016**, *55*, 467–481. [CrossRef]
2. Chen, H.; Si, Y.; Chen, Y.; Yang, H.; Chen, D.; Chen, W. NO_x precursors from biomass pyrolysis: Distribution of amino acids in biomass and Tar-N during devolatilization using model compounds. *Fuel* **2017**, *187*, 367–375. [CrossRef]
3. Shan, F.; Lin, Q.; Zhou, K.; Wu, Y.; Fu, W.; Zhang, P.; Song, L.; Shao, C.; Yi, B. An experimental study of ignition and combustion of single biomass pellets in air and oxy-fuel. *Fuel* **2017**, *188*, 277–284. [CrossRef]
4. Wang, S.; Hu, Y.; Wang, Q.; Xu, S.; Lin, X.; Ji, H.; Zhang, Z. TG-FTIR-MS analysis of the pyrolysis of blended seaweed and rice husk. *J. Therm. Anal. Calorim.* **2016**, *126*, 1689–1702. [CrossRef]
5. Houshfar, E.; Løvås, T.; Skreiberg, Ø. Experimental Investigation on NO_x Reduction by Primary Measures in Biomass Combustion: Straw, Peat, Sewage Sludge, Forest Residues and Wood Pellets. *Energies* **2012**, *5*, 270–290. [CrossRef]
6. Molina-Moreno, V.; Leyva-Díaz, J.; Sánchez-Molina, J. Pellet as a Technological Nutrient within the Circular Economy Model: Comparative Analysis of Combustion Efficiency and CO and NO_x Emissions for Pellets from Olive and Almond Trees. *Energies* **2016**, *9*, 777. [CrossRef]
7. Yang, X.; Wang, H.; Strong, P.J.; Xu, S.; Liu, S.; Lu, K.; Sheng, K.; Guo, J.; Che, L.; He, L.; et al. Thermal Properties of Biochars Derived from Waste Biomass Generated by Agricultural and Forestry Sectors. *Energies* **2017**, *10*, 469. [CrossRef]
8. Gao, P.; Xue, L.; Lu, Q.; Dong, C. Effects of Alkali and Alkaline Earth Metals on N-Containing Species Release during Rice Straw Pyrolysis. *Energies* **2015**, *8*, 13021–13032. [CrossRef]
9. Ren, X.; Sun, R.; Meng, X.; Vorobiev, N.; Schiemann, M.; Levendis, Y.A. Carbon, sulfur and nitrogen oxide emissions from combustion of pulverized raw and torrefied biomass. *Fuel* **2017**, *188*, 310–323. [CrossRef]

10. Ren, Q.; Zhao, C. Evolution of fuel-N in gas phase during biomass pyrolysis. *Renew. Sustain. Energy Rev.* **2015**, *50*, 408–418. [CrossRef]
11. Ghouma, I.; Jeguirim, M.; Sager, U.; Limousy, L.; Bennici, S.; Däuber, E.; Asbach, C.; Ligotski, R.; Schmidt, F.; Ouederni, A. The Potential of Activated Carbon Made of Agro-Industrial Residues in NO_x Immissions Abatement. *Energies* **2017**, *10*, 1508. [CrossRef]
12. Glarborg, P.; Jensen, A.D.; Johnsson, J.E. Fuel nitrogen conversion in solid fuel fired systems. *Prog. Energy Combust. Sci.* **2003**, *29*, 89–113. [CrossRef]
13. Chen, H.; Wang, Y.; Xu, G.; Yoshikawa, K. Fuel-N Evolution during the Pyrolysis of Industrial Biomass Wastes with High Nitrogen Content. *Energies* **2012**, *5*, 5418–5438. [CrossRef]
14. Yuan, S.; Zhou, Z.J.; Li, J.; Chen, X.L.; Wang, F.C. HCN and NH_3 (NO_x precursors) released under rapid pyrolysis of biomass/coal blends. *J. Anal. Appl. Pyrolysis* **2011**, *92*, 463–469. [CrossRef]
15. Ren, Q.; Zhao, C.; Wu, X.; Liang, C.; Chen, X.; Shen, J.; Wang, Z. Formation of NO_x precursors during wheat straw pyrolysis and gasification with O_2 and CO_2. *Fuel* **2010**, *89*, 1064–1069. [CrossRef]
16. Yuan, S.; Chen, X.L.; Li, W.F.; Liu, H.F.; Wang, F.C. Nitrogen conversion under rapid pyrolysis of two types of aquatic biomass and corresponding blends with coal. *Bioresour. Technol.* **2011**, *102*, 10124–10130. [CrossRef] [PubMed]
17. Yuan, S.; Zhou, Z.J.; Li, J.; Chen, X.L.; Wang, F.C. HCN and NH_3 Released from Biomass and Soybean Cake under Rapid Pyrolysis. *Energy Fuels* **2010**, *24*, 6166–6171. [CrossRef]
18. Tian, F.J.; Yu, J.; McKenzie, L.J.; Hayashi, J.I.; Li, C.Z. Conversion of Fuel-N into HCN and NH_3 during the Pyrolysis and Gasification in Steam: A Comparative Study of Coal and Biomass. *Energy Fuels* **2007**, *21*, 517–521. [CrossRef]
19. Tian, F.J.; Yu, J.L.; Mckenzie, L.J.; Hayashi, J.I.; Chiba, T.; Li, C.Z. Formation of NO precursors during the pyrolysis of coal and biomass. Part VII. Pyrolysis and gasification of cane trash with steam. *Fuel* **2005**, *84*, 371–376. [CrossRef]
20. Chang, L.; Xie, Z.; Xie, K.C.; Pratt, K.C.; Hayashi, J.I.; Chiba, T.; Li, C.Z. Formation of NO_x precursors during the pyrolysis of coal and biomass. Part VI. Effects of gas atmosphere on the formation of NH_3 and HCN. *Fuel* **2003**, *82*, 1159–1166. [CrossRef]
21. Tan, L.L.; Li, C. Formation of NO_x and SO_x precursors during the pyrolysis of coal and biomass. Part I. Effects of reactor configuration on the determined yields of HCN and NH_3 during pyrolysis. *Fuel* **2000**, *79*, 1883–1889. [CrossRef]
22. Zhan, H.; Yin, X.; Huang, Y.; Yuan, H.; Xie, J.; Wu, C.; Shen, Z.; Cao, J. Comparisons of Formation Characteristics of NO_x Precursors during Pyrolysis of Lignocellulosic Industrial Biomass Wastes. *Energy Fuels* **2017**, *31*, 9557–9567. [CrossRef]
23. Hansson, K.M.; Samuelsson, J.; Tullin, C.; Åmand, L.E. Formation of HNCO, HCN, and NH_3 from the pyrolysis of bark and nitrogen-containing model compounds. *Combust. Flame* **2004**, *137*, 265–277. [CrossRef]
24. Zhu, X.; Yang, S.; Wang, L.; Liu, Y.; Qian, F.; Yao, W.; Zhang, S.; Chen, J. Tracking the conversion of nitrogen during pyrolysis of antibiotic mycelial fermentation residues using XPS and TG-FTIR-MS technology. *Environ. Pollut.* **2016**, *211*, 20–27. [CrossRef] [PubMed]
25. Wang, X.; Si, J.; Tan, H.; Ma, L.; Pourkashanian, M.; Xu, T. Nitrogen, Sulfur, and Chlorine Transformations during the Pyrolysis of Straw. *Energy Fuels* **2010**, *24*, 5215–5221. [CrossRef]
26. De Jong, W.; Di Nola, G.; Venneker, B.C.; Spliethoff, H.; Wójtowicz, M.A. TG-FTIR pyrolysis of coal and secondary biomass fuels: Determination of pyrolysis kinetic parameters for main species and NO_x precursors. *Fuel* **2007**, *86*, 2367–2376. [CrossRef]
27. Becidan, M.; Skreiberg, Ø.; Hustad, J.E. NO_x and N_2O Precursors (NH_3 and HCN) in Pyrolysis of Biomass Residues. *Energy Fuels* **2007**, *21*, 1173–1180. [CrossRef]
28. Ren, Q.; Zhao, C. Effect of mineral matter on the formation of NO_x precursors during biomass pyrolysis. *J. Anal. Appl. Pyrolysis* **2009**, *85*, 447–453. [CrossRef]
29. Ren, Q.; Zhao, C. NO_x and N_2O Precursors from Biomass Pyrolysis: Role of Cellulose, Hemicellulose and Lignin. *Environ. Sci. Technol.* **2013**, *47*, 8955–8961. [CrossRef] [PubMed]
30. Ren, Q.; Zhao, C. NO_x and N_2O precursors (NH_3 and HCN) from biomass pyrolysis: Interaction between amino acid and mineral matter. *Appl. Energy* **2013**, *112*, 170–174. [CrossRef]
31. Ren, Q.; Zhao, C. NO_x and N_2O Precursors from Biomass Pyrolysis: Nitrogen Transformation from Amino Acid. *Environ. Sci. Technol.* **2012**, *46*, 4236–4240. [CrossRef] [PubMed]

32. Jie, L.; Yuwen, L.; Jingyan, S.; Zhiyong, W.; Ling, H.; Xi, Y.; Cunxin, W. The investigation of thermal decomposition pathways of phenylalanine and tyrosine by TG–FTIR. *Thermochim. Acta* **2008**, *467*, 20–29. [CrossRef]
33. Li, J.; Wang, Z.; Yang, X.; Hu, L.; Liu, Y.; Wang, C. Evaluate the pyrolysis pathway of glycine and glycylglycine by TG–FTIR. *J. Anal. Appl. Pyrolysis* **2007**, *80*, 247–253. [CrossRef]
34. Titantah, J.T.; Lamoen, D. Carbon and nitrogen 1s energy levels in amorphous carbon nitride systems: XPS interpretation using first-principles. *Diam. Relat. Mater.* **2007**, *16*, 581–588. [CrossRef]
35. Schmiers, H.; Friebel, J.; Streubel, P.; Hesse, R.; Köpsel, R. Change of chemical bonding of nitrogen of polymeric N-heterocyclic compounds during pyrolysis. *Carbon* **1999**, *37*, 1965–1978. [CrossRef]
36. Jansen, R.J.J.; van Bekkum, H. XPS of nitrogen-containing functional groups on activated carbon. *Carbon* **1995**, *33*, 1021–1027. [CrossRef]
37. Deng, L.; Jin, X.; Zhang, Y.; Che, D. Release of nitrogen oxides during combustion of model coals. *Fuel* **2016**, *175*, 217–224. [CrossRef]
38. Hansson, K.; Samuelsson, J.; Åmand, L.; Tullin, C. The temperature's influence on the selectivity between HNCO and HCN from pyrolysis of 2,5-diketopiperazine and 2-pyridone. *Fuel* **2003**, *82*, 2163–2172. [CrossRef]
39. Johnsson, J.E. Formation and reduction of nitrogen oxides in fluidized-bed combustion. *Fuel* **1994**, *73*, 1398–1415. [CrossRef]
40. Ren, Q.; Zhao, C.; Chen, X.; Duan, L.; Li, Y.; Ma, C. NO_x and N_2O precursors (NH_3 and HCN) from biomass pyrolysis: Co-pyrolysis of amino acids and cellulose, hemicellulose and lignin. *Proc. Combust. Inst.* **2011**, *33*, 1715–1722. [CrossRef]
41. Lifshitz, A.; Tamburu, C.; Suslensky, A. Isomerization and Decomposition of Pyrrole at Elevated Temperatures: Studies with a Single-Pulse Shock Tube. *J. Chem. Phys.* **1989**, *93*, 5802–5808. [CrossRef]
42. Zhai, L.; Zhou, X.; Liu, R. A Theoretical Study of Pyrolysis Mechanisms of Pyrrole. *J. Phys. Chem. A* **1999**, *103*, 3917–3922. [CrossRef]
43. Mackie, J.C.; Colket, M.B.; Nelson, P.F.; Esler, M. Shock Tube Pyrolysis of Pyrrole and Kinetic Modeling. *Int. J. Chem. Kinet.* **1991**, *23*, 733–760. [CrossRef]
44. Li, C.; Tan, L.L. Formation of NO_x and SO_x precursors during the pyrolysis of coal and biomass. Part III. Further discussion on the formation of HCN and NH_3 during pyrolysis. *Fuel* **2000**, *79*, 1899–1906. [CrossRef]
45. Binod, P.; Sindhu, R.; Singhania, R.R.; Vikram, S.; Devi, L.; Nagalakshmi, S.; Kurien, N.; Sukumaran, R.K.; Pandey, A. Bioethanol production from rice straw: An overview. *Bioresour. Technol.* **2010**, *101*, 4767–4774. [CrossRef] [PubMed]
46. Saha, B.C. Hemicellulose bioconversion. *J. Ind. Microbiol. Biotechnol.* **2003**, *30*, 279–291. [CrossRef] [PubMed]
47. Wei, L.; Wen, L.; Liu, M.; Yang, T. Interaction Characteristics of Mineral Matter and Nitrogen during Sewage Sludge Pyrolysis. *Energy Fuels* **2016**, *30*, 10505–10510. [CrossRef]

© 2018 by the authors. Licensee MDPI, Basel, Switzerland. This article is an open access article distributed under the terms and conditions of the Creative Commons Attribution (CC BY) license (http://creativecommons.org/licenses/by/4.0/).

energies

MDPI

Article

Towards Biochar and Hydrochar Engineering—Influence of Process Conditions on Surface Physical and Chemical Properties, Thermal Stability, Nutrient Availability, Toxicity and Wettability

Alba Dieguez-Alonso [1,*], Axel Funke [2], Andrés Anca-Couce [3], Alessandro Girolamo Rombolà [4], Gerardo Ojeda [5], Jörg Bachmann [6] and Frank Behrendt [1]

1 Institute of Energy Engineering, Technische Universität Berlin, Chair for Energy Process Engineering and Conversion Technologies for Renewable Energies, Fasanenstr. 89, 10623 Berlin, Germany; frank.behrendt@tu-berlin.de
2 Institute of Catalysis Research and Technology (IKFT), Karlsruhe Institute of Technology, Hermann-von-Helmholtz-Platz 1, 76344 Eggenstein-Leopoldshafen, Germany; axel.funke@kit.edu
3 Institute of Thermal Engineering, Graz University of Technology, Inffeldgasse 25b, 8010 Graz, Austria; anca-couce@tugraz.at
4 Department of Chemistry "Giacomo Ciamician", C.I.R.I. Energia Ambiente and C.I.R.S.A., Università di Bologna, Ravenna Campus, Via S. Alberto 163, 48123 Ravenna, Italy; alessandro.rombola@unibo.it
5 Ecological and Forestry Applications Research Centre (CREAF), 08193 Cendanyola del Vallès, Spain; g.ojeda@creaf.uab.cat
6 Institute of Soil Science, Leibniz University of Hannover, Herrenhaeuser Str. 2, 30419 Hannover, Germany; bachmann@ifbk.uni-hannover.de
* Correspondence: alba.dieguezalonso@tu-berlin.de; Tel.: +49-(30)-314-24381

Received: 31 December 2017; Accepted: 11 February 2018; Published: 27 February 2018

Abstract: The impact of conversion process parameters in pyrolysis (maximum temperature, inert gas flow rate) and hydrothermal carbonization (maximum temperature, residence time and post-washing) on biochar and hydrochar properties is investigated. Pine wood (PW) and corn digestate (CD), with low and high inorganic species content respectively, are used as feedstock. CD biochars show lower H/C ratios, thermal recalcitrance and total specific surface area than PW biochars, but higher mesoporosity. CD and PW biochars present higher naphthalene and phenanthrene contents, respectively, which may indicate different reaction pathways. High temperatures (>500 °C) lead to lower PAH (polycyclic aromatic hydrocarbons) content (<12 mg/kg) and higher specific surface area. With increasing process severity the biochars carbon content is also enhanced, as well as the thermal stability. High inert gas flow rates increase the microporosity and wettability of biochars. In hydrochars the high inorganic content favor decarboxylation over dehydration reactions. Hydrochars show mainly mesoporosity, with a higher pore volume but generally lower specific surface area than biochars. Biochars present negligible availability of NO_3^- and NH_4^+, irrespective of the nitrogen content of the feedstock. For hydrochars, a potential increase in availability of NO_3^-, NH_4^+, PO_4^{3-}, and K^+ with respect to the feedstock is possible. The results from this work can be applied to "engineer" appropriate biochars with respect to soil demands and certification requirements.

Keywords: pyrolysis; hydrothermal carbonization; biochar engineering; porosity; nutrients; polycyclic aromatic hydrocarbon (PAH)

1. Introduction

The definitions of biochar provided by the European Biochar Certificate (EBC) [1] and the IBI (International Biochar Initiative) Biochar Standards [2] address biochar properties requirements for its application, as well as methodological standards to assess them, but they do not describe in detail the production process and its influence on biochar properties. As an example, the EBC considers mainly pyrolysis as the process to produce biochar, including gasification as part of the pyrolysis technology spectrum. However, the IBI Biochar Standards consider all forms of thermochemical conversion with limited presence of oxygen as appropriate technologies to produce biochar. Therefore, hydrothermal carbonization (HTC) could be included as well. In recent years, a lot of research has been done in the field of biochar to understand the impact of process conditions on biochar properties, as well as biochar dynamics once applied to soil and, consequently, its potential positive and/or negative impacts on crops, environment and soil. However, as Abiven et al. [3] pointed out, it is necessary to develop tailor-made biochar systems according to individual applications, taking into account soil type, climate and social environments, instead of considering biochar as an universal soil enhancer. Besides, biochar can have other applications, such as its use for soil and water remediation through the adsorption and immobilization of organic and inorganic contaminants [4–7]. Within its agronomic use, and according to a review by Mohan et al. [8], biochar can potentially increase nutrient availability (direct and indirect pathways), water retention, soil organic matter, microbial activity and crop yields. This may contribute to a reduction in nutrient leaching, fertilizer demand or emissions [9–11].

- Direct biochar contribution to nutrient availability relies on the macro- and/or micronutrients that biochar contains and their availability [5,9,10]. This is strongly dependent on the composition of the initial feedstock [10] and on the pyrolysis conditions. High retention of alkali species and P is reported for pyrolysis temperatures below 600–700 °C and low heating rates [12–15], with increase in total, soluble and exchangeable base cations with increasing process severity [13]. However, Uchimiya et al. [16] showed that NaOH-EDTA extractable P increased at 300–350 °C pyrolysis temperature and decreased at higher temperatures for plant and manure biochars. Hossain et al. [17] showed that total N content and N availability decreased with increasing pyrolysis temperature in wastewater sludge biochars.
- Indirect contribution to nutrient availability relies on the capacity of biochars to retain applied nutrients, potentially reducing leaching and increasing fertilizer-use efficiency, on their liming effect or on their impact on other soil properties, such as the potential increase in water-holding capacity, among others, as reviewed by Chan and Xu in [10]. Biochars nutrient retention capacity is associated to their surface charge and surface physical properties as stated by Chan and Xu in [10].
- Biochar surface charge will impact the biochar capacity to adsorb positively or negatively charged nutrients. The cation exchange capacity (CEC) is a measure of the biochar capacity to retain positively charged species, mainly through electrostatic interactions [7,18]. Budai et al. [19] reported that CEC is influenced by different factors, with no clear dominance. These may include: the presence of negatively charged oxygen-containing functional groups on the biochar surface, such as carboxylate (from carboxylic acid) and hydroxyl functional groups [13,18–20], which are reported to decrease with increasing conversion temperature [13,18,19,21,22]; the pH of the solution [18]; the content and composition of the inorganic fraction [23,24]. Values for biochars CEC and its dependence on process conditions and feedstock vary significantly in literature [18,19,24]. Biochars anion exchange capacity (AEC) is scarcely reported in literature [20], with studies even showing negligible AEC [18]. Little is known about the origin of AEC on the surface of biochar [20]. However, due to the relevance of this topic, especially towards the reduction in negatively charged nutrients leaching, such as phosphates and nitrates, plenty of recent research activity focuses on the modification of biochar surfaces to enhance their capacity or adsorb such species.

- Biochar specific surface area and pore volume increase with pyrolysis temperature [19,21,25] up to approximately 600–700 °C, when further ordering of the biochar structure may lead to a decrease in surface area [19,25]. Mainly micropores contribute to the specific surface area in biochars [21]. Other process parameters, such as biomass composition, specially inorganic species content, heating rate and pressure can have also a significant impact on porosity development [26,27]. Surface area and pore network may impact biochar adsorption capacity due to the influence on accessibility [18] and availability of adsorption sites.
- With respect to water retention, this depends on both the physical and chemical surface properties of biochar. The nature of surface functional groups impacts the hydrophobic/hydrophilic behavior or biochars [20]. As reported by Schimmelpfenning et al. [21], polar functional groups on the biochar surface may increase the uptake of water due to electrostatic interactions and hydrogen bonds. Their reduction can lead to higher hydrophobic caracter [28]. Hagemann et al. [29] reported that biochar-water interactions enhancement, leading to higher nutrient retention, can be achieved with higher mesoporosity, redox-active sites and hydrophilicity on the surface of biochars.
- Biochars pH is of high relevance for its application in soil, since it determines not only its potential liming effect, but it also has an influence on other properties, such as CEC, water holding capacity or adsorption capacity for different nutrients or heavy metals [18,30].

Consequently, in order to achieve the capacity of "engineering biochar", not only further knowledge of the mechanisms behind biochar interactions in soil (including quantification and durability of the impact and variability in response) [9,31] is required, but also a deeper mechanistic understanding of the influence of conversion process and feedstock on biochar properties and its function in soil. This is a complex issue due to the highly relevant influence of (1) feedstock, (2) type of process, and (3) process parameters on biochar characteristics, as briefly introduced.

For pyrolysis, temperature and feedstock properties are the main process parameters under consideration when investigating the influence of conversion process on biochar properties. However, other process variables such as inert gas flow rate, heating rate, particle size, atmosphere and pressure can dramatically change biochar properties as well [26,32,33]. Furthermore, with HTC the chemical pathways involved differ significantly from those of pyrolysis. The different nature of these chemical reactions open up the potential to design carbon materials with a variety of interesting functionalities [34].

Comparison of chars produced from pyrolysis (termed biochars in the following) and chars produced from HTC (termed hydrochars in the following) has been previously done in literature, as summarized in Table 1. Huff et al. [35] reported higher O/C ratios for hydrochars than for biochars, as well as a significantly higher CEC, which, however, did not correlate well with the capacity of these chars to adsorb organic compounds (methylene blue). Budai et al. [19] showed that volatile matter and H/C and O/C ratios can be good parameters to determine the carbonization degree, irrespective of conversion process and feedstock, but poor predictors for agronomic properties (SSA and CEC). Liu et al. [28] reported that HTC creates oxygen-containing functional groups on the hydrochar surface with respect to the feedstock, while pyrolysis reduces their presence. Both biochar and hydrochar develop a rough surface and pore structure and are able to remove metal species from wastewater, such as copper, although different adsorption mechanisms can be responsible [28]. Based on a wide comparison of biochars, produced through different methods, and hydrochars, quality indicators for biochar production were suggested, such as H/C ratios below 0.6, O/C ratios below 0.4 and black carbon content higher than 15% (based on C), to ensure stability in soil [21]. Moreover, BET SSA higher than 100 $m^2\ g^{-1}$ and PAHs content according to the precautionary values defined by the German federal soil protection ordinance ("Bundesbodenschutzverordnung") should be achieved [21]. Regarding chemical structure, it was shown that while biochar is mostly aromatic, with small traces of alkyl carbons, hydrochars contain mostly alkyl moieties [36]. This was further confirmed in [37], where it was also reported that hydrochars have higher nutrient retention capacity than biochars. At the same time, both were within the EBC [1] recommended limits for PAHs content [37]. It was concluded

that conversion conditions strongly affect the char properties and that, while biochar standards are described in the EBC [1], hydrochars need their own directive [37]. In [36], it was also shown that the aromatic cluster size of biochar is larger than the one of hydrochar. Furthermore, acid prewashing and water and acetone washing can change the chemical structure of hydrochars [36]. Genotoxic and phytotoxic risk assessment showed hydrochars to be phytotoxic, inhibiting germination, although this effect could be eliminated with biological post-treatment [38]. Moreover, hydrochar is less suitable for long-term C sequestration in comparison to biochar, due to a lower stability, but it can deliver essential nutrients, having therefore potential for soil amelioration [39].

The objective of the present work is to contribute to the comparison between biochars and hydrochars by investigating the influence of conversion process conditions and feedstock on relevant properties. For this purpose, biochars and hydrochars were produced from two biomass feedstocks with varying mineral content (pine wood and corn digestate). Biochar was produced by pyrolysis in a fixed bed reactor at two maximum conversion temperatures (400 and 600 °C) and two inert gas flow rates (20 and 40 NL min^{-1} of N_2). Hydrochars were produced by HTC in a batch autoclave at two conversion temperatures (200 and 240 °C), two residence times (10 and 360 min) and with and without water washing after production (3 and 6 times). Together with primary characterization properties, such as proximate and elemental analyses, other characteristics, which can contribute to the understanding of biochar and hydrochar behavior once applied to soil, are analyzed: pH, acidic surface functional groups, pore size distribution with N_2 and CO_2 adsorption, nutrient availability, thermal stability, PAHs content and wettability.

Comparing the objectives of the present work and the previously reviewed literature, this study introduces a more detailed analysis on (1) the influence of conversion process parameters and (2) the characterization of products properties. With respect to process conditions, temperature, time and water washing have been chosen for HTC because very little data is available in the above mentioned publications regarding their combined influence on hydrochars. Moreover, the influence of inert gas flow rate in pyrolysis, and therefore the retention time of volatiles in the bed, is a novelty in this comparative study. This work represents a fundamental characterization of char produced under different and relevant process conditions and, therefore, issues regarding the energetic costs associated with inert gas flow rates, process temperatures or residence times cannot be evaluated based on these laboratory scale results. Furthermore, beyond the investigated product properties in the reviewed literature, a deep analysis is performed for the first time on the porous structure of both biochars and hydrochars combining N_2 and CO_2 adsorption, as well as research and comparison on nutrient availability and wettability. Finally, the results are analyzed from a conversion process perspective, in order to achieve an advance in the state-of-the-art of the "engineering biochar" concept.

Table 1. Summary of literature studies comparing biochars and hydrochars. CEC: cation exchange capacity, FTIR: Fourier-transform infrared spectroscopy, SSA: specific surface area, SEM: scanning electron microscopy, EDS: energy-dispersive X-ray spectroscopy, CT: CarbonTerra (Augsburg, Germany), BC: Black-Carbon (Barrit, Denmark), AGT: Advanced Gasification Technology (Arosio, Italy).

Authors	Process Conditions	Feedstock	Methods
Budai et al. [19]	Biochars from slow pyrolysis (235–800 °C), flash carbonization char (600 °C) and hydrochars (230 °C for 6 h)	Corncob and miscanthus	Proximate and elemental (CHNO) analyses, pH, CEC, SSA with N_2 adsorption
Schimmelpfennig and Glaser [21]	Biochars from slow pyrolysis (Pyreg unit) (550 °C), hydrochars (200 °C), rotary kiln biochars (350–550, 750 °C), gasification biochars (800 °C), traditional kiln biochars (350 °C), other biochars (350, 500, 650, 800 °C)	Wood, animal meal, sugar cane/beet, wheat, bamboo, maize, rice hulls, peanut shells, sewage sludge, walnut shells, girasol, coconut shells, lop, bark/needles	Elemental (CHNO) analysis, black carbon content, SSA with N_2 adsorption, PAHs content
Liu et al. [28]	Biochars from slow pyrolysis (700 °C), hydrochars (300 °C for 20 min)	Pine wood	Proximate and elemental (CHNO) analyses, Boehm titration, pH, FTIR spectroscopy, surface morphology with SEM, SSA and micro-, meso- and macropores volume with N_2 adsorption, copper removal capacity (adsorption) from wastewater
Huff et al. [35]	Biochars from slow pyrolysis (300, 400 and 500 °C) and hydrochars (300 °C for 30 min)	Pine wood, peanut shell and bamboo	Proximate and elemental (CHN) analyses, methylene blue adsorption, CEC, FTIR spectroscopy
Cao et al. [36]	Biochars from slow pyrolysis (620 °C) and hydrochars (with acid prewashing and water and acetone washing) (250 °C for 20 h)	Swine-manure	Major chemical structural components with Quantitative ^{13}C Direct Polarization/Magic-Angle Spinning (DP/MAS) NMR, ^{13}C Cross-Polarization/Total Suppression of Sidebands (CP/TOSS) and ^{13}C CP/TOSS Plus Dipolar Dephasing, ^{13}C Chemical-Shift-Anisotropy (CSA) Filter. Connectivities of different functional groups in hydrochars with ^{1}H–^{13}C Two-Dimensional Heteronuclear Correlation (2D HETCOR) NMR. Aromatic cluster sizes with ^{1}H–^{13}C Long-Range Recoupled H–C Dipolar Dephasing Experiments
Wiedner et al. [37]	Biochars (pyrolysis-Pyreg up to 850 °C, pyrolysis/gasification-BC up to 760 °C, gasification-AGT up to 1200 °C, gasification-CT up to 550 °C) and hydrochars (1st stage at 230 °C for at least 15 min and 2nd stage at 180 °C for at least 75 min; 170 °C for 90 min)	Wheat straw-AGT, wood chips-AGT, poplar-AGT, sorghum-AGT, olive residues-AGT, wood chips-CT, wood chips-BC, draff-Pyreg, miscanthus-Pyreg. Maize silage, leftover food, biogas digestate, grass greenery and sewage sludge for hydorchars	pH, EC, ash content, elemental composition (CHNO), ^{13}C NMR, SEM-EDS, black carbon content, PAHs content, polychlorinated dibenzodioxines (PCDDs) and polychlorinated dibenzofurans (PCDFs) content
Busch et al. [38]	Biochars (gasification-AGT up to 1200 °C and pyrolysis at 400–600 °C) and hydrochars (230 °C for 1 h and 180 °C for at least 4 h; 170 °C)	Olive residues-AGT, poplar wood chips-AGT, wheat straw-AGT, miscanthus-pyrolysis. Maize silage, food leftovers, biogas digestate grass and sewage eludge for hydrochars	Tradescantia genotoxicity assay, plant germination and growth tests and impact on soil pH
Busch and Glasser [39]	Biochar (pyrolysis-Pyreg), hydrochar (230 °C for 1 h and 180 °C for at least 4 h), co-composted biochar (1:1 w/w) and hydrochar (1:3 w/w) with raw biomass residues from vegetable waste from horticulture and landscaping, kept for 4 weeks in temperature range 55–75 °C)	Conifer wood bark residues for biochar and maize silage for hydrochar	Stability of co-composted hydrochar and biochar under field conditions in a temperate soil. TOC, total N content, pH, EC and black carbon analysis of biochars, hydrochars, compost and co-composted biochars and hydrochars before and after application in soil

2. Materials and Methods

Two different raw materials, pine wood chips (PW) and corn digestate (CD), were used for the production of biochar (pyrolysis) and hydrochar (HTC). PW was provided by Robeta Holz OHG (Milmersdorf, Germany) while CD was obtained from an anaerobic digester in Dorf Mecklenburg (Germany). The substrate used for mesophilic (39 °C) anaerobic digestion was 70% corn silage and 30% cow manure. The digestate was dried and stored on site. Due to storing conditions, the dry digestate contained a significant amount of calcium carbonate. The properties of both raw materials are shown in Table 2.

Table 2. Raw material, conversion process, experimental conditions and solid yields for biochar and hydrochar production. Ash content and elemental composition of pine wood chips (PW) and corn digestate (CD). Determination of ash content was done according to the DIN norm 51719. Elemental analysis was performed using a Vario EL elemental analyzer. Oxygen content was obtained by difference. The values are given in % mass, dry basis (%, db). * Maximum conversion temperature measured in the reference position, according to the description provided in the Section 1 of Supplementary Material.

Material	**Ash (%, db)**	**C (%, db)**	**H (%, db)**	**O (%, db)**	**N (%, db)**	
CD	19.6 ± 0.1	40.7 ± 0.7	5.5 ± 0.1	31.7 ± 0.8	2.4 ± 0.5	
PW	0.2 ± 0.0	49.4 ± 0.4	6.7 ± 0.1	43.7 ± 0.4	0.1 ± 0.0	
Sample	Raw material	Process	HTT * (°C)	Flow (NL min^{-1})	Char yield (%, db)	
PW400-20	Pine wood	Pyrolysis	400	20	30.01 ± 0.18	
PW400-40	Pine wood	Pyrolysis	400	40	25.83 ± 2.12	
PW600-20	Pine wood	Pyrolysis	600	20	24.94	
PW600-40	Pine wood	Pyrolysis	600	40	22.82 ± 0.49	
CD400-20	Corn digest.	Pyrolysis	400	20	50.89 ± 0.36	
CD400-40	Corn digest.	Pyrolysis	400	40	52.00 ± 0.21	
CD600-20	Corn digest.	Pyrolysis	600	20	49.76 ± 0.40	
CD600-40	Corn digest.	Pyrolysis	600	40	48.54 ± 1.08	
Sample	Raw material	Process	HTT (°C)	Time (min)	Wash. times	Char yield (%, db)
PW200-10	Pine wood	HTC	200	10	-	82.30 ± 0.35
PW200-360	Pine wood	HTC	200	360	-	75.68 ± 0.01
PW240-10	Pine wood	HTC	240	10	-	76.26 ± 0.07
PW240-360	Pine wood	HTC	240	360	-	59.09 ± 0.19
CD200-10-0	Corn digest.	HTC	200	10	0	83.49
CD200-10-6	Corn digest.	HTC	200	10	6	73.49
CD200-360-0	Corn digest.	HTC	200	360	0	74.38
CD200-360-6	Corn digest.	HTC	200	360	6	70.29
CD220-185-3	Corn digest.	HTC	220	185	3	64.57 ± 2.02
CD240-10-0	Corn digest.	HTC	240	10	0	70.82
CD240-10-6	Corn digest.	HTC	240	10	6	66.85
CD240-360-0	Corn digest.	HTC	240	360	0	62.06

CD and PW biochars were produced at the Technische Universität Berlin (Berlin, Germany), in a technical-scale fixed-bed reactor, with capacity for several kg of biomass. The setup used in these experiments has been presented elsewhere [40]. In these experiments, the influence of maximum pyrolysis temperature (400 and 600 °C) and residence time of the volatiles in contact with the solid bed (with inert gas flow rates of 20 and 40 NL min^{-1}) was investigated. Experiments were conducted in duplicates.

The hydrothermal carbonization experiments were carried out at the Leibniz Institute for Agricultural Engineering and Bioeconomy (Potsdam, Germany). Distilled water was added to the dry digestate in each experiment to achieve the desired solid content of 20% by mass. The experiments were conducted in a 1 L autoclave (Series 4520, stainless steel T 316, Parr Instruments, Moline, IL, USA) equipped with a temperature controller. The influence of maximum conversion temperature (200, 220 and 240 °C), time at this temperature (10, 185 and 360 min) and washing effect (0, 3 and 6 times with distilled water) on hydrochar properties was investigated.

Further details on biochar and hydrochar production conditions are given in Table 2 and in the Suplementary Material.

Analytical Methods

Biochars ash content determination was done following the DIN norm 51719. Hydrochars ash content was characterized according to the method described in Chapter 8.4 from the VDLUFA Methodenbuch Band III [41]. Validation of both methods for both raw materials showed that the results according to the DIN norm are within the standard deviation of the results from the VDLUFA method. For elemental analysis (CHNS), a Vario EL elemental analyzer (Elementar Analysensysteme GmbH, Lagenselbold, Germany) was used for hydrochars and biochars. Inorganic elemental analysis for hydrochars was performed in an ICP-OES (iCap 6300 Duo, from Thermo Scientific, Schwerte, Germany). Prior to the analysis, milled samples were digested according to the method exposed in Chapter 10.8 of the VDLUFA Methodenbuch Band III [41], using a microwave (ultraClave-IV high pressure microwave, from MWS Vertriebs GmbH, Leutkirch, Germany) with nitric acid 65% (260 °C, 140 bar, 2 h) and stored at room temperature. Biochar inorganic elemental characterization was also performed with an ICP-OES (Varian 720-ES, now Agilent Technologies, Inc., Santa Clara, CA, USA) after digestion in a microwave (Multiwave 3000, from Anton Paar, Graz, Austria) with nitric acid 65% (Rotipuran ® p.a., ISO, max 0.005 ppm Hg, Carl Roth GmbH + Co. Kg, Karlsruhe, Germany) and hydrogen peroxide 30% (Rotipuran ® p.a., ISO, stabilisiert, Carl Roth GmbH + Co. Kg, Karlsruhe, Germany).

The pH of biochars and hydrochars was measured in deionized water solution. The determination of oxygen-containing functional groups on the char surface was done applying the Boehm titration method [42]. The experimental procedure is based on the description by Goertzen et al. [43], including the sample pretreament proposed by Tsechansky and Graber [44]. Further details on this characterization method are given in the Section 2 of Supplementary Material.

The pore structure, including specific surface area, pore volume and pore size distribution, was characterized with gas adsorption, combining the measurement of N_2 and CO_2 adsorption isotherms at 77 K and 273 K respectively. The pretreatment of the samples, prior to adsorption measurements, included milling and degassing in vacuum at 150 °C during 6 h, with the objective of cleaning the surfaces from other adsorbed species and reducing transport limitations (milling). For both degassing and adsorption/desorption measurements the gas sorption system Nova 2200, provided by Quantachrome Instruments (Boynton Beach, FL, USA), was used. Several methods were applied to the isotherms in order to derive pore surface areas and volumes, all of them included in the NovaWin software (Version 11.04, also from Quantachrome Instruments). The methods applied to the N_2 adsorption/desorption isotherms included: the BET method [45] to meaure the total specific surface area; the BJH method [46] to characterize the specific surface area and volume of pores bigger than ≈3 nm; and the density functional theory (DFT) [47] method, in particular, the quenched solid density functional theory (QSDFT) method, considering slit/cylindrical pores (Quantachrome Instruments). With the QSDFT method, the specific surface area and volume of micropores and mesopores up to ≈34 nm were characterized. The total pore volume was determined from the volume of N_2 adsorbed at a relative pressure $P/P_0 \approx 1$, assuming that at this point the pores are filled with liquid N_2. For CO_2 adsorption, the non local density functional theory (NLDFT) method (Quantachrome Instruments) was applied to determine the specific surface area and volume due to micropores up to ≈1.5 nm.

Biochar thermal stability was analyzed by thermogravimetric analysis (TGA 1, STARe system, from Mettler Toledo, Columbus, OH, USA) with a heating rate of 5 °C min^{-1}, in synthetic air (20.5% O_2, 200 mL min^{-1} air flow) and up to a temperature of 600 °C. Initial mass below 5 mg was used to guarantee kinetic regime and avoid self-heating due to the exothermicity of the oxidation reactions. Conversion rate of biochar oxidation is defined here as the change of conversion (α) over time ($\frac{d\alpha}{dt}$). Conversion (α) is defined as $1 - (m_o - m)/(m_o - m_f)$, where m is the biochar mass at each time step, m_o is the initial biochar mass and m_f is the mass of the combustion product at 600 °C, i.e., ash.

Plant available ammonium (NH_4^+) and nitrate (NO_3^-) were determined according to the DIN 19746:2005-06 (extraction of the samples with 0.0125 mol L^{-1} of $CaCl_2$ in distilled water). Plant available phosphate (PO_4^{3-}) and potassium (K^+) were determined according to VDLUFA Methodenbuch Band I [48], Chapter 6.2.1.1 (extraction with a solution of 0.02 mol L^{-1} of calcium lactate and 0.02 mol L^{-1} hydrochloric acid in distilled water). The analysis of the extracts was conducted by IC-CD (ICS 1000, from DIONEX). Anions were analyzed with an IonPac AS9-HC 4 × 250 mm column from DIONEX (chromatographic conditions: 9 mmol Na_2CO_3, 1.2 mL min^{-1}, 160 bar) and cations with an IonPac CS 16 5 × 250 mm column from DIONEX (chromatographic conditions: 30 mmol methanesulfonic acid (MSA), 1.0 mL min^{-1}, 80 bar, 40 °C).

The method applied for characterization of the 16 USEPA (United States Environmental Protection Agency) PAHs has been developed by Fabbri et al. [49], with the difference that in the present study a standard solution of deuterated 16 PAHs (PAH-Mix 9 deuterated, 10 mg L^{-1}, Dr. Ehrenstorfer, Augsburg, Germany) was used, instead of 3 deuterated PAHs as in [49]. Briefly, the biochar samples, spiked with 0.1 mL of a 5 mg L^{-1} solution of the above deuterated 16 PAHs solution, were Soxhlet extracted with an acetone (CHROMASOLV, for HPLC, ≥99.9%, Sigma–Aldrich, St. Louis, MO, USA)/cyclohexane (ACS reagent, ≥ 99.5%, Sigma–Aldrich, St. Louis, MO, USA) (1:1, *v*/*v*) solvent mixture for 36 h and then the PAHs were analyzed in an Agilent HP 6850 gas chromatograph (GC) coupled to an Agilent HP 5975 quadrupole mass spectrometer (MS) (Agilent Technologies, Inc., Santa Clara, CA, USA); GC-MS conditions were those detailed in [49].

Biochar wettability measurements were performed according to the method described by Ojeda et al. [50]. Briefly, a glass tube 6 cm high with 0.9 cm of internal diameter was filled with the different biochar samples up to a height of 3 cm. Then the tube was attached to a high precision scale (DCAT, dynamic contact angle measuring instrument, DataPhysics©, Germany). Below the tube, a glass filled with distilled water or n-hexane (AnalaR NORMAPUR –for synthesis– ≥95%) was placed and carefully risen until touching the bottom part of the tube. Distilled water/n-hexane capillary absorption was measured by registering the weight increase in the biochar column during 200 s.

3. Results and Discussion

3.1. Primary Characterization: Yields, Elemental and Proximate Analysis

In Table 2 biochars and hydrochars yields are presented. Hydrochars show significantly higher char yields than biochars, consistent with the lower conversion temperatures and the higher pressures. For biochars, the lower the conversion temperature the higher the char yield. CD biochars also present higher yields than PW biochars, due to the significantly higher inorganic species content, which remain in the solid product after pyrolysis. Besides, a higher N_2 flow rate during pyrolysis generally reduces the char yield, due to a reduction in the residence time of the volatiles in the bed, minimizing secondary reactions and formation of secondary char [12]. In the case of hydrochars, the solid yields for both raw materials are similar. Besides, both conversion temperature and retention time at the conversion temperature play an important role. Noteworthy to mention in the case of hydrochars is the impact of washing. With the same conversion temperature and retention time, washing the hydrochar after production can reduce up to 10% the solid yield. This indicates that a significant part of the solid is actually condensed volatiles and water soluble inorganic species.

In Figure 1 (left), the Van Krevelen diagram, i.e., the representation of H/C molar ratio versus O/C molar ratio is presented for biochars and hydrochars. This diagram is often used to illustrate the degree of maturity and aromaticity of chars [51]. Results in Figure 1 show that hydrochar and biochar chemical composition depends on the conversion conditions, but also on the initial feedstock composition, having potentially a significant impact on final char chemical properties. This is illustrated with the results of CD biochars/hydrochars versus those for PW biochars/hydrochars. For the same O/C molar ratio, the H/C molar ratio of CD biochars is lower than for PW biochars. Looking at the relation of these molar ratios with the volatiles content (% mass, dry ash free), it is observed that while biochar O/C molar ratio follows a linear trend with respect to the volatiles content, the behavior of H/C ratio seems only linear for PW biochars, while very scattered for CD biochars.

As it has been introduced in Section 2, corn digestate contains calcium carbonates, mainly due to storing conditions. The inorganic C content of CD biochars, due to carbonates, is approximately 4–5%, as determined by Rombolà et al. [52]. The presence of these carbonates could explain, to some extent, the higher volatiles content of CD biochars in comparison with PW biochars, since at the conversion temperatures used in this study (400 and 600 °C) carbonates are stable and therefore remain in the biochar. However, this could not explain the lower content in hydrogen for CD biochars. Besides, the elemental composition of CD presented in Table 2 is similar to the one reported by Mumme et al. [53] for maize silage digestate. This suggests different reaction pathways for low and high inorganic matter content biochars, with a potential enhancement of aromatization for high inorganic matter content biochars. Li et al. [54] also reported lower H/C ratios for biochar produced from pyrolysis of rice husk, blended with $CaCO_3$ prior pyrolysis, than for unmodified biochars, which they correlated with an increase in the carbon aromaticity degree. The potential formation of oxides or other metal composites on the biochar surface, associated to the high content of inorganic matter, could also play a role [55].

With respect to hydrochars, CD hydrochars present in general higher H/C ratios and lower O/C ratios than PW hydrochars, in some cases even lower than CD biochars. This indicates different reaction mechanisms for both materials. The higher H/C ratios of CD hydrochars suggests that decarboxylation reactions are favored over dehydration reactions [53]. In the case of PW hydrochars, dehydration reactions seem to be more significant in comparison to CD hydrochars, while the influence of decarboxylation reactions is lower, except for the highest conversion temperature and highest retention time (240 °C – 360 min), where both are relevant. This is further supported by the composition of the producer gas (collected during the HTC experiments in gas bags and analyzed with a SSM6000 analyzer from Pronova, Germany), with a concentration of CO_2 increasing from around 50% vol. to approximately 80% vol. for the highest conversion degree. It is also important to point out that retention time at the conversion temperature is as significant as the conversion temperature itself. With respect to CD hydrochars, CO_2 increases from approximately 58% vol. from the mildest conditions to around 75% for the most severe conditions. In this case, a significant emission of CH_4 (2.5% vol.) was also registered. Alkaline conditions during HTC enhance the formation of carboxylic acids, reducing therefore the O/C ratio of the hydrochar [56]. In the present study, although the pH of both solid and liquid products are acid, they are higher for CD hydrochars than for PW hydrochars, as shown in Section 3.2. Similar composition for digestate hydrochars has been also shown by Mumme et al. [53], who highlighted that this could be due to the decarboxylation reactions. Liu et al. [28], who compared a hydrochar produced at 300 °C with a biochar produced at 700 °C using pine wood, reported similar H/C and O/C ratios for their biochar as for the PW biochars produced at 600 °C in the present study. The values for the hydrochar were slightly higher in comparison to PW hydrochars produced at 240 °C during 360 min in the present study. Besides, for similar hydrochar H/C ratio, the hydrochar O/C ratio is lower in the present study than in [28]. This could be related to the high amount of ash reported by Liu et al. [28].

According to the guidelines given by the European Biochar Certificate (EBC) [1] and the International Biochar Initiative (IBI) Standards [2] on H/C and O/C ratios, the biochars presented in this Section could be considered as certified biochars. With respect to hydrochars, it is shown that it is also possible to produce hydrochars able to fulfill those requirements, with a conversion temperature of at least 240 °C and a retention time of 360 min, but only with starting HTC conditions enhancing both dehydration and decarboxylation reactions (as it is the case for PW), not only decarboxylation reactions (as in the case of CD).

Inorganic elemental characterization is shown in Table 4 and in the Supplementary Material (Table S1). It is observed that the elemental inorganic composition of CD hydrochars and biochars is much higher than the one for PW hydrochars and biochars, in good agreement with their high ash content.

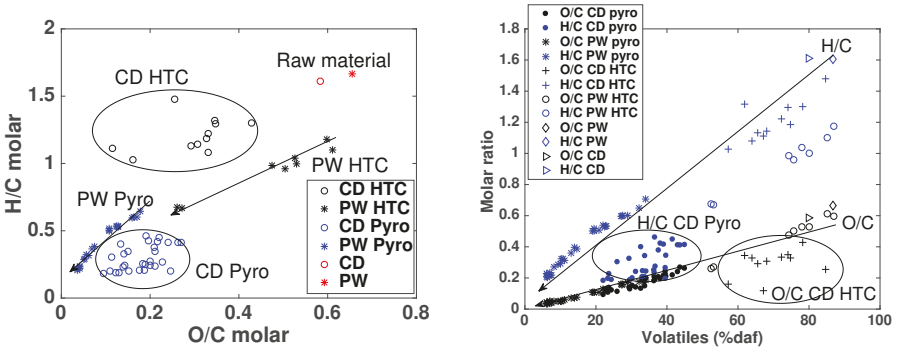

Figure 1. Left: Van Krevelen diagram, i.e., H/C molar ratio versus O/C molar ratio of PW and CD biochars and hydrochars. **Right**: H/C and O/C molar ratios versus volatiles content (% mass, daf) for PW and CD biochars and hydrochars.

3.2. pH and Surface Functional Groups

It has been reported in literature that pH may be dependent on both, the surface chemistry and the ash content [22,23,57,58]. These both influences are further confirmed in the present study. In Figure 2a,b the variation of pH with ash content is presented. Biochars with higher ash content show also higher pH. However, the strongest correlations for biochars are not between pH and the ash content, but between pH and H/C and O/C molar ratios. Specially remarkable is the correlation between pH of CD biochars and H/C molar ratio ($r = -0.95$, shown in Figure 2c, being r the Pearson correlation coefficient), when considering that the latter shows such scattered behavior in Figure 1. It must be also taken into account that CD contains calcium carbonate due to storing conditions, which has a high liming effect. However, the correlation between CD biochars ash content and pH is significantly worse than between pH and H/C. With respect to PW biochars, pH presents also stronger relations with H/C and O/C molar ratios ($r = -0.91$ and $r = -0.89$ respectively, shown in Figure 2d,f) than with ash content, being this correlation similar in both cases.

Therefore, with respect to biochars pH, it can be concluded that despite the fact that ash content has an influence on the pH value, a better correlation exists between the pH value and H/C and O/C ratios. In the case of CD biochars, the relation between pH and H/C ratio is strongly linear.

For hydrochars the behavior is slightly different. Figure 2a shows that pH of CD hydrochars has a stronger correlation with ash content ($r = 0.88$) than with H/C (Figure 2c) or O/C ratios (Figure 2e). Despite the fact that the slope of the linear fitting for pH-ash in Figure 2a for CD hydrochars is lower than those for pH-H/C for CD and PW biochars in Figure 2c,d respectively, the correlation is still much better for pH-ash than for pH-H/C or pH-O/C. This indicates that the pH in CD hydrochars is

mainly correlated to ash content, although with a weaker dependency than PW and CD biochars pH with H/C ratio. PW hydrochars show similar relations with H/C and O/C molar ratios.

In Figure 3, information about the acidic functional groups present on the chars surface is given, in particular, for carboxylic, phenolic and lactonic groups. In Figure 3a the total acidic functional groups (carboxylic, lactonic and phenolic) and the carboxylic functional goups with respect to the organic fraction of the chars (mmol g_{org}^{-1}, db) are plotted versus the O/C molar ratio for PW600-20, PW400-20, PW600-40, PW400-40, CD600-20, CD400-20, PW240-10. For biochars, independently of the inorganic matter content, a good correlation (r = 0.80) is observed between total acidic groups and O/C ratio. Hydrochar PW240-10 presents a high O/C molar ratio which does not correlate well with the total acidic functional groups, according to the biochars behavior. This may indicate that still a significant amount of oxygen is embedded in the hydrochar skeleton, which is in good agreement with the structure of hydrochar formed mainly by alkyl moieties reported by Cao et al. [36]. In Figure 3b the total acidic groups and the carboxylic goups (with respect to the organic fraction of the chars) are plotted versus H/C molar ratio. No good correlations are observed. However, in Figure 3c a quite strong linear correlation (r = 0.84) is present between the total surface acidic groups with respect to the total char mass (mmol g^{-1}, db) and the H/C molar ratio, independently of the inorganic matter content and the conversion process. Figure 3d shows the comparison of these groups with pH. A relation between the increase in pH and the decrease in total acidity of the biochar surface is observed.

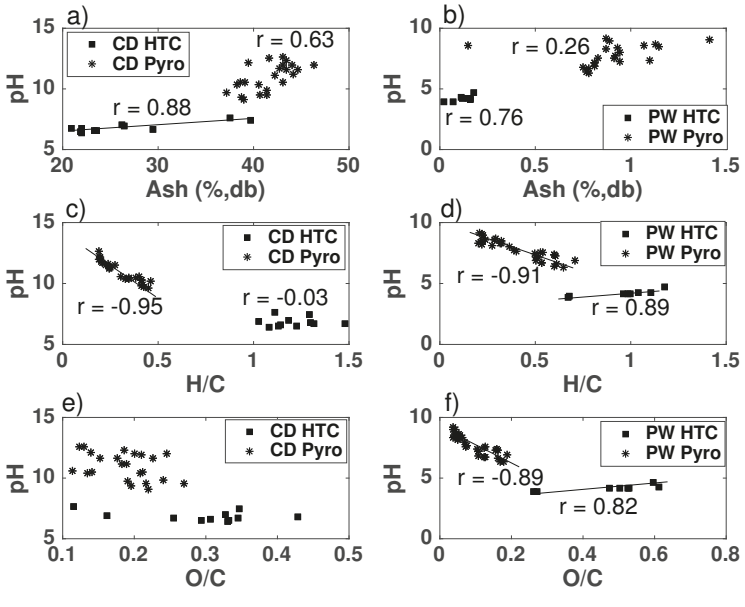

Figure 2. pH versus ash (% mass, db) in (**a**,**b**), H/C molar ratio in (**c**,**d**) and O/C molar ratio in (**e**,**f**) for CD (left) and PW (right) biochars and hydrochars. The strength of the correlations is indicated with the Pearson correlation coefficient (r).

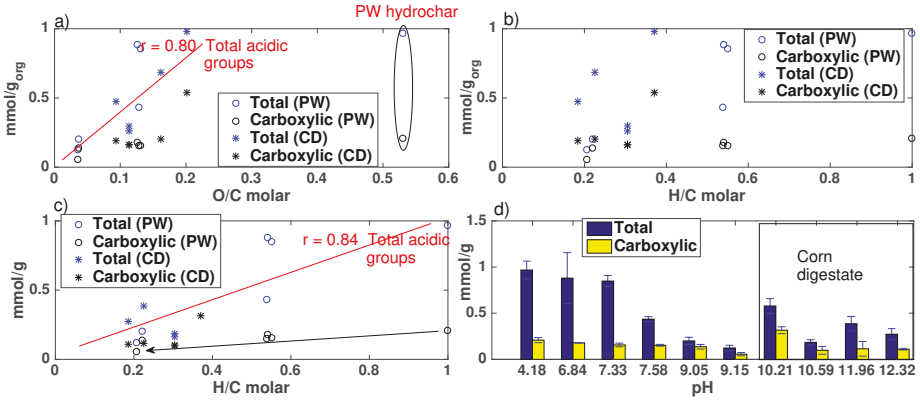

Figure 3. Surface oxygen-containing functional groups of the biochars determined with the Boehm titration method. (**a**,**b**) show the amount of functional groups with respect to the mass of the chars organic fraction versus the O/C and H/C molar ratios; (**c**) shows the amount of functional groups with respect to the total chars mass versus the H/C molar ratio; (**d**) shows the amount of functional groups versus the pH.

3.3. Porosity Characterization

In Figure 4, the evolution of the total specific surface area (BET method using N_2 adsorption) is plotted versus the biochars/hydrochars volatiles content (% mass, daf). In general, the lower the volatiles content, the higher the specific surface area (SSA). However, for CD biochars different BET SSA behaviors are observed for similar volatiles content. The highest SSA values correspond to biochar produced at 600 °C with a N_2 sweeping flow rate of 40 NL min^{-1}. In Figure 4b the SSA evolution is plotted versus the H/C molar ratio. The decrease of H/C molar ratio is indicative of the formation of structures containing unsaturated carbon such as aromatic rings [59], and therefore, represents the increase in aromaticity with charring degree, as reported in [25]. It is possible to observe that the behavior of CD biochars differs significantly from the one of PW biochars. Taking into account that CD biochars have around 40% ash content, the SSA would be higher as function of the organic fraction, but it would be still lower than for PW biochars. This may be a consequence of two possible phenomena: (a) porosity development is different for materials with high inorganic content and (b) potential filling or access blocking of micropores by the inorganic species [60,61], which could explain the lower SSA value despite the lower H/C molar ratio in CD biochars.

In order to further characterize the porous structure, in Figure 5 the pore size distribution according to pore surface area (left) and pore volume (right) is presented, characterized with the methods introduced in Section "Analytical Methods". SSA and volume from CO_2 adsorption are also shown in Figure 5. With CO_2 adsorption, micropores up to 1.5 nm in pore width are characterized. Despite this, the SSA area measured with CO_2 adsorption is higher than the total SSA (up to 100–200 nm in pore width, depending on the sample porous structure) measured with N_2 adsorption. This indicates that the samples have a microporous structure which cannot be completely characterized by N_2 adsorption, mostly due to diffusion limitations, consequence of the low temperature measurements in N_2 adsorption.

The CO_2 SSA is around 25% higher than the N_2 SSA for PW biochars produced at 600 °C, with inert gas flow rates of 20 and 40 NL min^{-1}. However, the CO_2 SSA for CD biochars produced in the same conditions is 90% and 80% higher respectively. This indicates that the diffusion limitations are stronger in CD biochars, in good agreement with the previous explanation for the low specific surface of high inorganic content biochar. That is to say, the inorganic species may provoke partial blocking or constriction of the porous structure, limiting the access of N_2 to micropores but not of CO_2.

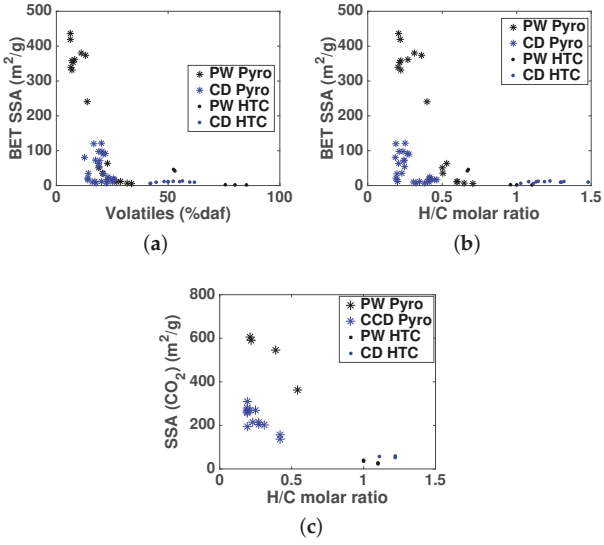

Figure 4. (**a**): Total specific surface area (SSA) determined with the BET method (N_2 adsorption) versus the volatiles content (% mass, daf) for PW and CD biochars and hydrochars; (**b**): SSA determined with the BET method (N_2 adsorption) versus H/C molar ratio for PW and CD biochars and hydrochars; (**c**): SSA determined with CO_2 adsorption applying the NLDFT method versus H/C molar ratio for PW and CD biochars and hydrochars.

With respect to the pore volume, higher N_2 pore volume than CO_2 pore volume is measured for PW biochars produced at 600 °C. This is due to the smaller size of pores characterized by CO_2 adsorption. Noteworthy to mention is the fact that higher N_2 sweeping flow during the pyrolysis process leads to higher SSA and pore volume in the biochar. For PW biochars the effect is clearer when looking at the pore volume distribution. This is also stronger for biochars produced at 400 °C than for biochars produced at 600 °C. For CD biochars the difference for biochars produced at 600 °C is already very significant, as introduced in Figure 4. This shows that higher flow rates lead to a more open porous structure, due potentially to a combination of higher removal of volatiles (more significant for biochars produced at 400 °C) and inorganic species (present in CD biochars), together with lower extent of intraparticle heterogeneous secondary reactions, leading to the formation of secondary char.

Interestingly, while the major contribution to pores in PW biochars comes from micropores (observed in the CO_2 adsorption results), in CD biochars the contribution of mesopores is also significant. Therefore, inorganics in CD biochars would not only reduce the presence of micropores through potential blocking, but could also enhance the development of mesopores.

Comparing the porous structure of hydrochars with the one of biochars, the former follows quite a different behavior. According to Figure 4, hydrochars present low SSA, in good agreement with the high volatiles content and high H/C molar ratio. This suggests low charring and aromatization degree in comparison with biochars. However, in Figure 5, results for hydrochars pore size distribution, according to volume (bottom right), show that the volume of these samples is in many cases higher than the one of biochars. Contribution of micropore volume to the total pore volume of hydrochars is low. Therefore, it can be concluded that porosity (pore volume) in hydrochars is mainly due to meso- and macropores. Comparing PW hydrochars and CD hydrochars produced at 240 °C, with a retention time at maximum conversion temperature of 360 min, it is possible to see that PW hydrochars present significantly higher SSA and volume. This could be attributed to the high inorganic matter content

of CD hydrochars. However, PW hydrochars produced at 240 °C during 10 min or at 200 °C during 360 and/or 10 min show lower SSA and volume than CD hydrochars produced at 240 °C and 200 °C during 360 min. Comparing the behavior of CD hydrochars produced at 240 °C and 200 °C during 360 min, the SSA and pore volume of the latter are higher despite the lower conversion temperatures. This is due to the washing of the hydrochar produced at 200 °C during 360 min. This washing removes inorganics and volatiles partially blocking the pores, which leads to an underestimation of the porous structure with N_2 adsorption, as previously introduced for biochars. However, CO_2 adsorption results show similar values of microporosity for both cases, indicating that this pore blocking does not affect CO_2 adsorption.

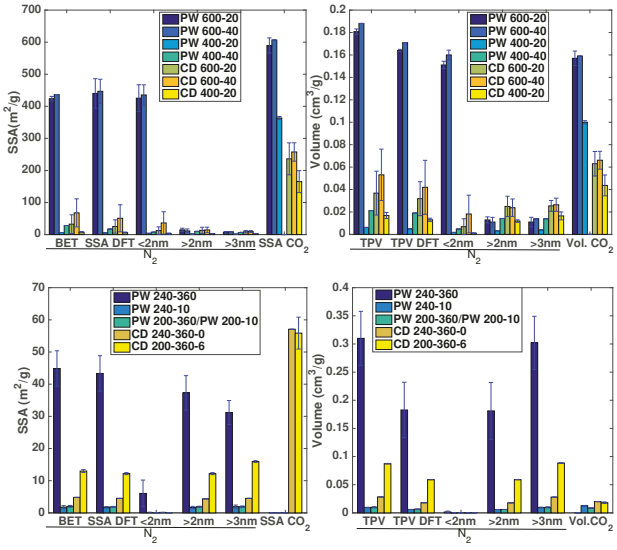

Figure 5. Pore size distribution (PSD) of PW and CD biochars (**top**) and hydrochars (**bottom**). **Top left**: SSA distribution with pore size for biochars according to the BET method (for total specific surface area), quenched solid density functional theory (QSDFT, for total specific surface area, surface area due to pores < 2 nm and pores 2 nm $<$ pore size < 34 nm) method, and BJH method (surface area due to pores > 3 nm). Total specific surface area for pores < 1.5 nm determined with CO_2 adsorption. **Top right**: Volume distribution with pore size for biochars. **Bottom left**: SSA distribution with pore size for hydrochars according to the aforementioned methods. **Bottom right**: Volume distribution with pore size for hydrochars. CO_2 adsorption was not measured for samples PW400-40 and PW240-360.

3.4. Thermal Stability

Oxidation behavior of biochar in the presence of synthetic air has been performed in a thermogravimetric analyzer (TGA) to assess biochar stability to oxidation [62,63].

In Figure 6, the conversion rate under oxidation conditions is plotted versus the temperature for hydrochars (top) and biochars (bottom). The higher the temperature correspondent to the peak of the conversion rate, the lower the reactivity, and therefore, the higher the stability to oxidation.

For most hydrochars, except the ones produced under the highest severity (240 °C, 360 min retention time), a first peak in the conversion rate is observed at temperatures slightly above 300 °C, consistent with further oxidative pyrolysis of the sample [64]. The second peak at higher temperatures is related to char oxidation. For PW hydrochars, these oxidation peaks take place at significantly higher temperatures than for CD hydrochars. At the same time, water washing of the hydrochars after production seems to also affect their oxidation behavior. Those not being washed experience an

earlier second oxidation peak. For biochars, the higher the conversion temperature, the higher the temperature correspondent to the maximum of the oxidation peak. For hydrochars, residence time at the maximum conversion temperature and post-washing, as previously introduced, also play a significant role.

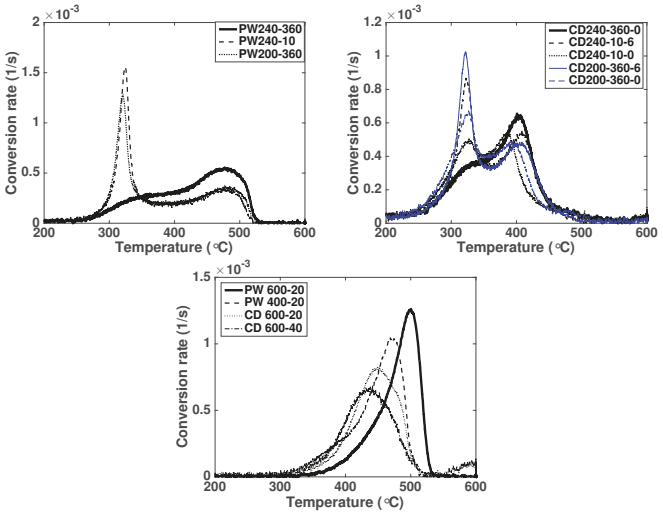

Figure 6. Conversion rate of char oxidation for PW hydrochars (**top left**), CD hydrochars (**top right**), PW and CD biochars (**bottom**).

The initial feedstock seems to have a stronger influence on the thermal stability (based on the shape and peak position of the char oxidation curve) than the conversion process conditions. It is known from literature [12] that char reactivity (in oxidation and gasification conditions) depends on the char structure at molecular level, the inorganic matter in the carbon skeleton, specially alkali and alkaline earth metals (AAEM), and the concentration and type of functional groups in the carbon skeleton. Consequently, the high inorganic content of CD biochars, including AAEM, could act as catalyst in biochar oxidation. This is also consistent with the washing of hydrochars, since with washing, inorganic species can be removed from the hydrochar surface. Harvey et al. [65] showed a similar behaviour with biochars (produced in [66]) from loblolly pine and cord grass, i.e., lower $R_{50,biochar}$ for biochars with high inorganic content (up to 30% ash content for cord grass). However, regardless of the inorganic content, they attributed the differences in biochar thermal stability to the extent of carbonization/aromatization. Therefore, samples with similar H/C and O/C ratios can have different recalcitrance depending on the rearragement of these atoms in the biochar structure [65].

Correlation between the thermal stability and the biogeochemical stability of soil organic matter has been proposed by Plante et al. [67]. Harvey et al. [65] reported also a strong negative exponential-type relationship between biochar degradabitlity (based on the amount of carbon mineralized after 1 year of incubation [68]) and the thermal recalcitrance $R_{50,biochar}$, defined according to Equation (1). $T_{50,biochar}$ is the temperature correspondent to 50% conversion of biochar (i.e., 50% of the total mass loss due to oxidation/volatilization) and $T_{50,graphite}$ is analog for graphite. In Table 3, the $R_{50,biochar}$ values for several biochars and hydrochars are shown, considering $T_{50,graphite}$ = 844 °C [62]. If a $T_{50,graphite}$ = 886 °C is used, as measured by Harvey et al. [65], slightly lower $R_{50,biochar}$ values are registered (values between parentheses in Table 3).

$$R_{50,biochar} = \frac{T_{50,biochar}}{T_{50,graphite}} \quad (1)$$

Table 3. $R_{50,biochar}$, C (% mass, daf), H/C and O/C molar ratios for biochar and hydrochar samples. The $R_{50,biochar}$ values are calculated considering a $T_{50,graphite}$ = 844 °C [62]. The $R_{50,biochar}$ values between parentheses correspond to a $T_{50,graphite}$ = 886 °C [65].

	$R_{50,biochar}$	C (% mass, daf)	H/C (molar)	O/C (molar)
PW200-360	0.43 (0.41)	56.94	0.96	0.50
PW240-10	0.41(0.39)	55.77	1.00	0.53
PW240-360	0.51 (0.48)	70.33	0.67	0.27
CD200-360-0	0.41 (0.39)	62.93	1.19	0.33
CD200-360-6	0.41 (0.39)	62.86	1.22	0.33
CD240-10-0	0.43 (0.41)	61.69	1.29	0.35
CD240-10-6	0.42 (0.40)	61.77	1.32	0.35
CD240-360-0	0.45 (0.43)	76.35	1.11	0.12
PW400-20	0.53 (0.50)	82.10	0.54	0.13
PW600-20	0.57 (0.54)	93.49	0.22	0.04
CD600-20	0.52 (0.50)	84.62	0.18	0.09
CD600-40	0.52 (0.50)	81.99	0.19	0.13

According to a biochar classification proposed by Harvey et al. [65], all analyzed biochars are Class B biochars ($0.50 \leq R_{50,biochar} < 0.70$), with intermediate C sequestration potential, while the rest are Class C biochars ($R_{50,biochar} < 0.50$), which indicate that those chars have carbon sequestration potential comparable to uncharred biomass. The PW240-360 hydrochar could belong to both classes, depending on the considered $T_{50,graphite}$.

3.5. Nutrients

The total content of macronutrients, such as Ca, Mg, N, P and K, is presented in Table 4 for PW and CD biochars and hydrochars. These values are compared with the available nutrient content in the form of NH_4^+, NO_3^-, PO_4^{3-} and K^+.

Due to methodical issues, the values of hydrochars nutrient availability, determined from the solid fraction, cannot be directly compared with those for biochars. A significant fraction of the investigated species is solved in the liquid phase during HTC, which might still be present upon drying of the hydrochar. This fact leads to measured nutrient availability in the hydrochar that is not a representative hydrochar characteristic [69]. Instead, the behavior of the nutrients under consideration is investigated via measurements of the liquid phase for the case of hydrochars. Therefore, for hydrochars, the content of Ca, Mg, K and P in the solid and in the liquid phase are presented.

It is observed that the main factor affecting nutrient content in the final product is the feedstock, since both present very different composition, with higher inorganic species and N content in CD. It is obvious that PW has negligible potential for direct nutrient value from this point of view. Such direct nutrient value is high for CD due to high amount of available N, P, and K (see Table 4). In the case of CD it becomes important to investigate how the total nutrient content and their availability changes with the conversion process. PW results are also presented as comparison.

The ratio C/N can be used as a possible indicator for nitrogen mineralization or immobilization, taking $C/N < 20$ as predictor for nitrogen mineralization and $C/N > 30$ as indicator of initial net nitrogen immobilization [37,70]. For PW biochars the molar C/N ratio is very high, with values above 500, which could potentially lead to a high degree of N immobilization once applied to soil, as previously explained. This is due to the low content of nitrogen in the initial feedstock, which would

still decrease during the conversion process due to nitrogen volatilization, leaving negligible amount of available N-species in the biochar [17]. In the case of CD, the initial nitrogen content in feedstock is significantly higher, leading to C/N ratios between 20 and 30, which would indicate possibility of mineralization or higher availability for plants once applied to soil [37]. However, the amount of available N-species for CD biochars is negligible, similar to PW biochars. It must be taken into account that the C/N ratios for hydrochars are indicative, due to the aforementioned methodical issues.

With respect to P and K, PW biochars present higher nutrient availability (PO_4^{3-} and K^+) in comparison to the raw feedstock. This may be explained by accumulation of these elements due to release of volatile organic matter during pyrolysis for the case of K^+ availability, which also shows a highly significant ($p < 0.001$) dependency on pyrolysis temperature. PO_4^{3-} availability does not seem to be dependent on temperature but rather on N_2 gas flow at 600 °C ($p < 0.05$). In contrast to PW, CD biochars PO_4^{3-} availability is reduced in comparison to the feedstock. Also, there is the same significant ($p < 0.05$) dependency on N_2 gas flow at 600 °C pyrolysis temperature. The observed reduction in K^+ availability for the case of CD is not significant due to the high uncertainty associated with the results (which stems from the high heterogeneity of the feedstock).

A reduction in the availability of PO_4^{3-} has been reported elsewhere, but different to the observed results in this study, a dependency on pyrolysis temperature has been reported [16,17]. Instead, in this study an increase in N_2 flow leads to a significant increase in PO_4^{3-} availability at high pyrolysis temperature. This hints to the hypothesis that P is somehow included in carbonaceous solids formed upon recondensation of primary pyrolysis vapors because it has been shown that biochar extractable P is primarily orthophosphate at pyrolysis temperatures > 350 °C [16]. More detailed studies are required to understand this phenomenon. Finally it has to be concluded that pyrolysis leads to a significant loss of plant available nutrient species, specifically NH_4^+, NO_3^-, and PO_4^{3-}, which has to be considered when nutrient rich feedstock is being used.

In contrast to the observations from pyrolysis experiments, HTC of PW does lead to a significant increase of N, P, and K availability (as defined by the analytical method applied here). Twice to ten times the amount of nutrients are recovered in the process water of HTC as compared to the leachate after extracting with $CaCl_2$ or double lactate (see Table 4, note that at least four times as much process water is present after HTC as dry solid input). These leached nutrients are lost to the hydrochar, but can be potentially re-used together with the process water. Different to pyrolysis, nitrogen compounds are not lost during the conversion process [69,71]. HTC of nutrient rich CD leads to different observations: the same amount of available nutrients of the feedstock are recovered in the process water for the case of NH_4^+ and K^+, but there is a significant reduction of NO_3^- and PO_4^{3-}. This is likely due to the precipitation of salts, leading to a recovery of these nutrients with the solids [72]. Indeed, the observed high amount of extractable PO_4^{3-} on the hydrochar (data not shown) cannot be explained by solved PO_4^{3-} in the hydrochars moisture content, i.e., that a significant amount of solid PO_4^{3-} precipitates during the reaction. It is also noted that the P contained in the liquid phase is almost exclusively detected as PO_4^{3-} whereas only a fraction of the hydrochars P is extractable by the applied methods (10–30%). The recovery of nutrients in the process water allows for a decoupling of fertilizing and soil amendment with the potential to flexibly combine these two in a designed hydrochar product. There is only little influence of the applied HTC process conditions on these findings. For the case of PW, more severe carbonization leads to a significant but small reduction of NH_4^+ and PO_4^{3-} in the liquid phase ($p < 0.05$). This might be due to an increase in adsorption capacity of the produced hydrochar or increased precipitation of these species. For the case of CD, this decrease with reaction severity is only observed for NO_3^- and PO_4^{3-} ($p < 0.05$). These results are in contrast to observations from other HTC experiments, which reported an increase of NH_4^+ in the liquid phase with reaction temperature or no significant change at all [69,72]. These contradicting results can be possibly explained with the varying nutrient concentrations used in the different experiments.

Table 4. Total content of N, Mg, Ca, P and K, as well as available N, P and K (mean ± standard deviation). The inorganic species content is given for the solid phase (sol) in biochars and for the solid (sol) and liquid phase (liq) in hydrochars. [a] determined by biochar extraction. [b] measured in the liquid phase of the hydrothermal carbonization experiments. n.d.: not detected. * The ratio C/N is molar ratio.

	C/N_{sol} *	N_{sol} (db)	Mg_{sol} (db)	Ca_{sol} (db)	P_{sol} (db)	K_{sol} (db)	Mg_{liq}	Ca_{liq}	P_{liq}	NH_4^+	NO_3^-	PO_4^{3-}	K^+
	-	%	mg/kg	mg/kg	mg/kg	mg/kg	-	-	-	mg/kg [a]	mg/kg [a]	mg/kg [a]	mg/kg [a]
PW	912.7	0.1	178.1 ± 38.7	894.5 ± 305.7	-	322.1 ± 81.6	-	-	-	2.3	0.9	13	230
CD	20.1	2.4	-	-	13,900 ± 440	9600 ± 360	-	-	-	1200 ± 110	1800 ± 130	1800 ± 160	6100 ± 350
PW400-20	550.9 ± 57.9	0.2 ± 0.0	-	-	-	-	-	-	-	n.d.	0.9	27 ± 9	300 ± 30
PW400-40	729.2 ± 54.2	0.1 ± 0.0	-	-	-	-	-	-	-	n.d.	n.d.	37 ± 2	370 ± 60
PW600-20	634.1 ± 106.8	0.2 ± 0.0	-	-	-	-	-	-	-	0.9 ± 0.2	n.d.	16 ± 2	900 ± 40
PW600-40	694.3 ± 91.3	0.2 ± 0.0	-	-	-	-	-	-	-	0.4 ± 0.1	0.6	43 ± 6	750 ± 40
CD400-20	22.6 ± 3.5	2.4 ± 0.4	20,568.0 ± 2233.3	139,051.2 ± 23,155.2	26,458.0 ± 2163.8	11,882.6 ± 1303.1	-	-	-	1.2 ± 0.5	n.d.	1360 ± 110	4610 ± 1680
CD400-40	22.4 ± 0.2	2.3 ± 0.1	22,608.3 ± 3140.2	154,160.6 ± 25,380.1	30,319.7 ± 3287.0	13,184.2 ± 1594.7	-	-	-	2.6	n.d.	1650	7460
CD600-20	29.4 ± 1.5	1.8 ± 0.1	21,796.2 ± 1781.4	135,010.5 ± 15,103.8	27,975.3 ± 2270.6	12,410.9 ± 1441.5	-	-	-	1.4 ± 0.4	11	960 ± 130	7890 ± 1580
CD600-40	29.6 ± 1.4	1.7 ± 0.1	22,150.4 ± 2930.0	156,042.0 ± 13,715.9	29,015.1 ± 3091.5	12,601.1 ± 1442.5	-	-	-	1.3 ± 0.1	n.d.	1510 ± 50	8210 ± 1410
	[-]	%	mg/kg	mg/kg	mg/kg	mg/kg	mg/kg	mg/kg	mg/kg	mg/kg [b]	mg/kg [b]	mg/kg [b]	mg/kg [b]
PW200-10	522.8 ± 80.7	0.1 ± 0.0	95.8 ± 9.8	733.1 ± 54.3	61.5 ± 4.2	213.1 ± 19.5	60.0 ± 8.8	126.7 ± 38.3	31.7 ± 9.4	5.1 ± 0.2	5.3 ± 0.5	24.2 ± 7.5	124 ± 20
PW200-360	841.7 ± 68.6	0.1 ± 0.0	99.3 ± 14.8	446.6 ± 14.1	78.7 ± 31.3	255.4 ± 9.6	48.2 ± 8.7	145.1 ± 10.7	16.0 ± 1.1	1.1 ± 0.1	5.5 ± 1.9	11.4 ± 1.1	112 ± 2
PW240-10	616.1 ± 248.0	0.1 ± 0.1	72.0 ± 0.1	500.1 ± 4.0	48.9 ± 3.0	183.4 ± 9.3	42.8 ± 0.4	135.6 ± 1.2	22.3 ± 0.1	2.1 ± 0.2	5.9 ± 0.0	17.4 ± 0.6	115 ± 3
PW240-360	1802.3 ± 1351.3	0.1 ± 0.1	118.4 ± 4.6	624.8 ± 16.7	71.2 ± 1.3	336.0 ± 31.1	40.9 ± 1.0	143.3±1.2	10.4 ± 1.1	1.2 ± 0.3	5.0 ± 3.3	3.5 ± 0.6	121 ± 6
CD200-10-0/6	28.8 ± 2.1	1.9 ± 0.1	9565.4	44,518.8 ± 5535.0	15,735.0 ± 1087.1	5359.6 ± 2479.4	3.5	1027.5 ± 298.6	341.2 ± 131.4	230 ± 30	19.2 ± 4.2	190 ± 48	1490 ± 20
CD200-360-0/6	27.3 ± 1.8	2.0 ± 0.1	11,292.0	54,222.0 ± 9737.7	18,429.3 ± 602.5	4226.9 ± 2928.9	189.0 ± 263.3	2356.9 ± 439.9	63.9 ± 19.1	260 ± 65	16.0 ± 4.1	60 ± 31	2180 ± 160
CD220-185-3	25.6 ± 0.5	2.2 ± 0.0	12,970.2	53,535.0± 1943.2	19,555.3 ± 671.9	2141.8 ± 492.8	3.1	1985.0 ± 99.0	60.8 ± 6.0	180 ± 62	8.3 ± 2.3	51 ± 8	1890 ± 360
CD240-10-0/6	27.3 ± 1.9	1.8 ± 0.1	10,753.2 ± 1330.7	101,258.3 ± 50,630.1	15,962.0 ± 435.4	3158.0 ± 1476.1	473.3 ± 618.1	2301.6 ± 530.4	112.9 ± 84.6	360 ± 81	8.1 ± 1.9	100 ± 80	1870 ± 240
CD240-360-0	22.5	2.5	-	110,882.0	20,862.4	4656.2	-	2172 .0	50.5	140	1.6	32	1470

3.6. PAH

The PAHs content in the biochar is dependent on the process conditions, mainly maximum temperature reached in the process, feedstock and mass transport limitations due to potential enhancement of heterogeneous secondary reactions. For example, as reported in [73], the emission of PAHs (detected in the vapor phase) for pine wood chips starts when the temperatures inside the solid bed range between 300–350 °C, being at those temperatures 2- and 3-ring aromatic compounds the main species. This is in good agreement with the results shown in Figure 7, where it is already observable that in the temperature range from 350–400 °C the highest amount of PAHs is present in the PW biochar, being phenanthrene the most significant species, as shown in Figure 7 (bottom left and right). However, as the temperature increases, the presence of PAHs decreases significantly. At those temperatures almost no more volatiles, which can further react within the solid matrix, are being produced and the temperatures are also high enough for a good part of the PAHs still present in the solid matrix to be removed. Inert gas flow rate may have also a significant impact on the formation of PAHs, since higher flow rates lead to lower volatiles concentration and retention time in the gas phase. Hence, the potential intraparticle heterogeneous secondary reactions may be reduced, main mechanism for PAHs formation at conversion temperatures lower than 500 °C [40,64,73]. This is further confirmed by results recently shown by Buss et al. [74].

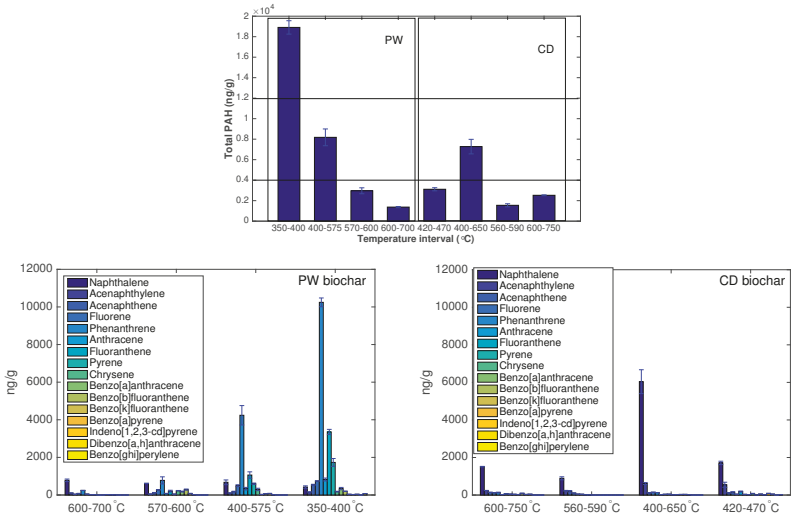

Figure 7. Top: Total content in PAHs (16 EPA PAHs) for PW and CD biochars. Horizontal lines correspond to the limits of PAHs content for basic (12 mg/kg) and premium (4 mg/kg) class biochars (EBC). **Bottom**: Content of PAHs species for PW and CD biochars.

For CD, however, the trend is not the same, since the highest contents in PAHs are shifted to higher temperatures, suggesting that the pathways behind their formation are different from the ones of PW biochar. This is further supported by their composition. In Figure 7, bottom left and right, it is shown that PAHs present in CD biochar are mainly naphthalene and acenaphthylene, while for PW biochars phenanthrene and fluoranthene are the main species at low temperatures. At high temperatures, naphthalene is the main species.

It must be taken also into account that the ash content in the CD biochar is very high, with values around 40% in mass, dry basis. Since the PAHs are produced in the organic phase, to compare the total PAHs in the same basis for CD and PW biochars (% mass, dry ash free basis), the PAHs content in the

case of CD should be multiplied by an approximate factor of 1.7. This leads to higher PAHs content, as function of the organic fraction, in CD than PW, except PW biochars produced at around 400 °C.

Regarding the application of biochar to soil, while in almost all cases a basic grade biochar is obtained, it can be concluded that for a high quality biochar temperatures close to 600 °C must be reached.

According to Schimmelpfennig and Glaser [21], hydrochars have very low total PAH content and low naphthalene/phenanthrene ratios, similar to PW biochars produced at low temperatures. Therefore, PAHs content in hydrochars should not be a major issue with respect to their application and they have not been measured in this study.

3.7. Wettability

In Figure 8, the water absorption behavior of several biochars is shown. On the top, those for PW biochars and, on the bottom, the behavior for CD biochars. CD biochars show increasing capacity in water absorption with higher conversion severity, probably due to an increase in porosity and reduction in surface functional groups. PW biochars present two completely different behaviors. While chars produced at the highest severity (600 °C, 40 NL min^{-1}) show similar patterns to those from CD biochars (although with slightly lower capacity to absorb water), those produced at lower temperatures do not show almost capacity to absorb water, reaching an asymptotic behavior after the first seconds.

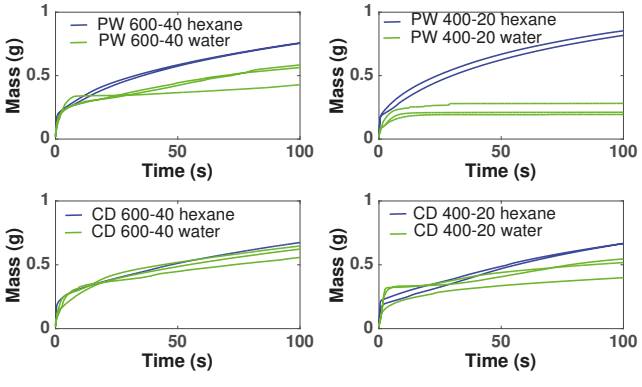

Figure 8. Water and hexane absorption curves of PW600-40, PW400-20, CD600-40, CD400-20.

When water is substituted by hexane, CD biochars still show similar absorption capacity in comparison to water, however the capacity of absorbing hexane by pine wood biochars is much higher than the one for water. If both absorption curves are compared, the contact angle can be determined, as explained in [50]. The contact angles obtained are shown in the Supplementary Material (Table S2). PW biochars present contact angles close to 90°, except PW600-40, while CD biochars present slightly lower contact angles. Although the theoretical definition of hydrophobicity is contact angle >90°, the fact that the values reported here are so close to 90° is an indication of high potential hydrophobicity [50]. From these results it can be concluded that biochars present mostly hydrophobic behavior, although this could be reduced with higher inert flow gas rates during the pyrolysis process, suggesting that a potential source of hydrophobicity is the condensation of volatiles on the char surface. It has been also shown in literature [50] that after one year in soil, biochars loose part of their hydrophobicity.

4. Conclusions

The influence of process conditions and feedsctock on several biochars and hydrochars properties has been studied in a comprehensive way and analyzed from mechanistic perspectives. This work

aims at contributing to biochar engineering, i.e., the capacity of designing and producing biochars able to perform a specific function for given soil, crop and climate requirements and constraints. Based on the current results, the following conclusions can be derived:

- Regarding primary characterization, biochars O/C molar ratio is linearly correlated to volatiles content, independently of the pyrolysis conditions and feedstock. However, H/C molar ratios of CD biochars are generally lower than those of PW biochars, which may be attributed to the higher inorganic matter content of CD, leading to different pyrolysis reaction pathways and enhancing aromatization. PW hydrochars H/C molar ratio and CD hydrochars O/C molar ratio are also outliers with respect to the linear behavior. This shows that elemental and proximate analysis are not enough to determine the chemical properties of biochars [19], due to the influence of feedstock properties on reaction pathways.
- The pH depends on both conversion process parameters and feedstock, having in general higher pH biochars and hydrochars produced from CD, with much higher inorganic content, including carbonates. In both PW and CD biochars pH correlates strongly with H/C molar ratio. PW biochars and PW hydrochars present also correlation with the O/C ratio. Only CD hydrochars show good correlation (r = 0.88) with the ash content. This shows that the H/C molar ratio may be a better indicator of surface chemistry than O/C ratios or volatiles content, which is also supported by measurements of the total acidic functional groups.
- The porous structure varies greatly among biochars. PW biochars produced at 600 °C present mainly microporosity with N_2-SSAs around 400 $m^2\ g^{-1}$. In CD biochars this microporosity is lower ($<$100 $m^2\ g^{-1}$). The significantly lower microporosity for all CD biochars is attributed to the high inorganic content, which could potentially block the micropores and enhance mesoporosity. PW and CD biochars produced at 400 °C present also micropores (as shown by CO_2 adsorption), but much less developed than at higher temperatures, i.e., microporosity must be still developed through volatiles release, to open the pores, and further solid aromatization. Furthermore, a higher N_2 sweeping flow during pyrolysis enhances microporosity (more than double for CD biochars at 600 °C). This indicates that micropores blocking is related to volatiles, which may further react to form secondary char or condense in the pores to a greater extent for lower flow rates, when the concentration and retention time of volatiles is higher. Hydrochars, on the contrary, present mainly mesoporosity, independently of the raw material and the process severity, having higher pore volume but generally lower SSA than biochars. Washing of hydrochars further increases the SSA and pore volume due to removal of condensed species.
- Regarding nutrients, NO_3^- and NH_4^+ availability is negligible after pyrolysis, irrespective of feedstock nitrogen content. The absolute availability of PO_4^{3-} is reduced compared to the feedstock. For PW biochars the relative availability increases with the pyrolysis conversion. Higher inert gas flow rate leads also to higher PO_4^{3-} availability. For hydrochars, HTC can potentially lead to an increase in availability of NO_3^-, NH_4^+, PO_4^{3-}, and K^+; however, these species are primarily solved in the process water. One exception is PO_4^{3-} which appears to form precipitates at higher concentration, i.e., for feedstocks with high direct nutrient potential. Similar to pyrolysis, there is the tendency that the availability of the investigated species is decreased at higher HTC temperatures.
- Biochars have a higher stability to oxidation than hydrochars. Besides the influence of process conditions, PW biochars show higher thermal stability than CD biochars. The same holds true for hydrochars. This may be related to the catalytic effect of AAEM during oxidation reactions.
- PAHs are already produced in biochars at temperatures as low as 340 °C. The maximum quantity is detected for temperatures around 400 °C, exceeding in the case of PW the maximum level for certification. At higher temperatures the PAHs content is reduced again due to vaporization of these species from the solid matrix, achieving a premium quality for temperatures above 550 °C. The composition of these species is highly dependent on the feedstock: naphthalene is the main

species in CD biochars, while phenanthrene and fluoranthene are the main species in PW biochars at low temperatures.

- Both PW and CD biochars present mostly a hydrophobic behavior, although it can be reduced with higher conversion temperatures and higher inert gas flow rates during pyrolysis, which reduces the extent of secondary reactions and recondesation of volatiles.

Based on the previous conclusions, the following general recommendations for biochar and hydrochar production can be derived. Pyrolysis temperatures above 550 °C guarantee low H/C and O/C ratios, PAHs content below the limit according to quality criteria (EBC), independently of the initial feedstock, higher SSAs and lower hydrophobicity. N_2 flow during pyrolysis can also contribute to further microporosity development and hydrophobicity reduction. High inorganic content in the feedstock potentially reduces SSA and hydrophobicity, but increases mesoporosity and pH. With respect to hydrochars, the EBC requirement regarding elemental composition can only be fulfilled for high temperature and residence times PW hydrochars. Hydrochars have a lower SSA than biochars, but a higher mesoporosity, total pore volume and nutrient availability. Washing of hydrochars after production further increases their surface area and pore volume. The results from this work can be applied to "engineer" appropriate biochars with respect to soil demands and certification requirements, as well as to improve biochar certification, and they are summarized in Figure 9.

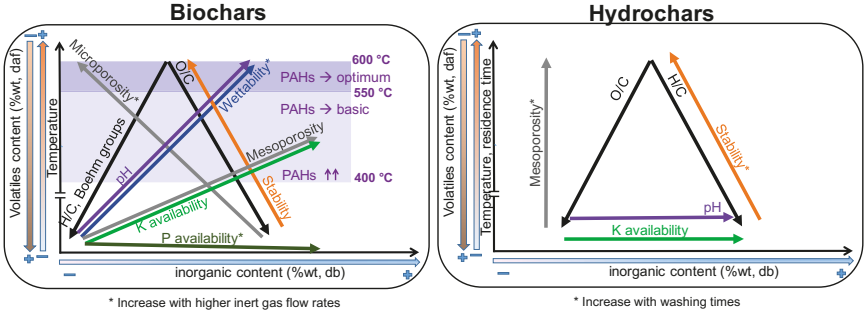

Figure 9. Conclusions. The direction of the arrows indicates increasing values for all properties.

Supplementary Materials: The following are available online at www.mdpi.com/1996-1073/11/3/496/s1.

Acknowledgments: The authors thank Susanne Hoffmann, Hernán Almuina Villar, Alba Domínguez Yebra, Alberto García Rueda and Christina Eichenauer (Technische Universität Berlin) for their support with the analytic characterization of biochars and hydrochars. The authors also thank the Leibniz Institute for Agricultural Engineering and Bioeconomy (Potsdam, Germany) for preparation of hydrochar samples. The authors acknowledge support by the German Research Foundation and the Open Access Publication Funds of Technische Universität Berlin.

Author Contributions: Alba Dieguez-Alonso, Axel Funke and Andrés Anca-Couce conceived and designed the experiments; Alba Dieguez-Alonso and Axel Funke performed the pyrolysis and hydrothermal carbonization experiments respectively; Alba Dieguez-Alonso, Axel Funke, Alessandro Girolamo Rombolà, Gerardo Ojeda and Jörg Bachmann analyzed the different biochar and hydrochar properties, with the further support from those mentioned in the acknowledgements; Alba Dieguez-Alonso, Andrés Anca-Couce, Axel Funke, Alessandro Girolamo Rombolà, Gerardo Ojeda and Jörg Bachmann and Frank Behrendt analyzed the data. Alba Dieguez-Alonso wrote the paper with important contributions from Andrés Anca-Couce and Axel Funke; the rest of the co-authors reviewed the manuscript and contributed to it when necessary according to their data analysis and interpretation. Frank Behrendt supervised the work.

Conflicts of Interest: The authors declare no conflict of interest.

Abbreviations

The following abbreviations are used in this manuscript:

CD	Corn digestate
PW	Pine wood
HTC	Hydrothermal carbonization
PSD	Pore size distribution
PAH	Polycyclic aromatic hydrocarbon
USEPA	United States Environmental Protection Agency

References

1. European Biochar Certificate (EBC). *European Biochar Certificate—Guidelines for Sustainable Production of Biochar*; Version 6.2E; European Biochar Foundation (EBC): Arbaz, Switzerland, 2012. Available online: http://www.europeanbiochar.org/en/download (accessed on 4 February 2016).
2. Standardized Product Definition and Product Testing Guidelines for Biochar That Is Used in Soil. International Biochar Intiative. Version 2.1. 2015. Available online: http://www.biochar-international.org/characterizationstandard (accessed on 19 October 2016).
3. Abiven, S.; Schmidt, M.; Lehmann, J. Biochar by design. *Nat. Geosci.* **2014**, *7*, 326–327.
4. Lee, M.E.; Park, J.H.; Chung, J.W. Adsorption of Pb(II) and Cu(II) by Ginkgo-Leaf-Derived Biochar Produced under Various Carbonization Temperatures and Times. *Int. J. Environ. Res. Public Health* **2017**, *14*, 1528.
5. Frišták, V.; Pipíška, M.; Soja, G. Pyrolysis treatment of sewage sludge: A promising way to produce phosphorus fertilizer. *J. Clean. Prod.* **2018**, *172*, 1772–1778.
6. Frišták, V.; Pipíška, M.; Lesný, J.; Soja, G.; Friesl-Hanl, W.; Packová, A. Utilization of biochar sorbents for Cd^{2+}, Zn^{2+}, and Cu^{2+} ions separation from aqueous solutions: Comparative study. *Environ. Monit. Assess.* **2014**, *187*, 4093, doi:10.1007/s10661-014-4093-y.
7. Inyang, M.I.; Gao, B.; Yao, Y.; Xue, Y.; Zimmerman, A.; Mosa, A.; Pullammanappallil, P.; Ok, Y.S.; Cao, X. A review of biochar as a low-cost adsorbent for aqueous heavy metal removal. *Crit. Rev. Environ. Sci. Technol.* **2016**, *46*, 406–433.
8. Mohan, D.; Sarswat, A.; Ok, Y.S.; Charles, U.P., Jr. Organic and inorganic contaminants removal from water with biochar, a renewable, low cost and sustainable adsorbent—A critical review. *Bioresour. Technol.* **2014**, *160*, 191–202.
9. Sohi, S.P.; Krull, E.; Lopez-Capel, E.; Bol, R. Chapter 2—A Review of Biochar and Its Use and Function in Soil. In *Advances in Agronomy*; Sparks, D.L., Ed.; Academic Press: Cambridge, MA, USA, 2010; Volume 105, pp. 47–82.
10. Chan, K.Y.; Xu, Z. Nutrient Properties and Their Enhancement. In *Biochar for Environmental Management. Science and Technology*; Earthscan: Abingdon, UK, 2009; Chapter 5, pp. 67–84, ISBN 978-1-84407-658-1.
11. Thies, J.E.; Rillig, M.C. Characteristics of Biochar: Biological Properties. In *Biochar for Environmental Management. Science and Technolgy*; Earthscan: Abingdon, UK, 2009; Chapter 6, pp. 85–105.
12. Anca-Couce, A.; Dieguez-Alonso, A.; Zobel, N.; Berger, A.; Kienzl, N.; Behrendt, F. Influence of Heterogeneous Secondary Reactions during Slow Pyrolysis on Char Oxidation Reactivity of Woody Biomass. *Energy Fuels* **2017**, *31*, 2335–2344.
13. Yuan, J.H.; Xu, R.K.; Zhang, H. The forms of alkalis in the biochar produced from crop residues at different temperatures. *Bioresour. Technol.* **2011**, *102*, 3488–3497.
14. Angst, T.E.; Sohi, S.P. Establishing release dynamics for plant nutrients from biochar. *GCB Bioenergy* **2013**, *5*, 221–226.
15. Zambon, I.; Colosimo, F.; Monarca, D.; Cecchini, M.; Gallucci, F.; Proto, R.A.; Lord, R.; Colantoni, A. An Innovative Agro-Forestry Supply Chain for Residual Biomass: Physicochemical Characterisation of Biochar from Olive and Hazelnut Pellets. *Energies* **2016**, *9*, 526.
16. Uchimiya, M.; Hiradate, S.; Antal, M.J. Dissolved Phosphorus Speciation of Flash Carbonization, Slow Pyrolysis, and Fast Pyrolysis Biochars. *ACS Sustain. Chem. Eng.* **2015**, *3*, 1642–1649.
17. Hossain, M.K.; Strezov, V.; Chan, K.Y.; Ziolkowski, A.; Nelson, P.F. Influence of pyrolysis temperature on production and nutrient properties of wastewater sludge biochar. *J. Environ. Manag.* **2011**, *92*, 223–228.

18. Mukherjee, A.; Zimmerman, A.; Harris, W. Surface chemistry variations among a series of laboratory-produced biochars. *Geoderma* **2011**, *163*, 247–255.
19. Budai, A.; Wang, L.; Gronli, M.; Strand, L.T.; Antal, M.J.; Abiven, S.; Dieguez-Alonso, A.; Anca-Couce, A.; Rasse, D.P. Surface Properties and Chemical Composition of Corncob and Miscanthus Biochars: Effects of Production Temperature and Method. *J. Agric. Food Chem.* **2014**, *62*, 3791–3799.
20. Lawrinenko, M.; Laird, D.A. Anion exchange capacity of biochar. *Green Chem.* **2015**, *17*, 4628–4636.
21. Schimmelpfennig, S.; Glaser, B. One step forward toward characterization: Some important material properties to distinguish biochars. *J. Environ. Qual.* **2011**, *42*, 1001–1013.
22. Zhao, S.X.; Ta, N.; Wang, X.D. Effect of Temperature on the Structural and Physicochemical Properties of Biochar with Apple Tree Branches as Feedstock Material. *Energies* **2017**, *10*, 1293.
23. Carrier, M.; Hardie, A.G.; Uras, A.; Görgens, J.; Knoetze, J.H. Production of char from vacuum pyrolysis of South-African sugar cane bagasse and its characterization as activated carbon and biochar. *J. Anal. Appl. Pyrolysis* **2012**, *96*, 24–32.
24. Gaskin, J.W.; Steiner, C.; Harris, K.; Das, K.C.; Bibens, B. Effect of low-temperature pyrolysis conditions on biochar for agricultural use. *Trans. ASABE* **2008**, *51*, 2061–2069.
25. Keiluweit, M.; Nico, P.S.; Johnson, M.G.; Kleber, M. Dynamic Molecular Structure of Plant Biomass-Derived Black Carbon (Biochar). *Environ. Sci. Technol.* **2010**, *44*, 1247–1253.
26. Cetin, E.; Moghtaderi, B.; Gupta, R.; Wall, T. Influence of pyrolysis conditions on the structure and gasification reactivity of biomass chars. *Fuel* **2004**, *83*, 2139–2150.
27. Downie, A.; Crosky, A.; Munroe, P. Physical Properties of Biochar. In *Biochar for Environmental Management. Science and Technology*; Earthscan: Abingdon, UK, 2009; Chapter 2, pp. 13–32, ISBN 978-1-84407-658-1.
28. Liu, Z.; Zhang, F.S.; Wu, J. Characterization and application of chars produced from pinewood pyrolysis and hydrothermal treatment. *Fuel* **2010**, *89*, 510–514.
29. Hagemann, N.; Joseph, S.; Schmidt, H.P.; Kammann, C.I.; Harter, J.; Borch, T.; Young, R.B.; Varga, K.; Taherymoosavi, S.; Elliott, K.W.; et al. Organic coating on biochar explains its nutrient retention and stimulation of soil fertility. *Nat. Commun.* **2017**, *8*, 1089, doi:10.1038/s41467-017-01123-0.
30. Van Zwieten, L.; Kimber, S.; Morris, S.; Chan, K.Y.; Downie, A.; Rust, J.; Joseph, S.; Cowie, A. Effects of biochar from slow pyrolysis of papermill waste on agronomic performance and soil fertility. *Plant Soil* **2010**, *327*, 235–246.
31. McCormack, S.A.; Ostle, N.; Bardgett, R.D.; Hopkins, D.W.; Vanbergen, A.J. Biochar in bioenergy cropping systems: Impacts on soil faunal communities and linked ecosystem processes. *GCB Bioenergy* **2013**, *5*, 81–95.
32. Antal, M.J.; Grønli, M. The Art, Science, and Technology of Charcoal Production. *Ind. Eng. Chem. Res.* **2003**, *42*, 1619–1640.
33. Brassard, P.; Godbout, S.; Raghavan, V.; Palacios, H.J.; Grenier, M.; Zegan, D. The Production of Engineered Biochars in a Vertical Auger Pyrolysis Reactor for Carbon Sequestration. *Energies* **2017**, *10*, 288.
34. Titirici, M.M.; White, R.J.; Falco, C.; Sevilla, M. Black perspectives for a green future: Hydrothermal carbons for environment protection and energy storage. *Energy Environ. Sci.* **2012**, *5*, 6796–6822.
35. Huff, M.D.; Kumar, S.; Lee, J.W. Comparative analysis of pinewood, peanut shell, and bamboo biomass derived biochars produced via hydrothermal conversion and pyrolysis. *J. Environ. Manag.* **2014**, *146*, 303–308.
36. Cao, X.; Ro, K.S.; Chappell, M.; Li, Y.; Mao, J. Chemical Structures of Swine-Manure Chars Produced under Different Carbonization Conditions Investigated by Advanced Solid-State 13C Nuclear Magnetic Resonance (NMR) Spectroscopy. *Energy Fuels* **2011**, *25*, 388–397.
37. Wiedner, K.; Naisse, C.; Rumpel, C.; Pozzi, A.; Wieczorek, P.; Glaser, B. Chemical modification of biomass residues during hydrothermal carbonization—What makes the difference, temperature or feedstock? *Org. Geochem.* **2013**, *54*, 91–100.
38. Busch, D.; Stark, A.; Kammann, C.I.; Glaser, B. Genotoxic and phytotoxic risk assessment of fresh and treated hydrochar from hydrothermal carbonization compared to biochar from pyrolysis. *Ecotoxicol. Environ. Saf.* **2013**, *97*, 59–66.
39. Busch, D.; Glaser, B. Stability of co-composted hydrochar and biochar under field conditions in a temperate soil. *Soil Use Manag.* **2015**, *31*, 251–258.
40. Dieguez-Alonso, A.; Anca-Couce, A.; Zobel, N. On-line tar characterization from pyrolysis of wood particles in a technical-scale fixed-bed reactor by applying Laser-Induced Fluorescence (LIF). *J. Anal. Appl. Pyrolysis* **2013**, *102*, 33–46.

41. Naumann, C.; Bassler, R.; Seibold, R.; Barth, C. *Methodenbuch. Band III, Die Chemische Untersuchung von Futtermitteln*; VDLUFA-Verlag: Darmstadt, Germany, 1997.
42. Boehm, H.P.; Diehl, E.; Heck, W.; Sappok, R. Surface Oxides of Carbon. *Angew. Chem. Int. Ed.* **1964**, *3*, 669–677.
43. Goertzen, S.L.; Theriault, K.D.; Oickle, A.M.; Tarasuk, A.C.; Andreas, H.A. Standardization of the Boehm titration. Part I. CO_2 expulsion and endpoint determination. *Carbon* **2010**, *48*, 1252–1261.
44. Tsechansky, L.; Graber, E.R. Methodological limitations to determining acidic groups at biochar surfaces via the Boehm titration. *Carbon* **2014**, *66*, 730–733.
45. Brunauer, S.; Emmett, P.H.; Teller, E. Adsorption of Gases in Multimolecular Layers. *J. Am. Chem. Soc.* **1938**, *60*, 309–319.
46. Barrett, E.P.; Joyner, L.G.; Halenda, P.P. The Determination of Pore Volume and Area Distributions in Porous Substances. I. Computations from Nitrogen Isotherms. *J. Am. Chem. Soc.* **1951**, *73*, 373–380.
47. Seaton, N.; Walton, J.; Quirke, N. A new analysis method for the determination of the pore-size distribution of porous carbons from nitrogen adsorption measurements. *Carbon* **1989**, *27*, 853–861.
48. Hoffmann, G. *Methodenbuch. Band I, Die Untersuchung von Böden*; VDLUFA-Verlag: Darmstadt, Germany, 1991.
49. Fabbri, D.; Rombola, A.G.; Torri, C.; Spokas, K.A. Determination of polycyclic aromatic hydrocarbons in biochar and biochar amended soil. *J. Anal. Appl. Pyrolysis* **2013**, *103*, 60–67.
50. Ojeda, G.; Mattana, S.; Avila, A.; Alcaniz, J.M.; Volkmann, M.; Bachmann, J. Are soil-water functions affected by biochar application? *Geoderma* **2015**, *249–250*, 1–11.
51. Krull, E.S.; Baldock, J.A.; Skjemstad, J.O.; Smernik, R.J. Characteristics of Biochar: Organo-Chemical Properties. In *Biochar for Environmental Management. Science and Technology*; Earthscan: Abingdon, UK, 2009; Chapter 4, pp. 53–65, ISBN 978-1-84407-658-1.
52. Rombolà, A.G.; Fabbri, D.; Meredith, W.; Snape, C.E.; Dieguez-Alonso, A. Molecular characterization of the thermally labile fraction of biochar by hydropyrolysis and pyrolysis-GC/MS. *J. Anal. Appl. Pyrolysis* **2016**, *121*, 230–239.
53. Mumme, J.; Eckervogt, L.; Pielert, J.; Diakité, M.; Rupp, F.; Kern, J. Hydrothermal carbonization of anaerobically digested maize silage. *Bioresour. Technol.* **2011**, *102*, 9255–9260.
54. Li, F.; Cao, X.; Zhao, L.; Wang, J.; Ding, Z. Effects of Mineral Additives on Biochar Formation: Carbon Retention, Stability, and Properties. *Environ. Sci. Technol.* **2014**, *48*, 11211–11217.
55. Liu, W.J.; Jiang, H.; Yu, H.Q. Development of Biochar-Based Functional Materials: Toward a Sustainable Platform Carbon Material. *Chem. Rev.* **2015**, *115*, 12251–12285.
56. Yin, S.; Mehrotra, A.K.; Tan, Z. Alkaline hydrothermal conversion of cellulose to bio-oil: Influence of alkalinity on reaction pathway change. *Bioresour. Technol.* **2011**, *102*, 6605–6610.
57. Pulido-Novicio, L.; Hata, T.; Kurimoto, Y.; Doi, S.; Ishihara, S.; Imamura, Y. Adsorption capacities and related characteristics of wood charcoals carbonized using a one-step or two-step process. *J. Wood Sci.* **2001**, *47*, 48–57.
58. Nguyen, B.T.; Lehmann, J. Black carbon decomposition under varying water regimes. *Org. Geochem.* **2009**, *40*, 846–853.
59. Baldock, J.A.; Smernik, R.J. Chemical composition and bioavailability of thermally altered *Pinus resinosa* (Red pine) wood. *Org. Geochem.* **2002**, *33*, 1093–1109.
60. Lee, J.W.; Kidder, M.; Evans, B.R.; Paik, S.; Buchanan, A.C., III; Garten, C.T.; Brown, R.C. Characterization of Biochars Produced from Cornstovers for Soil Amendment. *Environ. Sci. Technol.* **2010**, *44*, 7970–7974.
61. Ronsse, F.; van Hecke, S.; Dickinson, D.; Prins, W. Production and characterization of slow pyrolysis biochar: Influence of feedstock type and pyrolysis conditions. *GCB Bioenergy* **2013**, *5*, 104–115.
62. Yang, F.; Zhao, L.; Gao, B.; Xu, X.; Cao, X. The Interfacial Behavior between Biochar and Soil Minerals and Its Effect on Biochar Stability. *Entviron. Sci. Technol.* **2016**, *50*, 2264–2271.
63. Guizani, C.; Jeguirim, M.; Valin, S.; Limousy, L.; Salvador, S. Biomass Chars: The Effects of Pyrolysis Conditions on Their Morphology, Structure, Chemical Properties and Reactivity. *Energies* **2017**, *10*, 796.
64. Anca-Couce, A. Reaction mechanisms and multi-scale modelling of lignocellulosic biomass pyrolysis. *Prog. Energy Combust. Sci.* **2016**, *53*, 41–79.
65. Harvey, O.R.; Kuo, L.J.; Zimmerman, A.R.; Louchouarn, P.; Amonette, J.E.; Herbert, B.E. An Index-Based Approach to Assessing Recalcitrance and Soil Carbon Sequestration Potential of Engineered Black Carbons (Biochars). *Environ. Sci. Technol.* **2012**, *46*, 1415–1421.

66. Kuo, L.J.; Herbert, B.E.; Louchouarn, P. Can levoglucosan be used to characterize and quantify char/charcoal black carbon in environmental media? *Org. Geochem.* **2008**, *39*, 1466–1478.
67. Plante, A.F.; Fernández, J.M.; Haddix, M.L.; Steinweg, J.M.; Conant, R.T. Biological, chemical and thermal indices of soil organic matter stability in four grassland soils. *Soil Biol. Biochem.* **2011**, *43*, 1051–1058.
68. Zimmerman, A.R. Abiotic and Microbial Oxidation of Laboratory-Produced Black Carbon (Biochar). *Environ. Sci. Technol.* **2010**, *44*, 1295–1301.
69. Funke, A. Fate of Plant Available Nutrients during Hydrothermal Carbonization of Digestate. *Chem. Ing. Tech.* **2015**, *87*, 1713–1719.
70. Singh, B.; Singh, B.P.; Cowie, A.L. Characterisation and evaluation of biochars for their application as a soil amendment. *Aust. J. Soil Res.* **2010**, *48*, 516–525.
71. Funke, A.; Mumme, J.; Koon, M.; Diakité, M. Cascaded production of biogas and hydrochar from wheat straw: Energetic potential and recovery of carbon and plant nutrients. *Biomass Bioenergy* **2013**, *58*, 229–237.
72. Kruse, A.; Koch, F.; Stelzl, K.; Wüst, D.; Zeller, M. Fate of Nitrogen during Hydrothermal Carbonization. *Energy Fuels* **2016**, *30*, 8037–8042.
73. Dieguez-Alonso, A.; Anca-Couce, A.; Zobel, N.; Behrendt, F. Understanding the primary and secondary slow pyrolysis mechanisms of holocellulose, lignin and wood with laser-induced fluorescence. *Fuel* **2015**, *153*, 102–109.
74. Buss, W.; Graham, M.C.; MacKinnon, G.; Masek, O. Strategies for producing biochars with minimum {PAH} contamination. *J. Anal. Appl. Pyrolysis* **2016**, *119*, 24–30.

© 2018 by the authors. Licensee MDPI, Basel, Switzerland. This article is an open access article distributed under the terms and conditions of the Creative Commons Attribution (CC BY) license (http://creativecommons.org/licenses/by/4.0/).

energies

MDPI

Article

Estimation of Effective Diffusion Coefficient of O_2 in Ash Layer in Underground Coal Gasification by Thermogravimetric Apparatus

Xi Lin, Qingya Liu and Zhenyu Liu *

Beijing Advanced Innovation Center for Soft Matter Science and Engineering, and State Key Laboratory of Chemical Resource Engineering, Beijing University of Chemical Technology, Beijing 100029, China; buctlinxi@outlook.com (X.L.); qyliu@mail.buct.edu.cn (Q.L.)

* Correspondence: liuzy@mail.buct.edu.cn; Tel.: +86-(0)10-6442-1073

Received: 28 January 2018; Accepted: 14 February 2018; Published: 22 February 2018

Abstract: Underground coal gasification (UCG) proceeds generally in the presence of an ash layer on coal (or char) surface. The ash layer increases the mass transfer resistance of O_2 to the gasification surface, which may become the limiting step of whole process. This paper studies O_2 diffusion in ash layer formed on cylindrical char samples using a specially designed one-dimension setup in a thermogravimetric apparatus (TGA). The effective internal diffusion coefficient (D_e) is found to increase with an increase in ash layer thickness, due to an increase in median pore diameter. Methods are established to correlate D_e with operating conditions and to estimate the role of internal diffusion resistance in overall mass transfer resistance.

Keywords: underground coal gasification; ash layer; effective diffusion coefficient; internal diffusion resistance

1. Introduction

Underground coal gasification (UCG) has been viewed as a potential technology because it requires no mining and transportation of coal and leaves the gasification residue underground. In UCG, gasification agents, such as O_2 and H_2O, are injected into predrilled cavity in which the reaction of O_2 with coal yields a high temperature, in a range of 1173–1473 K [1], to allow the reactions of H_2O and CO_2 with coal to occur to produce CO and H_2. The CO and H_2 can be used as feedstock for many chemical industries and fuels for various purposes [2]. This process has been tested for more than one hundred years, such as in the former Soviet Union, and has been studied extensively in recent decades in many countries including Poland, China, Australia and Ukraine [3]. These studies, ranged from field scale to laboratory scale, have advanced this technology significantly. However, there is still no commercial application of this technology to date due mainly to difficulties in steady state operation for a sufficient long period of time. Therefore, laboratory studies in all aspects of the process were emphasized by many researchers. For instance, Urych studied UGC in a TGA/DSC system and evaluated pyrolysis of coal, a step prior to gasification, in a temperature range of 298–1173 K [4]. Prabu et al. studied UCG through combustion of wood block and coal in laboratory to simulate the cavity formation [5]. The impact of reactant gas composition and injection rate on UCG product distribution are also studied by laboratory research [6,7].

It has been found in past studies that the main gasification reaction in UCG is the reaction of coal pyrolysis char with the gasification agents, which is also the limiting step in overall UCG process [8]. In this gasification reaction, minerals in char, which usually accounts 10–20 wt. % of coal, up to 50 wt. % in some coals [9], form an ash layer on the char surface due to exhaustion of carbon by

gasification. This ash layer increases the internal resistance of gas and makes the mass transfer of gasification agents the rate controlling step [10,11].

Experimental and numerical modeling studies have been carried out to study mass transfer in the ash layer in UCG. Some experimental studies [12,13] observed formation of cracks and fractures in coal during gasification, which shatters coal char and ash layer and reduces the mass transfer resistance of gasification agents in ash layer. However, this shattering effect was found by a percolation model [14] to be insufficient to diminish the mass transfer limitation of the gasification agents because the new char surface formed would be quickly covered by an ash layer. The laboratory [15] and field test [16] studies of UCG showed that the ash layers in the order of centimeter on the char surface, as well as in char cracks, constitute the major scenes of internal diffusion.

Conventional modeling studies on UCG [17–19] also studied mass transfer of gasification agents from the bulk gas flow to the surface of solid, which depends largely on temperature distribution and turbulence extent of gasification agents. It should be noted that, however, this mass transfer resistance, from the bulk gas flow to the surface of solid, varies little with the flow rate of gasification agents in the channel of UCG because they are perpendicular to each other [20] (pp. 1835–1836). Huang et al. [21] showed the vertical velocity to the surface is mainly affected by the permeability and fracture of solid, rather than the air flow rate in the axle direction.

Since it is hard to reduce diffusion resistance in ash layer in UCG by manipulating the operating conditions only a few studies addressed the diffusion behavior of gasification agents in ash layer, and most of them assumed a constant diffusion coefficient in the ash layer. However, many coal gasification and combustion studies, other than those of UCG, showed obvious changes in ash structure during the course of gasification, so do the mass transfer coefficients. For instance, Barea et al. [22] suggested the effective diffusion coefficients of CO_2 depends on temperature and porosity of char, and obvious mass transfer resistance was found in char bed as thin as several millimeters in a TGA study. Yan [23] studied combustion of 10 coals and showed that the diffusion coefficient is proportional to effective porosity in ash layers. Liu [24] studied the anisotropy of the ash layer of oil shale, showed that the diffusion coefficients increased with increasing ash layer thickness, but the reaction turns to internal diffusion control under an ash layer of several millimeters.

Due to the importance of mass transfer in ash layer in UCG and little information can be found in the literature on the subject, this work studies the mass transfer behavior of O_2 with increasing thickness of ash layer at various temperatures and O_2 concentrations using a specially designed one-dimensional gasification setup in a TGA.

2. Materials and Methods

2.1. Theoretical Section

In principle, as shown in Figure 1, the mass transfer of O_2 during the gasification of char with an ash layer includes the following steps: (a) diffusion of O_2 with a concentration of C_f in the bulk gas to the external surface of the ash layer, (b) diffusion of O_2 with a concentration of C_{S1} at the surface of ash layer to the char interface, and (c) reaction of O_2 with a concentration of C_{S2} at the char interface with char following the first order reaction [25] respecting to O_2 to produce CO then to CO_2 as shown in our previous study [26]. Under the quasi-steady state, the flux of O_2 (N_{O_2}) from the bulk gas to the external surface of ash layer is equal to the flux of O_2 diffusing through the ash layer, as well as to the reaction of O_2 at the char interface. These steps can be expressed by Equation (1), where K_c is the mass transfer coefficient of convection, L is the thickness of ash layer, D_e is the effective diffusivity in the ash layer, K is the rate constant of C-O_2 reaction, while C_f, C_{S1} and C_{S2} are O_2 concentration in the gas bulk, at the external surface of ash layer, and at the char surface, respectively:

$$N_{O_2} = K_c(C_f - C_{S1}) = \frac{D_e}{L}(C_{S1} - C_{S2}) = KC_{S2} \quad (1)$$

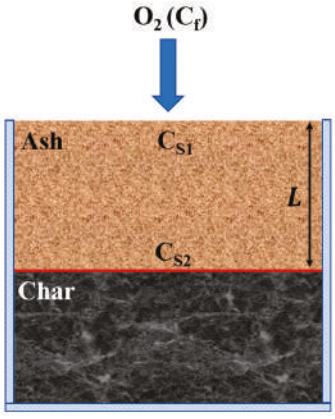

Figure 1. Schematic representation of a char sample with one-dimensional ash layer formation.

N_{O_2} can also be expressed by Equation (2) in terms of mass transfer resistance of these steps or by Equation (3) in terms of carbon consumption rate at the char surface. In these equations M_C is molecular mass of carbon (char), dn_c/dt is carbon consumption rate in mole/min, dm/dt is carbon consumption rate in g/min, and DTG is mass loss rate of sample in g/min measured by TGA. Based on these equations D_e can be expressed by Equation (4).

$$N_{O_2} = \frac{C_f}{\frac{1}{K_c} + \frac{L}{D_e} + \frac{1}{K}} \tag{2}$$

$$N_{O_2} = -\frac{dn_C}{dt} = -(\frac{1}{M_C}\frac{dm}{dt}) = -\frac{DTG}{M_C} \tag{3}$$

$$D_e = \frac{L}{-\frac{M_C C_f}{DTG} - (\frac{1}{K_c} + \frac{1}{K})} \tag{4}$$

Since the ash layer thickness L at a given gasification time is not easy to be determined accurately by the sample's appearance it is estimated from the amount of carbon gasified by Equation (5) based on the following assumptions: (a) The cylindrical char samples consist of C and ash only, and they are distributed uniformly; (b) The ash remained in the gasification maintains the same cylindrical shape as the char sample; and (c) There is no C in the ash layer. In Equation (5), L_f is the final ash layer thickness in an experiment, Δm and Δm_f are the mass losses at the given time and the end of the experiment, respectively.

$$L = \frac{\Delta m}{\Delta m_f} \times L_f \tag{5}$$

The rate constant of C-O_2 reaction (K) can be expressed by Equation (6), where A, E_a, R and T are the pre-exponential factor, the apparent activation energy, the gas constant, and temperature, respectively.

$$K = AT^n e^{-E_a/RT} \tag{6}$$

The convective mass-transfer coefficient (K_c) can be estimated by the Sherwood number (Sh) that is the ratio of convective mass transfer and diffusion mass transfer as shown in Equation (7), where L' is the feature size of char sample, D_{O_2} is the molecular diffusivity of oxygen in the bulk gas.

$$Sh = \frac{K_c L'}{D_{O_2}} \tag{7}$$

When the fluid flows through a single particle as in this paper, the Sherwood number can be approximated by Equation (8) according to Bews et al. [27], where *Re* is the Reynolds number, *Sc* is the Schmidt number, *d* is the inner diameter of TGA tube, *u* is the flow velocity, *v* is the kinematic viscosity of gas flow.

$$Sh = 2.0 + 0.69Sc^{1/3}Re^{1/2} = 2.0 + 0.69(\frac{\nu}{D_{O_2}})^{1/3}(\frac{ud}{\nu})^{1/2} \quad (8)$$

The combination of Equations (7) and (8) yields Equation (9) for K_c.

$$K_c = \frac{D_{O_2}}{L'}(2.0 + 0.69(\frac{\nu}{D_{O_2}})^{1/3}(\frac{ud}{\nu})^{1/2}) \quad (9)$$

2.2. Experimental Section

A Chinese low volatile bituminous coal, Luxian coal, is used in the study. After pyrolysis at 1173 K in N_2 for 3 h, a char with 37 wt. % ash was obtained. The char was crushed and sieved to 60–100 mesh size and then pressed to cylindrical form of 10 mm in diameter and 9 mm in length. The porosity of cylindrical char sample is 0.37, similar to that of the char prior to crushing, 0.35. The purpose of crushing and pelletizing the char is to minimize the macroscopic anisotropy of char structure [24]. In addition, the diameter range of crashed char powder, 0.15–0.25 mm, is much larger than the mean free path of O_2 and the size of the large pores (around 0.0001 mm).

The cylindrical char sample is enclosed in a size-compatible cylindrical TGA crucible with an inner diameter of 10 mm and a depth of 9 mm as shown in Figure 2. Since only the top of char sample is in contact with the gasification reagent, the gasification proceeds along the axial direction with a constant gasification area and the ash layer remained in the gasification maintains the cylindrical shape as the char, similar to that described by the shrinking-core model [28]. After been heated to a gasification temperature in Ar at a rate of 20 K/min, the char sample was exposed to a flow of 10% O_2 in balance Ar at a rate of 100 mL/min, which replaced 99% Ar in the TGA in 5 min. After a given gasification time, the gas flow was switched to Ar and the char sample was cool down to room temperature. *Re* at 1273 K is about 5, the same magnitude as that reported on the coal surface in an underground study [21].

Figure 2. The appearance of char sample before and after gasification at 1273 K for 99 min.

3. Results and Discussion

Figure 3 shows the cross-section view of samples gasified at 1273 K for about 19 and 99 min with mass losses of 90 and 338 mg, respectively. Clearly the gasification front moves along the axial direction of the cylindrical char as expected by the one-dimensional shrinking-core model and the ash remained adheres to the char surface to form a layer of similar thickness. The ash shrinks slightly as evidenced in the radial direction and small amounts of char at the lateral surface closing to the reacting front

gasify due to diffusion of O_2 into the gap between the crucible wall and the sample. Based on the ash layer of 4.0 mm thick in the axis at a mass loss of 338 mg an ash layer of 1.07 mm thick is determined by Equation (5) for a mass loss of 90 mg, which is very close to the observed ash layer thickness of 1.02 mm, indicating sufficient accuracy of Equation (5) in estimating the ash layer thickness.

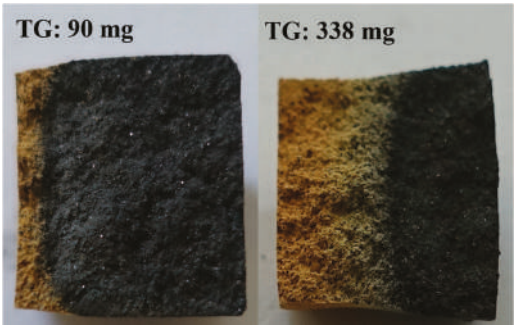

Figure 3. The cross-section view of a sample gasified at 1273 K to different mass losses.

Figure 4 shows the TG and DTG curves of char gasification at 1273 K which yield the samples in Figure 3. The maximum gasification rate (DTG) appears at the beginning, about 5.42 mg/min, due to the absence of an ash layer. As the gasification proceeds, the DTG decreases continuously to about 2.47 mg/min at 99 min, indicating an increase in diffusion resistance of O_2 with an increase in ash layer thickness. This behavior, however, may also include changes in the effective diffusion coefficient D_e.

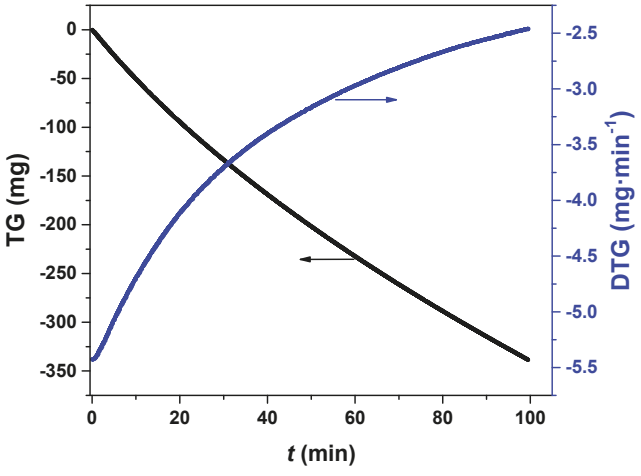

Figure 4. TG and DTG curves during gasification at 1273 K.

3.1. Estimation of Effective Diffusion Coefficient

Since the gasification temperature in Figures 3 and 4 is higher than 1173 K, the boundary of oxidation zone in the "three zones theory" [29], higher than which the resistance of C-O_2 reaction is negligible compared with that of interparticle diffusion [30], Equation (4) can be simplified to Equation (10).

$$D_e = \frac{L}{-\frac{M_C C_f}{DTG} - \frac{1}{K_c}} \tag{10}$$

Figure 5 shows D_e determined by Equation (10). As expected D_e increases with an increase in temperature, 1.51×10^{-4} m^2/s at 1173 K while 2.82×10^{-4} m^2/s at 1373 K both at the mass loss of 250 mg, corresponding to an ash layer thickness of 3 mm. The range of D_e is the same as that determined in our previous study [26] in coal gasification (around 1×10^{-4} m^2/s) and that reported by Chen et al. [31] for combustion of coal particles of 16 mm in diameter with 53% ash (1.5×10^{-4} m^2/s at 1145 K). Figure 5 also shows that D_e increases with increasing time, indicating increasing pore size or fractures in the ash layer over time. This behavior is similar to that reported by Sotirchos [32], who studied combustion of a char with 25% ash and showed increasing macropore volume over time for ash layers of millimeter thick, and increasing D_e over time in a range around 1×10^{-4} m^2/s at 1173 K. Clearly, the compressed cylindrical char sample prepared in this work can be used to study D_e of char particles.

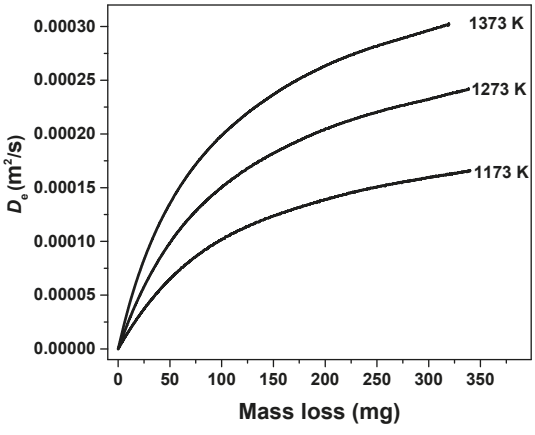

Figure 5. Diffusion coefficient at different temperatures in gasification.

It is noted that in addition to porosity, pore size distribution in the ash layer may also influence mass transfer rate of O_2. To explore this effect ash layers formed on cylindrical char samples during gasification at 1273 K for different time, as shown in Figure 6, were sampled at every 2 mm thick and subjected to mercury intrusion porosimetry analysis. The ash samples listed in Table 1 are these formed initially, 0–2 mm in Figure 6a (Sample 1); 0–2 mm in Figure 6b (Sample 2) that exposed to 1273 K longer than that of Sample 1; 2–4 mm in Figure 6b (Sample 3); and that exposed to 1273 K for a time much longer than other samples (Sample 4) in addition. The t in the table is the residence time the ash sample exposed to 1273 K. It seems that the porosity of these samples is similar, around 0.7, but the median pore diameter of these samples increases with an increase in gasification time, from about 1400 nm in 20–30 min to 1700 nm in 175 min. Since these median pore diameters are less than 5 times the mean free path of O_2 at 1273 K (about 381 nm), in which the collision between gas molecule and the pore wall cannot be ignored, so the increasing D_e in gasification in Figure 5 can be attributed to increasing pore diameter in the ash layers during the gasification.

Table 1. Median pore diameter of ash samples from gasification at 1273 K for different time.

Parameter	Sample 1	Sample 3	Sample 2	Sample 4
t (min)	20	30	65	175
Porosity	0.68	0.69	0.70	0.70
diameter (nm)	1397	1401	1601	1710

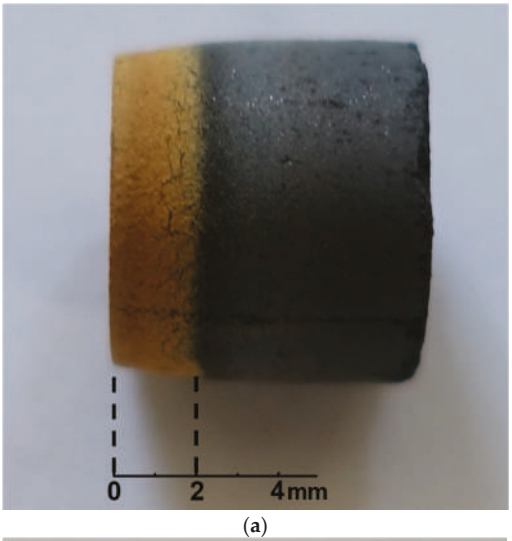

(**a**)

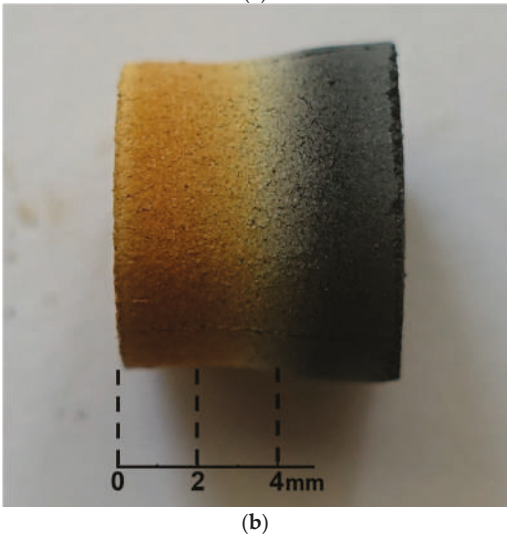

(**b**)

Figure 6. Samples subjected to gasification at 1273 K for different time: (**a**) with an ash layer of 2 mm; (**b**) with an ash layer of 4 mm.

3.2. Internal Diffusion Resistance

For a one-dimensional gas-solid reaction, the traditional shrinking-core model suggests a linear relationship between reaction time (t) and square of ash thickness (L) if internal diffusion is the rate limiting step and effective diffusivity D_e is constant [33]. The plot in Figure 7 shows that the L–$t^{0.5}$ relation of this work is close to a linear relation at ash layer thickness of greater than 2 mm. This however does not necessarily indicate that the gasification is under internal diffusion control because the D_e in the ash layer varies with ash layer thickness as indicated in Figure 5.

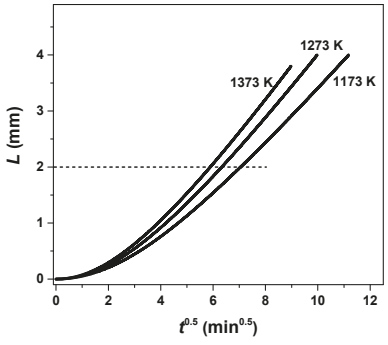

Figure 7. Relation between $t^{0.5}$ and thickness of ash layer L.

To understand the role of O_2 diffusion in ash layer the internal diffusion resistance (L/D_e) at the ash layer thickness of 1, 2 and 3 mm is compared with the reaction resistance at the char surface ($1/K$) and the convection resistance in the bulk gas ($1/K_c$) in Table 2. The $1/K$ and $1/K_c$ are determined by Equations (6) and (9) based on the experimental data of this work and those in the literature [34]. It can be seen that the reaction resistance ($1/K$) is much smaller than the diffusion resistances of $1/K_c$ and L/D_e under the conditions used, indicating that the overall gasification rate is always under mass transfer control. The L/D_e increases with an increase in ash layer thickness although D_e also increases with an increase in ash layer thickness as shown in Figure 5, suggesting that the diffusion resistance of O_2 in the ash layer is more affected by L than by D_e.

Table 2. Resistance of reaction and mass transfer in gas film and ash layer (s/m).

Resistance	1173 K	1273 K	1373 K
$1/K$	0.3	0.07	0.02
$1/K_c$	6.4	5.6	5.0
L/D_e (L = 1 mm)	10.8	7.3	5.5
L/D_e (L = 2 mm)	15.4	10.5	8.1
L/D_e (L = 3 mm)	19.8	13.5	10.6

The contribution of L/D_e to overall mass transfer resistance (η) can be determined with sufficient accuracy by Equation (11), ignoring the contribution of $1/K$, and shown in Figure 8. Clearly, η increases nonlinearly with an increase in ash layer thickness while decreases almost linearly with an increase in temperature, and the O_2 diffusion in ash layer plays a dominant role especially when the ash layer thickness is greater than 1 mm. For instance, at 1273 K, $1/K_c$ is 5.6 s/m while η is around 70% at an ash thickness of 3 mm, corresponding to a mass loss about 250 mg. This η indicates that the diffusion resistance in ash layer is more than twice as much as the external diffusion resistance. This increase in diffusion resistance in the ash layer leads to a decrease in O_2 diffusion rate and a decrease in overall gasification rate, by about 50% from the initial value as indicated in Figure 4. This behavior is similar to that reported by Perkins et al. [35] in which a 20% reduction in gasification rate was observed at an ash layer of 1 mm thick in a meter-scale UCG simulation study.

$$\eta = \frac{L/D_e}{\frac{L}{D_e} + \frac{1}{K_c}} \times 100\% \tag{11}$$

The temperature effect on η in Figure 8 shows that the diffusion resistance in ash layer is more important at a lower temperature than that at a higher temperature. For instance, at an ash layer thickness of 3 mm, the η is about 75.5% at 1173 K but 70.7% and 68.0% at 1273 and 1373 K, respectively.

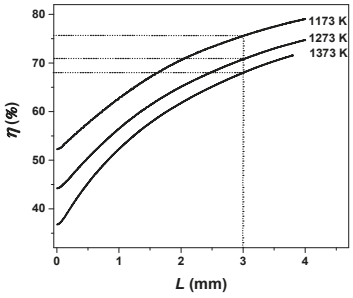

Figure 8. The contribution of L/D_e to overall mass transfer resistance (η) at different ash layer thickness.

3.3. The Influence of Gas Concentration

In UCG, O_2 concentration decreases from the injection well to the production well due to its consumption in gasification. A higher O_2 concentration leads to a higher gasification rate and perhaps also to a change in D_e due to local melting of ash caused by the heat of reaction between O_2 and CO in the ash layer as indicated in our earlier study [26]. It can be seen in Figure 9 that at 1273 K the gasification rate increases with an increase in O_2 concentration, the time needed for gasifying 300 mg char is 115 min under 7.5% O_2 but 72 min under 12% O_2. It can also be seen in Figure 10 that D_e determined by Equation (10) varies little with O_2 concentration at the temperatures used, indicating little ash melting under these conditions, agreeing with our earlier study that the apparent ash melting of this particular coal is at 1573 K [26]. The data in Figure 10 suggest that O_2 concentration plays a minor role while temperature and ash layer thickness play major roles in D_e in Equation (10).

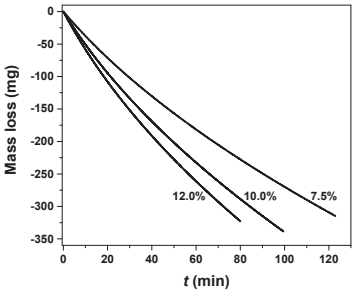

Figure 9. Gasification at 1273 K under different O_2 concentrations.

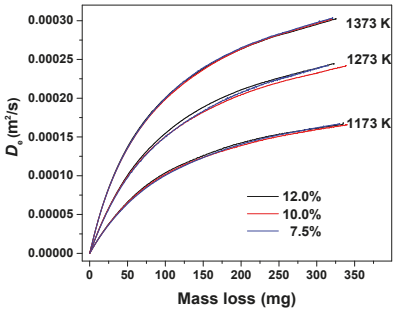

Figure 10. Effective diffusion coefficient in ash layer under different temperatures and O_2 concentrations.

3.4. Effective Diffusion Coefficient with Temperature and Ash Layer Thickness

Since it is not easy to obtain flow parameters in UCG and therefore to estimate $1/K_c$, and the $1/K_c$ is smaller than L/D_e when ash layer is thick, Equation (10) can be simplified to Equation (12) by omitting $1/K_c$ with accuracy θ defined by Equation (13). It can be seen in Figure 11 that θ increases with an increase in ash layer thickness and is higher than 50% when ash layer thickness is higher than 1 mm, especially at low temperatures. For instance, at 1273 K, θ is 44% initially but becomes 76% at an ash layer thickness of 4 mm. Clearly in a continuous operation of UCG with a much thicker ash layer the O_2 diffusion resistance in ash layer is the dominant resistance.

$$D'_e = -\frac{L \times DTG}{M_C C_f} \tag{12}$$

$$\theta = \frac{D'_e}{D_e} \times 100\% = \frac{DTG}{DTG + \frac{M_C C_f}{K_c}} \times 100\% \tag{13}$$

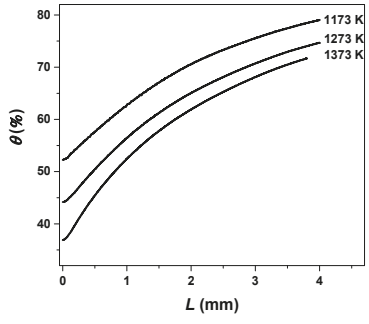

Figure 11. Accuracy of diffusion coefficient (θ) under omitting external diffusion resistance.

Since L/D_e dominants the overall mass transfer resistance in UCG it is useful to establish a relation between D_e in the ash layer and the D_{O_2} in the bulk gas. At a reaction temperature this relation however involves correlations in two regions separated by the pore size that is 10 times the mean free path of O_2, 10 λ, i.e., free diffusion in pores (and fractures) of larger than 10 λ in size with the coefficient approximately D_{O_2} and restrictive diffusion in pores of smaller than 10 λ in size with a coefficient D_1, which is smaller than D_{O_2}. Previous study [36] suggested that D_1 is proportional to the porosity as shown in Equation (14), where ε_1 is porosity of the pores with diameters less than 10 λ and τ is tortuosity of pores generally within 2 to 6 [37].

$$D_1 = \frac{\varepsilon_1}{\tau} \times D_{O_2} \tag{14}$$

$$D_e = (0.7 - \varepsilon_1) D_{O_2} + \varepsilon_1 D_1 \tag{15}$$

$$D_e = D_{O_2}(0.7 - \varepsilon_1 + \frac{{\varepsilon_1}^2}{\tau}) \tag{16}$$

As shown in Table 1 the total porosity of ash layer is approximately 0.7, hence the fraction of pores with diameter larger than 10 λ is $0.7 - \varepsilon_1$ which is also the porosity of any cross section in the ash layer [38]. The effective diffusion coefficient D_e therefore can be expressed by Equation (15), and the relation between D_e and D_{O_2} can be expressed as Equation (16).

If the pores in the ash layer coalesce in continuous high temperature UCG operation ε_1 can be described by Equation (17) according to the format of relationship between porosity and time in porous ceramics at high temperature [39] (p. 380), where t is time while B and c are parameters obtained by

fitting experimental data. Then Equation (16) can be rewritten as Equation (18) and then Equation (19) because time t is proportionate linearly with the square of ash layer thickness as discussed earlier.

$$\varepsilon_1 = Be^{-ct} \tag{17}$$

$$D_e = D_{O_2}(0.7 - Be^{-ct} + \frac{B^2}{\tau} \times (e^{-ct})^2) \tag{18}$$

$$D_e = D_{O_2}(0.7 - Be^{-cdL^2} + \frac{B^2}{\tau}(e^{-cdL^2})^2) \tag{19}$$

Since the higher-order term in Equation (20), $\frac{B^2}{\tau}(e^{-cdL^2})^2$, is relatively small at a higher ash layer thickness and can be omitted, and D_{O_2} is proportional to $T^{1.75}$ according to the formula proposed by Fuller Schettler Giddings [38] Equation (19) can be rewritten as Equation (20) with F as the product of c and d.

$$D_e = 1.78 \times 10^{-5}(\frac{T}{273})^{1.75}(0.7 - Be^{-FL^2}) \tag{20}$$

Table 3 shows the parameters B and F determined by fitting Equation (20) with the data at 1173, 1273 and 1373 K using the least squares method. It can be found that B changes little with a change in temperature indicating that B is determined by the physical properties of ash layer, while F varies relatively strongly with temperature.

Table 3. Parameters of Equation (20).

Parameter	1173 K	1273 K	1373 K
B	0.530	0.548	0.556
F	114,914	210,240	279,638

Figure 12 shows D_e determined by Equation (20) and that observed in the experiments (dots) under different temperatures and ash layer thickness. Clearly the D_e determined from Equation (20) fits the experimental data well with small residual sum of square, approximately 7.1×10^{-11} m^4/s^2 at 1273 K and ash layer thickness of 2.5–3.5 mm, for example.

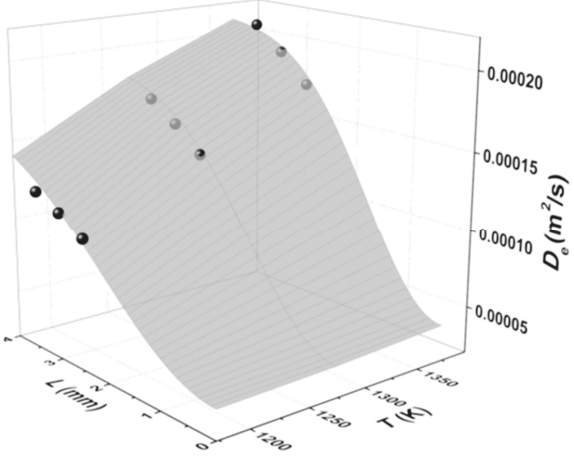

Figure 12. Diffusion coefficient in ash layer under different temperature and ash layer thickness.

Figure 13 shows η, the proportion of internal diffusion resistance in overall mass transfer resistance defined earlier by Equation (11), under different temperatures and ash layer thickness. The contours of η of 70, 75 and 80% show that the internal diffusion resistance plays a major role in overall mass transfer resistance, more than 75% when the ash layer is thicker than 2.5 mm at 1250–1300 K, for example.

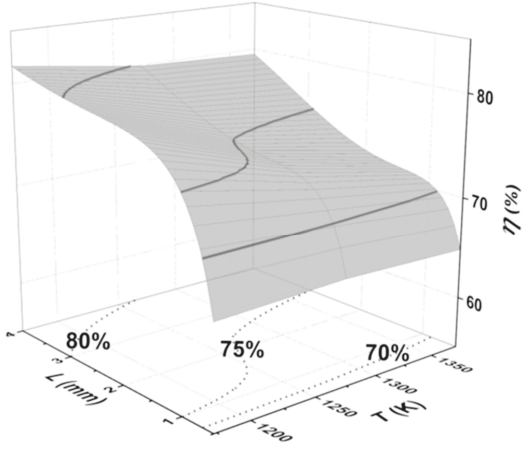

Figure 13. The contribution of L/D_e to overall mass transfer resistance (η) under different temperatures and ash layer thickness.

The increase in η with increasing ash layer thickness would reduce the O_2 flux through ash layer leading to reduced gasification rate and low char conversion, as well as a shift of gasification zone toward the downstream in a UCG operation. This agrees with that reported in the field test [40], where 30% char was not converted even though spalling of coal and ash were observed.

4. Conclusions

This paper studies mass transfer of oxygen in ash layer of UCG using cylindrical char samples in a TGA. It is found that an ash layer is formed and remained on the surface of char, which reduces the rate of carbon conversion significantly in gasification. The effective internal diffusion coefficient of O_2 (D_e) is estimated based on the ash layer thickness observed and estimated from carbon conversion. The mean pore diameter of ash layer increases with an increase in ash layer thickness, so does the D_e. The mass transfer resistance of O_2 in the ash layer (L/D_e) also increases with an increase in ash layer thickness, which is the dominant resistance when the ash layer is a few millimeters thick.

Acknowledgments: The work is financially supported by the National Key Research and Development Program of China (2016YFB0600300).

Author Contributions: Zhenyu Liu and Qingya Liu designed research; Xi Lin performed the experiment; Xi Lin and Qingya Liu analyzed the data; Xi Lin and Zhenyu Liu wrote the paper.

Conflicts of Interest: The authors declare no conflict of interest.

References

1. Najafi, M.; Jalali, S.M.E.; KhaloKakaie, R. Thermal–mechanical–numerical analysis of stress distribution in the vicinity of underground coal gasification (UCG) panels. *Int. J. Coal Geol.* **2014**, *134–135*, 1–16. [CrossRef]
2. Otto, C.; Kempka, T. Prediction of steam jacket dynamics and water balances in underground coal gasification. *Energies* **2017**, *10*, 739. [CrossRef]
3. Shafirovich, E.; Varma, A. Underground coal gasification: a brief review of current status. *Ind. Eng. Chem. Res.* **2009**, *48*, 7865–7875. [CrossRef]

4. Urych, B. Determination of kinetic parameters of coal pyrolysis to simulate the process of underground coal gasification (UCG). *J. Sustain. Min.* **2014**, *13*, 3–9. [CrossRef]
5. Prabu, V.; Jayanti, S. Simulation of cavity formation in underground coal gasification using bore hole combustion experiments. *Energy* **2011**, *36*, 5854–5864. [CrossRef]
6. Konstantinou, E.; Marsh, R. Experimental study on the impact of reactant gas pressure in the conversion of coal char to combustible gas products in the context of underground coal gasification. *Fuel* **2015**, *159*, 508–518. [CrossRef]
7. Hamanaka, A.; Su, F.; Itakura, K.; Takahashi, K.; Kodama, J.; Deguchi, G. Effect of injection flow rate on product gas quality in underground coal gasification (UCG) based on laboratory scale experiment: development of Co-Axial UCG system. *Energies* **2017**, *10*, 238. [CrossRef]
8. Ollero, P.; Serrera, A.; Arjona, R.; Alcantarilla, S. Diffusional effects in TGA gasification experiments for kinetic determination. *Fuel* **2002**, *81*, 1989–2000. [CrossRef]
9. Sadhukhan, A.K.; Gupta, P.; Saha, R.K. Modelling of combustion characteristics of high ash coal char particles at high pressure: shrinking reactive core model. *Fuel* **2010**, *89*, 162–169. [CrossRef]
10. Park, K.Y.; Edgar, T.F. Modeling of early cavity growth for underground coal gasification. *Ind. Eng. Chem. Res.* **1987**, *26*, 237–246. [CrossRef]
11. Perkins, G.; Sahajwalla, V. Modelling of heat and mass transport phenomena and chemical reaction in underground coal gasification. *Chem. Eng. Res. Des.* **2007**, *85*, 329–343. [CrossRef]
12. Su, F.; Nakanowataru, T.; Itakura, K.; Ohga, K.; Deguchi, G. Evaluation of structural changes in the coal specimen heating process and UCG model experiments for developing efficient UCG Systems. *Energies* **2013**, *6*, 2386–2406. [CrossRef]
13. Prabu, V.; Jayanti, S. Heat-affected zone analysis of high ash coals during ex-situ experimental simulation of underground coal gasification. *Fuel* **2014**, *123*, 167–174. [CrossRef]
14. Wang, Z.; Liang, J.; Shi, L.; Xi, J.; Li, S.; Cui, Y. Expansion of three reaction zones during underground coal gasification with free and percolation channels. *Fuel* **2017**, *190*, 435–443. [CrossRef]
15. Daggupati, S.; Mandapati, R.N.; Mahajani, S.M.; Ganesh, A.; Mathur, D.K.; Sharma, R.K.; Aghalayam, P. Laboratory studies on combustion cavity growth in lignite coal blocks in the context of underground coal gasification. *Energy* **2010**, *35*, 2374–2386. [CrossRef]
16. Cena, R.J.; Britten, J.A.; Thorsness, C.B. Excavation of the partial CRIP underground coal gasification test site. In Proceedings of the 13th Annual Underground Coal Gasification Symposium, Laramie, WY, USA, 24–30 August 1987.
17. Yang, L.H. Three-Dimensional non-linear numerical analysis on the oxygen concentration field in underground coal gasification. *Fuel Process. Technol.* **2004**, *85*, 1605–1622. [CrossRef]
18. Eftekhari, A.A.; Wolf, K.H.; Rogut, J.; Bruining, H. Mathematical modeling of alternating injection of oxygen and steam in underground coal gasification. *Int. J. Coal Geol.* **2015**, *150*, 154–165. [CrossRef]
19. Kuyper, R.A.; Meer, T.H.V.D.; Hoogendoorn, C.J. Turbulent natural convection flow due to combined buoyancy forces during underground coal gasification of thin seams. *Chem. Eng. Sci.* **1994**, *49*, 851–861. [CrossRef]
20. Elliott, M.A. *Chemistry of Coal Utilization*; John Wiley and Sons: New York, NY, USA, 1981; pp. 1835–1836.
21. Huang, J.; Bruining, J.; Wolf, K.-H.A.A. Modeling of gas flow and temperature fields in underground coal fires. *Fire Saf. J.* **2001**, *36*, 477–489. [CrossRef]
22. Barea, A.G.; Ollero, P.; Arjona, R. Reaction-diffusion model of TGA gasification experiments for estimating diffusional effects. *Fuel* **2005**, *84*, 1695–1704. [CrossRef]
23. Yan, J.; Ni, M.; Zhao, H.; Cen, K. Gas diffusion through the ash layer of coal particle during the combustion process. *Int. J. Thermophys.* **1994**, *15*, 341–344. [CrossRef]
24. Liu, J.G.; Yan, J.W.; Han, X.X.; Jiang, X.M. Study on the anisotropy of mass transfer for oxygen in the ash layer of shale char particles. *Energy Fuels* **2010**, *24*, 3488–3497. [CrossRef]
25. Hwang, M.; Song, E.; Song, J. One-dimensional modeling of an entrained coal gasification process using kinetic parameters. *Energies* **2016**, *9*, 99. [CrossRef]
26. Lin, X.; Liu, Q.; Liu, Z.; Guo, X.; Wang, R.; Shi, L. The role of ash layer in syngas combustion in underground coal gasification. *Fuel Process. Technol.* **2016**, *143*, 169–175. [CrossRef]
27. Bews, I.M.; Hayhurst, A.N.; Richardson, S.M.; Taylor, S.G. The order, Arrhenius parameters, and mechanism of the reaction between gaseous oxygen and solid carbon. *Combust. Flame* **2001**, *124*, 231–245. [CrossRef]

28. Khan, M.M.; Mmbaga, J.P.; Shirazi, A.S.; Trivedi, J.; Liu, Q.; Gupta, R. Modelling underground coal gasification—A review. *Energies* **2015**, *8*, 12603–12668. [CrossRef]
29. Yang, L.H.; Zhang, X.; Liu, S.Q.; Yu, L.; Zhang, W.L. Field test of large-scale hydrogen manufacturing from underground coal gasification (UCG). *Int. J. Hydrogen Energy* **2008**, *33*, 1275–1285. [CrossRef]
30. Su, J.L.; Perlmutter, D.D. Effect of Pore Structure on Char Oxidation Kinetics. *AIChE J.* **1985**, *31*, 973–981. [CrossRef]
31. Chen, C.; Kojima, T. Single char particle combustion at moderate temperature: effects of ash. *Fuel Process. Technol.* **1996**, *47*, 215–232. [CrossRef]
32. Sotirchos, S.V.; Amundson, N.R. Dynamic behavior of a porous char particle burning in an oxygen-containing environment. *AIChE J.* **1984**, *30*, 537–549. [CrossRef]
33. Wen, C.Y. Non-Catalytic Heterogeneous Solid-Fluid Reaction Models. *Ind. Eng. Chem.* **1968**, *60*, 34–54. [CrossRef]
34. Perkins, G. Mathematical Modelling of Underground Coal Gasification. Ph.D. Thesis, The University of New South Wales, Sydney, Australia, 2005.
35. Perkins, G.; Sahajwalla, V. A numerical study of the effects of operating conditions and coal properties on cavity growth in underground coal gasification. *Energy Fuels* **2006**, *20*, 596–608. [CrossRef]
36. Sadhukhan, A.K.; Gupta, P.; Saha, R.K. Analysis of the dynamics of coal char combustion with ignition and extinction phenomena: shrinking core model. *Int. J. Chem. Kinet.* **2008**, *40*, 569–582. [CrossRef]
37. Kelebopile, L.; Sun, R.; Wang, H.; Zhang, X.; Wu, S.H. Pore development and combustion behavior of gasified semi-char in a drop tube furnace. *Fuel Process. Technol.* **2013**, *111*, 42–54. [CrossRef]
38. Parlange, J.Y. Reviewed Work: Dynamics of Fluids in Porous Media by J. BEAR. *Am. Sci.* **1973**, *6*, 758–759.
39. Kingery, W.D. *Introduction to Ceramics*, 1st ed.; Wiley: New York, NY, USA, 1960; p. 380, ISBN 0471478601.
40. Hill, R.W.; Hill, C.B. *Summary Report on Large Block Experiments in Underground Coal Gasification, Tono Basin, Washington: Volume 1. Experimental Description and Data Analysis*; Report No. UCRL-53305; Lawrence Livermore National Laboratory, University of California: Berkeley, CA, USA, 9 July 1982.

© 2018 by the authors. Licensee MDPI, Basel, Switzerland. This article is an open access article distributed under the terms and conditions of the Creative Commons Attribution (CC BY) license (http://creativecommons.org/licenses/by/4.0/).

energies

MDPI

Article

Steam Gasification of Sawdust Biochar Influenced by Chemical Speciation of Alkali and Alkaline Earth Metallic Species

Dongdong Feng, Yijun Zhao *, Yu Zhang, Shaozeng Sun and Jianmin Gao

School of Energy Science and Engineering, Harbin Institute of Technology, Harbin 150001, China; 08031175@163.com (D.F.); 14B902024@hit.edu.cn (Y.Z.); sunsz@hit.edu.cn (S.S.); yagjm@hit.edu.cn (J.G.)
* Correspondence: zhaoyijun@hit.edu.cn; Tel.: +86-451-8641-3231; Fax: +86-451-8641-2528

Received: 8 December 2017; Accepted: 8 January 2018; Published: 15 January 2018

Abstract: The effect of chemical speciation (H_2O/NH_4Ac/HCl-soluble and insoluble) of alkali and alkaline earth metallic species on the steam gasification of sawdust biochar was investigated in a lab-scale, fixed-bed reactor, with the method of chemical fractionation analysis. The changes in biochar structures and the evolution of biochar reactivity are discussed, with a focus on the contributions of the chemical speciation of alkali and alkaline earth metallic species (AAEMs) on the steam gasification of biochar. The results indicate that H_2O/NH_4Ac/HCl-soluble AAEMs have a significant effect on biochar gasification rates. The release of K occurs mainly in the form of inorganic salts and hydrated ions, while that of Ca occurs mainly as organic ones. The sp^3-rich or sp^2-sp^3 structures and different chemical-speciation AAEMs function together as the preferred active sites during steam gasification. H_2O/HCl-soluble AAEMs could promote the transformation of biochar surface functional groups, from ether/alkene C-O-C to carboxylate COO^- in biochar, while they may both be improved by NH_4Ac-soluble AAEMs. H_2O-soluble AAEMs play a crucial catalytic role in biochar reactivity. The effect of NH_4Ac-soluble AAEMs is mainly concentrated in the high-conversion stage (biochar conversion >30%), while that of HCl-soluble AAEMs is reflected in the whole activity-testing stage.

Keywords: biochar; steam; gasification; chemical speciation; AAEMs

1. Introduction

Compared to fossil fuels, biomass—which is a carbon neutral renewable energy, since the CO_2 from its utilization can be captured via photosynthesis—exhibits great prospects for limiting global gas pollution (NO_x, SO_2 and greenhouse gases) and the energy crisis [1]. Biomass gasification is considered a promising technology with relatively lower temperatures, low energy consumption and a high ability of CO_2 capture, attracting a lot of attention all over the world [2]. Usually, gasification can be divided into two steps, namely biomass devolatilization (first stage, relatively fast) and biochar gasification (second stage, relatively slow). According to previous studies [3–7], the gasification of pyrolysis biochar is the rate-limiting step for the overall gasification reaction, which is usually the focus of research on biomass gasification reactions. Besides, among the various gasifying agents (air, oxygen, CO_2 and steam) for biomass/biochar gasification [8,9], steam is preferred for increasing the heating value of syngas and producing a gaseous fuel with relatively higher H_2 for application in the fuel cells and hydrogen engines [10]. Thus, the steam gasification of pyrolysis biochar is urged to be investigated, especially for catalytic steam gasification [11], where the most important heterogeneous gasification reactions are the water gas reaction ($C + H_2O \rightarrow CO + H_2$), the Boudouard reaction ($C + CO_2 \rightarrow 2CO$) and the heterogeneous methanation ($C + 2H_2 \leftrightarrow CH_4$) [12].

In the current investigation, many researchers [13–18] found that alkali and alkaline earth metallic species (AAEMs) dispersed in biomass and/or biochar as different chemical speciations, play significant catalytic roles in biochar gasification reactivity, and that AAEMs volatilized as a gaseous phase would also take part in homogeneous reforming reactions [19]. The concentration and dispersion of AAEMs, according to the results obtained by Wu et al. [20], is a significant factor affecting the catalytic activity of AAEMs during biomass gasification, which varies constantly due to the carbon consumption and the release/migration of AAEMs [21,22]. Moreover, for various gasifying agents, the AAEMs show different catalytic abilities when chars react with various gasifying agents such as H_2O and CO_2, because their catalysis mechanisms during biochar gasification may be different [19,23–25]. In addition, for the comparison of AAEM catalytic activities, Zhang et al. [26] studied the gasification reactivity of several biochar samples catalyzed by metals and reported that the gasification reactivity was enhanced with the alkali metals followed by alkaline earth metals. Furthermore, for the catalytic role of AAEMs on the microcosmic chemical bonds during gasification, the oxidation-reduction cycle [27–31] was postulated, in which O atoms/ions dissociated from the gasifying agents could transferred to the carbon active sites through catalytically-active AAEMs, where the breakage of C-C bonds would occur to realize the liberation of the C(O) structure.

In addition, as our previous study mentioned [32], the AAEMs in biomass/biochar usually exist in a variety of chemical speciations, such as inorganic salts/ion states, organic forms linked to biochar and/or crystal forms. Jordan et al. [33] investigated the speciation and distribution of AAEMs in raw biomass and major ash-forming elements during gasification to evaluate the volatilization of these elements into the syngas, although they did not mention the state of AAEMs in biochar and their effects on the gasification reactivity of biochar. Besides, the catalytic effects of AAEMs with different chemical speciations on biochar reactivity are obviously different [34]. Thus, it is easy to deduce that their influence on the characteristics of biochar gasification would be significant, although relevant studies are rarely reported. In order to characterize the chemical speciation of AAEMs in biomass/biochar, a sequential selective extraction procedure known as chemical fractionation analysis (CFA) was introduced and standardized [35,36]. This method was first developed by Benson and Holm [37] for coals and had been modified by Zevenhoven-Onderwater et al. [38] and Petterson et al. [39] for biomass fuels. Moreover, besides their direct catalytic effects on biochar gasification, the AAEMs could have a dynamic impact on the biochar structures, including the carbon skeleton, side chains and functional groups [21,22,40]. It has been confirmed that the changes in biochar structure catalyzed by AAEMs are an important aspect influencing biochar reactivity during gasification [41]. However, there are few reports on the effect of AAEMs with different speciations on the biochar structure during gasification, which would in turn affect the biochar gasification reactivity. Biochar gasification can be significantly altered via the catalytic alteration of the above reaction pathways by different speciations of AAEMs. Thus a good understanding of the effect of the chemical speciation of AAEMs during biochar steam gasification would lay a solid foundation for developing a gasification technology for biomass.

The objectives are to understand the steam gasification behavior of pyrolysis biochar with different speciations of AAEMs, the key inherent chemical speciation of AAEMs affecting biochar reactivity, and the most probable catalytic route of AAEMs on biochar structure and reactivity during steam gasification, all of which are essential to gasification process design and development.

2. Experimental

2.1. Origin Biochar Preparation

Manchurian walnut sawdust, obtained from Harbin, Heilongjiang Province, China, was used in the experiments. The sawdust samples were dried overnight at 105 °C, pulverized and sieved to obtain a fraction with particle sizes between 0.15 and 0.25 mm. The proximate and ultimate analyses for the sawdust samples are listed in Table 1.

Table 1. Proximate and ultimate analysis of the origin sawdust sample. (Note: diff. = by difference, ad. = air dry basis.)

Samples	Proximate Analysis				Ultimate Analysis				
	$M_{ad.}$	$A_{ad.}$	$V_{ad.}$	$FC_{ad.}$	$C_{ad.}$	$H_{ad.}$	$O_{ad.(diff.)}$	$N_{ad.}$	$S_{t,ad.}$
	(wt%)	(wt%)	(wt%)	(wt%)	(wt%)	(wt%)	(wt%)	(wt%)	(wt%)
Sawdust	9.49	0.96	77.13	12.42	43.72	5.31	40.39	0.12	0.01

As shown in Figure 1, the origin pyrolysis biochar samples were obtained in the entrained-flow reactor at 800 °C with nitrogen gas of 5.70 L/min. The details of the pyrolysis experimental system can be seen in our previous investigation [32]. The origin pyrolysis biochar was used for the following treatment and steam gasification.

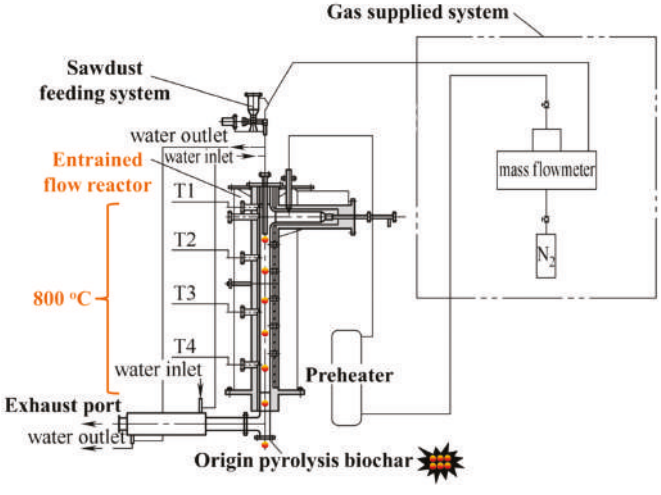

Figure 1. Schematic diagram of the entrained-flow reactor.

2.2. Sample Preparation

In order to investigate the effects of the solid-phase chemical speciation of AAEMs on the steam gasification of sawdust biochar, the CFA process was carried out. There are four kinds of chemical speciation of AAEMs in biochar [42]: One is a separate form of AAEM ions, which is soluble in water, also soluble in a solution of ammonium acetate (NH_4Ac) and hydrochloric acid (HCl); The second is organic matter, which is in the form of carboxylate and/or coordination connected with the oxygen functional groups on the biochar surface, and is insoluble in water, but soluble in a solution of NH_4Ac and HCl; The third is attached to the clay surface in an amorphous form, which is insoluble in water and NH_4Ac solution, but soluble in hydrochloric acid; The fourth is in the aluminosilicate form, which is insoluble in water, NH_4Ac and HCl. In the CFA process, as shown in Figure 2, the pyrolysis biochar is leached step-wise in increasingly aggressive solvents: deionized water, 1.0 mol/L ammonium acetate solution, and 1.0 mol/L hydrochloric acid solution with a mass ratio (1:30) of solid to liquid, in order to classify the AAEMs with respect to solubility.

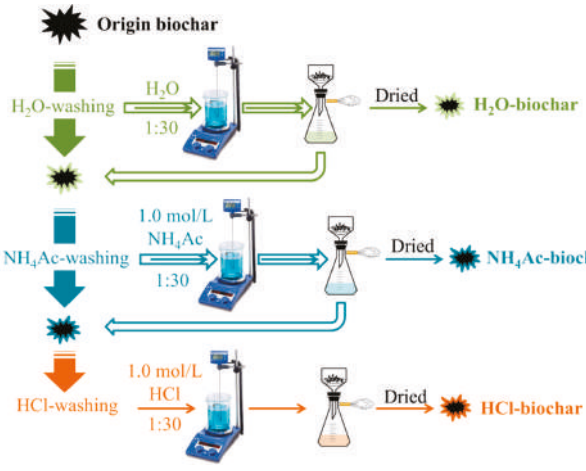

Figure 2. Schematic of the chemical fractionation analysis of biochar.

2.3. Steam Gasification of Biochar

As shown in Figure 3, the steam gasification of sawdust biochar was carried out. A total of 0.5 g of biochar from the CFA, namely the origin-biochar/H_2O-biochar/NH_4Ac-biochar/HCl-biochar samples, were pre-loaded into the top fixed-bed stage of the reactor. After being purged for 5 min by argon (Ar), the system was heated up to 800 °C with argon gas of 1.53 L/min at a heating rate of 20 °C/min. As the temperature stabilized at 800 °C, the atmosphere was switched to 15 vol% steam for the gasification reaction, which was achieved by feeding deionized water of 0.214 L/min through a high-performance liquid chromatography (HPLC) pump into the heated zone of reactor where the water was evaporated into steam directly. The steam gasification reaction of biochar at 800 °C lasted for 10 min. After that, reactions were terminated by switching the atmosphere to argon and removing the reactor from the furnace. Argon was passed through the reactor until the reactor had completely cooled to room temperature to avoid oxidation. The steam gasification biochar was collected and stored at 4 °C for further analysis.

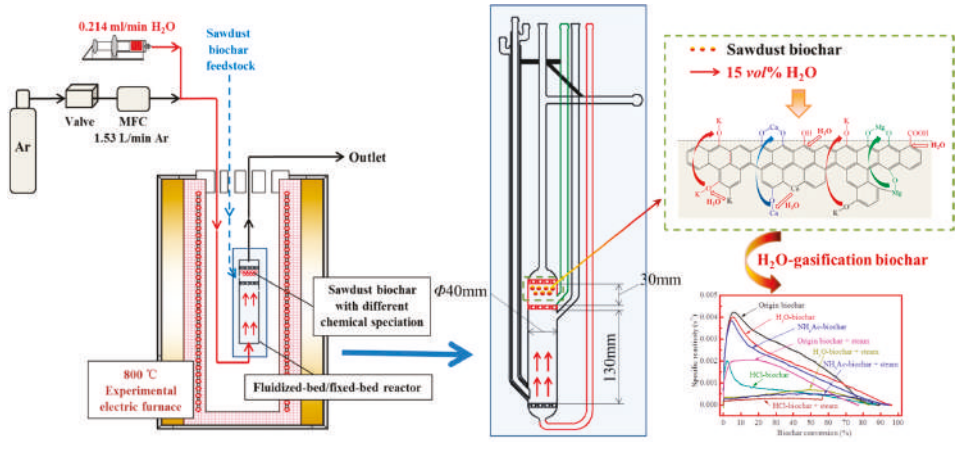

Figure 3. A schematic diagram of the steam gasification experimental process.

2.4. Analysis of Biochar

2.4.1. Gasification Rate

The gasification rate of biochar was measured three times by weighing the biochar-containing reactor before and after the reactions. Each experiment was repeated at least three times, and the test results are well-reproducible.

2.4.2. AAEM Analysis

The chemical speciation of AAEMs in biochar was quantified by inductively-coupled plasma-atomic emission spectroscopy (ICP-AES). The biochar sample (0.1 g) was digested in a 1:3:8 ($v/v/v$) mixture of 40% HF, 30% H_2O_2, and 65% HNO_3 at 200 °C for 60 min.

The percentage of AAEMs released during the steam gasification of biochar can be obtained by Equation (1) as follows:

$$X_{Release}\% = \left[1 - X_{\text{Steam gasification biochar}} \times \frac{(1 - \text{Gasification rate})}{X_{\text{Pyrolysis biochar}}}\right] \times 100\% \quad (1)$$

where X is the AAEM species (Na, K, Mg and Ca); $X_{Release}$ is the percentage of AAEM release during the steam gasification of biochar; $X_{\text{Pyrolysis biochar}}$ is the X in origin/H_2O-/NH_4Ac-/HCl-pyrolysis biochar; and $X_{\text{Steam gasification biochar}}$ is the X in origin/H_2O-/NH_4Ac-/HCl-steam gasification biochar.

2.4.3. Raman Analysis

The aromatic structure analysis of biochar was carried out in a Raman spectrometer (inVia, Renishaw, New Mills, UK), with an excitation laser at 633 nm. The sample was mixed and ground with spectroscopic-grade Potassium bromide (KBr) in the ratio of 0.25 wt% biochar. The Raman spectra at 800~1800 cm^{-1} were recorded.

2.4.4. FTIR Analysis

The surface functional groups of the biochar were analyzed by Fourier Transform infrared spectroscopy (Nicolet 5700, FTIR, Thermo Fisher Scientific, Waltham, MA, USA). Biochar was mixed and ground with spectroscopic-grade KBr in a ratio of 1:200. All FTIR spectra were obtained at a resolution of 4 cm^{-1} in the range of 400~4000 cm^{-1}.

2.4.5. Biochar Reactivity Analysis

The specific reactivity of the biochar was determined in air at 370 °C with a thermogravimetric analyzer (TGA: Mettler Toledo, Switzerland). Nearly 4 mg of biochar sample was placed in a Pt crucible and heated in Ar in the TGA to 105 °C to remove moisture from the sample. The stabilized weight of the biochar at 105 °C was taken as the weight of dry biochar. The temperature was then increased to 370 °C at 50 °C/min. After 2 min, the atmosphere was switched into air starting the biochar reactivity test. Once the mass was stable, the sample was heated at 50 °C/min to 600 °C, where it was held for another 30 min to ensure complete combustion. The calculation of biochar-specific reactivity from the differential thermal gravity (DTG) data (dW/dt) can be seen in our previous study [22].

3. Results and Discussion

3.1. Steam Gasification Rate

As shown in Figure 4, it can be seen that the steam gasification rate of pyrolysis biochar after the fraction of H_2O, NH_4Ac and HCl decreased sequentially, from 79.00% of origin biochar to 66.54% of HCl-biochar. Our previous investigation [43] indicated that during the chemical fractionation analysis, the changes in oxygen-containing functional groups and aromatic ring structures could be ignored.

It can be speculated that the difference in the gasification rate is mainly caused by the different chemical speciation of the AAEM species. The difference in gasification rate was used to describe the effect of different-speciation AAEMs on the steam gasification reaction of biochar, as shown in Figure 4. The decrease of 5.81% in the steam gasification rate from origin biochar to H_2O-biochar sample is entirely due to the removal of H_2O-soluble AAEMs, and this part mainly deals with K^+ and Na^+ ion salts in biochar [32]. After that, the decline of the biochar steam gasification rate is gradually reduced, to 4.20% and 2.45% due to the removal of the NH_4Ac-soluble and HCl-soluble AAEMs, respectively. Finally, the HCl-biochar sample, with only some insoluble aluminosilicate AAEMs, still retains a relative high gasification rate (as 66.54%), mainly due to the relatively active carbon structures and the insoluble AAEMs to maintain the basic reactions between carbon and steam.

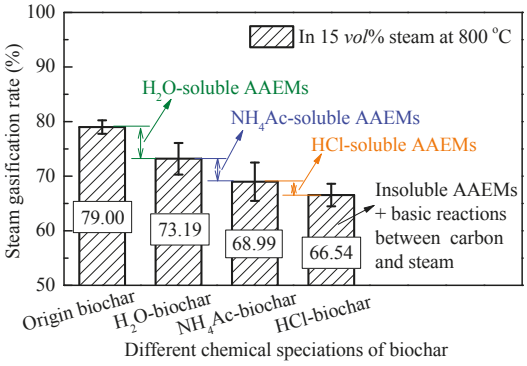

Figure 4. Steam gasification rate of biochar from chemical analysis fractionation.

3.2. AAEM Analysis of Steam-Gasified Biochar

Figure 5 shows the AAEM content of the origin pyrolysis biochar and their chemical speciation. In the original pyrolysis biochar at 800 °C, the AAEMs exhibited a rich distribution of K (0.70 wt%) and Ca (2.08 wt%), and less Na (0.05 wt%) and Mg (0.17%). Besides, the main existing form of K in pyrolysis biochar is a water-soluble form, while that of Ca is a NH_4Ac-soluble and insoluble form. As Mitsuoka et al. [44] suggested, the most significant catalysts for biochar gasification in woody biomass are calcium (Ca) and potassium (K), namely the two main kinds of AAEM.

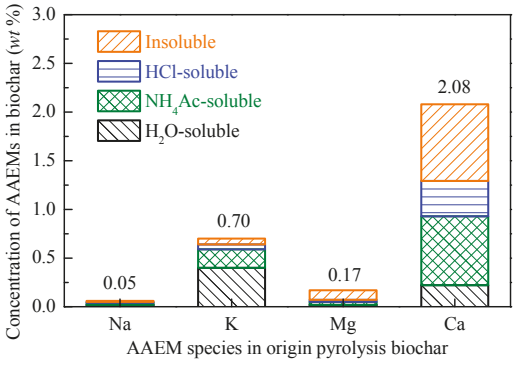

Figure 5. Concentration of AAEMs in origin pyrolysis biochar.

As mentioned above, the role of AAEMs is not only in the solid-phase heterogeneous transformation of biochar, their migration and precipitation characteristics also play a significant role in homogeneous steam reform. It is often agreed that the volatilization of AAEMs occurs during gasification [45,46]. According to Marschner et al. [47], the behavior of Na and K were different from that of Mg and Ca, at least partly due to the different chemical status of K/Na and Mg/Ca in the biomass/biochar. It is also related to the different occurrence of K/Na and Mg/Ca. For the H_2O-soluble AAEMs, the specific precipitation amount of AAEMs cannot be calculated directly by the difference in this paper. However, the total amount of AAEMs in the fractional speciation can be calculated to characterize the precipitation of AAEMs in the absence of H_2O-soluble ones. This effectively avoids the influence of AAEM transformation with different chemical speciations during steam gasification [33].

The release of K and Ca during the steam gasification of biochar can be seen in Figure 6. $K_{Release}$ and $Ca_{Release}$ did not change significantly after H_2O washing, and it can be seen that the H_2O-washing removal amount and the amount of volatilization during the gasification of K and Ca were very close, indicating that the precipitation rate of H_2O-soluble K and Ca was close to 100%. After the fraction of NH_4Ac and HCl solution, the $K_{Release}$ was significantly reduced and $Ca_{Release}$ was still relatively high, indicating that during gasification the release of K occurs mainly in the form of inorganic salts and hydrated ions, while volatilization of the organic compounds is the main release mechanism for Ca.

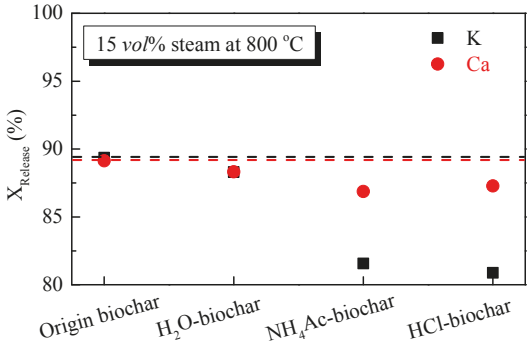

Figure 6. Release of K and Ca species during the steam gasification of biochar.

3.3. Raman Analysis of Steam-Gasified Biochar

As shown in Figure 7, the total Raman area between 800 and 1800 cm^{-1} of the pyrolysis biochar samples from the CFA process changed little, with a total intensity of 1.62~1.72 $\times$ 10^6. The total Raman peak areas could reflect electron-rich structures such as O/N-containing functional groups in biochar [48–51]. During the steam gasification of biochar, it can be seen that the total Raman areas of gasified biochar decreased from 3.58 $\times$ 10^6 to 2.23 $\times$ 10^6 with the fractionation of H_2O, NH_4Ac and HCl in turn. According to Guo et al. [41], both the thermal decomposition of biochar, and biochar gasification reactions leading to the loss of oxygen and hydrogen from biochar, could result in changes to biochar structures during gasification with a decrease of total Raman intensity. Also, another possible factor may be the preferential consumption of smaller rings due to their gasification and/or conversion to larger ones. Briefly, during steam gasification, the decrease in Raman intensity with the CFA process reflected the limited increase in O-containing functional groups and, more importantly, the condensation/growth of aromatic ring systems. For the HCl-biochar, with few active AAEMs (in the absence of catalysts), the O-containing functional groups formed in the biochar during steam gasification were closely associated with the aromatic structure and thus tended to loosen the aromatic structure. The non-catalyzed gasification was slow and took place on some specific (especially sp^3-rich or sp^2-sp^3 mixture) sites distributed throughout the biochar [52]. While the gasification of biochar

took place everywhere but slowly in the HCl-biochar in order to consume the small ring systems selectively, the reaction in the AAEM-containing biochar was more focused on/around the AAEM sites and took place much more rapidly [53]. As shown in Figure 7, comparing the results of steam-gasified origin biochar and H_2O-biochar samples, there is a significant decrease of 0.65×10^6, showing that the increase of surface O-containing functional groups during gasification was limited after the fraction of H_2O, mainly due to the H_2O-soluble AAEMs, namely the K and Na species. For the total Raman area between gasified H_2O-biochar and NH_4Ac-biochar, the decrease was only 0.22×10^6, showing that the effects of NH_4Ac-soluble AAEMs were limited. Although the AAEM content is relatively large, their low ability of migration led to a limited catalytic role. After that, the effect of HCl-soluble AAEMs, namely the organic Ca species, led to another obvious decrease of 0.48×10^6 in the total Raman area, showing its significant catalytic role on the formation of surface O-containing functional groups.

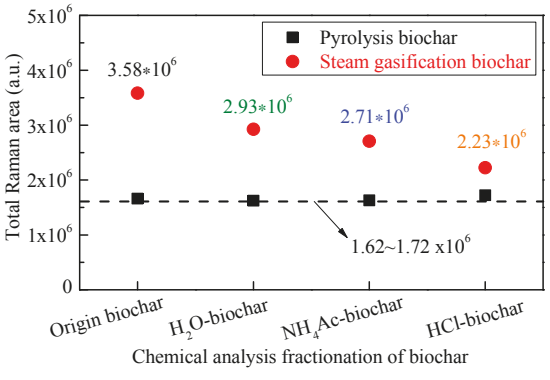

Figure 7. Total Raman area of biochar during steam gasification.

As shown in Figure 8, the Raman spectrum of the gasified biochar was divided into 10 small peaks, representing the typical structures of biochar. Other detailed information on this part can be seen in our previous studies [19,32], where the $I_{(Dr+Vl+Vr)}/I_D$ represents the ratio of the smaller aromatic rings in the biochar to the larger aromatic ring structures, and I_S/I_{Total} refers to the content of sp^3-rich structures as alkyl–aryl C-C structures and methyl carbon dangling to an aromatic ring, including some surface O-containing structures in biochar, with little long chain aliphatics and hydroaromatic structures.

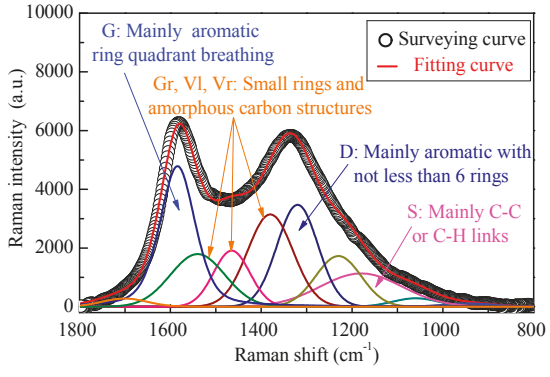

Figure 8. Curve fitting of the Raman spectrum of biochar.

As shown in Table 2, the influence of chemical fraction analysis on biochar aromatic ring structures could be ignored, while both NH_4Ac and HCl can change the cross-linking structures of biochar [43]. During steam gasification, according to Chen et al. [54], the sites on either the zigzag face or the armchair face of large aromatic layers of biochar are believed to be active for gasification reactions and they are affected by AAEMs. In addition, according to Li et al. [52], the smaller aromatic ring systems were preferentially consumed during gasification. During the steam gasification of biochar, with the presence of H_2O-soluble AAEMs, the $I_{(Dr+Vl+Vr)}/I_D$ decreased significantly from 1.84 to 0.64, indicating the transformation of the smaller aromatic ring systems into larger ones to a great extent. The conversion of biochar during steam gasification is believed to be due to the rapid penetration of H radicals from the biochar surface deep into the biochar matrix [55]. Also the AAEMs, as the active sites for the gasification reaction, could promote the process of this transformation to a large extent, especially for the alkali metal species (K and Na). With the fraction of NH_4Ac and HCl solutions, the decrease of $I_{(Dr+Vl+Vr)}/I_D$ became more and more weak, showing the smaller catalytic effect of NH_4Ac/HCl-soluble AAEMs on the aromatic ring structures in biochar. As shown in Table 2, due to the steam gasification of HCl-biochar, the I_S/I_{Total} decreased from 0.18 to 0.10. These data indicate that the sp^3-rich or sp^2-sp^3 mixed structures represented by the S band are the preferential sites of reaction with steam with few active AAEMs catalysts, with only insoluble ones left. The results are consistent with the opinion of Li et al. [52] for coal char. In addition, the effect of the NH_4Ac/HCl-soluble AAEMs is limited as the active site during gasification, and consequently the corresponding I_S/I_{Total} decreases, since the sp^3-rich or sp^2-sp^3 structures are consumed. However, few changes in the relative intensity of S band were observed for the corresponding biochars from the origin biochar during gasification (from 0.38 to 0.37). This indicated that with the H_2O-soluble AAEMs, the S band structures were no longer the preferred sites for reactions with steam. The AAEM catalytic species appeared to be preferentially accommodated on carbons of an aromatic nature.

Table 2. Ratios of band peak areas in pyrolysis and steam gasification biochar from Chemical fractionation analysis (CFA.).

Conditions	Band Ratio	Origin Biochar	H_2O-Biochar	NH_4Ac-Biochar	HCl-Biochar
Pyrolysis	$I_{(Vl+Dr+Vr)}/I_D$	1.84	1.97	2.06	2.19
	I_S/I_{Total}	0.38	0.34	0.22	0.18
Gasification	$I_{(Vl+Dr+Vr)}/I_D$	0.64	1.51	1.91	2.02
	I_S/I_{Total}	0.37	0.28	0.17	0.10

3.4. FTIR Analysis of Steam-Gasified Biochar

The CFA process has less destructive effects on the surface carbon–oxygen functional groups of pyrolysis biochar, which was already present in our previous study [43]. With the result of the total Raman area related with the surface functional groups, the additional O-containing functional groups were not present in the pyrolysis biochar before steam gasification. To gain evidence for the formation of additional O-containing functional groups during gasification, the FTIR spectra of the biochar samples were recorded, as shown in Figure 9. According to Černý et al. [56], the FTIR spectra of 4000~400 cm^{-1} are divided into 3600~3000 cm^{-1}, 3000~2800 cm^{-1}, 1800~1000 cm^{-1} and 900~700 cm^{-1}, which represent the surface hydroxyl group, aliphatic hydrocarbons, oxygen-containing functional groups, and aromatic hydrocarbons, respectively. As shown in Figure 9, for the steam-gasified biochar with different chemical fractions, the main difference appears in the oxygen-containing functional groups. In order to describe in detail the changes in the various oxygen-containing functional groups, the FTIR curve was fitted into the aromatic C=C structure at 1480 cm^{-1}, the carboxylate COO^- structure at 1400 cm^{-1} and the aromatic ether/alkene C-O-C at 1243 and 1080 cm^{-1} [57,58].

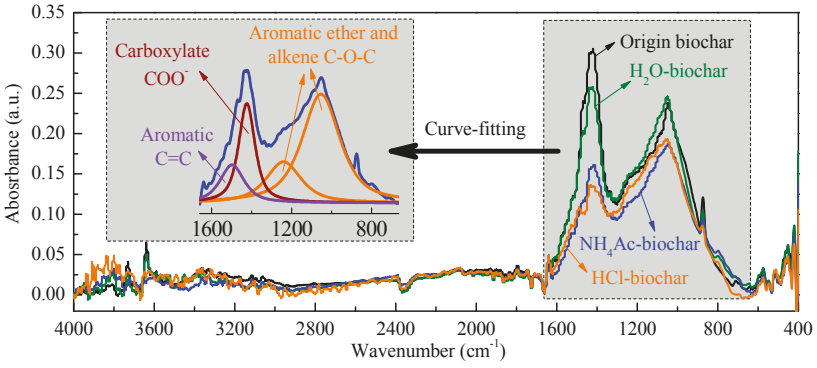

Figure 9. FTIR analysis of steam-gasified biochar with different chemical fractions.

The result of the curve-fitting FTIR analysis on O-containing functional groups can be seen in Table 3.

Table 3. FTIR analysis of O-containing functional groups on steam-gasified biochar surface.

Steam-Gasified Biochar	Surface Main Functional Groups		
	Aromatic C=C	Carboxylate COO^-	Aromatic Ether/Alkene C-O-C
Gasified origin biochar	10.63	26.46	62.90
Gasified H_2O-biochar	9.94	21.82	68.23
Gasified NH_4Ac-biochar	10.27	14.10	75.62
Gasified HCl-biochar	11.39	9.98	78.62

The FTIR curve between the two successive steps can be used to indirectly reflect the specific catalytic effect of different AAEMs on the formation of oxygen-containing functional groups during steam gasification. Walker and co-workers [59] have also pointed out in a review that a significant amount of O complex builds up on the surface of active sites, which is referred to the AAEMs. The content of aromatic C=C on the steam gasified biochar from different CFA processes fluctuated in the range of 9.94~11.39%, with little change. In addition, the main changes existed between the carboxylate COO^- and aromatic ether/alkene C-O-C. In the absence of active AAEMs, the HCl-biochar exhibits the lowest surface functional group content, which is consistent with the Raman analysis results. The HCl-soluble AAEMs (mainly for the organic Ca compounds mentioned above), are mainly used to promote the formation of carboxylate COO^- (from 9.98% to 14.10%), and to limit the increase of aromatic ether/alkene C-O-C (from 78.62% to 75.62%), which can be considered to be the transformation from ether/alkene C-O-C to carboxylate COO^- catalyzed by HCl-soluble AAEMs. However, for the NH_4Ac-soluble AAEMs, as shown in Figure 9, the relative contents of carboxylate COO^- and aromatic ether/alkene C-O-C were both significantly improved, indicating that the AAEMs played a positive role in promoting the formation of surface oxygen-containing functional groups. Compared to the FTIR results for the origin biochar and the H_2O-biochar after gasification, the catalytic effect of the H_2O-soluble AAEMs in biochar was investigated. A similar result can be seen in that during the steam gasification, the H_2O-soluble AAEMs promote the increase of the total amount of oxygen-containing functional groups, and the catalytic effect on the increase of carboxylate COO^- is the most significant.

3.5. Biochar Reactivity in Air

The specific reactivity of biochar in combustion as a function of biochar conversion can be seen in Figure 10. As usual, the biochar reactivity is mainly controlled by two factors: the biochar structure [60]

and AAEM species in biochar [3]. The chemical fractionation process has little effect on the pyrolysis biochar structure [43], thus the AAEMs in the biochar are considered to be the main controlling factor affecting the pyrolysis biochar activity in this experiment. Given the high quantities of AAEMs and their possible catalytic activities, the catalytic activity of AAEMs may be the most likely factor causing the difference in reactivity, because reactions under a steam atmosphere make a difference in the concentration and dispersion of AAEMs in the resulting chars [40]. During steam gasification, the AAEMs only increase the concentration of the active complexes on carbon rather than changing the reaction pathway [61–65]. Figure 10 shows the typical specific reactivity of the pyrolysis biochar samples from the CFA process. After the chemical fractionation, the content of AAEMs decreased gradually, resulting in a decrease of the total reaction activity of the pyrolysis biochar. The specific reactivity showed broad maxima at about 5.8%, 5.2%, 5.0% and 2.0% char conversions for the pyrolysis origin biochar, H_2O-biochar, NH_4Ac-biochar and HCl-biochar, respectively. The maximum reactivity tended to shift towards lower conversion levels with the CFA steps. The main reason for the initial increase in the biochar reactivity (Figure 10) at small biochar conversion levels was the accumulation of AAEMs on the biochar surface with the removal of carbonaceous matter. During the air gasification of biochar, the high mobility of AAEMs allows them to migrate onto the biochar surface to form catalytically-active species such as –O–AAEM and/or AAEM clusters [66]. At high biochar conversion levels, where the biochar structure is more inert and highly condensed, the catalytic activity of AAEMs is reduced compared to its activity at low biochar conversion levels. In other words, at the beginning, the increase of AAEMs on the biochar surface are the main factor influencing the biochar reactivity. At a later stage, changes in the biochar structure become significant. The preferential removal of smaller aromatic ring systems and the persistence of crosslinking structures mean that the large aromatic ring systems are increasingly concentrated with little flexibility [52].

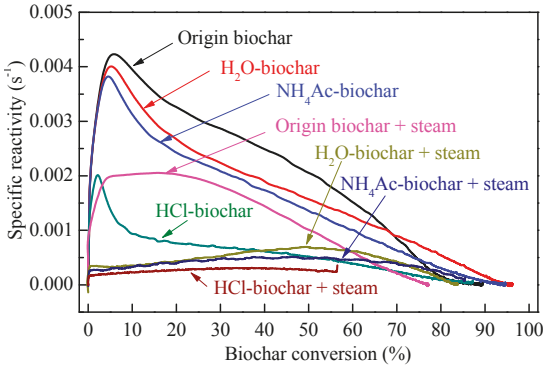

Figure 10. Specific reactivity of biochar samples as a function of biochar conversion.

For the steam-gasified biochar samples, the catalytic activity of AAEMs is a result of the interaction between AAEMs and biochar/carbon structures. As in the initial stage of the biochar reactivity test, unlike the pyrolytic one, there were significant differences in the biochar structure (i.e., O-containing functional groups and aromatic structures) by CFA in the steam gasification process. Furthermore, the AAEM-containing species in the biochar during the steam gasification improved the O-containing functional groups that would be consumed quickly during the reactivity measurement, contributing to the increase in reactivity [67], while the AAEMs would decrease the relative content of small aromatic ring structures in the biochar during steam gasification leading to the decrease in reactivity. Thus, the final decision of the steam-gasified biochar depends on the synergetic effects of the biochar structure and AAEMs [22]. According to Li et al. [68], the AAEMs would not be volatilized during the oxidation of biochar with air in the TGA at 370 °C during the measurement of biochar reactivity. However, during

gasification, it can be seen from Section 3.4 that the AAEMs could be significantly precipitated, especially for the H_2O-soluble AAEMs (nearly 100% volatilization). As shown in Figure 10, there is a significant decrease of biochar reactivity between the "origin biochar + steam" and the other three samples. For the biochar gasification in 15 vol% steam at 800 °C, the water-soluble AAEMs play a crucial role in the catalytic activity of gasification biochar. Despite its nearly complete volatilization, the water-soluble AAEMs have a significant effect on the biochar structure, which is a key factor in determining the highest reactivity of the biochar. The difference between "H_2O-biochar + steam" and "NH_4Ac-biochar + steam" is mainly concentrated in the higher carbon conversion stage (biochar conversion >30%), which is mainly due to the biochar structure determining the reaction [66]. The effect of HCl-soluble AAEMs on the biochar reactivity functions from start to finish. For "HCl-biochar + steam", the reactivity is the lowest, mainly due to the least amount of catalytically active elements (AAEMs) and the less active structure formation in the biochar.

4. Conclusions

(1) The AAEMs in different chemical speciations, such as the H_2O/NH_4Ac/HCl-soluble ones, have significant effects on the steam gasification rate of sawdust biochar. During steam gasification, the release of K occurs mainly in the form of inorganic salts and hydrated ions, while the release of Ca is mainly for the organic ones.

(2) During steam gasification, the limited increase of O-containing functional groups and, more importantly, the condensation/growth of aromatic ring systems existed for the AAEMs with different chemical speciations. Without the active AAEMs (such as HCl-biochar), the sp^3-rich or sp^2-sp^3 structures are the preferred sites for steam gasification. With NH_4Ac/HCl-soluble AAEMs, the preferred sites with sp^3-rich or sp^2-sp^3 structures are gradually shared by AAEMs, until the presence of H_2O-soluble AAEMs completely replaces them as the gasification sites.

(3) H_2O/HCl-soluble AAEMs promote the transformation from ether/alkene C-O-C to carboxylate COO^- while promoting the increase of total surface oxygen functional groups. The relative contents of carboxylate COO^- and aromatic ether/alkene C-O-C were significantly improved by the NH_4Ac-soluble AAEMs.

(4) The H_2O-soluble AAEMs play a crucial role in the catalytic activity of gasification biochar and is a key factor in determining its highest reactivity. The effect of NH_4Ac-soluble AAEMs on gasification biochar activity is mainly concentrated in the high carbon conversion stage (biochar conversion >30%), and the effect of HCl-soluble AAEMs is reflected in the whole activity-testing stage.

Acknowledgments: The Collaborative Innovation Center of Clean Coal Power Plant with Poly-Generation, the national key R&D program of China (2016YFE0102500) and the National Natural Science Foundation innovation research group Heat Transfer and Flow Control (51421063) are gratefully acknowledged.

Author Contributions: D.F., Y.Z. and S.S. conceived and designed the experiments; D.F. and Y.Z. performed the experiments; D.F., J.G. and Y.Z. analyzed the data; J.G. and Y.Z. contributed reagents/materials/analysis tools; D.F. wrote the paper.

Conflicts of Interest: The authors declare no conflict of interest.

Nomenclature

AAEMs	Alkali and alkaline earth metallic species
X	AAEMs (Na, K, Mg and Ca)
$X_{Release}$	X(AAEMs) release during gasification
$X_{Pyrolysis\ biochar}$	X(AAEMs) in pyrolysis biochar
$X_{Steam\ gasification\ biochar}$	X(AAEMs) in steam gasification biochar
CFA	Chemical fractionation analysis
NH_4Ac	Ammonium acetate
H_2O-soluble	Soluble in water
NH_4Ac-soluble	Soluble in NH_4Ac solution

HCl-soluble	Soluble in HCl solution
Insoluble	Insoluble in water/NH_4Ac/HCl
H_2O	Deionized water
HCl	Hydrochloric acid
Origin-biochar	Origin pyrolysis biochar
H_2O-biochar	H_2O-washed biochar
NH_4Ac-biochar	NH_4Ac-washed biochar
HCl-biochar	HCl-washed biochar

References

1. Damartzis, T.; Zabaniotou, A. Thermochemical conversion of biomass to second generation biofuels through integrated process design—A review. *Renew. Sustain. Energy Rev.* **2011**, *15*, 366–378. [CrossRef]
2. Parthasarathy, P.; Narayanan, K.S. Hydrogen production from steam gasification of biomass: Influence of process parameters on hydrogen yield—A review. *Renew. Energy* **2014**, *66*, 570–579. [CrossRef]
3. Li, C.-Z. Importance of volatile–char interactions during the pyrolysis and gasification of low-rank fuels—A review. *Fuel* **2013**, *112*, 609–623. [CrossRef]
4. Nowicki, L.; Markowski, M. Gasification of pyrolysis chars from sewage sludge. *Fuel* **2015**, *143*, 476–483. [CrossRef]
5. Qi, X.; Guo, X.; Xue, L.; Zheng, C. Effect of iron on Shenfu coal char structure and its influence on gasification reactivity. *J. Anal. Appl. Pyrolysis* **2014**, *110*, 401–407. [CrossRef]
6. Duman, G.; Uddin, M.A.; Yanik, J. The effect of char properties on gasification reactivity. *Fuel Proc. Technol.* **2014**, *118*, 75–81. [CrossRef]
7. Liu, L.; Cao, Y.; Liu, Q. Kinetics studies and structure characteristics of coal char under pressurized CO_2 gasification conditions. *Fuel* **2015**, *146*, 103–110. [CrossRef]
8. Shen, Y.; Zhao, P.; Shao, Q.; Ma, D.; Takahashi, F.; Yoshikawa, K. In-situ catalytic conversion of tar using rice husk char-supported nickel-iron catalysts for biomass pyrolysis/gasification. *Appl. Catal. B Environ.* **2014**, *152–153*, 140–151. [CrossRef]
9. Kirtania, K.; Joshua, J.; Kassim, M.A.; Bhattacharya, S. Comparison of CO_2 and steam gasification reactivity of algal and woody biomass chars. *Fuel Proc. Technol.* **2014**, *117*, 44–52. [CrossRef]
10. Luo, S.; Xiao, B.; Hu, Z.; Liu, S.; Guo, X.; He, M. Hydrogen-rich gas from catalytic steam gasification of biomass in a fixed bed reactor: Influence of temperature and steam on gasification performance. *Int. J. Hydrogen Energy* **2009**, *34*, 2191–2194. [CrossRef]
11. Li, C.-Z. Special issue—Gasification: A route to clean energy. *Proc. Saf. Environ. Prot.* **2006**, *84*, 407–408. [CrossRef]
12. Nanou, P.; Gutiérrez Murillo, H.E.; van Swaaij, W.P.M.; van Rossum, G.; Kersten, S.R.A. Intrinsic reactivity of biomass-derived char under steam gasification conditions-potential of wood ash as catalyst. *Chem. Eng. J.* **2013**, *217*, 289–299. [CrossRef]
13. Kajita, M.; Kimura, T.; Norinaga, K.; Li, C.-Z.; Hayashi, J.-I. Catalytic and noncatalytic mechanisms in steam gasification of char from the pyrolysis of biomass. *Energy Fuels* **2009**, *24*, 108–116. [CrossRef]
14. Eom, I.-Y.; Kim, J.-Y.; Kim, T.-S.; Lee, S.-M.; Choi, D.; Choi, I.-G.; Choi, J.W. Effect of essential inorganic metals on primary thermal degradation of lignocellulosic biomass. *Bioresour. Technol.* **2012**, *104*, 687–694. [CrossRef] [PubMed]
15. Lahijani, P.; Zainal, Z.A.; Mohamed, A.R.; Mohammadi, M. CO_2 gasification reactivity of biomass char: Catalytic influence of alkali, alkaline earth and transition metal salts. *Bioresour. Technol.* **2013**, *144*, 288–295. [CrossRef] [PubMed]
16. Yu, M.M.; Masnadi, M.S.; Grace, J.R.; Bi, X.T.; Lim, C.J.; Li, Y. Co-gasification of biosolids with biomass: Thermogravimetric analysis and pilot scale study in a bubbling fluidized bed reactor. *Bioresour. Technol.* **2015**, *175*, 51–58. [CrossRef] [PubMed]
17. Zolin, A.; Jensen, A.; Jensen, P.A.; Frandsen, F.; Dam-Johansen, K. The influence of inorganic materials on the thermal deactivation of fuel chars. *Energy Fuels* **2001**, *15*, 1110–1122. [CrossRef]

18. Long, J.; Song, H.; Jun, X.; Sheng, S.; Lun-shi, S.; Kai, X.; Yao, Y. Release characteristics of alkali and alkaline earth metallic species during biomass pyrolysis and steam gasification process. *Bioresour. Technol.* **2012**, *116*, 278–284. [CrossRef] [PubMed]
19. Feng, D.; Zhao, Y.; Zhang, Y.; Sun, S. Effects of H_2O and CO_2 on the homogeneous conversion and heterogeneous reforming of biomass tar over biochar. *Int. J. Hydrogen Energy* **2017**, *42*, 13070–13084. [CrossRef]
20. Wu, H.; Quyn, D.M.; Li, C.-Z. Volatilisation and catalytic effects of alkali and alkaline earth metallic species during the pyrolysis and gasification of Victorian brown coal. Part III. The importance of the interactions between volatiles and char at high temperature. *Fuel* **2002**, *81*, 1033–1039. [CrossRef]
21. Feng, D.; Zhao, Y.; Zhang, Y.; Zhang, Z.; Sun, S. Roles and fates of K and Ca species on biochar structure during in-situ tar H_2O reforming over nascent biochar. *Int. J. Hydrogen Energy* **2017**, *42*, 21686–21696. [CrossRef]
22. Feng, D.; Zhao, Y.; Zhang, Y.; Zhang, Z.; Zhang, L.; Gao, J.; Sun, S. Synergetic effects of biochar structure and AAEM species on reactivity of H_2O-activated biochar from cyclone air gasification. *Int. J. Hydrogen Energy* **2017**, *42*, 16045–16053. [CrossRef]
23. Walker, P.L.; Matsumoto, S.; Hanzawa, T.; Muira, T.; Ismail, I.M. Catalysis of gasification of coal-derived cokes and chars. *Fuel* **1983**, *62*, 140–149. [CrossRef]
24. De Lecea, C.S.-M.; Almela-Alarcón, M.; Linares-Solano, A. Calcium-catalysed carbon gasification in CO_2 and steam. *Fuel* **1990**, *69*, 21–27. [CrossRef]
25. Feng, D.; Zhao, Y.; Zhang, Y.; Sun, S.; Meng, S.; Guo, Y.; Huang, Y. Effects of K and Ca on reforming of model tar compounds with pyrolysis biochar under H_2O or CO_2. *Chem. Eng. J.* **2016**, *306*, 422–432. [CrossRef]
26. Zhang, Y.; Ashizawa, M.; Kajitani, S.; Miura, K. Proposal of a semi-empirical kinetic model to reconcile with gasification reactivity profiles of biomass chars. *Fuel* **2008**, *87*, 475–481. [CrossRef]
27. Holstein, W.; Boudart, M. Uncatalyzed and platinum-catalyzed gasification of carbon by water and carbon dioxide. *J. Catal.* **1982**, *75*, 337–353. [CrossRef]
28. Radovic, L.R.; Walker, P.L.; Jenkins, R.G. Importance of catalyst dispersion in the gasification of lignite chars. *J. Catal.* **1983**, *82*, 382–394. [CrossRef]
29. Moulijn, J.A.; Cerfontain, M.; Kapteijn, F. Mechanism of the potassium catalysed gasification of carbon in CO_2. *Fuel* **1984**, *63*, 1043–1047. [CrossRef]
30. Mims, C.; Pabst, J. Alkali-catalyzed carbon gasification kinetics: Unification of H_2O, D_2O, and CO_2 reactivities. *J. Catal.* **1987**, *107*, 209–220. [CrossRef]
31. Chang, J.-S.; Lauderback, L.L.; Falconer, J.L. Aes and sims analysis of potassium/graphite surfaces. *Carbon* **1991**, *29*, 645–652. [CrossRef]
32. Zhao, Y.; Feng, D.; Zhang, Y.; Huang, Y.; Sun, S. Effect of pyrolysis temperature on char structure and chemical speciation of alkali and alkaline earth metallic species in biochar. *Fuel Proc. Technol.* **2016**, *141*, 54–60. [CrossRef]
33. Andrea Jordan, C.; Akay, G. Speciation and distribution of alkali, alkali earth metals and major ash forming elements during gasification of fuel cane bagasse. *Fuel* **2012**, *91*, 253–263. [CrossRef]
34. Feng, D.; zhao, Y.; Zhang, Y.; Sun, S. Effect of speciation of AAEM species on reactivity of biochar. *J. Harbin Inst. Technol.* **2017**, *49*, 69–73.
35. Nutalapati, D.; Gupta, R.; Moghtaderi, B.; Wall, T. Assessing slagging and fouling during biomass combustion: A thermodynamic approach allowing for alkali/ash reactions. *Fuel Proc. Technol.* **2007**, *88*, 1044–1052. [CrossRef]
36. Miller, S.F.; Miller, B.G. The occurrence of inorganic elements in various biofuels and its effect on ash chemistry and behavior and use in combustion products. *Fuel Proc. Technol.* **2007**, *88*, 1155–1164. [CrossRef]
37. Benson, S.A.; Holm, P.L. Comparison of inorganic constituents in three low-rank coals. *Ind. Eng. Chem. Prod. Res. Dev.* **1985**, *24*, 145–149. [CrossRef]
38. Zevenhoven-Onderwater, M.; Backman, R.; Skrifvars, B.-J.; Hupa, M. The ash chemistry in fluidised bed gasification of biomass fuels. Part I: Predicting the chemistry of melting ashes and ash–bed material interaction. *Fuel* **2001**, *80*, 1489–1502. [CrossRef]
39. Pettersson, A.; Åmand, L.-E.; Steenari, B.-M. Chemical fractionation for the characterisation of fly ashes from co-combustion of biofuels using different methods for alkali reduction. *Fuel* **2009**, *88*, 1758–1772. [CrossRef]

40. Bai, Y.; Zhu, S.; Luo, K.; Gao, M.; Yan, L.; Li, F. Coal char gasification in H_2O/CO_2: Release of alkali and alkaline earth metallic species and their effects on reactivity. *Appl. Therm. Eng.* **2017**, *112*, 156–163. [CrossRef]
41. Guo, X.; Tay, H.L.; Zhang, S.; Li, C.-Z. Changes in char structure during the gasification of a Victorian brown coal in steam and oxygen at 800 °C. *Energy Fuels* **2008**, *22*, 4034–4038. [CrossRef]
42. Weng, Q.C.; Wang, C.A.; Che, D.F.; Fu, Z.W. Alkali metal occurrence mode and its influence on combustion characteristics in zhundong coals. *J. Combust. Technol.* **2014**, *20*, 216–221.
43. Feng, D.; Zhang, Y.; Liu, P.; Guo, Y.; Huang, Y.; Sun, S. Effects of chemical fractionation analysis on physical and chemical structures of biomass char. *CIESC J.* **2015**, *66*, 4634–4642.
44. Mitsuoka, K.; Hayashi, S.; Amano, H.; Kayahara, K.; Sasaoaka, E.; Uddin, M.A. Gasification of woody biomass char with CO_2: The catalytic effects of K and Ca species on char gasification reactivity. *Fuel Proc. Technol.* **2011**, *92*, 26–31. [CrossRef]
45. Manzoori, A.R.; Agarwal, P.K. The fate of organically bound inorganic elements and sodium chloride during fluidized bed combustion of high sodium, high sulphur low rank coals. *Fuel* **1992**, *71*, 513–522. [CrossRef]
46. Srinivasachar, S.; Helble, J.; Ham, D.; Domazetis, G. A kinetic description of vapor phase alkali transformations in combustion systems. *Prog. Energy Combust. Sci.* **1990**, *16*, 303–309. [CrossRef]
47. Marschner, H. *Marschner's Mineral Nutrition of Higher Plants*; Academic Press: Cambridge, MA, USA, 2011.
48. Nordgreen, T.; Liliedahl, T.; Sjöström, K. Metallic iron as a tar breakdown catalyst related to atmospheric, fluidised bed gasification of biomass. *Fuel* **2006**, *85*, 689–694. [CrossRef]
49. Zhang, S.; Min, Z.; Tay, H.-L.; Asadullah, M.; Li, C.-Z. Effects of volatile–char interactions on the evolution of char structure during the gasification of Victorian brown coal in steam. *Fuel* **2011**, *90*, 1529–1535. [CrossRef]
50. Tay, H.-L.; Kajitani, S.; Zhang, S.; Li, C.-Z. Effects of gasifying agent on the evolution of char structure during the gasification of Victorian brown coal. *Fuel* **2013**, *103*, 22–28. [CrossRef]
51. Leites, L.A.; Bukalov, S.S. Raman intensity and conjugation with participation of ordinary σ-bonds. *J. Raman Spectrosc.* **2001**, *32*, 413–424. [CrossRef]
52. Li, X.; Hayashi, J.; Li, C. Volatilisation and catalytic effects of alkali and alkaline earth metallic species during the pyrolysis and gasification of Victorian brown coal. Part VII. Raman spectroscopic study on the changes in char structure during the catalytic gasification in air. *Fuel* **2006**, *85*, 1509–1517. [CrossRef]
53. Li, X.; Li, C. Volatilisation and catalytic effects of alkali and alkaline earth metallic species during the pyrolysis and gasification of Victorian brown coal. Part VIII. Catalysis and changes in char structure during gasification in steam. *Fuel* **2006**, *85*, 1518–1525. [CrossRef]
54. Chen, S.; Yang, R. The Active Surface Species in Alkali-Catalyzed Carbon Gasification: Phenolate (C-O-M) Groups vs Clusters (Particles). *J. Catal.* **1993**, *141*, 102–113. [CrossRef]
55. Li, C.-Z. Some recent advances in the understanding of the pyrolysis and gasification behaviour of Victorian brown coal. *Fuel* **2007**, *86*, 1664–1683. [CrossRef]
56. Černý, J. Structural dependence of CH bond absorptivities and consequences for FT-i.r. analysis of coals. *Fuel* **1996**, *75*, 1301–1306. [CrossRef]
57. Lua, A.C.; Yang, T. Effects of vacuum pyrolysis conditions on the characteristics of activated carbons derived from pistachio-nut shells. *J. Colloid Interface Sci.* **2004**, *276*, 364–372. [CrossRef] [PubMed]
58. Lin-Vien, D.; Colthup, N.B.; Fateley, W.G.; Grasselli, J.G. *The Handbook of Infrared and Raman Characteristic Frequencies of Organic Molecules*; Elsevier: Amsterdam, The Netherlands, 1991.
59. Walker, P.; Taylor, R.; Ranish, J. An update on the carbon-oxygen reaction. *Carbon* **1991**, *29*, 411–421. [CrossRef]
60. Liu, X.; Xu, M.; Yao, H.; Gu, Y.; Si, J.; Xiong, C. Comparison of char structural characteristics and reactivity during conventional air and oxy-fuel combustion. In *Cleaner Combustion and Sustainable World*; Springer: Berlin, Germany, 2013; pp. 989–998.
61. Kelemen, S.; Freund, H. Model CO_2 gasification reactions on uncatalyzed and potassium catalyzed glassy carbon surfaces. *J. Catal.* **1986**, *102*, 80–91. [CrossRef]
62. Freund, H. Gasification of carbon by CO_2: A transient kinetics experiment. *Fuel* **1986**, *65*, 63–66. [CrossRef]
63. Pereira, P.; Csencsits, R.; Somorjai, G.A.; Heinemann, H. Steam gasification of graphite and chars at temperatures <1000 K over potassium-calcium-oxide catalysts. *J. Catal.* **1990**, *123*, 463–476.
64. Kapteijn, F.; Peer, O.; Moulijn, J.A. Kinetics of the alkali carbonate catalysed gasification of carbon: 1. CO_2 gasification. *Fuel* **1986**, *65*, 1371–1376. [CrossRef]
65. Freund, H. Kinetics of carbon gasification by CO_2. *Fuel* **1985**, *64*, 657–660. [CrossRef]

66. Quyn, D.M.; Wu, H.; Hayashi, J.-I.; Li, C.-Z. Volatilisation and catalytic effects of alkali and alkaline earth metallic species during the pyrolysis and gasification of Victorian brown coal. Part IV. Catalytic effects of NaCl and ion-exchangeable Na in coal on char reactivity. *Fuel* **2003**, *82*, 587–593. [CrossRef]
67. Yu, J.; Tian, F.-J.; Chow, M.C.; McKenzie, L.J.; Li, C.-Z. Effect of iron on the gasification of Victorian brown coal with steam: Enhancement of hydrogen production. *Fuel* **2006**, *85*, 127–133. [CrossRef]
68. Li, C.-Z.; Sathe, C.; Kershaw, J.; Pang, Y. Fates and roles of alkali and alkaline earth metals during the pyrolysis of a Victorian brown coal. *Fuel* **2000**, *79*, 427–438. [CrossRef]

© 2018 by the authors. Licensee MDPI, Basel, Switzerland. This article is an open access article distributed under the terms and conditions of the Creative Commons Attribution (CC BY) license (http://creativecommons.org/licenses/by/4.0/).

energies

MDPI

Article

Efficient Low Temperature Hydrothermal Carbonization of Chinese Reed for Biochar with High Energy Density

Chang Liu [1,2], Xin Huang [1] and Lingzhao Kong [2,*]

[1] School of Environmental and Chemical Engineering, Shanghai University, Shanghai 200444, China; liuchang@sari.ac.cn (C.L.); huangxin2008@shu.edu.cn (X.H.)
[2] Shanghai Advanced Research Institute, CAS. No. 100 Haike Road, Shanghai 201210, China
* Correspondence: konglz@sari.ac.cn; Tel.: +86-21-2060-8002

Received: 15 November 2017; Accepted: 6 December 2017; Published: 11 December 2017

Abstract: Hydrothermal carbonization (HTC), as an environmental friendly process, presents wide potential applicability for converting biomass to biochar with high energy density. Reed, a major energy crop, was converted by a HTC process in a batch reactor at 200–280 °C for 0.5 to 4 h. Biochar mass yield changed from 66.7% to 19.2% and high heating value (HHV) from 20.0 kJ/g to 28.3 kJ/g, respectively, by increasing the carbonization temperature from 200 °C to 280 °C and decreasing the residence time from 2 h to 1 h. The Fourier Transform infrared spectroscopy (FTIR), X-ray Diffraction (XRD), and Scanning Electron Microscope (SEM) results indicated the lignocellulosic crosslink structure of reed is broken and biochar having a high energy density is obtained with the increase of temperature. The microcrystal features of reed are destroyed and biochar contained mainly lignin fractions. The HTC of biocrude is carried out at 200–280 °C for 2.0 h and the results showed that the obtained biochar has uniform particles filled with carbon microspheres.

Keywords: hydrothermal carbonization (HTC); Chinese reed; biocrude; biochar; high heating value (HHV)

1. Introduction

Recently, abundant research efforts have been focused on the use of renewable biomass for producing energy, chemicals and materials. During the whole process for biomass growth and utilization, the carbon balance has been realized, so the concentration of CO_2 in the atmosphere theoretically remains constant during this cycle [1]. Most of the biomass is inefficiently used for the heating purposes in the absence of other reliable and cheaper sources of energy. The biomass has been exploited in ways involving pyrolysis, gasification, fermentation and hydrothermal processes to obtain the useful clean energy, materials and biochemicals. H_2 [2], ethanol [3], lactic acid [4], biochemicals [5], and biochar [6–8] can be obtained in different reaction processes. Recently, the acceleration of carbonization in a hydrothermal medium by a factor of 10^6–10^9 under rather mild conditions, down to a scale of hours, makes it a useful pathway for biochar production. The research attention has largely focused on the conversion of biomass to biochar which has higher heating value (over 28.0 kJ/g) and better carbonaceous materials performance [9].

Hydrothermal carbonization (HTC) is a thermochemical process to produce biochar from raw biomass or carbohydrates under mild temperatures (180–350 °C) and self-generated pressures in subcritical water. Compared to the typical carbonization routes such as pyrolysis (500 to 800 °C), HTC is able to explore fresh feedstock without any drying treatment [10,11]. During the HTC process, subcritical water serves as green solvent, reagent and catalyst that facilitate the hydrolysis and cleavage of lignocellulosic biomass [12,13]. Hydrolysis, dehydration, decarboxylation, condensation

polymerization and aromatization take place during the HTC process [14]. In the past decades, HTC has been explored the reveal the mechanisms of natural coalification in the coal-forming process, but attention was seldom paid to the production of solid residues. The biochar obtained by the HTC process from fresh biomass even bio-waste, can be used as a solid fuel, adsorbent and soil amendment with wide applicability. Some research has indicated a series of novel carbon materials with specific properties could be prepared through the HTC process under mind conditions using carbohydrates as starting materials [15,16].

A HTC process was used for the conversion of eucalyptus bark (EB) into biochar in the range of 220–300 °C after 2–10 h. The results showed that the biochar yield decreased slightly from 46.4% at 220 °C to 40.0% at 300 °C and high heating value (HHV) increased from 20.2 to 29.2 kJ/g [17]. The optimum conditions for maximum yield production of biochar through HTC of palm shell were also discussed. Using 180 °C, 0.5 h, and 1.60 wt.%, optimized biochar was obtained and the temperature was proven to have a greater influence on the efficiency of biochar production [18]. Liu carried out HTC of glucose, sucrose, and starch at temperatures ranging from 170 to 240 °C. The results indicated that biochar is made up of uniform spherical micrometer-sized particles that have a 0.4–6 mm diameter, which can be modulated by modifying the preparation conditions [19]. Sevilla et al. provided a method for producing carbonaceous materials by means of the HTC of cellulose at 220–250 °C. The formation of this material essentially follows the path of a dehydration process, similar to the HTC of saccharides such as glucose, sucrose or starch [20,21].

In the present work, our interest was the production of biochar with higher energy density and carbonaceous materials from biocrude, so the HTC process was explored to convert reed into biochar and biocrude in a batch reactor under mild conditions. The effect of reaction time, temperature and pressure in the range of 0.5–4 h, 200–280 °C and 2.4–27.2 MPa, respectively, were studied. The HTC of biocrude was carried out in a batch reactor at 200 °C for 2 h. Through Fourier Transform infrared spectroscopy (FTIR), X-ray Diffraction (XRD), and Scanning Electron Microscope (SEM) analysis of the biochar produced from reed, the transformation process, structure performance and energy value of biochar were discussed. Based on the yields and SEM analysis, the possible pathways for HTC of biocrude into carbon microspheres were provided.

2. Results

The characteristics of the reed raw material are presented in Table 1. Details of yield, HHV and energy yield of biochar prepared under various conditions using the setup illustrated in Figure 1 are shown in Table 2. In general, biochar yield (wt.%) decreased with temperature whereas HHV increased. The results are discussed in the following sections. The effects of residence time and pressure on the carbonization of reed for biochar production at 200 °C and 230 °C are discussed. The time and pressure ranged from 2.0 to 4.0 h and 17.6 and 27.2 MPa, respectively. The reed and biochar were characterized by FTIR (wave number: 4000–400 cm^{-1}) and a typical spectrum was shown in Figure 2. Typically bands in FTIR spectrum for reed and biochar were listed in Table 3. As the hydrolysis product of reed in the HTC process, biocrude contains various sugars and organic acids. The glucose, lactic acid, acetic acid, HMF (5-hydroxymethylfurfural) and furan in biocrude obtained from 200 °C to 280 °C are listed in the Table 4.

Table 1. The main properties of the reed.

Properties	Mass
Moisture (wt.%)	2.6
Lignin (wt.%)	23.5
Cellulose (wt.%)	39.5
Hemicellulose (wt.%)	26.7
Carbon (wt.%)	44.6
HHV (kJ/g)	17.1

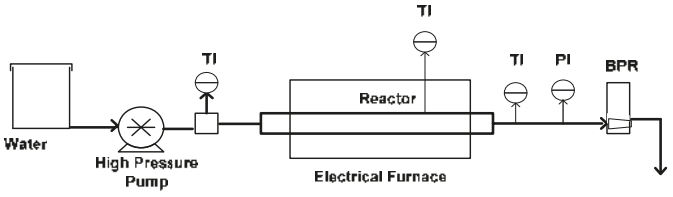

Figure 1. Setup for hydrothermal carbonization (HTC) of reed biomass to produce biochar.

Table 2. Experiment summary and results.

Run	Temp. (°C)	Time (h)	P (MPa)	Yield (wt.%)	HHV (kJ/g)	Energy Yield (%)
1	200	2.0	17.2	59.8	21.5	75.2
2	200	2.0	27.6	66.7	20.9	81.5
3	200	4.0	17.2	63.2	21.5	79.5
4	200	4.0	27.6	60.6	21.8	77.2
5	230	2.0	17.2	48.9	26.9	76.9
6	230	4.0	27.6	45.6	24.3	64.8
7	230	2.0	17.2	52.8	25.7	79.4
8	230	4.0	27.6	49.1	25.4	72.9
9	200	4.0	2.4	66.4	20.3	78.9
10	230	4.0	4.1	37.8	23.5	51.9
11	260	4.0	6.5	28.4	25.9	43.0
12	280	4.0	8.3	19.0	28.1	31.2
13	280	0.5	7.2	20.7	24.7	29.9
14	280	1.0	7.2	19.2	28.3	31.8

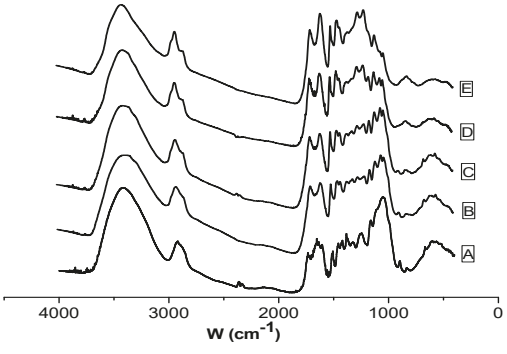

Figure 2. Transform infrared spectroscopy (FTIR) results of reed and biochar, processing time 4.0 h (A—Reed, B—200 °C, C—230 °C, D—260 °C, E—280 °C).

Table 3. FRIR spectrum of the reed and biochar.

Position of the Bands (cm^{-1})	Functional Group
3401	O–H stretching vibration
2920	CH, CH_2 stretching vibration
1700	Carbonyl C=O stretching vibration
1600	C=C stretching vibration
1513	Benzene ring stretching vibration
1424	CH_2 shearing, CH_2 bending vibration
1383	CH bending vibration
1267	C–O–C stretching vibration in alkyl aromatic
1160	C–O–C asymmetry stretching vibration
1060	C–O stretching vibration

Table 4. The main organic compounds in biocrude.

Composition	200 °C	230 °C	260 °C	280 °C
Glucose (g/L)	2.7	1.2	0.4	0.3
Lactic acid (g/L)	3.2	3.5	3.6	2.7
Acetic acid (g/L)	-	0.6	1.1	0.9
HMF (g/L)	-	-	-	0.7
Furan (g/L)	-	-	-	1.9

3. Discussion

3.1. Performance of HTC for Biochar

At 200 °C, the higher yield and HHV for biochar were obtained at 2.0 h, 27.6 MPa and 4.0 h, 27.6 MPa, respectively, and the values were determined as 66.7% and 21.8 kJ/g. A higher temperature favored the conversion of raw materials to higher energy density fuel and HHV, as indicated by the values provided at 230 °C which were 26.9 kJ/g at 2 h and 17.2 MPa. Compared to the yield of biochar at 200 °C, it showed a descending trend at the same conditions for 230 °C. Higher yield and HHV can be obtained at 200 °C and 230 °C, respectively. The desired pressure was achieved by pumping water into the reactor. The increased pressure of the reaction system keeps the water in its aqueous phase and influences the density properties of water [10]. At comparatively low temperature (200–230 °C), the amorphous components of reed were mainly hydrolyzed and the liquid product mainly contained oligomers and monomers produced by the hydrolysis of the sugar components in reed. The HHV of the product biochar remained low because of low deoxygenation rate in this temperature range.

Temperature plays a key role in the conversion of reed to biochar. Further experiments were performed at 200 °C to 280 °C for 4.0 h and the results are shown in the Table 2. Fifty mL of water was added into the reactor and the mass ratio of biomass and water was changed from 1:6.5 (shown in the Table 2) to 1:25. The pressure was autogenously adjusted and it increased above the vapor pressure of water because of the formation of gaseous products during the HTC process. The influence of temperature is obviously, though biochar yield decreased at 280 °C, the HHV of the product was increased considerably with temperature.

The highest yield of 60.6% for biochar was obtained at 200 °C. At the same time, the higher temperature is propitious to obtain higher energy density fuel and this value reached 28.1 kJ/g at 280 °C. The yield and HHV obtained at 230 °C are 37.8% and 23.5 kJ/g, which lower than the results under the set pressure. The results showed that high pressure provides a higher yield and HHV for the conversion of reed to biochar despite it being lower from the influence of temperature. Based on the results of yield and HHV at different temperatures, the energy conversion efficiency, which was defined as the ratio of contained energy in raw reed and obtained biochar, were 52.4%, 43.0%, and 31.2% at 230, 260, and 280 °C, respectively. The results indicated that energy conversion efficiency displays a decreasing tendency with the increase of temperature. To obtain a higher energy conversion efficiency and biochar with higher energy density, a higher temperature should be used and the reaction conditions should be changed to improve the HHV of biochar.

Table 2 displays the obtained biochar yield and HHV at 280 °C from 0.5 to 4.0 h. The yield of biochar shows a descending curve, but the values of HHV increase slightly from 0.5 h to 4.0 h. The HHV obtained from 0.5 h at 280 °C is higher than that of 4 h at 230 °C, but the yield (20.7%) is lower than with the former conditions (37.8%). Reed provides less biochar yield in the case of 1.0 h at 280 °C than 4.0 h at 260 °C, but the HHV for biochar were high as 28.4 and 25.9 kJ/g. Similar biochar yield and HHV results were obtained at 1.0 h and 4.0 h under 280 °C. Future work will focus on getting the optimal conditions for conversion of reed to biochar with higher yield and energy density.

3.2. Characterization of Reed and Biochar

The FTIR spectrum of biochar was partly similar to that of reed and the typical peaks of lignin were maintained in biochar. These results indicated that the biochar had a high degree of polymerization oligomers with lingo-like molecular structures. The reed was not liquefied completely for the appearance of absorption peaks at 1060 and 1160 cm^{-1} at 200 °C and 230 °C. From Figure 2, it can be seen that the absorbance peaks in the raw, 200 °C and 230 °C materials are similar and hemicellulose and cellulose were present in the biochar obtained at lower temperature [22]. As for 260 °C and 280 °C, the FTIR displays peak changes for the biochar obtained at higher temperature which is different from reed and lower temperature product. The results showed that the two kinds of biochar have a different functional groups than reed. In the higher temperature process, the hemicellulose and cellulose were converted and a polymerization process was realized. From the spectral difference of FTIR spectra of these biochar obtained at higher temperature and reed, the absorbance peak appeared in the range of 1600–650 cm^{-1}. It was shown that the aromatic rings started to recombine at this temperature. The possible presence of alkenes was indicated by the absorbance peaks between 1680 and 1580 cm^{-1}. The ether linkages around 1200 cm^{-1} and 1000 cm^{-1} between the cellulose skeleton units were hydrolyzed with the hydrothermal treatment from 260 °C to 280 °C under subcritical conditions [23–25]. As for the skeleton structure of reed, the lignin remained in the biochar when the temperature increased from 200 °C to 280 °C. The results were confirmed by the lignin peaks at 1265, 1424 and 1513 cm^{-1} in the FTIR. At the same time, peaks of polymeric product were also shown in the FTIR spectra at 1600 and 1700 cm^{-1}. These results proved that the biochar was composed by the conserved lignin and polymeric products produced in the HTC process [22].

We conducted SEM observations of reed and biochar after the HTC process. The SEM images for biochar and reed are shown in Figure 3. These results suggested that biochar has a different macromolecular structure from reed and their average particle sizes grew smaller at the temperature reached 260 °C. The results show that the lignocellulosic structure of reed was destroyed as the hemicellulose and cellulose were hydrolyzed in the HTC process. Small globular particles which come from the polymer particles of reed decomposition can be seen precipitated over thin fibers. The cross-linked structure which was made up by the lignin and cellulose in reed was broken in the HTC process as the cellulose was hydrolyzed into aqueous phase [26,27]. Compared with lignin, the microcrystal structure of cellulose is relatively easily damaged under higher temperature conditions and the results were demonstrated in the FTIR analysis. As shown in the Figure 3B, the lignin can resist the higher temperature disruption and form the main skeleton structure for biochar obtained in higher temperature.

The XRD patterns for biochar (obtained 280 °C, 4.0 h) and reed were compared and are shown in Figure 4. The distinct sharp crystalline cellulosic peak ($2\theta = 22.7°$) which comes from the crystal structure of cellulose was displayed in the reed, but the peak was absent in the biochar, which confirms that it contained mainly less crystalline or amorphous components. As the cellulose in the reed was decomposed, the transformation from microcrystal features to a non-crystalline structure were realized in the HTC process. A carbon-rich product with an amorphous structure and lignin as the major component was retained in the biochar. The results are consistent with the FTIR and SEM analyses. Through the analysis of FTIR, SEM and XRD for the reed and obtained biochar, the change for structure, morphology and composition from reed to biochar were displayed to help understand the HTC process for biochar production. Through fragmentations and deoxygenation, reed conversion into biochar is realized. The main components of the biochar obtained at higher temperature are lignin and cellulose was hydrolyzed into biocrude. The elemental analysis of the biochar obtained at 280 °C indicated that the elemental carbon is over 70%. The results confirm that O/C ratio decrease with temperature from 0.90 for reed to 0.32 for biochar obtained at 280 °C. The decrease in O/C ratio may be attributed to the deoxygenation, caused mainly by the dehydration of reed.

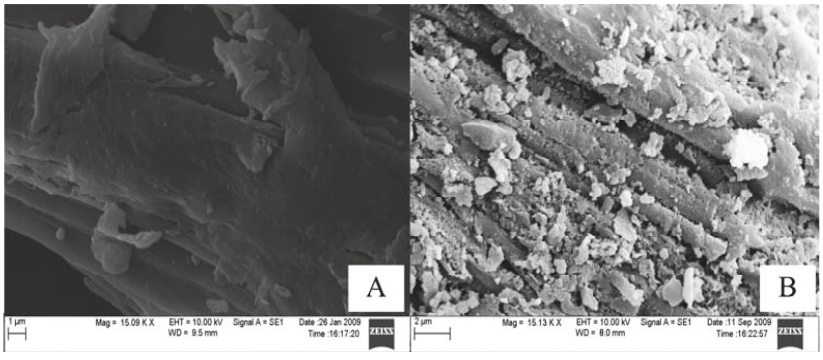

Figure 3. Scanning Electron Microscope (SEM) results for reed (**A**) and biochar (**B**) obtained at 260 °C, 4.0 h.

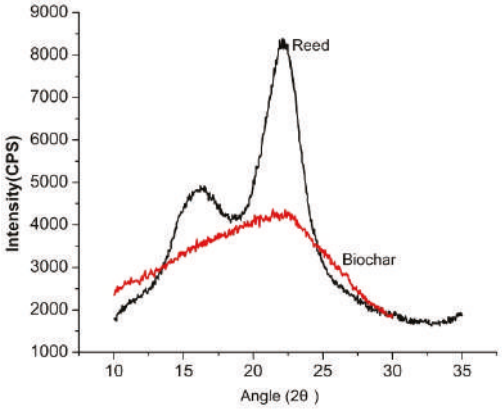

Figure 4. X-ray Diffraction (XRD) results for reed and biochar obtained at 280 °C, 4.0 h.

3.3. HTC of Biocrude for Biochar

From Table 4 we know that glucose serves as the main contributor in the biocrude which is obtained at low temperature. The main hydrolysis products of reed include glucose, acetic acid, lactic acid, HMF and furan. The oligomers and glucose constitute the majority of the organic compounds in the liquefaction of reed at low temperatures such as 200 °C. Organic acids and aromatic compounds are formed by different pathways, especially in the high temperature interval. As the temperature increases from 200 °C to 280 °C, the amount of glucose decreases whereas that of organic acids displays an upward trend. For the hydrolysis product of hemicellulose and cellulose, lower temperature is favorable for the production of glucose and higher temperature is beneficial for producing organic acids. We carried out experiments on the HTC of biocrude at 200 °C for 2.0 h. The biocrude was obtained in the HTC of reed in a temperature range from 200 °C to 280 °C. The conversion efficiency of carbon from biocrude to biochar is shown in Figure 5. The conversion efficiency of carbon was 35.5% when the biocrude was obtained at 200 °C. As for the biocrude obtained at 280 °C and 4.0 h, the value decreased to 4.4%. The conversion efficiency of carbon for biocrude obtained from 230 °C and 260°C were 26.2% and 6.5%, respectively. The experimental results indicated that biocrude produced at lower temperature is favorable for the conversion of organic carbon to biochar. Sugar plays an important role in the HTC process for biochar production which was similar to that use the glucose as a raw material. Through polycondensation and molecular rearrangements

of sugar, the conversion of biocrude to biochar was realized in the HTC process [28]. The SEM image for HTC conversion biocrude obtained at 200 °C to biochar is shown in Figure 6.

As shown in the Figure 6, the biochar obtained in the HTC of biocrude has uniform features. Interestingly, the majority of the 2 μm particles are composed of the biochar and biocrude transformed into carbon microspheres during the hydrothermal carbonization process. A comparison of biochar produced from reed and biocrude indicated that different formation pathways lead to various biochar properties. The biochar obtained the HTC of reed can be used as a higher energy density fuel for its higher carbon content. Because of the homogenization characteristics, the biochar resulting from the HTC of biocrude can provide a new method for producing carbonaceous materials.

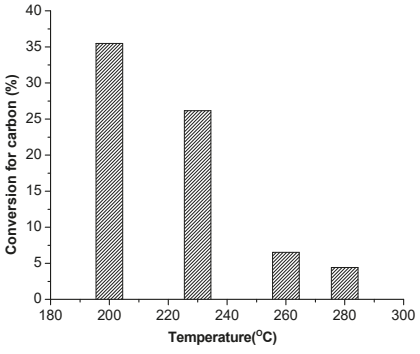

Figure 5. The conversion efficiency of carbon from biocrude obtained at different temperature (experiments on the HTC of biocrude at 200 °C, 2.0 h).

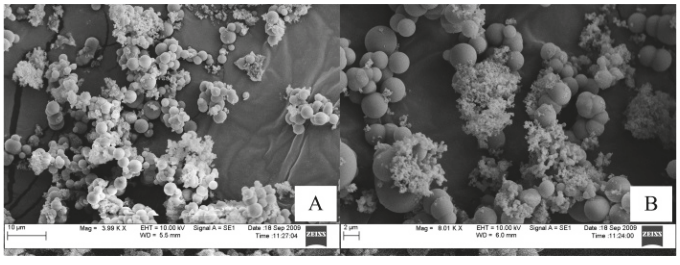

Figure 6. SEM image of biochar (HTC of biocrude obtained at 200 °C), 200 °C, 2.0 h. (**A**: scale: 10 μm; **B**: scale: 2 μm.)

4. Materials and Methods

4.1. Material

Reed (2–5 mm long pieces, powdered) was used as raw material for the HTC experiments. The physical and chemical properties of the reed are listed in Table 1. Biocrude obtained from liquefaction of reed also was used for producing biochar.

4.2. Apparatus and Procedure

HTC of reed was carried out in a batch reactor with an internal volume of 65.0 cm^3 (Figure 1). The experiments were carried out at 200–280 °C for 0.5–4.0 h. The HTC process was as follows: the desired amount of reed (10.0 g) and water (45 cm^3) was put into the reactor, which was then sealed. The reactor was heated up to a desired temperature for HTC of reed. After the set time, the reactor

was rapidly cooled to room temperature using air flow. The reaction time was defined as the time at the reaction temperature excluding preheating and cooling time. To study the effect of pressure on HTC process, reactor pressure was controlled by pumping water into the reactor until the set value was reached. After HTC of Chinese reed, the biochar and biocrude were separated with a 0.22 μm filtration membrane. The biocrude was used as starting material for preparing carbon materials. As for the biochar produced from the biocrude, the experiments on the HTC of biocrude were carried out at 200 °C for 2.0 h in the batch reactor. The reactor was filled with liquid phase (biocrude) which was obtained from the different HTC processes and the biochar was collected through a 0.22 μm filtration membrane after the reaction. The biochar obtained from biomass and biocrude was washed using deionized water and oven dried for 24 h at 105 °C.

4.3. Characterization

Surface morphology of the sample was recorded using an environmental scanning electron microscope (SEM, EVO 50, Zeiss, Jena, Germany). XRD patterns of the reed and biochar were obtained on a Miniflex powder X-ray diffractometer (Rigaku, Tokyo, Japan) with a Cu Kα radiation source in a 2θ range from 10° to 35° with a scanning rate of 1°/min. Infrared spectra (4000–400 cm^{-1}) were analyzed by a IR100 infra-red spectroscopy (FTIR) instrument (Nicolet, Waltham, MA, USA) which was equipped with a TGS/PE detector and a silicon beam splitter with 1 cm^{-1} resolution. The higher heating value (HHV) of reed and biochar was determined by an IKA-C200 calorimeter (IKA Works, Wilmington, NC, USA). The collected liquid solution was filtered through a 0.22 μm pore-size filter prior to analysis. The main products in the resultant solution were identified based on standard compounds and their structures were further confirmed by HPLC (LC-20AD system, Shimadzu, Tokyo, Japan) equipped with an Aminex HPX-87H Ion Exclusion Column, 300 mm × 7.8 mm) with a differential refraction detector (RID-10A). The column was held at 65°C. H_2SO_4 (0.01 mol/L) was used as the mobile phase at a flow rate of 1.0 mL/min. The peak identification was accomplished by comparison of sample peak retention times with those of standard solutions of pure compounds. The total organic carbon (TOC) in aqueous phase was measured with a TOC analyzer (Shimadzu TOC 5000 A).

5. Conclusions

Reed was converted into biochar in a temperature range of 200–280 °C for 0.5–4.0 h in a batch reactor. Compared with the residence time and pressure, the temperature plays a key role in the conversion of reed to biochar. Higher temperature is favorable for the production of a higher energy density fuel but is negative for the mass of biochar. The yield of biochar decreased when the temperature increased from 200 °C to 280 °C. The FTIR and SEM results suggested that the complete breakdown of the lignocellulosic crosslinked structure of reed is realized at higher temperature and biochar contained mainly lignin fractions. The XRD image of untreated reed and biochar indicated that the microcrystal features are converted into a non-crystalline structure in the HTC process. HTC of biocrude for biochar production were carried out from 200–280 °C and 2.0 h. The results indicated that biocrude obtained at lower temperature is favorable for biochar production and polycondensation of sugar is the major factor in the HTC of biocrude. The biochar obtained from the HTC of biocrude has a uniform particle size filled with globular carbon microspheres.

Acknowledgments: Authors acknowledge financial supports provided by the National Natural Science Foundation of China (21406255), the Shanghai Science and Technology Committee (16dz1207200) and the Youth Innovation Promotion Association CAS (2015231).

Author Contributions: Xin Huang and Lingzhao Kong conceived and designed the experiments; Chang Liu performed the experiments; Chang Liu and Lingzhao Kong analyzed the data; Chang Liu and Xin Huang contributed reagents/materials/analysis tools; Lingzhao Kong wrote the paper.

Conflicts of Interest: The authors declare no conflict of interest.

References

1. Matsumura, Y.; Sasaki, M.; Okuda, K. Supercritical water treatment of biomass for energy and material recovery. *Combust. Sci. Technol.* **2006**, *178*, 509–536. [CrossRef]
2. Lee, I.; Kimm, M.; Ihm, S. Gasification of glucose in supercritical water. *Ind. Eng. Chem. Res.* **2002**, *41*, 1182–1188. [CrossRef]
3. Motonobu, G.; Ryusaku, O.; Tsutomu, H. Hydrothermal conversion of municipal organic waste into resources. *Bioresour. Technol.* **2004**, *93*, 279–284.
4. Kong, L.Z.; Li, G.M.; Wang, H. Hydrothermal catalytic conversion of biomass for lactic acid production. *J. Chem. Technol. Biotechnol.* **2008**, *83*, 383–388. [CrossRef]
5. Selhan, K.; Thallada, B.; Akinori, M. Low-temperature catalytic hydrothermal treatment of wood biomass: Analysis of liquid products. *Chem. Eng. J.* **2005**, *108*, 127–133.
6. Sevilla, M.; Macia-Agullo, J.A.; Fuertes, A.B. Hydrothermal carbonization of biomass as a route for the sequestration of CO_2: Chemical and structural properties of the carbonized products. *Biomass Bioenergy* **2011**, *35*, 3152–3159. [CrossRef]
7. Liu, W.J.; Zeng, F.X.; Jiang, H. Preparation of high adsorption capacity bio-chars from waste biomass. *Biomass Bioenergy* **2011**, *102*, 8247–8252.
8. Libra, J.A.; Ro, K.S.; Kammann, C. Hydrothermal carbonization of biomass residuals: A comparative review of the chemistry, processes and applications of wet and dry pyrolysis. *Biofuels* **2011**, *2*, 89–124. [CrossRef]
9. Gupta, R.B.; Kumar, S.; Kong, L.Z. Biomass to Biochar Conversion in Subcritical Water. U.S. Patent 8,637,718 B2, 8 January 2014.
10. Sevilla, M.; Fuertes, A.B. The production of carbon materials by hydrothermal carbonization of cellulose. *Carbon* **2009**, *47*, 2281–2289. [CrossRef]
11. Sevilla, M.; Fuertes, A.B. Chemical and structural properties of carbonaceous products obtained by hydrothermal carbonization of saccharides. *Chem. A Eur. J.* **2009**, *15*, 4195–4203. [CrossRef] [PubMed]
12. Titirici, M.M.; Thomas, A.; Antonietti, M. Back in the black: Hydrothermal carbonization of plant material as an efficient chemical process to treat the CO_2 problem? *New J. Chem.* **2007**, *31*, 787–788. [CrossRef]
13. Phillip, E. Organic chemical reactions in supercritical water. *Chem. Rev.* **1999**, *99*, 603–621.
14. Hu, B.; Yu, S.H.; Wang, K.; Liu, L.; Xu, X.W. Functional carbonaceous materials from hydrothermal carbonization of biomass: An effective chemical process. *Dalton Trans.* **2008**, *6*, 5414–5423. [CrossRef] [PubMed]
15. Laginhas, C.; Valente Nabais, J.M.; Titirici, M.M. Activated carbons with high nitrogen content by a combination of hydrothermal carbonization with activation. *Microporous Mesoporous Mater.* **2016**, *226*, 125–132. [CrossRef]
16. Kumar, S.; Loganathan, V.A.; Gupta, R.B.; Barnett, M.O. An Assessment of U(VI) removal from groundwater using biochar produced from hydrothermal carbonization. *J. Environ. Manag.* **2011**, *92*, 2504–2512. [CrossRef] [PubMed]
17. Gao, P.; Zhou, Y.Y.; Meng, F.; Zhang, Y.H.; Liu, Z.H.; Zhang, W.Q.; Xue, G. Preparation and characterization of hydrochar from waste eucalyptus bark by hydrothermal carbonization. *Energy* **2016**, *97*, 238–245. [CrossRef]
18. Nizamuddin, S.; Mubarak, N.M.; Jayakumar, N.S.; Sahu, J.N.; Ganesan, P. Chemical, dielectric and structural characterization of optimized hydrochar produced from hydrothermal carbonization of palm shell. *Fuel* **2016**, *163*, 88–97. [CrossRef]
19. Liu, Z.G.; Zhang, F.S. Removal of copper (II) and phenol from aqueous solution using porous carbons derived from hydrothermal chars. *Desalination* **2011**, *267*, 101–106. [CrossRef]
20. Watanabe, M.; Sato, T.; Inomata, H.; Smith, R.L., Jr.; Arai, K., Jr.; Kruse, A.; Dinjus, E. Chemical reactions of C_1 compounds in near-critical and supercritical water. *Chem. Rev.* **2004**, *104*, 5803–5821.
21. Savova, D.; Apak, E.; Ekinci, E.; Yardim, F.; Petrov, N.; Budinova, T.; Razvigorova, M.; Minkova, V. Biomass conversion to carbon adsorbents and gas. *Biomass Bioenergy* **2011**, *21*, 133–142. [CrossRef]
22. Kong, L.Z.; Miao, P.J.; Qin, J.G. Characteristics and pyrolysis dynamic behaviors of hydrothermally treated micro crystalline cellulose. *J. Anal. Appl. Pyrolysis* **2013**, *100*, 67–74. [CrossRef]
23. Sakanishi, K.; Ikeyama, N.; Sakaki, T. Comparison of the hydrothermal decompositionreactivities of chitin and cellulose. *Ind. Eng. Chem. Res.* **1999**, *38*, 2177–2181. [CrossRef]
24. Kong, L.Z.; Li, G.M.; He, W.Z. Reutilization disposal of sawdust and maize straw by hydrothermal reaction. *Energy Sources Part A* **2009**, *31*, 876–887. [CrossRef]

25. Biagini, E.; Barontini, F.; Tognotti, L. Devolatilization of biomass fuels and biomass components studied by TG/FTIR technique. *Ind. Eng. Chem. Res.* **2006**, *45*, 4486–4493. [CrossRef]
26. Kobayashi, N.; Okada, N.; Hirakawa, A.; Sato, T.; Kobayashi, J.; Hatano, S.; Itay, Y.; Mori, S. Characteristics of solid residues obtained from hot-compressed-water treatment of woody biomass. *Ind. Eng. Chem. Res.* **2009**, *48*, 373–379. [CrossRef]
27. Zhu, N.Y.; Yan, T.M.; Qiao, J. Adsorption of arsenic, phosphorus and chromium by bismuth impregnated biochar: Adsorption mechanism and depleted adsorbent utilization. *Chemosphere* **2016**, *164*, 32–40. [CrossRef] [PubMed]
28. Kumar, S.; Kothari, U.; Lee, Y.Y.; Gupta, R.B. Hydrothermal pretreatment of switchgrass and corn stover for production of ethanol and carbon microspheres. *Biomass Bioenergy* **2011**, *35*, 956–968. [CrossRef]

© 2017 by the authors. Licensee MDPI, Basel, Switzerland. This article is an open access article distributed under the terms and conditions of the Creative Commons Attribution (CC BY) license (http://creativecommons.org/licenses/by/4.0/).

energies

MDPI

Article

Gasification under CO_2–Steam Mixture: Kinetic Model Study Based on Shared Active Sites

Xia Liu †, Juntao Wei †, Wei Huo and Guangsuo Yu *

Key Laboratory of Coal Gasification and Energy Chemical Engineering of Ministry of Education, East China University of Science and Technology, Shanghai 200237, China; lxia@ecust.edu.cn (X.L.); icct-wjt@foxmail.com (J.W.); howell26@sina.com (W.H.)

* Correspondence: gsyu@ecust.edu.cn; Tel.: +86-21-64252974

† These authors contributed equally to this work.

Received: 16 October 2017; Accepted: 15 November 2017; Published: 17 November 2017

Abstract: In this work, char gasification of two coals (i.e., Shenfu bituminous coal and Zunyi anthracite) and a petroleum coke under a steam and CO_2 mixture (steam/CO_2 partial pressures, 0.025–0.075 MPa; total pressures, 0.100 MPa) and CO_2/steam chemisorption of char samples were conducted in a Thermogravimetric Analyzer (TGA). Two conventional kinetic models exhibited difficulties in exactly fitting the experimental data of char–steam–CO_2 gasification. Hence, a modified model based on Langmuir–Hinshelwood model and assuming that char–CO_2 and char–steam reactions partially shared active sites was proposed and had indicated high accuracy for estimating the interactions in char–steam–CO_2 reaction. Moreover, it was found that two new model parameters (respectively characterized as the amount ratio of shared active sites to total active sites in char–CO_2 and char–steam reactions) in the modified model hardly varied with gasification conditions, and the results of chemisorption indicate that these two new model parameters mainly depended on the carbon active sites in char samples.

Keywords: gasification; kinetic model; active site; chemisorption

1. Introduction

Gasification is an important technology for the clean and efficient utilization of coal, petroleum coke, and other solid fuels, and is available for large-scale industry due to its high efficiency, high production intensity, and near-zero pollution emission [1,2]. Fundamental research of gasification processes identified the rate of char gasification as a significant factor controlling gasification behaviors. This was mainly attributed to the relatively slow kinetics of char–CO_2 reactions and char–steam reactions under gasification conditions [3]. Therefore, it is important to make a clear understanding of the gasification kinetics of char–CO_2 and char–steam.

Many researchers [4–7] have developed reaction models of char–CO_2 and char–steam respectively to determine their reaction rates. Moreover, the kinetics of char–CO_2 gasification and char–steam gasification have also been studied in detail [8–11]. However, these models and studies, carried out in the system with a sole gasifying agent, could hardly be applied in systems where char–CO_2 and char–steam reactions occur simultaneously. Under realistic gasification conditions, chars are reacted with the gasifying agent mixtures consisting of steam and CO_2. Therefore, the researchers in [12] investigated the gasification reactivities of metallurgical coke in a mixture of steam and CO_2, but it was hard to analyze the intrinsic char–CO_2–steam reaction because the particle size of the tested samples was large (3–6 mm), which resulted in the effect of internal diffusion. Muhlen et al. [13] have also studied the mechanism of coal char gasification under a mixture of steam and CO_2, and the proposed empirical approach could well describe the effect of the carbon conversion degree on the gasification rate.

Recently, some researchers [14–18] came to investigate interactions in the char–CO_2–steam reaction using the Langmuir–Hinshelwood (L–H) model based on the theory of absorption and desorption. Roberts and Harris [14] found that char–CO_2 and char–steam reactions occur at the common active sites and indicated that steam and CO_2 competed for active sites of chars. However, some other researchers proposed an opposite view. Both Huang et al. [15] and Everson et al. [16] thought that the char–CO_2 reaction and char–steam reaction proceeded at separate active sites and the overall gasification rate should be equal to the sum of the char–CO_2 reaction rate and the char–steam reaction rate. Li et al. [17] also pointed out that the reaction mechanism of lignite char gasification was in accordance with the separate reactive site reaction mechanism under lower gasification pressures, whereas it was superior to the common reactive site reaction mechanism when gasification pressures further increased. On the other hand, Chen et al. [18] found that the overall gasification rate is not equal to the sum of the char–CO_2 reaction rate and char–steam reaction rate, but there was no evidence proving that the two gasifying agents competed for active sites. An L–H model with two dimensionless parameters was proposed by Umemoto et al. [19] to evaluate the rate of char–CO_2–steam gasification, and could estimate interactions more accurately than other models. However, the mechanism of the two proposed parameters is unclear.

Accordingly, a modified kinetic model based on the concept of active sites was proposed in this study to evaluate the interaction in char–CO_2–steam gasification, and it was validated by char–CO_2–steam gasification experiments of carbonaceous materials (two coals of different ranks and a petroleum coke) using a Thermogravimetric Analyzer (TGA). Additionally, CO_2 and steam chemisorption of chars were also conducted in a TGA to measure chemisorption quantities so as to explore the correlation between kinetic parameters of the modified model and chemisorption quantities. This work can provide not only theoretical basis for simulation but also scientific basis for gasification industry.

2. Materials and Methods

2.1. Char Preparation

Two typical gasification coals (Shenfu bituminous coal (SF) and Zunyi anthracite (ZY) from China) and a petroleum coke (PC) from Sinopec Shanghai Gaoqiao Petrochemical Co., Ltd. (Shanghai, China) were chosen as raw materials in this study. During char preparation, all pulverized raw samples were heated at 25 °C/min to 850 °C and held 30 min under the high purity nitrogen atmosphere in a fixed bed reactor. After devolatilization, the prepared chars with particle sizes of <40 μm were used for further analysis. The proximate analysis, ultimate analysis, and specific surface area of char samples are listed in Table 1.

Table 1. Properties of tested char samples.

Samples	Proximate Analysis/d, %			Ultimate Analysis/daf, %					Specific Surface Area/$m^2 \cdot g^{-1}$
	VM	FC	A	C	H	N	S	O	
SF char	8.60	81.33	10.07	95.96	1.02	1.40	0.40	1.22	2.05
ZY char	5.50	73.48	21.02	96.11	0.95	1.68	1.04	0.22	1.52
PC char	4.11	90.86	5.03	95.95	0.73	1.19	2.08	0.05	0.41

SF-Shenfu bituminous coal; ZY-Zunyi anthracite; PC-petroleum coke; VM-volatile matter; FC-fixed carbon; A-ash; d-dry basis; daf-dry and ash free basis.

2.2. Isothermal Gasification Tests

The tests of isothermal char gasification were carried out using a TGA (NETZSCH STA449-F3). In all cases, approximately 5 mg of char particles was placed in an alumina crucible and heated at 25 °C/min to the prescribed temperature (850–950 °C) under high purity nitrogen atmosphere (80 mL/min). Then, nitrogen was switched to gasifying agents to initiate the isothermal gasification.

In char gasification tests, nitrogen was used to adjust the concentration of the gasifying agents. For char gasification with sole gasifying agent (steam or CO_2), the partial pressures of the gasifying agents varied from 0.025 to 0.100 MPa. For char gasification with a mixture of steam and CO_2, the partial pressures of steam and CO_2 varied from 0.025 to 0.075 MPa, and the total pressure was always 0.100 MPa. The effects of external and internal diffusion were eliminated by previous tests [20].

The carbon conversion was expressed by the following equation [21]:

$$x = \frac{w_0 - w_t}{w_0 - w_{ash}} \tag{1}$$

where w_0 is the initial mass of char (wt. %); w_t is the sample mass at gasification time of t (wt. %); and w_{ash} is the final sample mass at the end of gasification.

Gasification rate was defined as following:

$$r = -\frac{1}{w_0 - w_{ash}} \frac{dw}{dt} = \frac{dx}{dt} \tag{2}$$

2.3. CO_2/Steam Chemisorption

CO_2/steam chemisorption of chars was fulfilled by TGA, and the test procedures have been reported in previous literature [22–24]. Approximately 15 mg of char particles was first heated at 25 °C/min to 850 °C and then held for 30 min under a continuous high purity nitrogen flow, in order to remove any impurity which could be adsorbed during CO_2 or steam chemisorption. Then, the temperature was decreased to 300 °C and stabilized for 10 min. Whereafter, nitrogen was switched to pure CO_2 or steam to start the chemisorption test. After another 30 min of adsorption, pure CO_2 or steam was finally switched to high purity nitrogen, and the char samples were degassed for 30 min, in order to remove all weakly chemisorbed CO_2 or steam molecules. The flow rates of steam, CO_2, and high-purity nitrogen were all set as 80 mL/min.

As a representative, the steam chemisorption curve of PC char is shown in Figure 1. Three sets of chemisorption data can be observed in Figure 1. The first one is the total quantity of chemisorption (C_t). The second one is the quantity of weak chemisorption (C_w). The weak chemisorption of steam or CO_2 was desorbed from char surface during the process of degassing. The last one is the quantity of strong chemisorption (C_s). Strong chemisorption of steam or CO_2 still stayed on the surface of the char after degassing.

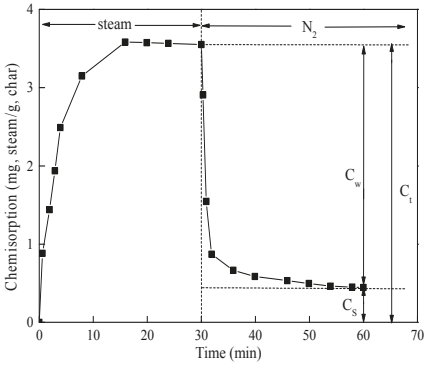

Figure 1. Steam chemisorption of petroleum coke (PC) char.

3. Results and Discussion

3.1. Choice of Kinetic Model of Char–CO_2–Steam Gasification

The mechanism of the char–CO_2 reaction is widely accepted by following description:

$$C_f + CO_2 \underset{k_2}{\overset{k_1}{\rightleftharpoons}} C(O) + CO \tag{3}$$

$$C(O) \xrightarrow{k_3} CO + C_f \tag{4}$$

Based on the Langmuir–Hinshelwood (L–H) model derived from the theory of absorption and desorption, the char–CO_2 reaction rate can be expressed as Equation (5):

$$r_{CO_2} = \frac{k_1 P_{CO_2}}{1 + (k_2/k_3)P_{CO_2} + (k_1/k_3)P_{CO}} \tag{5}$$

The equation can also be written as:

$$r_{CO_2} = \frac{K_a P_{CO_2}}{1 + K_b P_{CO_2} + K_c P_{CO}} \tag{6}$$

Here, K_a, K_b, and K_c can be defined as following:

$$K_i = A_i e^{\frac{-E_i}{RT}} \tag{7}$$

According to Equation (5), $E_a = E_1$, $E_b = E_2 - E_3$, $E_c = E_1 - E_3$, $A_a = A_1$, $A_b = A_2/A_3$, $A_c = A_1/A_3$. Similarly, the char–steam reaction rate can be expressed as Equation (8):

$$r_{steam} = \frac{K_d P_{H_2O}}{1 + K_e P_{H_2O} + K_f P_{H_2}} \tag{8}$$

In this study, chars were gasified with a steam–CO_2 mixture, so the mechanism of the char–steam–CO_2 reaction should be defined. Interactions in a char–steam–CO_2 reaction have been studied recently [14,16,19], and there were two kinds of mechanisms accepted by researchers. The first assumed that char–CO_2 and char–steam reactions occur at separate active sites (Model A in Figure 2a). Based on this assumption, the overall reaction rate was equal to the sum of rates of these two reactions and can be described as following:

$$r = \frac{K_a P_{CO_2}}{1 + K_b P_{CO_2} + K_c P_{CO}} + \frac{K_d P_{H_2O}}{1 + K_e P_{H_2O} + K_f P_{H_2}} \tag{9}$$

The second mechanism assumed that these two reactions occur at common active sites (Model B in Figure 2b). This means that these two reactions compete for the same active sites, so the overall reaction rate was slower than the sum of reaction rates of these two reactions and can be described as following:

$$r = \frac{K_a P_{CO_2} + K_d P_{H_2O}}{1 + K_b P_{CO_2} + K_c P_{CO} + K_e P_{H_2O} + K_f P_{H_2}} \tag{10}$$

In general, a CO_2 molecule can enter into pores with sizes larger than 1.5 nm, while a steam molecule can enter into pores with sizes larger than 0.6 nm. This led to a phenomenon where some active sites existed in pores with sizes smaller than 1.5 nm and could only be occupied by steam molecules. In addition, the catalytic effect of the inherent mineral on the char–CO_2 reaction was quite different from that on the char–steam reaction [25]. Based on these reasons, it was conjectured that

char–CO_2 and char–steam reactions may share active sites partially, and the modified model was proposed as shown in Figure 2c. Some new parameters were introduced to quantify the amount of shared active sites for char–steam and char–CO_2 reactions. They were defined as following:

$$a = \frac{n_{share}}{n_{CO_2}} \tag{11}$$

$$b = \frac{n_{share}}{n_{steam}} \tag{12}$$

Here, a and b are dimensionless parameters, representing the ratio of the amount of shared active sites to the total amount of active sites for the char–CO_2 reaction and char–steam reaction, respectively. n_{share} is the amount of shared active sites for the char–steam and char–CO_2 reactions. n_{CO_2} and n_{steam} represent the total amount of active sites for the char–CO_2 reaction and char–steam reaction, respectively.

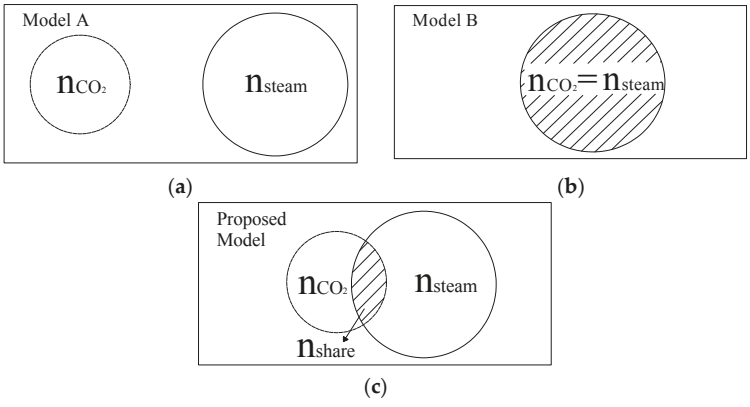

Figure 2. Models of char–CO_2–steam gasification: (**a**) Model A; (**b**) Model B; (**c**) Modified model.

Based on the assumption and these parameters, the overall reaction rate of the char–steam–CO_2 reaction can be derived as:

$$r = \frac{(1-a)K_aP_{CO_2}}{1+K_bP_{CO_2}+K_cP_{CO}} + \frac{(1-b)K_dP_{H_2O}}{1+K_eP_{H_2O}+K_fP_{H_2}} + \frac{aK_aP_{CO_2}+bK_dP_{H_2O}}{1+K_bP_{CO_2}+K_cP_{CO}+K_eP_{H_2O}+K_fP_{H_2}} \tag{13}$$

It was noteworthy that the proposed model (Equation (13)) was the same as Model A (Equation (9)) in the case of $a = b = 0$ ($n_{share} = 0$), while the proposed model was the same as Model B (Equation (10)) in the case of $a = b = 1$ ($n_{share} = n_{CO_2} = n_{steam}$).

3.2. Validation of the Modified Model

3.2.1. Kinetic Parameters of Char Gasification with Sole Gasifying Agent

In this study, the initial gasification rate (r_0) was used as a representative. The concentrations or partial pressures of H_2 and CO were very low and can be neglected at the initial stage of gasification. Therefore, P_{H_2} and P_{CO} were not shown in this study.

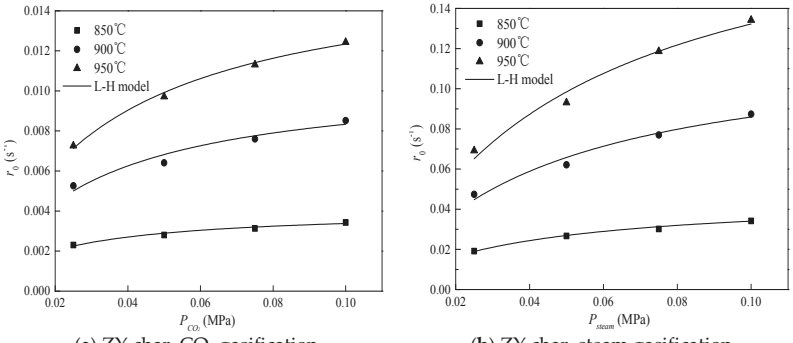

(**a**) ZY char–CO_2 gasification (**b**) ZY char–steam gasification

Figure 3. Effect of steam–CO_2 partial pressure on gasification rate.

Figure 3 shows the initial rate of ZY char gasification with a sole gasifying agent as a function of the partial pressure of the gasifying agent (steam/CO_2) and gasification temperature. It was evident that the initial gasification rate of ZY char depended strongly on temperature and steam/CO_2 partial pressure. The initial gasification rate of ZY char increased as the temperature and steam/CO_2 partial pressure increased. Moreover, it is shown in Figure 3 that the L–H model (the fitted line) fitted the experimental data well. In addition, the rate of steam gasification was faster than that of CO_2 gasification when the gasification temperature was fixed. These phenomena were also observed for the other two chars. The kinetic parameters (K_i, A_i, E_i) were determined by the L–H model and the results are listed in Table 2. The activation energies of tested char samples were similar to those reported in the literature [15,16].

Table 2. Kinetic parameters of char–CO_2 and char–steam reactions.

K_i	SF Char		ZY Char		PC Char	
	A_i	E_i (kJ/mol)	A_i	E_i (kJ/mol)	A_i	E_i (kJ/mol)
K_a	2.02×10^7	161.9	1.69×10^4	105.4	1.28×10^6	149.8
K_b	9.50×10^{-3}	−78.6	0.14	−54.3	4.88	−32.0
K_d	4.78×10^6	131.1	6.07×10^7	165.0	1.08×10^7	168.6
K_e	0.21	−51.3	0.11	−52.0	1.90×10^{-4}	−101.1

3.2.2. Kinetic Parameters of Char Gasification with Gasifying Agent Mixture

Initial rates of SF char gasification with a mixture of steam and CO_2 are presented in Figure 4.

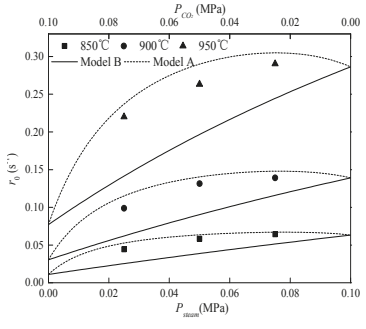

Figure 4. Comparison of experimental data and two conventional models.

In each experiment, the total system pressure was 0.100 MPa. The initial gasification rate of SF char increased as steam partial pressure increased or as CO_2 partial pressure decreased. In addition, the measured gasification rates were always a little lower than the gasification rates predicted by Model A and much higher than the gasification rates predicted by Model B. This means that char–CO_2 and char–steam reactions neither absolutely occur at separate active sites nor absolutely occur at common active sites. Thus, it can be inferred that char–CO_2 and char–steam reactions share active sites partially.

In order to evaluate the interactions by the char–CO_2–steam reaction accurately, the modified model was employed. Comparisons between experimental data and predictions by the modified model are shown in Figure 5.

For these three chars, the good agreement between experimental data and predictions confirmed the validity of the modified model. Parameters [*a*,*b*] were obtained by the fitting results and were equal to [0.47,0.25], [0.83,0.21], and [1.00,0.15] for SF char, ZY char, and PC char, respectively. The results shows that parameters [*a*,*b*] were constants and hardly varied with gasification temperature. For PC char, parameter *a* was equal to 1, but parameter *b* was not. This means that all active sites for char–CO_2 gasification were shared by steam gasification, but many active sites for char–steam gasification were not shared by CO_2 gasification. It is also noteworthy that the value of parameter *a* was always higher than that of parameter *b* for each char. It can be inferred that the total amount of active sites for steam gasification was larger than that for CO_2 gasification, based on the assumption of Equations (11) and (12). This result can also explain why rates of steam gasification were always faster than those of CO_2 gasification.

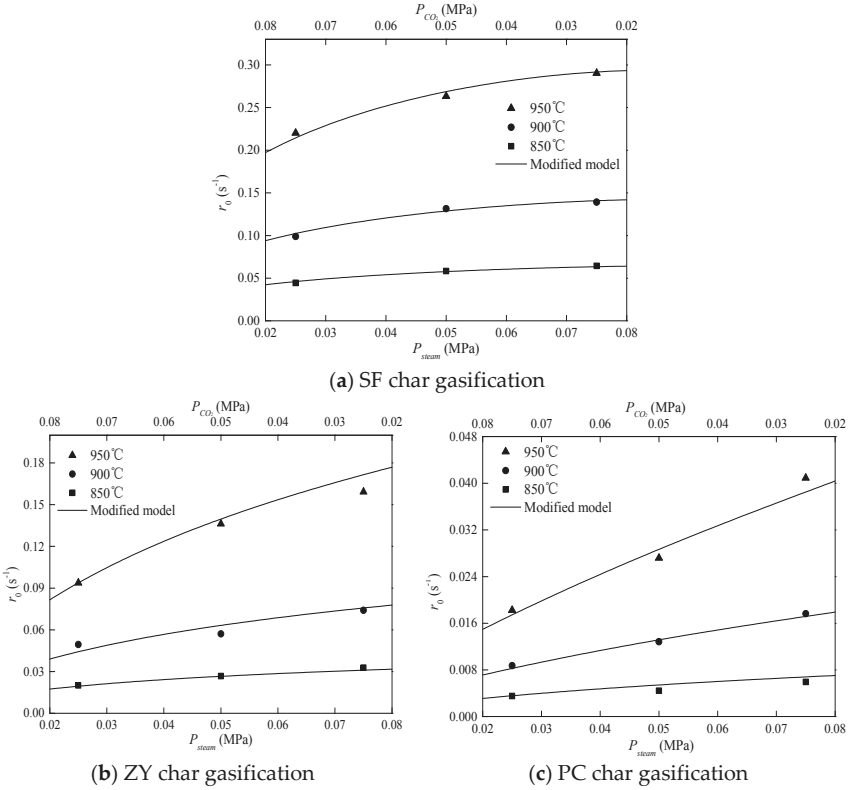

(**a**) SF char gasification

(**b**) ZY char gasification

(**c**) PC char gasification

Figure 5. Comparison of experimental data and the modified model.

3.3. Correlations between Chemisorption Quantity and Model Parameters [a,b]

Indeed, active sites play a pivotal role in gasification [26,27], so an experimental method of chemisorption was proposed to quantity the amount of active sites in previous work [23]. Molina et al. [23] found that C_w was related to the presence of the organic components (carbon active sites) of the char, and C_s was related to the presence of the inorganic matter (catalytic active sites) of the char. As shown in Figure 1, C_w, C_s, and C_t can be obtained by the chemisorption experiment. Table 3 lists the chemisorption parameters of the tested chars. For each char, the value of C_s was higher than that of C_w for CO_2 chemisorption, and the opposite trend was observed for steam chemisorption. It was indicated that the catalytic (mineral) matter possessed strong ability to withhold CO_2 molecules. In addition, for all these chars, the values of C_t and C_w for steam chemisorption were always higher than those for CO_2 chemisorption. This means that the total quantity of active sites and the quantity of carbon active sites for char–steam reactions were always more than those for char–CO_2 reactions. This result was in accordance with the result obtained by the modified model.

Table 3. Chemisorption parameters of tested chars.

Samples	CO_2 Chemisorption			Steam Chemisorption			$C_w(H_2O)/C_w(CO_2)$	$C_s(H_2O)/C_s(CO_2)$	$C_t(H_2O)/C_t(CO_2)$
	C_w	C_s	C_t	C_w	C_s	C_t			
SF char	1.127	1.298	2.425	2.069	0.463	2.531	1.84	0.36	1.04
ZY char	0.979	3.646	4.625	4.295	0.567	4.862	4.39	0.16	1.05
PC char	0.506	1.735	2.241	3.556	0.446	4.002	7.03	0.28	1.78

In order to further study the correlation between chemisorption quantity and parameters [*a*,*b*], an equation was derived from the assumption of Equations (11) and (12). It can be expressed by following.

$$n_{share} = bn_{steam} = an_{CO_2} \Rightarrow \frac{n_{steam}}{n_{CO_2}} = \frac{a}{b} \tag{14}$$

According to this equation, the ratio of the total amount of active sites for steam gasification to that for CO_2 gasification can be calculated. The ratio values for SF char, ZY char, and PC char were 1.88, 3.95, and 6.67, respectively. The ratio of C_w of steam chemisorption to that of CO_2 chemisorption can also be seen in Table 3. The result shows that values of $C_w(H_2O)/C_w(CO_2)$ for SF char, ZY char, and PC char were 1.84, 4.39, and 7.03, respectively. These values were nearly the same as the values of a/b. However, the values of $C_s(H_2O)/C_s(CO_2)$ or $C_t(H_2O)/C_t(CO_2)$ were absolutely not equal to those of a/b. This phenomenon indicates that parameters [*a*,*b*] depended on the presence of the organic components (carbon active sites) of the char and showed little relationship with others factors, including the gasification process and conditions. Based on the principle of gasification, all reactions were initiated at the carbon surface. In addition, carbon active sites consisted of three aspects: nascent sites attached to the aromatic clusters, carbon atoms bonded to heteroatoms, and the edge carbon atoms [24], which were all chemically unstable and could easily be reacted with gasifying agents. This indicates that the gasifying agents can easily occupy the carbon active sites and react with the char on the carbon active sites. Hence, it was concluded that the kinetic parameters [*a*,*b*] mainly depended on the carbon active sites of the char. Moreover, the results also validate the modified model proposed in this study.

4. Conclusions

The gasification of three different chars under a mixture of steam and CO_2 was carried out using a TGA. Initial gasification rates of these three chars all increased as steam partial pressure increased or as CO_2 partial pressure decreased. Two conventional gasification models were used to fit the experimental data but showed great difficulties in exactly describing the interactions in the

char–steam–CO_2 reaction. A modified model was proposed based on shared active sites and can exactly predict the gasification rates of these three char gasification with a mixture of steam and CO_2. The results indicate that char–CO_2 and char–steam reactions shared active sites partially and also show that two new parameters in the modified model were constants and did not vary with gasification conditions. In addition, the results from chemisorption tests show that these two parameters just depended on the carbon active sites of the char and thus validated the modified model.

Acknowledgments: This work has been supported by the National Natural Science Foundation of China (21376081; 21676091).

Author Contributions: Xia Liu and Juntao Wei designed the experiments and prepared the manuscript; Wei Huo performed the experiments and analyzed the data; Guangsuo Yu led the project and research.

Conflicts of Interest: The authors declare no conflict of interest.

Nomenclature

A_i	frequency factor for L–H model, $s^{-1}MPa^{-1}$ (I = *a*,*d*), MPa^{-1} (I = *b*,*c*,*e*,*f*)
A	parameter for the modified model, dimensionless
b	parameter for the modified model, dimensionless
C_s	the quantity of strong chemisorption, mg/mg-char
C_t	the total quantity of chemisorption, mg/mg-char
C_w	the quantity of weak chemisorption, mg/mg-char
E_i	activation energy for L–H model, kJ/mol
K_i	adsorption constant for L–H model, $s^{-1}MPa^{-1}$ (I = *a*,*d*), MPa^{-1} (I = *b*,*c*,*e*,*f*)
n_{CO_2}	the total amount of active sites for char–CO_2 reaction
n_{share}	the amount of shared active sites for char–steam and char–CO_2 reactions
n_{steam}	the total amount of active sites for char–steam reaction
P	the partial pressure of H_2/CO/steam/CO_2, MPa
r_0	initial gasification rate, s^{-1}
T	the thermodynamic temperature, K
w_0	the initial mass of char, wt. %
w_{ash}	the sample mass at the end of char gasification, wt. %
w_t	the sample mass at the gasification time of t, wt. %
x	carbon conversion

References

1. Kumar, A.; Jones, D.D.; Hanna, M.A. Thermochemical biomass gasification: A review of the current status of the technology. *Energies* **2009**, *2*, 556–581. [CrossRef]
2. Zaccariello, L.; Mastellone, M.L. Fluidized-bed gasification of plastic waste, wood, and their blends with coal. *Energies* **2015**, *8*, 8052–8068. [CrossRef]
3. Roberts, D.G.; Hodge, E.M.; Harris, D.J.; Stubington, J.F. Kinetics of Char Gasification with CO_2 under Regime II Conditions: Effects of Temperature, Reactant, and Total Pressure. *Energy Fuels* **2010**, *24*, 5300–5308. [CrossRef]
4. Bhatia, S.K.; Perlmutter, D.D. A random pore model for fluid-solid reactions: I. Isothermal, kinetic control. *AIChE J.* **1980**, *26*, 379–385. [CrossRef]
5. Bhatia, S.K.; Perlmutter, D.D. A random pore model for fluid-solid reactions: II. Diffusion and transport effects. *AIChE J.* **1981**, *27*, 247–254. [CrossRef]
6. Gavals, G.R. A random capillary model with application to char gasification at chemically controlled rates. *AIChE J.* **1980**, *26*, 577–585. [CrossRef]
7. Wen, C.Y. Noncatalytic heterogeneous solid-fluid reaction models. *Ind. Eng. Chem.* **1968**, *60*, 34–54. [CrossRef]
8. Bliek, A.; Lont, J.C.; Van Swaaij, W.P.M. Gasification of coal-derived chars in synthesis gas mixtures under intraparticle mass-transfer-controlled conditions. *Chem. Eng. Sci.* **1986**, *41*, 1895–1909. [CrossRef]
9. Kirtania, K.; Joshua, J.; Kassim, M.A.; Bhattacharya, S. Comparison of CO_2 and steam gasification reactivity of algal and woody biomass chars. *Fuel Process. Technol.* **2014**, *117*, 44–52. [CrossRef]

10. Ren, L.; Yang, J.; Gao, F.; Yan, J. Laboratory study on gasification reactivity of coals and petcokes in CO_2/steam at high temperatures. *Energy Fuels* **2013**, *27*, 5054–5068. [CrossRef]
11. Jayaraman, K.; Gökalp, I.; Jeyakumar, S. Estimation of synergetic effects of CO_2 in high ash coal-char steam gasification. *Appl. Therm. Eng.* **2017**, *110*, 991–998. [CrossRef]
12. Koba, K.; Ida, S. Gasification reactivities of metallurgical cokes with carbon dioxide, steam and their mixtures. *Fuel* **1980**, *59*, 59–63. [CrossRef]
13. Muhlen, H.J.; Van Heek, K.H.; Juntgen, H. Kinetic studies of steam gasification of char in the presence of H_2, CO_2 and CO. *Fuel* **1985**, *64*, 944–949. [CrossRef]
14. Roberts, D.G.; Harris, D.J. Char gasification in the mixtures of CO_2 and H_2O: Competition and inhibition. *Fuel* **2007**, *86*, 2672–2678. [CrossRef]
15. Huang, Z.M.; Zhang, J.S.; Zhao, Y.; Zhang, H.; Yue, G.X.; Suda, T.; Narukawa, M. Kinetic studies of char gasification by steam and CO_2 in the presence of H_2 and CO. *Fuel Process. Technol.* **2010**, *91*, 843–847. [CrossRef]
16. Everson, R.C.; Neomagus, H.W.J.P.; Kasaini, H.; Njapha, D. Reaction kinetics of pulverized coal-chars derived from inertinite-rich coal discards: Gasification with carbon dioxide and steam. *Fuel* **2006**, *85*, 1076–1082. [CrossRef]
17. Li, F.H.; Yan, Q.X.; Huang, J.J.; Zhao, J.T.; Fang, Y.T.; Wang, J.F. Lignite-char gasification mechanism in mixed atmospheres of steam and CO_2 at different pressures. *Fuel Process. Technol.* **2015**, *138*, 555–563. [CrossRef]
18. Chen, C.; Wang, J.; Liu, W.; Zhang, S.; Yin, J.S.; Luo, G.Q.; Yao, H. Effect of pyrolysis conditions on the char gasification with the mixtures of CO_2 and H_2O. *Proc. Combust. Inst.* **2013**, *34*, 2453–2460. [CrossRef]
19. Umemoto, S.; Kajitani, S.; Hara, S. Modeling of coal char gasification in coexistence of CO_2 and H_2O considering sharing of active sites. *Fuel* **2013**, *103*, 14–21. [CrossRef]
20. Wei, J.T.; Guo, Q.H.; Ding, L.; Yoshikawa, K.; Yu, G.S. Synergy mechanism analysis of petroleum coke and municipal solid waste (MSW)-derived hydrochar co-gasification. *Appl. Energy* **2017**, *206*, 1354–1363. [CrossRef]
21. Guizani, C.; Jeguirim, M.; Valin, S.; Limousy, L.; Salvador, S. Biomass chars: The effects of pyrolysis conditions on their morphology, structure, chemical properties and reactivity. *Energies* **2017**, *10*, 796. [CrossRef]
22. Jing, X.L.; Wang, Z.Q.; Zhang, Q.; Yu, Z.L.; Li, C.Y.; Huang, J.J.; Fang, Y.T. Evaluation of CO_2 gasification reactivity of different coal rank chars by physicochemical properties. *Energy Fuels* **2013**, *27*, 7287–7293. [CrossRef]
23. Molina, A.; Montoya, A.; Mondragon, F. CO_2 strong chemisorption as an estimate of coal char gasification reactivity. *Fuel* **1999**, *78*, 971–977. [CrossRef]
24. Xu, K.; Hu, S.; Su, S.; Xu, C.F.; Sun, L.S.; Shuai, C.; Jiang, L.; Xiang, J. Study on char surface active sites and their relationship to gasification reactivity. *Energy Fuels* **2013**, *27*, 118–125. [CrossRef]
25. Takarada, T.; Ida, N.; Hioki, A.; Kanbara, S.; Yamamoto, M.; Kato, K. Estimation of gasification of coal chars in steam-nitrogen and carbon dioxide–nitrogen atmospheres. *J. Fuel Soc. Jpn.* **1988**, *67*, 1061–1069. [CrossRef]
26. Huttinger, K.J.; Nill, J.S. A method for the determination of active sites and true activation energies in carbon gasification: (II) Experimental results. *Carbon* **1990**, *4*, 457–465. [CrossRef]
27. Miura, K.; Hashimoto, K.; Silveston, P.L. Factors affecting the reactivity of coal chars during gasification, and indexes representing reactivity. *Fuel* **1989**, *68*, 1461–1475. [CrossRef]

© 2017 by the authors. Licensee MDPI, Basel, Switzerland. This article is an open access article distributed under the terms and conditions of the Creative Commons Attribution (CC BY) license (http://creativecommons.org/licenses/by/4.0/).

energies

MDPI

Article

Energy Recovery Efficiency of Poultry Slaughterhouse Sludge Cake by Hydrothermal Carbonization

Seung-Yong Oh and Young-Man Yoon *

Biogas Research Center, Hankyong National University, 327 Jungang-ro, Anseong-si, Gyeonggi-do 17579, Korea; yong8109@hanmail.net

* Correspondence: yyman@hknu.ac.kr; Tel.: +82-31-670-5665

Received: 11 October 2017; Accepted: 13 November 2017; Published: 16 November 2017

Abstract: Hydrothermal carbonization (HTC) is a promising technology used for bioenergy conversion from bio-wastes such as sewage sludge, livestock manure, and food waste. To determine the optimum HTC reaction temperature in maximizing the gross energy recovery efficiency of poultry slaughterhouse sludge cake, a pilot-scale HTC reactor was designed and operated under reaction temperatures of 170, 180, 190, 200 and 22 °C. During the HTC reaction, the gross energy recovery efficiency was determined based on the calorific value of the HTC-biochar and ultimate methane potential of the HTC-hydrolysate. The poultry slaughterhouse sludge cake was assessed as a useful source for the bioenergy conversion with a high calorific value of approximately 27.7 MJ/kg. The calorific values of the HTC-biochar increased from 29.6 MJ/kg to 31.3 MJ/kg in accordance with the change in the reaction temperature from 170 °C to 220 °C. The ultimate methane potential of the HTC-hydrolysate was 0.222, 0.242, 0.237, 0.228 and 0.197 Nm^3/kg-COD_{added} for the reaction temperatures of 170, 180, 190, 200 and 220 °C, respectively. The potential energy of feedstock was 4.541 MJ/kg. The total gross energy recovery (GER_{total}) was 4318 MJ/kg, of which the maximum value in the HTC reaction temperature was attained at 180 °C. Thus, the optimum temperature of the HTC reaction was 180 °C with a maximum GER_{total} efficiency of 95.1%.

Keywords: hydrothermal carbonization; anaerobic digestion; poultry slaughterhouse; sludge cake; energy recovery efficiency

1. Introduction

In Korea, meat consumption (e.g., beef, pork, and poultry) has steeply increased, with food consumption patterns changing with economic growth. In particular, the poultry industry has been growing about 5% each year since 2000, and 993 million poultry heads were slaughtered in 2016. Due to the growth of the poultry industry, several environmental problems have occurred relating to the disposal of wastewater treatment sludge and various poultry processing residues (e.g., blood, feathers, bones) generated from the poultry slaughterhouse [1]. In general, poultry processing residues can be utilized as feedstock for animal feed or compost. However, sludge cake containing moisture above 80% is disposed of after incineration due to the prohibition of direct landfill and ocean disposal, although a high amount of drying energy is needed for the incineration of sludge cake [2]. Nowadays, the interest in energy conversion of sludge waste is increasing due to high sludge disposal costs and limited alternative disposal methods. Poultry slaughterhouses sludge cake is characterized by a high solid content that is composed of protein and fat [3–5]. Hence, sludge cake is considered an effective substrate for anaerobic digestion. However, it is difficult to be fed into conventional anaerobic digesters due to its high solid content [5]. Also, high ammonium nitrogen produced from protein degradation and long chain fatty acids from fat degradation can cause inhibition during the anaerobic digestion process [6].

For these reasons, hydrothermal carbonization (HTC) has recently emerged as an alternative technology for the energy conversion of the slaughterhouse sludge cake. HTC technology is a thermo-chemical process converting biomass to a coal-like material with higher carbon content [7,8]. The energy conversion of biomass by HTC technology has several advantages compared to common biological technology, such as anaerobic digestion. The HTC process requires a short operational time within hours, unlike that of biological processes that require 10 days or more [9]. In addition, waste biomass containing toxic substances cannot be biologically converted to bioenergy, and problems related to hygiene can be of concern when the byproducts generated from biological processing are further utilized. However, the high operational temperatures of the HTC process can decompose potentially toxic organic contaminants and sterilize pathogens. Because of these advantages, HTC technology could be a promising technology for the treatment of waste biomass such as sewage sludge, livestock manure, and food waste [10–12].

The HTC process is mainly composed of a relatively simple closed vessel reactor, containing the wet biomass. The HTC reactor is heated to 170–250 °C and maintained at the saturated vapor pressure that is formed in accordance with the given reaction temperature. During the HTC reaction of wet biomass, the oxygen and hydrogen content of feeding material is reduced, and the solid phase (biochar), the liquid phase (hydrothermal hydrolysate) and a small amount of gas (mainly carbon dioxide) are produced [13,14]. These products are attained by mechanisms including hydrolysis, dehydration, decarboxylation, polymerization and aromatization [8,15]. The solid phase, referred as biochar, can be easily separated due its dewatering property, and utilized as a solid fuel of high calorific value. The hydrothermal hydrolysate generated after the HTC processing requires further treatment since it contains a high amount of soluble organic material and ammonium nitrogen. Recently, anaerobic digestion is preferred for the treatment of hydrothermal hydrolysate in terms of energy recovery efficiency from biomass. In particular, for the HTC reaction, organic matter is solubilized by the hydrolysis reaction and the efficiency of anaerobic digestion can be improved [16,17]. The HTC technology has been studied for a wide range of biomass feedstocks, mainly focusing on herbal and woody biomasses with high contents of lignin, cellulose and hemicellulose, generated from the agricultural sector [13,18,19]. In the case of poultry slaughterhouse sludge cake mainly composed of protein and fat, the HTC process was not so widely investigated, but several studies focused on the properties of solid product, energy recovery rate, biochar yields and its combustion characteristic for slaughterhouse sludge cake. In particular, these studies have only focused on the determination of HTC reaction conditions for the energy recovery and their impacts on the quality of final product (HTC-biochar) without considering the appropriate treatment methods on the HTC-hydrolysate generated as the byproduct during the HTC reaction of sludge cake.

This research was focused on the assessment of total energy recovery from the HTC-biochar and HTC-hydrolysate generated from the HTC reaction with slaughterhouse sludge cake. The goal of this study was to determine the optimum HTC reaction temperature in maximizing the gross energy recovery efficiency from poultry slaughterhouse sludge cake in order to improve the operational efficiency of the HTC process. For this purpose, the energy conversion processes of HTC and anaerobic digestion were proposed. The gross energy recovery efficiency was determined based on the calorific value of the HTC-biochar and ultimate methane potential of the HTC-hydrolysate during the HTC reaction of poultry slaughterhouse sludge cake.

2. Materials and Methods

2.1. Materials

A sludge cake was collected from the wastewater treatment plant at the poultry slaughterhouse facility (Jincheon, South Korea), which has a slaughtering capacity of 300,000 heads per day. A total of 1500 m^3/day wastewater is generated and treated by the activated sludge process, and approximately 30 ton of sludge cake is generated daily.

2.2. Proposed Energy Conversion System

The energy conversion system proposed in this study is shown in Figure 1. The activated sludge generated from the wastewater treatment plant of the poultry slaughterhouse is dewatered using solid/liquid separation equipment (a filter press) and sludge cake is fed into the HTC reactor. During the HTC reaction, the organic solid of the sludge cake is fixed as the carbonized solid of high carbon content and solubilized as a lower molecular compound at the same time. Thereafter, the effluent of the HTC reactor is separated into liquid and solid fractions using filter pressing. The solid fraction (HTC-biochar) is utilized as solid fuel for the incineration boiler, and the liquid fraction (HTC-hydrolysate), with its high soluble organic and nitrogen contents, is used for the high performance anaerobic digester. Lastly, digestate discharged from the anaerobic digester is treated at the wastewater treatment plant. This system is able to simultaneously produce solid fuel and biogas through the stepwise process of thermochemical decomposition and biological degradation of organic solid waste.

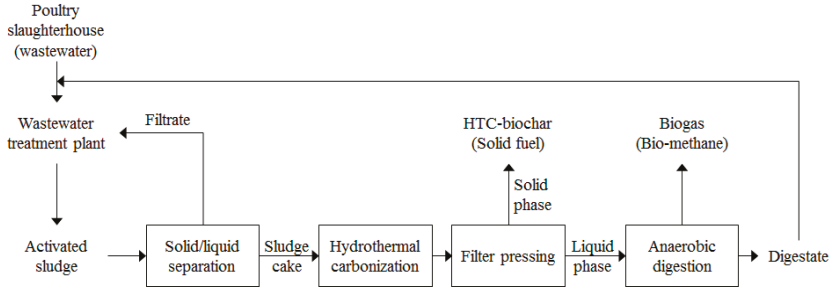

Figure 1. Scheme of the HTC (Hydrothermal carbonization) system for the energy conversion of sludge cake generated at the poultry slaughterhouse wastewater treatment plant.

2.3. Hydrothermal Carbonization

In order to assess the energy yield from the production of the HTC-biochar for several HTC reaction temperatures, a batch-type HTC reactor was designed for the thermochemical treatment of sludge cake (Figure 2). The HTC reactor is a closed system with no potential heat loss via vaporization and condensation loss. The designed HTC reactor has a working volume of 1.5 kg and is equipped with electric heater, temperature sensor, and pressure gauge. The reactor was equipped with a heating coil. A temperature sensor and pressure gauge were inserted into the reactor to monitor inner temperature and a saturated vapor pressure during the HTC reaction. For the HTC reaction test, 1.5 kg of sludge cake was directly placed without additional processing water and covered with an airtight sealant. Setting temperatures were 170, 180, 190, 200 and 220 °C. When each temperature was reached to the set point, each HTC reactor was maintained at the isothermic condition for 60 min. The inner vapor pressures were then maintained at 1.05 MPa at 170 °C, 1.18 MPa at 180 °C, 1.42 MPa at 190 °C, 1.78 MPa at 200 °C, and 2.51 MPa at 220 °C. At the end of the HTC reaction, the reactor was cooled to room temperature using a chiller. The effluent of the HTC reactor was separated into HTC-biochar and HTC-hydrolysate using a filter press. A weight loss of 5–10% occurred due to moisture absorption into the filtering cloth. However, for the theoretical valuation, moisture loss was included in the HTC-hydrolysate.

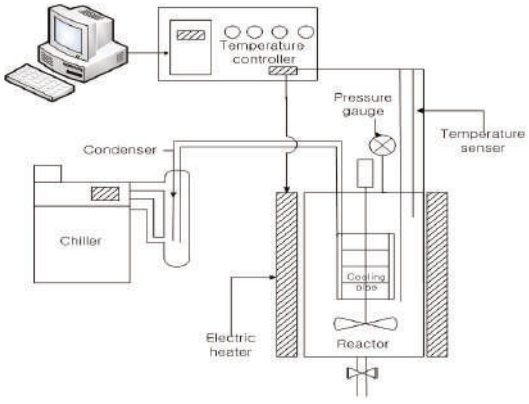

Figure 2. Schematic diagram of the lab-scale HTC batch reactor.

2.4. Methane Production Potential of HTC-Hydrolysate

To assess methane production of the HTC-hydrolysate, a batch type anaerobic reactor was operated under mesophilic conditions (38 °C). Anaerobic inoculum in pig slurry was collected from a farm-scale anaerobic digester located in Anseong city, South Korea. The chemical properties of the inoculum are shown in Table 1.

Table 1. Chemical characteristics of inoculum used in the methane potential assay of HTC-hydrolysate.

Sample	pH	TS [1]	VS [2]	COD_{Cr} [3]	TN [4]	NH_4^+-N	Alkalinity
	(-)	(wt. %, w.b. [5])	(wt. %, w.b.)	(g/L)	(wt. %, w.b.)	(wt. %, w.b.)	(g/L as $CaCO_3$)
Inoculum	8.2 (0.0) [6]	2.6 (0.0)	1.4 (0.0)	25.2 (0.1)	0.4 (0.0)	0.3 (0.0)	19.2 (0.3)

[1] Total solid, [2] Volatile solid, [3] Total chemical oxygen demand, [4] Total nitrogen, [5] Wet basis, [6] Standard deviation (n = 3).

In order to remove any remaining biodegradable fraction, the inoculum for methane production potential analysis of the HTC-hydrolysate was kept under the mesophilic condition at 38 °C for one week. The ratio of substrate to inoculum in all anaerobic batch reactors was equal to 0.3 ($g\text{-}VS_{substrate}/g\text{-}VS_{inoculum}$). A working volume for anaerobic batch fermentation was 80 mL of a 160 mL serum bottle. The head space of the serum bottle was filled with N_2 gas and sealed with a butyl rubber stopper. The anaerobic batch reactors for each sample and blank were incubated for up to 96 days in the convection incubator and manually mixed each day during the fermentation period. Methane production potential was calculated as the chemical oxygen demand (COD) content. Methane production potentials of the samples were corrected from the blank value and calibration was done under standard temperature and pressure (STP) conditions. To interpret the progress of cumulative methane production, the parallel first-order kinetic model Equation (1) was employed to fit the cumulative methane production data as in the following equation [20,21].

$$B_t = B_u\left\{1 - f_e e^{-k_1 t} - (1 - f_e)e^{-k_2 t}\right\} \quad (1)$$

where B_t (mL) is the amount of methane production at time t, B_u (mL) is the amount of ultimate methane production, f_e (%, g/g) is the organic distribution constant for two first-order kinetics, and k_1 and k_2 are the kinetic constants in the parallel first-order kinetics. This model considers that the degradation of organic matter is carried out in two stages. In addition, f_e distributes the characteristics of the two types of substrates with different reaction rates under anaerobic conditions, and k_1 and k_2 indicate the first-order kinetics constants for the first and the second organic degradation stages.

The degree of COD degradation (COD_{deg}) of the HTC-hydrolysate was defined as the amount of methane produced during the anaerobic fermentation of the HTC-hydrolysate for the theoretical methane potential, as shown in Equation (2) [22].

$$COD_{deg} = \frac{V_{biogas} \times C_{methane}}{320 \times m_{substrate} \times COD_{substrate}} \times 100 \quad (2)$$

where V_{biogas} is the volume of biogas (mL/day in STP), $C_{methane}$ is the concentration of methane (%), $m_{substrate}$ is the amount of substrate added to the anaerobic reactor (mL), $COD_{substrate}$ is the COD of the substrate (g/mL), and 320 (mL/g-COD_{added} in STP) is the theoretical biochemical methane potential under practical conditions assuming that about 10% of COD added to the anaerobic reactor is consumed in the reformation of biomass.

2.5. Analysis

Total solids (TS), volatile solids (VS), pH, chemical oxygen demand (COD_{Cr}), total nitrogen (TN), ammonium nitrogen (NH_4^+-N) and alkalinity were determined based on standard methods [23]. Volatile fatty acid (VFA) concentrations were measured using a gas chromatograph (GC2010, Shimazhu Scientific Instrument, Inc., Columbia, MD, USA) equipped with a flame ionization detector with an automatic sampler. This chemical analysis was performed in three replicates. Element composition (C, H, N, O, S) was determined using an element analyzer (EA1108, Thermo Finnigan LLC, San Jose, CA, USA). The higher heating value (HHV) was measured by the Bomb calorimeter (AC-350, LECO Corporation, St. Joseph, MI, USA) for a dry sample. In the anaerobic batch reactor experiment, total gas production was measured daily for the first five days and then every two or three days, followed by the displacement of acidified brine solution in a burette and recording the volume of displaced solution after correcting for atmospheric pressure [24]. To investigate the gas composition, the CH_4 and CO_2 concentrations in the gas samples were determined using a gas chromatograph (Clarus 680, PerkinElmer, Inc., Waltham, MA, USA) equipped with a thermal conductivity detector and a HayeSepQ packed column (CRS, Inc., Louisville, KY, USA). The column was operated with helium carrier gas at a constant flow rate of 5 mL/min. The set temperatures of the injector, the oven, and the detector were 150 °C, 90 °C and 150 °C, respectively.

2.6. Efficiency Parameters

The energy recovery by the HTC was assessed using gross energy recovery GER, Equation (3), that was presented as the calorific value of the product (biochar and methane) by HHV. Net energy recovery NER, Equation (4), was calculated by subtracting the thermal energy consumed during the HTC reaction and the drying energy of HTC-biochar. The GER efficiency, Equation (6), of the product was estimated as the ratio of the $GER_{product}$ of the product and the gross energy potential $GEP_{feedstock}$, Equation (5), estimated from the HHV of the dried sludge cake. NER efficiency, Equation (7), was calculated using the ratio between the $NER_{product}$ and $GEP_{feedstock}$.

$$GER_{product} = \text{HHV of product} \quad (3)$$

$$NER_{product} = GER_{product} - \text{Thermal energy}_{HTC} - \text{Drying energy}_{biochar} \quad (4)$$

$$GEP_{feedstock} = \text{HHV of feedstock} \quad (5)$$

$$GER_{product}\ \text{efficiency}(\%) = \frac{GER_{product}\ (MJ)}{GEP_{feedstock}\ (MJ)} \times 100 \quad (6)$$

$$NER_{product}\ \text{efficiency}(\%) = \frac{NER_{product}\ (MJ)}{GEP_{feedstock}\ (MJ)} \times 100 \quad (7)$$

3. Results and Discussion

3.1. Physicochemical Properties of Sludge Cake

The physicochemical characteristics of the sludge cake generated from the slaughterhouse wastewater treatment plant are shown in Table 2. The physicochemical properties of the sludge cake used in this study were typically different from those of the reported agricultural biomass, such as corn silage, dry straw, cabbage residue, poultry manure, and bedding material. These types of agricultural biomass have a carbon content of 40.7–46.9% and oxygen content of 30.1–44.4%, and calorific values lie between the ranges of 17.8–19.6 MJ/kg [25]. The sludge cake used in this study showed a higher carbon content and lower oxygen content compared to the reported agricultural biomass. In addition, the calorific value was much higher than the reported agricultural biomass.

Table 2. Physicochemical properties of raw sludge cake.

Parameters	Sludge Cake	
Elemental composition (wt. %, d.b. [1])	C	61.9
	H	7.2
	O	5.3
	N	6.5
	S	0.0
	Ash	19.1
pH (-)	7.1 (0.0) [8]	
TS [2] (wt. %, w.b. [3])	16.4 (0.4)	
VS [4] (wt. %, w.b.)	13.9 (0.1)	
VS/TS (%)	84.8 (0.1)	
COD_{Cr} [5] (g/L)	208.2 (30.4)	
TN [6] (wt. %, w.b.)	11.0 (0.3)	
NH_4^+-N (wt. %, w.b.)	2.6 (0.2)	
Calorific value [7] (MJ/kg, d.b.)	27.7 (1.1)	

[1] Dry basis, [2] Total solid, [3] Wet basis, [4] Volatile solid, [5] Total chemical oxygen demand, [6] Total nitrogen, [7] Calorific value by higher heating value, [8] Standard deviation (n = 3).

3.2. Physicochemical Properties of HTC-Biochar and HTC-Hydrolysate

Table 3 shows the physicochemical properties of the products (HTC-biochar) from the HTC reaction. Output yields on a wet basis ranged from 23.8% to 37.7%, showing a decreasing trend as the reaction temperature increased. Solid yields on a dry basis showed a similar trend and the yields were 75.9%, 73.5%, 72.4%, 69.6% and 66.8% at 170, 180, 190, 200 and 220 °C, respectively. TS contents increased from 33.0% to 46.1%, and the ratios of VS to TS decreased from 88.2% to 85.7% with increase in the reaction temperature. These results imply that the rise of the reaction temperature caused an increase in the dewater ability of the product. The O/C atomic ratios of the HTC-biochar did not show any significant changes between 170–200 °C, and fell to 0.06 for the reaction temperature of 220 °C. The H/C atomic ratios decreased from 1.87 to 1.70 with the increase of reaction temperature. The HTC process has similar reaction characteristics as the slow pyrolysis, which is characterized by gradual heating over a wide range of temperatures to produce biochar [26]. The yield and characteristics of pyrolysis products are influenced by different factors, including biomass feedstock and pyrolysis operating parameters (solid residence time, vapor residence time, temperature, heating rate, and carrier gas flow rate). Biochars, which are produced at a slow pyrolysis rate of forest residues, switchgrass, and the solid fraction of pig manure, have elemental characteristics with an O/C ratio between 0.1 and 0.3 and H/C ratio between 0.5 and 0.9 [27]. The calorific values obtained were 29.6, 30.1, 30.2, 30.8 and 31.3 MJ/kg for the reaction temperatures of 170, 180, 190, 200 and 220 °C, respectively, and the energy densification increased from 1.07 for 170 °C to 1.13 for 220 °C. These increased calorific values improve the quality of the HTC-biochar as biofuel. Generally, this effect can be attributed to reaction mechanisms, including hydrolysis, dehydration, decarboxylation [8,15]. The hydrolysis reaction can

convert macro-molecules, such as proteins and lipids, to smaller molecules, and the decarboxylation and dehydration reactions that release H_2O and CO_2 improve the fuel properties of the HTC-biochar [28–30]. According to Qian et al. [31], those colorific values of HTC-biochar are comparable to high quality coal, which typically has a calorific value of 25–35 MJ/kg. Anderson et al. [32] also reported that biochars derived from woody plants had higher calorific values. In a recent study, bamboo sawdust biochar pyrolysis at 500 °C had a high colorific value of 32.4 MJ/kg [33], which was comparable to the calorific value (31.2 MJ/kg for 220 °C) of HTC-biochar in this study. Therefore, the HTC technique is effective in creating a high quality biochar from sludge cake at lower temperatures as compared to lignocellulosic feedstocks. The physicochemical properties of HTC-hydrolysate are shown in Table 4. The output yields of the HTC-hydrolysate were 62.3%, 69.5%, 69.0%, 74.6% and 76.2% for the reaction temperatures of 170, 180, 190, 200 and 220 °C, respectively. The COD content of the HTC-hydrolysate was in the range of 97.9–103.4 g/L. The alkalinity decreased from 9.5 g/L to 8.6 g/L for the reaction temperatures between 170–180 °C and increased to 12.1 g/L for the reaction temperature of 220 °C. Essentially, the HTC reaction is a simultaneous reaction of hydrolysis and carbonization [34]. Therefore, the COD contained in the HTC-hydrolysate may be composed of a soluble substance caused by the hydrolysis reaction during the HTC reaction. In addition, alkalinity appeared to be caused by the decarboxylation reaction during the HTC reaction [35]. The physicochemical properties of HTC-hydrolysate obtained from sludge cake are typically characterized by a high moisture content over 90% compared to the bio oil produced by pyrolysis of lignocellulosic feedstocks with less than 10% moisture content [36]. The high moisture content of HTC-hydrolysate is primarily affected by the moisture content of feedstock, which attenuates the severity of thermo-chemical reaction.

Table 3. Physicochemical properties of HTC-biochar produced at different HTC reaction temperatures.

Parameters		HTC Reaction Temperatures				
		170 °C	**180 °C**	**190 °C**	**200 °C**	**220 °C**
Output yield [1] (wt. %, w.b. [2])		37.7 (0.1) [10]	30.5 (0.1)	31.0 (0.1)	25.4 (0.1)	23.8 (0.1)
Solid yield [3] (wt. %, d.b. [4])		75.9 (0.2)	73.5 (0.2)	72.4 (0.2)	69.6 (0.2)	66.8 (0.3)
Elemental composition (wt. %, d.b.)	C	59.9	58.9	57.9	59.2	60.8
	H	9.4	8.9	8.4	8.6	8.7
	O	7.0	6.2	6.9	6.7	5.0
	N	4.1	3.9	4.4	3.7	3.8
	S	0.0	0.0	0.0	0.0	0.0
	Ash	19.6	22.1	22.4	21.8	21.7
Atomic ratio (-)	O/C	0.09	0.08	0.09	0.09	0.06
	H/C	1.87	1.81	1.73	1.73	1.70
pH (-)		6.2 (0.0)	5.9 (0.0)	5.6 (0.0)	6.0 (0.0)	6.1 (0.0)
TS [5] (wt. %, w.b.)		33.0 (0.7)	39.5 (0.1)	38.3 (0.1)	44.8 (0.7)	46.1 (0.4)
VS [6] (wt. %, w.b.)		29.1 (0.8)	34.5 (0.0)	33.5 (0.0)	39.0 (0.5)	39.5 (0.1)
VS/TS (%)		88.2 (0.5)	87.4 (0.3)	87.4 (0.2)	87.0 (0.1)	85.7 (0.3)
TN [7] (g/kg)		14.0 (0.7)	11.5 (0.7)	10.5 (0.5)	12.0 (1.6)	12.5 (1.5)
NH_4^+-N (g/kg)		3.2 (0.1)	3.2 (0.3)	3.8 (0.2)	3.6 (0.1)	3.8 (0.0)
Calorific value [8] (MJ/kg, d.b.)		29.6 (0.4)	30.1 (0.1)	30.2 (0.2)	30.8 (0.1)	31.3 (0.4)
Energy densification [9]		1.07 (0.02)	1.09 (0.01)	1.09 (0.01)	1.11 (0.00)	1.13 (0.01)

[1] Mass of output/mass of feedstock, [2] Wet basis, [3] Mass of solid in product/mass of solid in feedstock, [4] Dry basis, [5] Total solid, [6] Volatile solid, [7] Total nitrogen, [8] Calorific value by higher heating value, [9] Calorific value of product/calorific value of feedstock, [10] Standard deviation (n = 3).

Table 4. Physicochemical properties of HTC-hydrolysate produced at different HTC reaction temperature.

Parameters	HTC Reaction Temperatures				
	170 °C	**180 °C**	**190 °C**	**200 °C**	**220 °C**
Product yield [1] (wt. %, w.b. [2])	62.3 (0.1) [8]	69.5 (0.2)	69.0 (0.2)	74.6 (0.2)	76.2 (0.4)
pH	6.2 (0.0)	5.9 (0.0)	5.6 (0.0)	6.0 (0.0)	6.1 (0.0)
TS [3] (wt. %, w.b.)	6.1 (0.1)	6.6 (0.1)	6.2 (0.01)	6.9 (0.1)	7.2 (0.2)

Table 4. *Cont.*

Parameters	HTC Reaction Temperatures				
	170 °C	**180 °C**	**190 °C**	**200 °C**	**220 °C**
VS [4] (wt. %, w.b.)	5.9 (0.1)	6.3 (0.1)	6.0 (0.0)	6.7 (0.1)	6.9 (0.1)
VS/TS (%)	96.7 (0.1)	95.5 (0.2)	96.8 (0.2)	97.1 (0.0)	95.8 (0.9)
TN [5] (g/L)	9.7 (0.5)	10.5 (0.8)	9.8 (0.3)	10.9 (0.5)	11.5 (0.5)
NH_4^+-N (g/L)	3.2 (0.5)	2.9 (0.0)	3.3 (0.0)	3.5 (0.3)	5.3 (0.1)
COD_{Cr} [6] (g/L)	99.3 (1.6)	103.4 (1.3)	101.1 (3.7)	103.0 (1.6)	97.9 (1.9)
VFAs [7] (mg/L)	188.2 (3.3)	195.7 (2.2)	204.3 (1.5)	191.4 (5.1)	251.6 (2.7)
Alkalinity (g/L)	9.5 (0.0)	9.1 (0.0)	8.6 (0.0)	9.6 (0.4)	12.1 (0.3)

[1] Mass of output/mass of feedstock, [2] Wet basis, [3] Total solid, [4] Volatile solid, [5] Total nitrogen, [6] Chemical oxygen demand, [7] Volatile fatty acids, [8] Standard deviation (n = 3).

3.3. Methane Production Potential of HTC-Hydrolysate

The cumulative methane production of HTC-hydrolysate in each batch anaerobic reactor and the optimization curves fitted by the parallel first order kinetics model are presented in Figure 3. The model parameters and ultimate methane yield are shown in Table 5. In the anaerobic digestion of the HTC-hydrolysate, the degradation of substrate began immediately with the start of anaerobic digestion, with no inhibitory effects observed. Methane production increased steeply for 15 days, and thereafter, showed a slow increase. The cumulative methane production curves were well explained by the parallel first-order kinetics model. The ultimate methane potentials (B_u) of the HTC-hydrolysate were 0.222, 0.242, 0.237, 0.228 and 0.197 Nm^3/kg-COD_{added} for the reaction temperatures of 170, 180, 190, 200 and 220 °C, respectively. The COD_{deg} were 70.6%, 75.6%, 74.7%, 72.8% and 62.8% for the reaction temperatures of 170, 180, 190, 200 and 220 °C, respectively. In the anaerobic digestion of the HTC-hydrolysate, there was significant relationship between the COD_{deg} and ultimate methane yields. The highest B_u and COD_{deg} were obtained at the reaction temperature of 180 °C, while the highest reaction temperature (220 °C) caused the lowest B_u and COD_{deg}. In addition, the organic distribution constants (f_e) decreased from 0.927 to 0.717 as the reaction temperature increased. These results indicated that the degraded fractions of organic matter decreased according to the increase of the reaction temperature during the first anaerobic degradation stage. These results are in agreement with Mottet et al. [37]. They reported that the methane yield increased to 0.215 Nm^3/kg-COD_{added} with a COD degradability of 56% in the thermal hydrolysis of 165 °C, while the methane yield decreased to 0.142 Nm^3/kg-COD_{added} with a COD degradability of 41% in the thermal hydrolysis of 220 °C. These results, along with the reduced methane yield and COD degradability at high thermal reaction temperatures, can be attributed to the Maillard reactions, in which carbohydrates react with amino acids to form melanoidines with a low biodegradability [38,39]. Such a recalcitrant compound is not always generated under conditions of high-temperatures and pressure, while a rapid increase in temperatures within the HTC reactor can more strongly affect the degree of generation of the recalcitrant compound [2].

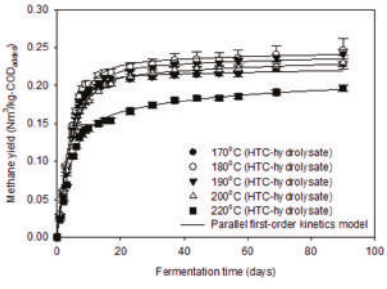

Figure 3. Cumulative methane production and optimization curves based on the parallel first-order kinetics model in the anaerobic digestion of HTC-hydrolysate (vertical bars denote standard deviations).

Table 5. Ultimate methane potential and model parameters based on the parallel first-order kinetics model.

Parameters	HTC Reaction Temperatures				
	170 °C	**180 °C**	**190 °C**	**200 °C**	**220 °C**
B_u [1] (Nm^3/kg-COD_{added})	0.222	0.242	0.237	0.228	0.197
f_e [2] (-)	0.927	0.903	0.903	0.873	0.717
k_1 [3] (1/day)	0.228	0.215	0.190	0.203	0.230
k_2 [3] (1/day)	0.011	0.028	0.019	0.020	0.024
COD_{Deg} [4] (%)	70.6	75.6	74.7	72.8	62.8

[1] Ultimate methane yield, [2] Organic distribution constant in the parallel first-order kinetics, [3] Kinetic constants in the parallel first order kinetics, [4] Degree of COD degradation.

3.4. Energy Recovery Efficiency

The gross energy recovery (GER) efficiency is shown in Table 6. The potential energy ($GEP_{feedstock}$) of 1 kg feedstock was 4.541 MJ/kg as HHV. The solid products (i.e., HTC-biochar) produced from 1 kg feedstock were 0.125, 0.121, 0.119, 0.114 and 0.110 kg, and the recovered energy values ($GER_{biochar}$) from each solid products were 3.689, 3.627, 3.583, 3.516 and 3.432 MJ/kg_{input} for the reaction temperatures of 170, 180, 190, 200 and 220 °C, respectively. The $GER_{biochar}$ efficiencies of the HTC-biochar lie in the range of 75.6–81.2% and decreased with the increase in reaction temperature. Meanwhile, the methane yields produced by the HTC-hydrolysate were 12.0, 15.2, 14.5, 15.3 and 12.9 NL (Volume in STP condition), and the recovered energy values ($GER_{methane}$) were 0.546, 0.691, 0.657, 0.696 and 0.584 MJ/kg_{input} for the reaction temperatures of 170, 180, 190, 200 and 220 °C, respectively. The $GER_{methane}$ efficiencies ranged from 12.0% to 15.3%. Therefore, the highest GER_{total} was 4.318 MJ/kg at 180 °C, the lowest value was 4.016 MJ/kg at 220 °C and the optimum HTC reaction temperature for maximizing GER_{total} efficiency was 180 °C, which maximized GER_{total} efficiency by 95.1%. The optimum HTC reaction conditions appear to be the net result of two competing mechanisms from the solubilizing transformation of the refractory particulate organics to degradable particulate organic and the stabilizing transformation of soluble organics to undefined refractory compounds [34]. Therefore, further studies concerned with the structural characteristics of the HTC-biochar and the relative biodegradability of the HTC-hydrolysate inherent in structural characteristics are needed to elucidate the optimum conditions of the HTC reaction. Rodríguez-Abalde et al. [3] and Salminen et al. [4] reported methane potentials of 0.46–0.58 Nm^3/kg-VS_{added} and 0.60 Nm^3/kg-VS_{added} in the anaerobic digestion of poultry slaughterhouse sludge waste, respectively. These values were estimated to be equivalent to 2.776–3.503 MJ/kg_{input} and 3.625 MJ/kg_{input}. Comparing the results of this study, the GER efficiency of the HTC system was much higher than the anaerobic digestion efficiency, suggesting that the GER efficiency of the sludge cake can be improved by adopting HTC technology. However, the results of this study did not take into account the energy consumed during the operation of the HTC reactor and anaerobic digester and only assessed the GER efficiency from the input biomass. Therefore, in order to evaluate the energy conversion efficiency of the sludge cake in terms of commercialization, further work on the net energy balance of the HTC system, considering consumed energy (such as electric power etc.) in the HTC process operation, is needed.

Table 7 shows NER efficiency for the case of direct utilization (e.g., solid fuel) of the sludge cake by simple drying and for the other case of energy conversion by the HTC process. In the case of direct utilization as solid fuel, the drying energy of 1.885 MJ/kg-sludge cake for the solid fuel production was estimated to be physically consumed, considering moisture vaporizing energy (2.255 MJ/kg-moisture). Therefore, the NER and NER efficiency by the simple drying of sludge were assessed as 2.656 MJ/kg_{input} and 58.5%, respectively. In the case of the HTC process, thermal energy for the HTC reaction was estimated to be 0.183 MJ/kg/kg_{input} on the basis of the reported thermal energy of 0.31 kWh/kg-feedstock [40] consumed in the HTC operation, and the drying energy of the HTC-biochar was calculated as 0.416 MJ/kg_{input}. The NER and NER efficiency were calculated as

3.628 MJ and 79.9%, respectively, during energy conversion from the HTC process. Therefore, the HTC technique was assessed to be more efficient than solid fuel production by simple drying of the sludge cake. These results were physically reasonable as a high amount of energy was consumed for the drying of moist sludge cakes with the moisture content above 80%.

Table 6. Gross energy recovery efficiency of sludge cakes in the poultry slaughterhouse with the HTC system.

Parameters		Sludge Cake	HTC Reaction Temperature (°C)				
			170	180	190	200	220
Feedstock	Solid product (kg/kg_{input})	0.164	-	-	-	-	-
	$GEP_{feedstock}$ [1] (MJ/kg_{input})	4.541	-	-	-	-	-
HTC-biochar	Solid product (kg/kg_{input})	-	0.125	0.121	0.119	0.114	0.11
	$GER_{biochar}$ [2] (MJ/kg_{input})	-	3.689	3.627	3.583	3.516	3.432
	$GER_{biochar}$ efficiency [3] (%)	-	81.2	79.9	78.9	77.4	75.6
HTC-hydrolysate	Methane yield (NL/kg_{input})	-	12.0	15.2	14.5	15.3	12.9
	$GER_{methane}$ [4] (MJ/kg_{input})	-	0.546	0.691	0.657	0.696	0.584
	$GER_{methane}$ efficiency [5] (%)	-	12.0	15.2	14.5	15.3	12.9
GER_{total} [6] (MJ/kg_{input})		-	4.234	4.318	4.240	4.212	4.016
GER_{total} efficiency [7] (%)		-	93.2	95.1	93.4	92.7	88.5

[1] Gross energy potential: calorific value as the HHV of sludge cake, [2] Gross energy recovery: calorific value as HHV × solid product of HTC-biochar, [3] $GER_{biochar}/GEP_{feedstock} \times 100$, [4] Gross energy recovery: methane yield × HHV of methane, [5] $GER_{methane}/GEP_{feedstock} \times 100$, [6] Total GER: $GER_{biochar} + GER_{methane}$, [7] $GER_{total}/GEP_{feedstock} \times 100$.

Table 7. Net energy recovery efficiency of sludge cakes in the poultry slaughterhouse with the HTC system.

Parameters	Sludge Cake (Simple Drying)	HTC (180 °C)	
		Biochar	Hydrolysate
Input and output (kg)	1.000	0.305	0.695
Moisture content (kg)	0.836	0.185	-
HTC thermal energy [1] (MJ/kg_{input})	-	0.183	
Drying energy [2] (MJ/kg_{input})	1.885	0.416	-
GER [3] (MJ/kg_{input})	4.541	3.627	0.691
NER [4] (MJ/kg_{input})	2.656	3.628	
NER efficiency [5] (%)	58.5	79.9	

[1] Thermal energy consumed in the HTC reaction (specific thermal energy consumption = 0.31 $kWh/kg_{feedstock}$ [40]), [2] Drying energy consumed for the solid fuel production (2.255 MJ/kg-moisture), [3] Gross energy recovery as HHV, [4] Net energy recovery: GER-HTC thermal energy-Drying energy, [5] NER/GER of sludge cake × 100.

4. Conclusions

The sludge cake generated from the wastewater treatment plant of the poultry slaughterhouse was a useful source for bioenergy conversion due its high calorific value of approximately 27.7 MJ/kg. The solid yield of the HTC-biochar decreased from 75.9% to 66.8% with the increase of reaction temperature from 170 °C to 220 °C, while the calorific values increased from 29.6 MJ/kg to 31.3 MJ/kg, and the energy densification increased from 1.07 to 1.13. The output yields of the HTC-hydrolysate increased from 62.3% to 76.2% with the rise of the reaction temperature from 170 °C to 220 °C, and the COD contents of the HTC-hydrolysate were in the range of 97.9 and 103.4 g/L. The B_u of the HTC-hydrolysate increased from 0.222 $Nm^3/kg\text{-}COD_{added}$ to 0.242 $Nm^3/kg\text{-}COD_{added}$ with the increase of reaction temperature from 170 °C to 180 °C, and decreased to 0.197 $Nm^3/kg\text{-}COD_{added}$ until 220 °C, in analysis based on the parallel first-order kinetics model. The potential energy of feedstock (1 kg) was 4.541 MJ/kg. The $GER_{biochar}$ efficiencies of the HTC-biochar from the sludge

decreased from 81.2% to 75.6% with the increase of reaction temperature. The $GER_{methane}$ efficiencies were calculated as 12.0, 15.2, 14.5, 15.3 and 12.9 for the reaction temperatures of 170, 180, 090, 200 and 220 °C, respectively. Consequently, the GER_{total} peaked at 4318 MJ/kg for the reaction temperature of 180 °C, and exhibited its lowest value (4016 MJ/kg) for the reaction temperature of 220 °C. Therefore, the optimum HTC reaction temperature for maximizing GER efficiency was 180 °C, and the maximum gross energy recovery efficiency was 95.1%. Also, NER efficiency at the production of solid fuel by simple drying was 58.5% (NER-solid fuel = 2656 MJ/kg_{input}) and NER efficiency at the energy conversion by the HTC process was 79.9% (NER-HTC = 3628 MJ/kg_{input}). These results suggested that the GER and NER efficiencies from the HTC system are much higher than those of the direct utilization of the sludge cake by simple drying and the GER and NER efficiencies of the sludge cake can be improved by adopting HTC technology.

Acknowledgments: This research was supported by a grant (17IFIP-B113506-02) from the development of plant program funded by the Ministry of Land, Infrastructure and Transport of Korean government.

Author Contributions: Seung-Yong Oh and Young-Man Yoon conceived and designed the experiments; Seung-Yong Oh performed the experiments; Young-Man Yoon analyzed the data; Young-Man Yoon wrote the paper.

Conflicts of Interest: The authors declare no conflict of interest. The founding sponsors had no role in the design of the study; in the collection, analysis, or interpretation of data; in the writing of the manuscript, nor in the decision to publish the results.

References

1. Jeon, Y.-W.; Kang, J.-W.; Kim, H.; Yoon, Y.-M.; Lee, D.-H. Unit mass estimation and characterization of litter generated in the broiler house and slaughter house. *Int. Biodeterior. Biodegrad.* **2013**, *85*, 592–597. [CrossRef]
2. Kim, S.-H.; Kim, H.; Kim, C.-H.; Yoon, Y.-M. Effect of the pretreatment by thermal hydrolysis on biochemical methane potential of piggery sludge. *Korean J. Soil Sci. Fertil.* **2012**, *45*, 524–531. [CrossRef]
3. Rodríguez-Abalde, A.; Fernández, B.; Silvestre, G.; Flotats, X. Effects of thermal pre-treatments on solid slaughterhouse waste methane potential. *Waste Manag.* **2011**, *31*, 1488–1493. [CrossRef] [PubMed]
4. Salminen, E.; Einola, J.; Rintala, J. The methane production of poultry slaughtering residues and effects of pre-treatments on the methane production of poultry feather. *Environ. Technol.* **2003**, *24*, 1079–1086. [CrossRef] [PubMed]
5. Salminen, E.; Rintala, J. Anaerobic digestion of organic solid poultry slaughterhouse waste—A review. *Bioresour. Technol.* **2002**, *83*, 13–26. [CrossRef]
6. Angelidaki, I.; Ahring, B. Thermophilic anaerobic digestion of livestock waste: The effect of ammonia. *Appl. Microbiol. Biotechnol.* **1993**, *38*, 560–564. [CrossRef]
7. Kleinert, M.; Wittmann, T. Carbonisation of biomass using hydrothermal approach: State-of-the-art and recent developments. In Proceedings of the 17th European Biomass Conference and Exhibition, Hamburg, Germany, 29 June–3 July 2009.
8. Funke, A.; Ziegler, F. Hydrothermal carbonization of biomass: A summary and discussion of chemical mechanisms for process engineering. *Biofuels Bioprod. Biorefin.* **2010**, *4*, 160–177. [CrossRef]
9. Titirici, M.-M.; Thomas, A.; Antonietti, M. Back in the black: Hydrothermal carbonization of plant material as an efficient chemical process to treat the co 2 problem? *New J. Chem.* **2007**, *31*, 787–789. [CrossRef]
10. Libra, J.A.; Ro, K.S.; Kammann, C.; Funke, A.; Berge, N.D.; Neubauer, Y.; Titirici, M.-M.; Fühner, C.; Bens, O.; Kern, J. Hydrothermal carbonization of biomass residuals: A comparative review of the chemistry, processes and applications of wet and dry pyrolysis. *Biofuels* **2011**, *2*, 71–106. [CrossRef]
11. Liu, Z.; Quek, A.; Hoekman, S.K.; Balasubramanian, R. Production of solid biochar fuel from waste biomass by hydrothermal carbonization. *Fuel* **2013**, *103*, 943–949. [CrossRef]
12. Manara, P.; Zabaniotou, A. Towards sewage sludge based biofuels via thermochemical conversion—A review. *Renew. Sustain. Energy Rev.* **2012**, *16*, 2566–2582. [CrossRef]
13. Basso, D.; Patuzzi, F.; Castello, D.; Baratieri, M.; Rada, E.C.; Weiss-Hortala, E.; Fiori, L. Agro-industrial waste to solid biofuel through hydrothermal carbonization. *Waste Manag.* **2016**, *47*, 114–121. [CrossRef] [PubMed]

14. Kim, D.; Yoshikawa, K.; Park, K. Characteristics of biochar obtained by hydrothermal carbonization of cellulose for renewable energy. *Energies* **2015**, *8*, 14040–14048. [CrossRef]
15. Hoekman, S.K.; Broch, A.; Robbins, C. Hydrothermal carbonization (htc) of lignocellulosic biomass. *Energy Fuels* **2011**, *25*, 1802–1810. [CrossRef]
16. Ramke, H.-G.; Blöhse, D.; Lehmann, H.-J.; Fettig, J. Hydrothermal carbonization of organic waste. In Proceedings of the Twelfth International Waste Management and Landfill Symposium, Sardinia, Italy, 5–9 October 2009.
17. Costa, J.C.; Barbosa, S.G.; Alves, M.M.; Sousa, D.Z. Thermochemical pre- and biological co-treatments to improve hydrolysis and methane production from poultry litter. *Bioresour. Technol.* **2012**, *111*, 141–147. [CrossRef] [PubMed]
18. Mäkelä, M.; Kwong, C.W.; Broström, M.; Yoshikawa, K. Hydrothermal treatment of grape marc for solid fuel applications. *Energy Convers. Manag.* **2017**, *145*, 371–377. [CrossRef]
19. Volpe, M.; Fiori, L. From olive waste to solid biofuel through hydrothermal carbonisation: The role of temperature and solid load on secondary char formation and hydrochar energy properties. *J. Anal. Appl. Pyrolysis* **2017**, *124*, 63–72. [CrossRef]
20. Rao, M.; Singh, S. Bioenergy conversion studies of organic fraction of msw: Kinetic studies and gas yield–organic loading relationships for process optimisation. *Bioresour. Technol.* **2004**, *95*, 173–185. [CrossRef] [PubMed]
21. Oh, S.Y.; Yoon, Y.M. Assessment of methane potential in hydro-thermal carbonization reaction of organic sludge using parallel first order kinetics. *Korean J. Environ. Agric.* **2016**, *35*, 128–136. [CrossRef]
22. VDI Standard. *VDI 4630: Fermentation of Organic Materials—Characterization of the Substrate, Sampling, Collection of Material Data, Fermentation Tests*; VDI: Düsseldorf, Germany, 2006; Volume 92.
23. Association, A.P.H.; Water Environment Federation (1998). *Standard Methods for the Examination of Water and Wastewater*; American Public Health Association: Washington, DC, USA; American Water Works Association: Denver, CO, USA; Water Environment Federation: Alexandria, VA, USA, 1994.
24. Beuvink, J.; Spoelstra, S.; Hogendorp, R. An automated method for measuring time-course of gas production of feed-stuffs incubated with buffered rumen fluid. *Neth. J. Agric. Sci.* **1992**, *40*, 401.
25. Oliveira, I.; Blöhse, D.; Ramke, H.-G. Hydrothermal carbonization of agricultural residues. *Bioresour. Technol.* **2013**, *142*, 138–146. [CrossRef] [PubMed]
26. Ronsse, F.; van Hecke, S.; Dickinson, D.; Prins, W. Production and characterization of slow pyrolysis biochar: Influence of feedstock type and pyrolysis conditions. *GCB Bioenergy* **2013**, *5*, 104–115. [CrossRef]
27. Brassard, P.; Godbout, S.; Raghavan, V.; Palacios, J.; Grenier, M.; Zegan, D. The production of engineered biochars in a vertical auger pyrolysis reactor for carbon sequestration. *Energies* **2017**, *10*, 288. [CrossRef]
28. Byrappa, K.; Adschiri, T. Hydrothermal technology for nanotechnology. *Prog. Cryst. Growth Charact. Mater.* **2007**, *53*, 117–166. [CrossRef]
29. Sevilla, M.; Fuertes, A.B. The production of carbon materials by hydrothermal carbonization of cellulose. *Carbon* **2009**, *47*, 2281–2289. [CrossRef]
30. Quitain, A.T.; Faisal, M.; Kang, K.; Daimon, H.; Fujie, K. Low-molecular-weight carboxylic acids produced from hydrothermal treatment of organic wastes. *J. Hazard. Mater.* **2002**, *93*, 209–220. [CrossRef]
31. Qian, K.; Kumar, A.; Patil, K.; Bellmer, D.; Wang, D.; Yuan, W.; Huhnke, R. Effects of biomass feedstocks and gasification conditions on the physiochemical properties of char. *Energies* **2013**, *6*. [CrossRef]
32. Anderson, N.; Jones, J.; Page-Dumroese, D.; McCollum, D.; Baker, S.; Loeffler, D.; Chung, W. A comparison of producer gas, biochar, and activated carbon from two distributed scale thermochemical conversion systems used to process forest biomass. *Energies* **2013**, *6*, 164–183. [CrossRef]
33. Yang, X.; Wang, H.; Strong, P.; Xu, S.; Liu, S.; Lu, K.; Sheng, K.; Guo, J.; Che, L.; He, L.; et al. Thermal properties of biochars derived from waste biomass generated by agricultural and forestry sectors. *Energies* **2017**, *10*, 469. [CrossRef]
34. Stuckey, D.C.; McCarty, P.L. The effect of thermal pretreatment on the anaerobic biodegradability and toxicity of waste activated sludge. *Water Res.* **1984**, *18*, 1343–1353. [CrossRef]
35. Kim, D.; Lee, K.; Park, K.Y. Hydrothermal carbonization of anaerobically digested sludge for solid fuel production and energy recovery. *Fuel* **2014**, *130*, 120–125. [CrossRef]
36. Jahirul, M.; Rasul, M.; Chowdhury, A.; Ashwath, N. Biofuels production through biomass pyrolysis—A technological review. *Energies* **2012**, *5*, 4952–5001. [CrossRef]

37. Mottet, A.; Steyer, J.; Déléris, S.; Vedrenne, F.; Chauzy, J.; Carrère, H. Kinetics of thermophilic batch anaerobic digestion of thermal hydrolysed waste activated sludge. *Biochem. Eng. J.* **2009**, *46*, 169–175. [CrossRef]
38. Martins, S.I.; Jongen, W.M.; Van Boekel, M.A. A review of maillard reaction in food and implications to kinetic modelling. *Trends Food Sci. Technol.* **2000**, *11*, 364–373. [CrossRef]
39. Bougrier, C.; Delgenes, J.P.; Carrère, H. Effects of thermal treatments on five different waste activated sludge samples solubilisation, physical properties and anaerobic digestion. *Chem. Eng. J.* **2008**, *139*, 236–244. [CrossRef]
40. Lucian, M.; Fiori, L. Hydrothermal carbonization of waste biomass: Process design, modeling, energy efficiency and cost analysis. *Energies* **2017**, *10*, 211. [CrossRef]

© 2017 by the authors. Licensee MDPI, Basel, Switzerland. This article is an open access article distributed under the terms and conditions of the Creative Commons Attribution (CC BY) license (http://creativecommons.org/licenses/by/4.0/).

energies

MDPI

Article

Chemical Characteristics and NaCl Component Behavior of Biochar Derived from the Salty Food Waste by Water Flushing

Ye-Eun Lee [1,2], Jun-Ho Jo [1], I-Tae Kim [1] and Yeong-Seok Yoo [1,2,*]

[1] Division of Environment and Plant Engineering, Korea Institute of Civil Engineering and Building Technology 283, Goyang-daero, Ilsanseo-gu, Goyang-si, Gyeonggi-do 10223, Korea; yeeunlee@kict.re.kr (Y.-E.L.); junkr@kict.re.kr (J.-H.J.); itkim@kict.re.kr (I.-T.K.)

[2] Department of Construction Environment Engineering, University of Science and Technology, 217, Gajeong-ro, Yuseong-gu, Daejeon KS015, Korea

* Correspondence: ysyoo@kict.re.kr; Tel.: +82-31-910-0298; Fax: +82-31-910-0288

Received: 21 August 2017; Accepted: 30 September 2017; Published: 10 October 2017

Abstract: Biochar is the product of the pyrolysis of organic materials in a reduced state. In recent years, biochar has received attention due to its applicability to organic waste management, thereby leading to active research on biochar. However, there have been few studies using food waste. In particular, the most significant difference between food waste and other organic waste is the high salinity of food waste. Therefore, in this paper, we compare the chemical characteristics of biochar produced using food waste containing low- and high-concentration salt and biochar flushed with water to remove the concentrated salt. In addition, we clarify the salt component behavior of biochar. Peak analysis of XRD confirms that it is difficult to find salt crystals in flushed char since salt remains in the form of crystals when salty food waste is pyrolyzed washed away after water flushing. In addition, the Cl content significantly decreased to 1–2% after flushing, similar to that of Cl content in the standard, non-salted food waste char. On the other hand, a significant amount of Na was found in pyrolyzed char even after flushing resulting from a phenomenon in which salt is dissolved in water while flushing and Na ions are adsorbed. FT-IR analysis showed that salt in waste affects the binding of aromatic carbons to compounds in the pyrolysis process. The NMR spectroscopy demonstrated that the aromatic carbon content, which indicates the stability of biochar, is not influenced by the salt content and increases with increasing pyrolysis temperature.

Keywords: salty food waste; FT-IR; pyrolysis; biochar; NaCl

1. Introduction

The process of dealing with food waste affects climate change by emitting large amounts of greenhouse gases such as methane and carbon dioxide [1]. The Food and Agriculture Organization has reported that one-third of the produced food in the world is thrown away annually [2]. As a result, a new alternative is needed to deal with the vast amounts of food waste.

Biochar is the product that results from the pyrolysis of organic materials in a reduced state. It is distinguished from charcoal by its usage as a soil amendment [3]. Biochar can be produced from a variety of materials including wood, agricultural waste, and livestock waste [4]. Biochar also reduces the release of organic carbon into the air in the form of carbon dioxide by resisting microbial degradation [5,6]. It also helps to prevent climate change by reducing the emission of greenhouse gases such as nitrogen oxides from the soil and methane [7]. Mitchell et al. [8] studied the characteristics of biochar from pyrolyzed lignocellulosic municipal waste, and Prakongkep et al. [9] compared and analyzed 14 types of tropical plant-waste-derived biochar. In addition, Kwapinski et al. [10]

analyzed the temperature-related characteristics of biochar generated from pyrolyzing miscanthus, pine, and willow as a waste management method. They analyzed the characteristics of biochar as a soil amendment and fertilizer. Most studies on biochar have used wood or vegetable raw materials; few have used salty food wastes as raw materials.

As the applicability of biochar to organic waste management has received attention, various studies have been done on its chemical [11] and physical characteristics [12], and its effect on soil [13]. The major difference between other organic materials and biochar is the large proportion of aromatic carbon [14]. Secondly, biochar consists mostly of immobile carbon and nitrogen that microorganisms cannot use as energy sources, thereby having chemical stability (ASTM standard methodology) [15]. In addition, the difference involves cation exchange capacity (CEC) of biochar resulting from the surface charge. Pyrolysis condition is an important factor in determining the physicochemical characteristics of biochar [16]. Hossain et al. [17] revealed that the composition and chemical structure of biochar changed according to the pyrolysis temperature by pyrolyzing the sewage sludge at 300–700 °C. Cantrell et al. [18] showed that the source type could alter the physicochemical characteristics by pyrolyzing five types of manure at 350 and 700 °C.

The major difference between municipal waste (organic waste), such as sewage sludge, livestock waste, and agricultural by-products, and food waste is its high salinity [19,20]. The high salt content of food waste is a major obstacle to recycling and treating food waste. Therefore, we investigate the effect of salt on the conversion into biochar by analyzing the characteristics of pyrolyzed char according to salt content. In this paper, the chemical characteristics of biochar produced using food waste containing low- and high-concentration salt and biochar flushed with water to remove the concentrated salt are compared and analyzed. In addition, the salt component behavior of biochar is clarified.

2. Experimental

2.1. Raw Material

The food waste samples were prepared as shown in Table 1 according to the composition of the standard sample, which is the average food waste composition ratio as determined by the Ministry of Environment of Korea [21]. Food wastes were classified into grains, vegetables, fruits, and meat and fish, and the composition ratios were set to 16%, 51%, 14%, and 19%, respectively, using 10 kinds of materials. The food samples were dried at 80 °C for 48 h and then ground into powder form. NaCl solution was added such that the NaCl contents relative to the dry weight of the food samples became 1%, 3%, and 5%. The samples were then dried again.

Table 1. The standard food waste sample.

Classification	Composition Ratio (wt %)	Methods of Food Ingredient Processing	
		Food Ingredients	Processing Method
Grains	16	Rice (16)	
Vegetables	51	Napa cabbage (9)	Cutting width less than 100 mm.
		Potato (20) Onion (20) Daikon (2)	Chop into 5 mm size pieces.
Fruits	14	Apple (7) Mandarin/Orange (7)	Split into 8 pieces in lengthwise.
Meat and Fish	19	Meat (4)	Cutting width around 3 cm.
		Fish (12)	Split into 4 pieces.
		Egg shell (3)	
Total	100	100	

2.2. Experimental Methods

Dry food samples containing 1%, 3%, and 5% NaCl were pyrolyzed in a pyrolysis reactor of 300 °C, 400 °C, and 500 °C. They were pyrolyzed for 1 h and 30 min, and 10 L/min nitrogen gas was continuously injected. Figure 1 shows the schematic diagram of the pyrolysis apparatus used in this experiment, which consisted of a nitrogen inlet, specimen vat, sample chamber, furnace, a cooling device, and gas combustion device. The total dimensions of pyrolysis reactor are 150 cm * 180 cm * 50 cm and the cooler temperature is maintained at 10 °C. The specimen vat size is 4.5 cm * 5 cm * 20 cm (H * W * D) and only two specimen vat put in the reactor. Feed weight is 100 g each specimen vat. Nitrogen gas was injected 10 min before the samples were added to prevent oxidation of the samples. The temperature in the furnace increased to the target temperature of 300 °C, 400 °C, and 500 °C, and the samples in the sample chamber were then added. The mass yield of biochar at each temperature is 0.56, 0.38, and 0.32 as the pyrolysis temperature increases 300 to 500 °C, and the biochar yields are decreased as the pyrolysis temperature increases [22].

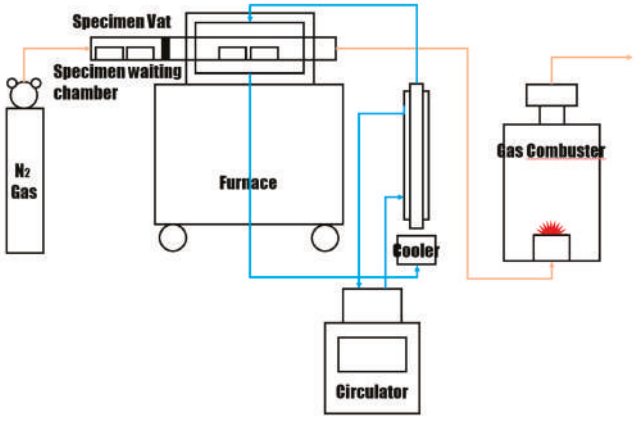

Figure 1. The schematic diagram of the pyrolysis apparatus.

After pyrolysis, the samples were removed, cooled to room temperature, weighed, and ground. They were flushed by stirring 30 g of char in 300 mL of distilled water at a ratio of 1:10 for 30 min. The flushed char was then separated using a filter paper and dried again at 80 °C for 24 h before being stored.

2.3. Analytical Methods

2.3.1. Characterization

A FLASH EA1112 instrument (Thermo Electron, Waltham, MA, USA) was used for the elementary analysis (C, H, S, N) of the salty food waste derived biochar. Oxygen is obtained by difference assuming the sum of C, H, S, N, O, Ash, and NaCl is 100%. In general, either Na or Cl is measured to determine the salt content. However, one study reported a phenomenon in which Na and Cl are independently volatilized in the pyrolysis process of saline-containing fossil fuel [23]. Therefore, both the Na and Cl contents were measured independently. Na content was measured using Agilent 5100 ICP-OES (Agilent Technologies, Santa Clara, CA, USA). Cl was carbonized after mixing 2.5–5 g samples with the milk of lime and drying. 1–2 drops of potassium chromate were added to the sample, which was filtrated after adding water and shaking. The solution was titrated with silver nitrate solution [24]. To measure Cation exchange capacity (CEC) values, 5 g of the sample was then placed in a 100 mL Erlenmeyer flask, and 50 mL of 1 M NH_4OA_c solution was added [25]. The sample was

then shaken for 30 min, filtered, and diluted. The CEC was measured using Agilent 5100 ICP-OES (Agilent Technologies). The Na, K, Mg, and Ca contents were calculated by converting the measured absorbance value (ppm) using the Brown's simplified method.

2.3.2. X-ray Diffraction Spectroscopy

X-ray diffraction (XRD) analysis was carried out to determine the structure of salt in the salty food waste derived-biochar and the change in the molecular structure both before and after flushing. The analytical equipment used was DMAX 2500 (Rigaku, Tokyo, Japan), and the X-ray generator had specifications of 18 kW and 60 kV/300 mA. The 2θ range of the recorded sample was 10–90°.

2.3.3. FT-IR

The infrared spectroscopic analysis was conducted to investigate the effect of salt in salty food waste on the biochars during pyrolysis and its effect on flushing. A VERTEX 80V (Bruker Optics, Ettlingen, Germany) device was used, and infrared rays of 400–4000 nm wavelength were transmitted to determine the characteristics. A transmission analysis was conducted using KBr powder.

2.3.4. NMR

The structure was analyzed using solid-state magic angle spinning ^{13}C NMR analysis to confirm the formation of aromatic carbons, which indicate the stability of the biochar. A DIGITAL AVANCE III 400 MHz (Bruker Biospin AG, Fällanden, Switzerland) was used with a 4 mm probe.

3. Results and Discussion

3.1. Chemical Composition of Salty Food-Waste-Derived Biochar

Table 2 shows the elementary analysis of the salty food waste derived biochar and Na and Cl contents. After flushing, the Cl content decreased to the Cl content in the STD sample, non-salted food waste sample. On the other hand, the Na content significantly increased after flushing compared to the Na content in the STD sample, non-salted food waste sample.

Table 2. The chemical compositions and atomic ratios of biochar produced by salty food waste.

Sample ID	Component, wt %							Atomic Ratio		
	C	H	N	O	Na	Cl	Ash	C/N	H/C	O/C
Dry	51.46	13.22	3.14	32.18	-	-	-	16.38	0.257	0.63
300 °C_STD	60.97	5.37	5.28	23.66	1.21	1.56	4.72	11.55	0.088	0.39
300 °C_1%_B	60.18	5.32	5.29	25.88	3.08	3.17	3.33	11.38	0.088	0.43
300 °C_1%_A	61.70	5.59	5.24	25.19	2.02	1.51	2.28	11.77	0.091	0.41
300 °C_3%_B	58.96	5.17	5.09	22.53	6.63	6.26	8.25	11.58	0.088	0.38
300 °C_3%_A	63.21	5.46	5.16	24.34	2.67	1.50	1.83	12.25	0.086	0.39
300°C_5%_B	57.29	5.04	4.98	20.83	9.30	8.74	11.86	11.5	0.088	0.36
300 °C_5%_A	62.08	5.81	5.42	23.03	2.62	1.50	3.66	11.45	0.094	0.37
400 °C_STD	64.69	3.64	5.09	17.82	1.92	1.90	8.76	12.71	0.056	0.28
400 °C_1%_B	63.27	3.60	5.38	17.98	4.74	4.18	9.77	11.76	0.057	0.28
400 °C_1%_A	68.71	4.28	5.04	17.60	4.01	1.20	4.37	13.63	0.062	0.26
400 °C_3%_B	57.85	3.24	4.16	21.08	9.22	8.25	13.67	13.91	0.056	0.36
400 °C_3%_A	65.43	3.70	5.26	20.94	3.43	1.19	4.67	12.44	0.057	0.32
400 °C_5%_B	56.15	3.20	3.99	18.74	16.53	12.66	17.92	14.07	0.057	0.33
400 °C_5%_A	68.43	4.34	4.51	19.47	4.64	1.36	3.25	15.17	0.063	0.28
500 °C_STD	70.11	2.81	5.23	8.83	0.51	0.90	13.02	13.41	0.04	0.13
500 °C_1%_B	68.82	2.71	5.22	10.45	3.98	3.74	12.80	13.18	0.039	0.15
500 °C_1%_A	72.07	2.93	5.13	9.43	3.43	1.03	10.44	14.05	0.041	0.13
500 °C_3%_B	65.72	2.69	4.63	10.33	9.65	9.42	16.63	14.19	0.041	0.16
500 °C_3%_A	72.10	2.98	5.13	11.32	5.14	1.49	8.47	14.05	0.041	0.16
500 °C_5%_B	61.78	2.43	4.44	10.50	15.56	13.80	20.85	13.91	0.039	0.17
500 °C_5%_A	73.28	2.92	4.92	11.80	5.35	1.45	7.08	14.89	0.04	0.16

Carbon content increased with the pyrolysis temperature, and there was a difference in the content before and after flushing that resulted from a slight increase in the carbon content relative to the total weight since salt was discharged while flushing.

Hydrogen content decreased as the pyrolysis temperature increased, and there was a difference in the content before and after flushing that resulted from increased relative weight since salt was discharged while flushing, as with carbon.

Nitrogen content did not show any tendency to increase or decrease according to the pyrolysis temperature. However, the nitrogen content of the biochar having 1% salt content decreased after flushing, while the nitrogen contents of the chars having 3% and 5% salt content increased after flushing.

The higher the pyrolysis temperature and the higher the salt content, the lower the O/C ratio, which indicates the stability of biochar [26]. There was a difference before and after flushing, but this phenomenon may have been caused by changes in salt content before and after flushing. When the O/C ratio is 0.2 or less, the half-life of biochar is estimated to be 1000 years or more. When the O/C ratio is 0.2–0.6, the half-life is estimated to be 100–1000 years [27]. The H/C ratio decreased as the pyrolysis temperature increased. There was an obvious difference according to pyrolysis temperature, but there was no difference according to the salt content. The Lower values of H/C and O/C at higher pyrolysis temperatures indicate a stable biochar with a low content of O-based functional groups by demethylation and decarboxylation [28].

A C/N ratio of 12:1 is the most favored for increasing the nitrogen pool plants can use, and a C/N ratio of 20:1 is used for soil conditioners, fertilizers and compost [29]. As the pyrolysis temperature increases, the C/N ratio increases [30]. The experimental result showed that the ratio increased and the ratio was 11–15, which is suitable for use in the soil when the temperature increased from 300 to 500 °C.

H/C, O/C, and C/N values are influenced by pyrolysis temperature, and the content of salt appears to have no noticeable effect on the chemical composition.

The CEC of salty food waste biochars varies depending on raw materials and pyrolysis conditions. Some studies have reported that the CEC value increases as the pyrolysis temperature increase from 300 to 500 °C in relation to the carboxyl groups on the biochar surface [31–33]. Table 3 shows that as the pyrolysis temperature increased from 300 to 400 °C, the CEC value increased, peaked at 400 °C, and decreased again at 500 °C. CEC is determined by substitution sites, O-based functional groups such as –OH or –COOH that are made by decarboxylation and deformation as the pyrolysis temperature. Although, further study is needed to specify the required energy for deformation to contain high CEC, it is reliable trend similar to Wu et al.'s study result [32]. These results may relate to specific surface area. Focusing on O-based functional groups, 300 °C should indicate highest CEC value. But in case of this, complex action between functional group and specific surface area, may be acted on the explanation of this phenomenon. O-based functional groups are decreased gradually as the pyrolysis temperature increases. Specific surface area is increased as the pyrolysis temperature increases [34]. At 300 °C, there could be more O based functional groups but there is lower specific surface area. Overall, the surface area of pyrolyzed char at 300 °C, including O-based functional groups, may be smaller than at 400 °C. About this assumption, further study is needed.

Table 3. CEC of salty food waste derived-biochar before and after flushing.

Sample ID	CEC (cmol/kg)	Extractable Cations (cmolc/kg)			
		Ca	K	Mg	Na
300 °C_STD	25.57	0.39	12.68	0.34	5.56
300 °C_1%_B	22.20	0.29	7.77	0.12	6.99
300 °C_1%_A	18.14	0.45	4.95	0.15	4.67
300 °C_3%_B	22.42	0.17	4.06	0.06	11.08
300 °C_3%_A	20.35	0.47	3.99	0.16	8.04
300 °C_5%_B	110.71	0.35	16.59	0.24	86.26
300 °C_5%_A	22.67	0.58	3.89	0.22	10.07
400 °C_STD	62.94	1.10	44.07	1.37	14.21
400 °C_1%_B	120.39	1.19	62.59	1.15	49.98
400 °C_1%_A	36.65	0.90	18.00	0.64	12.71
400 °C_3%_B	163.48	0.96	52.17	1.23	108.91
400 °C_3%_A	52.60	1.30	16.17	1.00	24.68
400 °C_5%_B	250.72	0.65	53.19	1.29	185.03
400 °C_5%_A	39.46	1.06	9.90	0.86	22.80
500 °C_STD	54.91	0.89	60.38	1.58	1.07
500 °C_1%_B	75.22	0.83	62.37	1.10	14.88
500 °C_1%_A	24.79	1.07	18.23	0.68	7.67
500 °C_3%_B	156.81	0.76	67.59	1.22	92.30
500 °C_3%_A	18.90	1.29	10.63	1.00	9.27
500 °C_5%_B	262.08	0.63	73.55	1.31	189.90
500 °C_5%_A	24.86	1.34	10.29	1.07	14.58

STD: Standard food waste biochar sample without NaCl. A: Salty food waste derived biochar after flushing. B: Salty food waste derived biochar before flushing.

Compared to the CEC value of the char unaffected by salt, the measured CEC value was higher before flushing and lower after flushing. This may have been the result of the phenomenon in which ionized Na^+ is adsorbed on the biochar surface during the flushing. VAN ZWIETEN et al. [35] showed that the application of biochar in a ferrosol significantly increased CEC of soil. In other words, the pyrolyzed salty food waste biochar is able to hold many cations which are nutritional content used by plants and helps the soil fertility improvement.

The extractable values of Na and K were much higher than those of other elements and significantly decreased after flushing. However, the extractable value of Ca increased after flushing. The value of Mg also increased in the case of 1% and 3% at 300 °C. This phenomenon will be discussed in relation to the result of Fourier transform infrared spectroscopy (FT-IR).

The CEC of soil is an important criterion for determining the ability of plants to retain the cations they use. Sandy soil, with its low organic content, has a CEC value of less than 3 cmolc/kg, but heavy clay soil or soil with a high organic content has a CEC value higher than 20 cmolc/kg [36]. Every sample except post-flushing samples (300 °C, 1%; 500 °C, 3%) obtained values higher than 20 cmolc/kg; therefore, it is expected that they are able to be used as soil conditioners.

3.2. XRD Analysis of Salty Food-Waste-Derived Biochar

Figures 2–5 show the XRD results of salty food waste chars before and after flushing according to the pyrolysis temperature, as well as those of NaCl. The crystalline form of NaCl has peaked at 32°, 45.5°, 56.5°, 66°, 75°, and 84° (2θ). When comparing these peaks with the XRD peaks of the salty food waste biochar, the graph before flushing clearly shows the NaCl peaks. On the other hand, the graph after flushing shows that the peaks of NaCl become blurred, and the peaks show a similar tendency to the peaks of standard food waste biochars containing no salt.

In other words, even after carbonization, NaCl remains in the form of crystals. However, after flushing, the remaining NaCl has washed away, and the peaks resemble those of the standard state.

The peak near 23° (2θ) corresponds to the diffuse graphite [37,38]. As the pyrolysis temperature increases, the peak shifts from 20° to 25° (2θ). This means that cellulose crystallinity decreases and turbostratic crystallinity increases [39].

As the pyrolysis temperature increases from 300 °C to 500 °C, the peak intensity near 28° (2θ) increases. This peak confirms the presence of calcite [40], and the sharper the peak, the better the calcite crystallization.

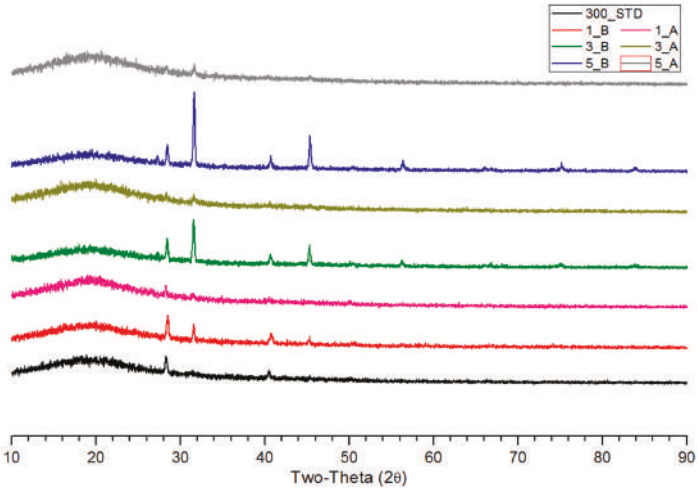

Figure 2. The XRD result of biochar pyrolyzed at 300 °C before and after flushing.

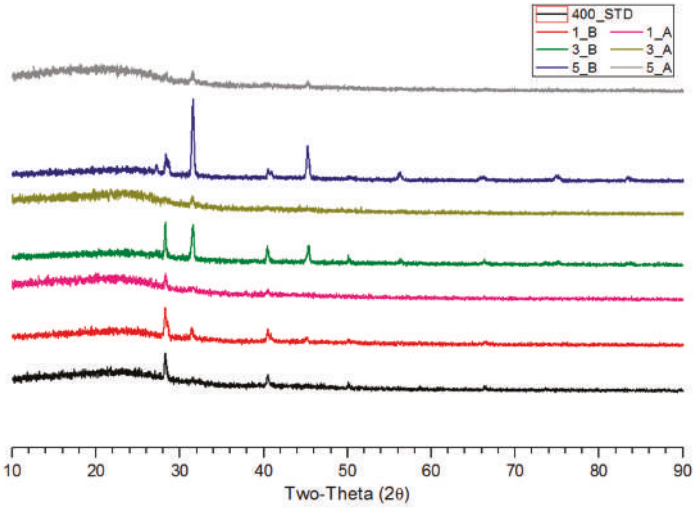

Figure 3. The XRD result of biochar pyrolyzed at 400 °C before and after flushing.

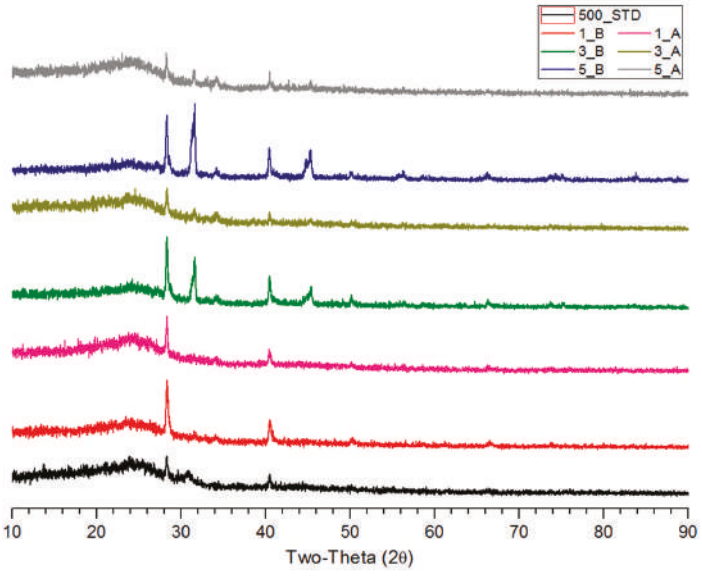

Figure 4. The XRD result of biochar pyrolyzed at 500 °C before and after flushing.

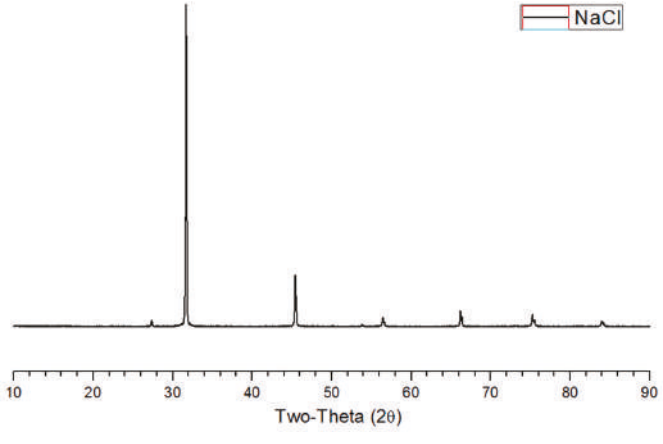

Figure 5. The XRD result of NaCl.

3.3. FT-IR Analysis of Salty Food-Waste-Derived Biochar

Figures 6–8, which show the FT-IR results for salty food waste biochars before and after flushing according to pyrolysis temperature, illustrate that the tendency varies significantly depending on the pyrolysis temperature.

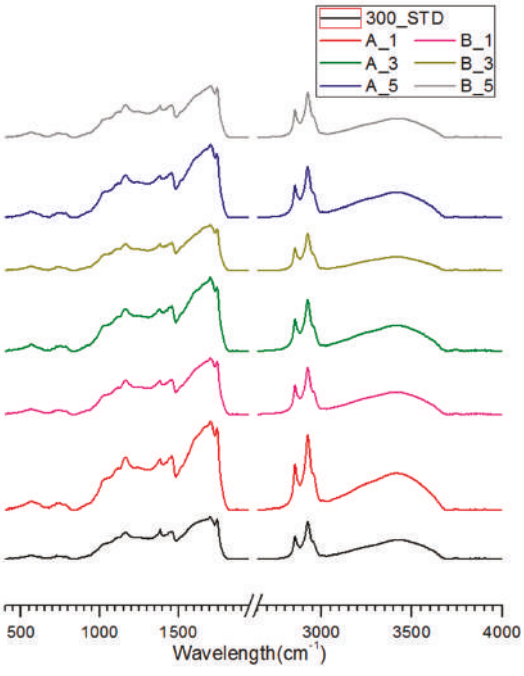

Figure 6. The FT-IR result of biochar pyrolyzed at 300 °C before and after flushing.

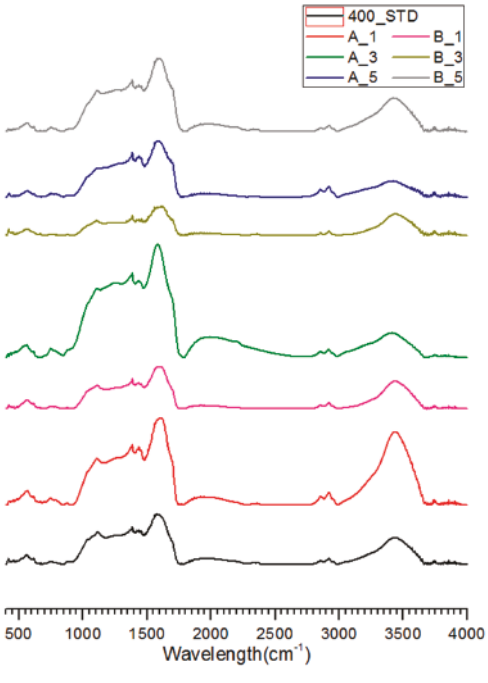

Figure 7. The FT-IR result of biochar pyrolyzed at 400 °C before and after flushing.

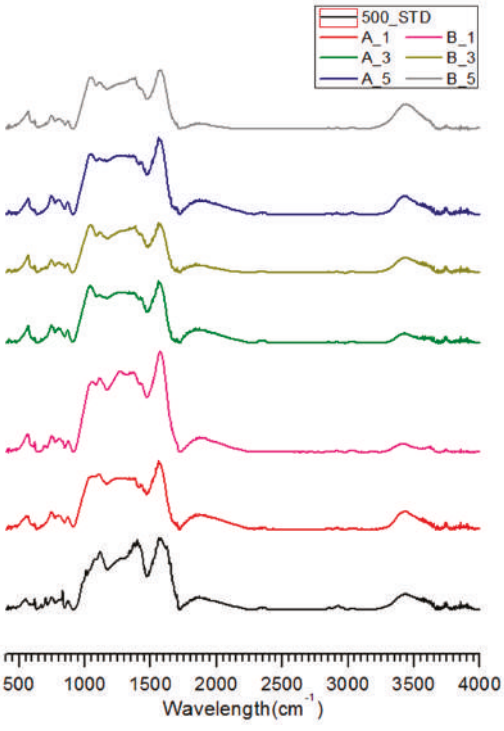

Figure 8. The FT-IR result of biochar pyrolyzed at 500 °C before and after flushing.

Carboxylic (COOH) bonds have a peak of 1700 cm^{-1} and are associated with CEC capability [41,42]. The peak near 1700 cm^{-1} that appeared clearly at 300 °C and 400 °C had almost disappeared at 500 °C. Decarboxylation occurred as the pyrolysis temperature increased, thereby decreasing the CEC value.

The peak near 1420–1440 cm^{-1} increased after flushing. This peak indicates a carboxylate anion [43]. It seems that NaCl is ionized while flushing and Na ions bind to the carboxylate anion, thereby intensifying the peak. The CEC values of Na and K were lower after flushing because Na was already bound, decreasing the capacity to exchange monovalent cations.

The distinctive peak change at 2800–3000 cm^{-1} indicates a change in aliphatic C-H, and the peak at 3600–3200 cm^{-1} reveals O-H hydroxyl groups [41,44]. As the pyrolysis temperature increased, the peak of the aliphatic C-H that was clear at 300 °C sharply decreased. The intensity of the peak was insignificant at 500 °C. The peak intensity of hydroxyl groups also gradually weakened. According to the elemental analysis, this demethylation phenomenon may have caused the decreased C/H ratio as the pyrolysis temperature increased.

The peak of aromatic C-H at 700–900 cm^{-1} [32,39] and the aromatic skeletal vibration peak at 1515–1590 cm^{-1} [42,45] became clearly visible and increased in intensity as the temperature increased from 300 °C to 500 °C. This confirms that aromatization occurred as the pyrolysis temperature and stability of biochar increased.

There were differences between the standard peak without any salt and the peak of pyrolyzed carbide containing salt. The peak shift from 550 cm^{-1} to 570 cm^{-1} was clearly shown as the pyrolysis temperature increased and salt content was higher. The peak near 550–600 cm^{-1} indicates C=O deformation of aromatic ketone [46]. Porchelvi and Muthu [47] investigated that the 552 cm^{-1} peak

results from SO_2 bound to deformed aromatic ketone and found that the 560 cm^{-1} peak appears due to cyano bound to a deformed aromatic ketone. In other words, a higher salt content induces more bonding of a specific compound to the aromatic ketone deformed in the pyrolysis process. More research is necessary for compounds that show a peak at about 570 cm^{-1}. In addition, the peak at 700 cm^{-1} appears in the standard without salt, while the peak is weak or does not appear at all in the presence of salt. This peak indicates the rocking vibration and binding of CH_2 with asymmetric deformation of aromatic ketone [47]. When salt is present, this bond is not induced. Thus, the salt contained in the food wastes affects the aromatic carbon in various biochar structures during the pyrolysis process.

Additionally, the peak at 520 cm^{-1}, which indicates the bonding of C-Cl [47], is not shown regardless of the pyrolysis temperature and salt content. This result demonstrates that the NaCl does not affect the biochar structure in the discrete state as Na^+ and Cl^-.

3.4. NMR Analysis of Salty Food Waste Derived Biochar

Figures 9–11 show the solid-state ^{13}C-NMR spectra. Although there is an apparent difference in the spectra according to the pyrolysis temperature, the peak shift by and influence of salt are negligible.

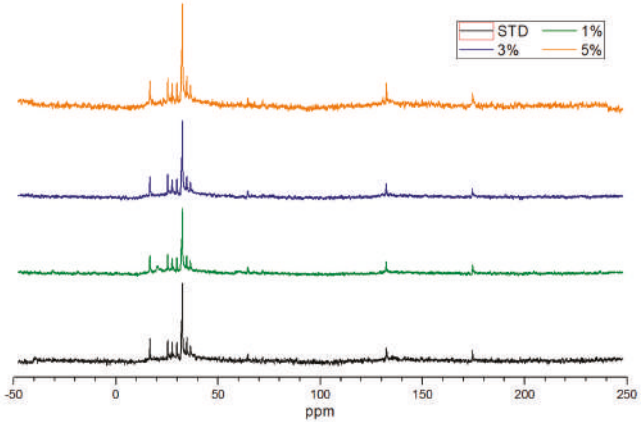

Figure 9. The NMR result of biochar pyrolyzed at 300 °C before and after flushing.

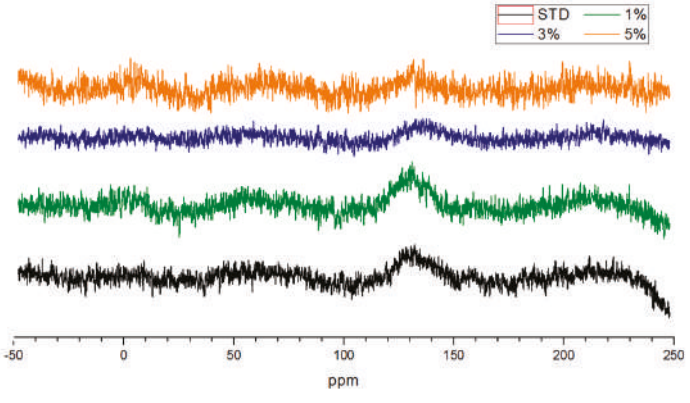

Figure 10. The NMR result of biochar pyrolyzed at 400 °C before and after flushing.

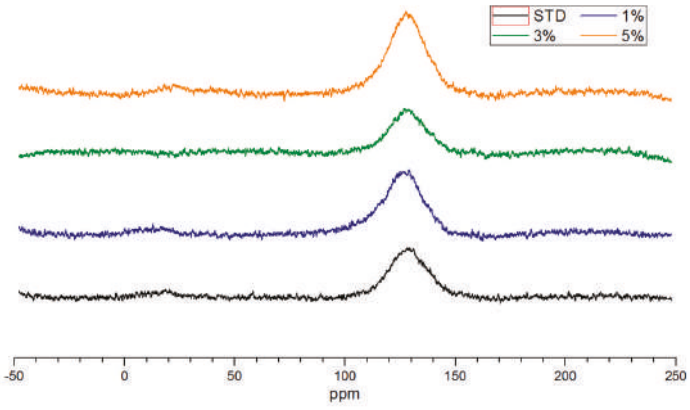

Figure 11. The NMR result of biochar pyrolyzed at 500 °C before and after flushing.

The peaks at 300 °C are shown at 16.5, 25–35, 64.5, 132, and 174.5 ppm, while broad peaks are seen from 128–132 ppm at 400 °C. At 500 °C, a weak peak is shown from 18–27 ppm and the distinct peak are seen from 110–150 ppm. The peak near 15 ppm represents CH_3 carbon, while the peak near 30–65 ppm indicates CH_2 carbon [48]. The aromatic C peak is shown narrowly around 130 ppm and also appears broadly in the range of 90–160 ppm [49,50]. The peak at 160–200 ppm means carboxylic or ketone C=O [41,50].

At 300 °C, significant amounts of CH_3 and CH_2 are present and form the main peak, while aromatic C is insufficient until demethylation occurs. As the pyrolysis temperature increases to 400 °C, sufficient dehydration occurs, and aromatic C is formed. At 500 °C, clearly visible aromatic C indicates the stabilized biochar.

4. Conclusions

In this paper, we analyzed the characteristics of pyrolyzed char according to salt content and temperature (300 °C to 500 °C) in order to determine the effect of salt on conversion into biochar. After flushing, NaCl that remains in crystalline form is washed away under all conditions, and some of Na ions that were washed off and ionized in water are adsorbed again. The pyrolysis temperature is a more important parameter than salt content for the biochar characteristics. As the charring temperature increases, salty food waste became a more stable biochar with lower H/C and O/C values and higher C/N values and aromatic carbon content. Salt content affects aromatic ketone bonding. The higher content of salt in food waste induces more bonding of a specific compound to the aromatic ketones formed in the pyrolysis process. Flushed salty food waste biochar could be recommended as a soil amendment, further studies are needed about the effect of aromatic ketone formation on the soil.

Acknowledgments: This study was supported by the major project (2017-0509) of the Korea Institute of Civil engineering and building Technology (KICT).

Author Contributions: Jun-Ho Jo and Yeong-Seok Yoo designed the experiment devices; Yeong-Seok Yoo and I-Tae Kim contributed to the analysis of experimental results; Ye-Eun Lee performed the experiments, analyzed the data, and wrote the paper.

Conflicts of Interest: The authors declare no conflict of interest.

References

1. Hall, K.D.; Guo, J.; Dore, M.; Chow, C.C. The progressive increase of food waste in America and its environmental impact. *PLoS ONE* **2009**, *4*, e7940. [CrossRef] [PubMed]

2. Venkat, K. The climate change and economic impacts of food waste in the United States. *Int. J. Food Syst. Dyn.* **2011**, *2*, 431–446.
3. Lehmann, J.; Joseph, S. Biochar for environmental management: An introduction. In *Biochar for Environmental Management: Science and Technology*; Lehmann, J., Joseph, S., Eds.; Earthscan: London, UK, 2009.
4. Ioannidou, O.; Zabaniotou, A. Agricultural residues as precursors for activated carbon production—A review. *Renew. Sustain. Energy Rev.* **2007**, *11*, 1966–2005. [CrossRef]
5. Lehmann, J. A handful of carbon. *Nature* **2007**, *447*, 143–144. [CrossRef] [PubMed]
6. Brassard, P.; Godbout, S.; Raghavan, V.G.S.; Palacios, J.H.; Grenier, M.; Zegan, D. The production of engineered biochars in a vertical auger pyrolysis reactor for carbon sequestration. *Energies* **2017**, *10*, 288. [CrossRef]
7. Taghizadeh-Toosi, A.; Clough, T.J.; Condron, L.M.; Sherlock, R.R.; Anderson, C.R.; Craigie, R.A. Biochar incorporation into pasture soil suppresses in situ nitrous oxide emissions from ruminant urine patches. *J. Environ. Qual.* **2011**, *40*, 468–476. [CrossRef] [PubMed]
8. Mitchell, P.J.; Dalley, T.S.L.; Helleur, R.J. Preliminary laboratory production and characterization of biochars from lignocellulosic municipal waste. *J. Anal. Appl. Pyrolysis* **2013**, *99*, 71–78. [CrossRef]
9. Prakongkep, N.; Gilkes, R.J.; Wiriyakitnateekul, W. Forms and solubility of plant nutrient elements in tropical plant waste biochars. *J. Plant Nutr. Soil Sci.* **2015**, *178*, 732–740. [CrossRef]
10. Kwapinski, W.; Byrne, C.M.P.; Kryachko, E.; Wolfram, P.; Adley, C.; Leahy, J.J.; Novotny, E.H.; Hayes, M.H.B. Biochar from biomass and waste. *Waste Biomass Valoriz.* **2010**, *1*, 177–189. [CrossRef]
11. Nguyen, B.T.; Lehmann, J.; Hockaday, W.C.; Joseph, S.; Masiello, C.A. Temperature sensitivity of black carbon decomposition and oxidation. *Environ. Sci. Technol.* **2010**, *44*, 3324–3331. [CrossRef] [PubMed]
12. Downie, A.; Alan, C.; Paul, M. Physical properties of biochar. In *Biochar for Environmental Management: Science and Technology*; Earthscan: London, UK, 2009.
13. Jin, H. Characterization of Microbial Life Colonizing Biochar and Biochar-Amended Soils. Ph.D. Thesis, Cornell University, Ithaca, NY, USA, 2010.
14. Lehmann, J.; Rillig, M.C.; Thies, J.; Masiello, C.A.; Hockaday, W.C.; Crowleye, D. Biochar effects on soil biota—A review. *Soil Biol. Biochem.* **2011**, *43*, 1812–1836. [CrossRef]
15. Deenik, J.L.; McClellan, T.; Uehara, G.; Antal, M.J.; Campbell, S. Charcoal volatile matter content influences plant growth and soil nitrogen transformations. *Soil Sci. Soc. Am. J.* **2010**, *74*, 1259–1270. [CrossRef]
16. Guizani, C.; Jeguirim, M.; Valin, S.; Limousy, L.; Salvador, S. Biomass Chars: The Effects of Pyrolysis Conditions on Their Morphology, Structure, Chemical Properties and Reactivity. *Energies* **2017**, *10*, 796. [CrossRef]
17. Hossain, M.K.; Strezov, V.; Chan, K.Y.; Ziolkowski, A.; Nelsona, P.F. Influence of pyrolysis temperature on production and nutrient properties of wastewater sludge biochar. *J. Environ. Manag.* **2011**, *92*, 223–228. [CrossRef] [PubMed]
18. Cantrell, K.B.; Hunt, P.G.; Uchimiya, M.; Novak, J.M.; Ro, K.S. Impact of pyrolysis temperature and manure source on physicochemical characteristics of biochar. *Bioresour. Technol.* **2012**, *107*, 419–428. [CrossRef] [PubMed]
19. Wang, X.; Selvam, A.; Chan, M.; Wong, J.W.C. Nitrogen conservation and acidity control during food wastes composting through struvite formation. *Bioresour. Technol.* **2013**, *147*, 17–22. [CrossRef] [PubMed]
20. Chan, M.T.; Selvam, A.; Wong, J.W.C. Reducing nitrogen loss and salinity during 'struvite' food waste composting by zeolite amendment. *Bioresour. Technol.* **2016**, *200*, 838–844. [CrossRef] [PubMed]
21. Ministry of Environment (MOE). *A Study on FoodWaste Reduction Equipment Guidelines and Quality Standard P*; Ministry of Environment: Sejong City, Korea, 2009.
22. Yang, X.; Wang, H.; Strong, P.J.; Xu, S.; Liu, S.; Lu, K.; Sheng, K.; Guo, J.; Che, L.; He, L.; et al. Thermal Properties of Biochars Derived from Waste Biomass Generated by Agricultural and Forestry Sectors. *Energies* **2017**, *10*, 469. [CrossRef]
23. Quyn, D.M.; Wu, H.; Li, C.-Z. Volatilisation and catalytic effects of alkali and alkaline earth metallic species during the pyrolysis and gasification of Victorian brown coal. Part I. Volatilisation of Na and Cl from a set of NaCl-loaded samples. *Fuel* **2002**, *81*, 143–149. [CrossRef]
24. Korea Rural Development Administration, National Academy of Agricultural Science. *A Method of Inspection of Physical and Chemical Fertilizers*; Rural Development Administration: Jeonju-si, Korea, 2016.

25. Korea Rural Development Administration, National Academy of Agricultural Science. *Methods of Soil Chemical Analysis*; Rural Development Administration: Jeonju-si, Korea, 2010.
26. Zambon, I.; Colosimo, F.; Monarca, D.; Cecchini, M.; Gallucci, F.; Proto, A.R.; Lord, R.; Colantoni, A. An innovative agro-forestry supply chain for residual biomass: Physicochemical characterisation of biochar from olive and hazelnut pellets. *Energies* **2016**, *9*, 526. [CrossRef]
27. Spokas, K.A. Review of the stability of biochar in soils: Predictability of O:C molar ratios. *Carbon Manag.* **2010**, *1*, 289–303. [CrossRef]
28. Mukome, F.N.D.; Zhang, X.; Silva, L.C.R.; Six, J.; Parikh, S.J. Use of chemical and physical characteristics to investigate trends in biochar feedstocks. *J. Agric. Food Chem.* **2013**, *61*, 2196–2204. [CrossRef] [PubMed]
29. Mukome, F.N.D.; Parikh, S.J. Chemical, Physical, and Surface characterization of Biochar. In *Biochar: Production, Characterization, and Applications*; CRC Press: Boca Raton, FL, USA, 2015.
30. Ok, Y.S.; Uchimiya, S.M.; Chang, S.X.; Bolan, N. (Eds.) *Biochar: Production, Characterization, and Applications*; CRC Press: Boca Raton, FL, USA, 2015.
31. Yuan, J.-H.; Xu, R.-K.; Zhang, H. The forms of alkalis in the biochar produced from crop residues at different temperatures. *Bioresour. Technol.* **2011**, *102*, 3488–3497. [CrossRef] [PubMed]
32. Wu, W.; Yang, M.; Feng, Q.; McGrouther, K.; Wang, H.; Lu, H.; Chen, Y. Chemical characterization of rice straw-derived biochar for soil amendment. *Biomass Bioenergy* **2012**, *47*, 268–276. [CrossRef]
33. Sohi, S.P.; Krull, E.; Lopez-Capel, E.; Bol, R. A review of biochar and its use and function in soil. *Adv. Agron.* **2010**, *105*, 47–82.
34. Zhao, S.-X.; Ta, N.; Wang, X.-D. Effect of Temperature on the Structural and Physicochemical Properties of Biochar with Apple Tree Branches as Feedstock Material. *Energies* **2017**, *10*, 1293. [CrossRef]
35. Van Zwieten, L.; Kimber, S.; Morris, S.; Chan, K.Y.; Downie, A.; Rust, J.; Joseph, S.; Cowie, A. Effects of biochar from slow pyrolysis of papermill waste on agronomic performance and soil fertility. *Plant Soil* **2010**, *327*, 235–246. [CrossRef]
36. Ketterings, Q.; Reid, S.; Rao, R. *Cornell University Agronomy Fact Sheet #22: Cation Exchange Capacity (CEC)*; Cornell University: Ithaca, NY, USA, 2007.
37. Bourke, J.; Manley-Harris, M.; Fushimi, C.; Dowaki, K.; Nunoura, T.; Antal, M.J., Jr. Do all carbonized charcoals have the same chemical structure? 2. A model of the chemical structure of carbonized charcoal. *Ind. Eng. Chem. Res.* **2007**, *46*, 5954–5967. [CrossRef]
38. Guerrero, M.; Ruiz, M.P.; Millera, Á.; Alzueta, M.U.; Bilbao, R. Characterization of biomass chars formed under different devolatilization conditions: Differences between rice husk and eucalyptus. *Energy Fuels* **2008**, *22*, 1275–1284. [CrossRef]
39. Keiluweit, M.; Nico, P.S.; Johnson, M.G.; Kleber, M. Dynamic molecular structure of plant biomass-derived black carbon (biochar). *Environ. Sci. Technol.* **2010**, *44*, 1247–1253. [CrossRef] [PubMed]
40. Herbert, L.; Hosek, I.; Kripalani, R. *The Characterization and Comparison of Biochar Produced from a Decentralized Reactor Using Forced Air and Natural Draft Pyrolysis*; California Polytechnic State University: San Luis Obispo, CA, USA, 2012.
41. Cheng, C.-H.; Lehmann, J.; Thies, J.E.; Burton, S.D.; Engelhardb, M.H. Oxidation of black carbon by biotic and abiotic processes. *Org. Geochem.* **2006**, *37*, 1477–1488. [CrossRef]
42. Boeriu, C.G.; Bravo, D.; Gosselink, R.J.A.; van Dam, J.E.G. Characterisation of structure-dependent functional properties of lignin with infrared spectroscopy. *Ind. Crop. Prod.* **2004**, *20*, 205–218. [CrossRef]
43. Kačuráková, M.; Wilson, R.H. Developments in mid-infrared FT-IR spectroscopy of selected carbohydrates. *Carbohydr. Polym.* **2001**, *44*, 291–303. [CrossRef]
44. Lammers, K.; Arbuckle-Keil, G.; Dighton, J. FT-IR study of the changes in carbohydrate chemistry of three New Jersey pine barrens leaf litters during simulated control burning. *Soil Biol. Biochem.* **2009**, *41*, 340–347. [CrossRef]
45. Kubo, S.; Kadla, J.F. Hydrogen bonding in lignin: A Fourier transform infrared model compound study. *Biomacromolecules* **2005**, *6*, 2815–2821. [CrossRef] [PubMed]
46. Parimala, K.; Balachandran, V. Structural study, NCA, FT-IR, FT-Raman spectral investigations, NBO analysis and thermodynamic properties of 2′, 4′-difluoroacetophenone by HF and DFT calculations. *Spectrochim. Acta Part A Mol. Biomol. Spectrosc.* **2013**, *110*, 269–284. [CrossRef] [PubMed]

47. Porchelvi, E.E.; Muthu, S. The spectroscopic (FT-IR, FT-Raman and NMR), NCA, Fukui function analysis first order hyperpolarizability, TGA of 6-chloro-3, 4dihydro-2H-1, 2, 4-benzothiazine-7-sulphonamide1, 1-dioxide by ab initio HF and Density Functional method. *Spectrochim. Acta Part A Mol. Biomol. Spectrosc.* **2014**, *123*, 230–240. [CrossRef] [PubMed]
48. Mcbeath, A.V.; Smernik, R.J.; Krull, E.S.; Lehmann, J. The influence of feedstock and production temperature on biochar carbon chemistry: A solid-state 13 C NMR study. *Biomass Bioenergy* **2014**, *60*, 121–129. [CrossRef]
49. Knicker, H.; Hilscher, A.; González-Vila, F.J.; Almendros, G. A new conceptual model for the structural properties of char produced during vegetation fires. *Org. Geochem.* **2008**, *39*, 935–939. [CrossRef]
50. Brewer, C.E.; Unger, R.; Schmidt-Rohr, K.; Brown, R.C. Criteria to select biochars for field studies based on biochar chemical properties. *BioEnergy Res.* **2011**, *4*, 312–323. [CrossRef]

© 2017 by the authors. Licensee MDPI, Basel, Switzerland. This article is an open access article distributed under the terms and conditions of the Creative Commons Attribution (CC BY) license (http://creativecommons.org/licenses/by/4.0/).

energies

MDPI

Article

Experimental Model Development of Oxygen-Enriched Combustion Kinetics on Porous Coal Char and Non-Porous Graphite

Gyeong-Min Kim [1,†], Jong-Pil Kim [1,†], Kevin Yohanes Lisandy [1] and Chung-Hwan Jeon [1,2,*]

[1] School of Mechanical Engineering, Pusan National University, Busan 46241, Korea; Energy_min@pusan.ac.kr (G.-M.K.); kjfeel@pusan.ac.kr (J.-P.K.); Kevinlie23@pusan.ac.kr (K.Y.L.)
[2] Pusan Clean Coal Center, Pusan National University, Busan 46241, Korea
* Correspondence: chjeon@pusan.ac.kr; Tel.: +82-51-510-3051; Fax: +82-51-510-5236
† These authors contributed equally to the work.

Received: 28 August 2017; Accepted: 15 September 2017; Published: 18 September 2017

Abstract: The effect of oxygen-enriched air on low-rank coal char combustion was experimentally investigated. In this work, a coal-heating reactor equipped with a platinum wire mesh in the reaction chamber was used to analyze the combustion temperature, reaction time, and reaction kinetics. Increasing the oxygen content of the primary combustion air increased the combustion temperature and decreased the reaction time. As the oxygen content increased from 21% to 30%, the average temperature increased by 47.72 K at a setup temperature of 1673 K, and the reaction time decreased by 30.22% at the same temperature. The graphite sample exhibited similar trends in temperature and reaction time, although the degree of change was smaller because the pores produced during char devolatilization expanded the active surface available for oxidation of the char sample. A mathematical model was used to define the intrinsic kinetics of the reaction. As the oxygen content increased from 21% to 30%, the reaction rate of the low-rank coal char increased. These results were also compared with those of the graphite sample.

Keywords: combustion; oxygen enrichment; low-rank coal char; char oxidation; reaction kinetics

1. Introduction

Coal is used to generate electricity in coal-fired power plants, despite it being an old technology, due to its abundance and low cost. However, almost half of reserves in the world are low-rank coal, and there is a policy burden due to the high price of high-rank coal. Therefore, in recent years several efforts have been made to develop technologies for utilizing the relatively inexpensive low-rank coal [1,2].

Drying and dewatering technologies for low-rank coal have been reported by many researchers. Both evaporative drying technologies such as rotary drying, fluidized-bed drying, and hot-oil-immersion drying, and non-evaporative drying technologies, such as the hydrothermal dewatering, mechanical/thermal dewatering, and solvent extraction have been studied to enable the utilization of low-rank coal as a high-efficiency energy resource [3]. Various reaction models have been suggested to improve the combustion of low-rank coal [4,5]. A wire-heating reactor was used to measure the temperature of low-rank coal char, and a spot-ignition model was suggested for the evaluation of the intrinsic reaction kinetics and the prediction of the ignition temperature [6]. A pressurized wire-heating reactor was also used to predict the gasification kinetics of low-rank coal char in a CO_2 atmosphere. The study indicated that the reaction kinetics were affected by elevated pressure (up to 30 atm) and high temperature (up to 1723 K) [7]. However, single particle measurements of coal char ignition temperature or gasification reaction kinetics cannot provide small

particle size char measurements (e.g., 75–90 μm); therefore, a method utilizing wire-mesh was used in this study. A pressurized wire-mesh reactor was also utilized in several studies for measuring the kinetics of different gasification reactions (e.g., reactions with O_2, CO_2, and H_2O) [3,6,7]. An attempt was made to study the use of sodium ions as an effective catalyst for the gasification of low-rank coal. The experimental results showed that the heat treatment of low-rank coal can thermochemically affect the gasification rate via carbon conversion [8].

On the other hand, oxy-fuel and oxygen-enriched combustion of pulverized coal have been studied in order to improve the efficiency while reducing emissions in coal-fired power plants. Several studies on oxy-fuel combustion have found it to be a promising technology for capturing CO_2 from power plants. The researchers reported combustion fundamentals and modeling under oxy-fuel conditions, including the combustion physics and chemistry [9]. In addition, the effect of the CO_2 gasification reaction on coal char combustion under oxy-fuel conditions was simulated. The results showed that the gasification reaction was affected by both the char burnout time and the relative carbon consumption [10]. Oxygen-enriched combustion, which enhances the energy efficiency and reduces emissions, has also been reported by many researchers as an emerging technology for more efficient power generation [11,12]. The combustion kinetics of coal chars in an oxygen-enriched atmosphere were studied [13–15]. The results showed that under these conditions, the char combustion temperature increased and the char burnout time was reduced [15]. Natural gas combustion systems can also use oxygen-enriched air. In order to investigate the heating rate, emissions, temperature distributions, and fuel consumption in a system with extra oxygen content, 21–30% excess oxygen was used in a gas-fired burner [16]. The effect of oxygen content in a biomass-fueled burner was also investigated. The results showed improvements in flame shape, emission reduction, and burnout for oxygen-enriched combustion using biomass as the fuel [17]. The oxygen enrichment of co-fired blended coal and biomass was studied, with experimental tests on NO_x and SO_x emissions and burnout in atmospheres enriched with 25–30% oxygen being conducted [18].

This study focused on the effect of oxygen-enriched air on combustion when utilizing low-rank coal as an energy source. Experiments on the combustion temperature and the reaction time were conducted using a coal-heating reactor equipped with a platinum wire mesh in the reaction chamber when the oxygen content of the primary combustion air was increased from 21% to 30%. The well-established random pore model (RPM) was proposed several decades ago by Gavalas, Bhatia, and Perlmutter [19–21]. However, the work of Lisandy et al. showed that in some applications, especially when modeling the development of low-rank coal char reaction rates, significant deviations from this model were observed [22–24]. Based on these studies, the reaction kinetics of low-rank coal char under oxygen-enriched combustion conditions were analyzed. A mathematical model was established incorporating experimental thermogravimetric analysis data. The results of the analysis and experiments were compared with those obtained for graphite, which has a poor pore structure.

2. Experimental Methods

2.1. Sample Preparation

Coal particle reactions in conventional coal-fired boilers can generally be divided into two concepts: coal devolatilization and char oxidation [25]. During the devolatilization of raw coal, most of the moisture and volatile matter in the coal are removed, and the remaining particles, referred to as char, are then employed in oxidization or combustion with oxygen at sufficiently high temperatures (1100–1400 °C). This study focused on char combustion at high temperatures. Coal char production for the experiment was performed using the following process.

Raw low-rank coal (Indonesian sub-bituminous coal, Figure 1a, was dried for 1 day at 45 °C. The sample powder used as fuel had particle sizes of 75–90 μm. After drying, the sample was heated to 1000 °C at a heating rate of 10 °C/min in a thermogravimetric analyzer (TGA701, LECO Co., St. Joseph, MI, USA) under a nitrogen atmosphere. Figure 1a,b show the differences between the morphologies of

the coal before and after the char production process [26]. As can be seen in Figure 1b, some pores developed in the char due to the removal of moisture and volatile matter. Figure 1c shows graphite powder with particles in the range of 75–90 μm to allow for a comparison with the characteristics of the char. Table 1 summarizes the results of the proximate and ultimate analyses of the raw coal, char, and graphite.

The initial specific surface area of the char was measured by the Brunauer-Emmett-Teller (BET) method using a Micromeritics ASAP 2020 device. The morphologies of the coal samples were examined by scanning electron microscopy (SEM, S3500N, Hitachi, Tokyo, Japan).

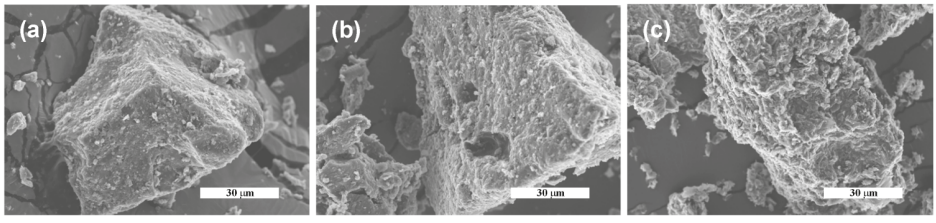

Figure 1. Scanning electron microscopy images of samples for oxygen-enriched combustion: (**a**) raw coal, (**b**) char, and (**c**) graphite.

Table 1. Proximate and ultimate analyses of samples.

Samples	Proximate Analysis (wt %, ad)				Ultimate Analysis (wt %, daf)				
	Moisture	Volatile Matter (daf)	Ash (dry)	Fixed Carbon (daf)	C	H	N	O	S
Raw low-rank coal	14.55	37.20	6.51	41.74	65.45	5.35	0.46	27.07	1.67
Low-rank coal char	1.84	2.16	9.15	86.85	93.26	0.23	0.42	5.78	0.31
Graphite	0.05	1.74	0.0	98.21	99.12	0.81	0.0	0.0	0.06

ad: air-dry basis; daf: dry and ash-free basis; Oxygen by difference.

2.2. Coal Heating Reactor

The experimental setup of the coal-heating reactor for the proposed oxygen-enriched combustion is shown in Figure 2 [27]. The heating reactor can be used for combustion under high-temperature conditions of up to 1750 K. A Pt wire mesh in the chamber was used to generate heat using a direct current (DC) electrical power supply (OPE-18100S, 4.7 kW, ODA Technologies Co., Ltd., Incheon, Korea) that was controlled using computer software. In this study, the temperatures used for coal heating were measured as 1373, 1473, 1573, and 1673 K.

The Pt mesh (99.9% purity) had a wire diameter of 0.04 mm, and the wire interval was 75 μm. In order to obtain the combustion temperature and reaction time, a thermocouple was located at the center of the Pt mesh.

Coal char samples were loaded onto the wire mesh in a thin layer configuration, as shown in Figure 2a. Figure 2b shows the heating state, in which the Pt mesh was heated in the coal-heating reactor. The primary reactant gas was introduced to the chamber during combustion from the atmosphere or from a mixed gas tank for the 21% and 30% oxygen conditions, respectively, and was released back into the atmosphere after combustion.

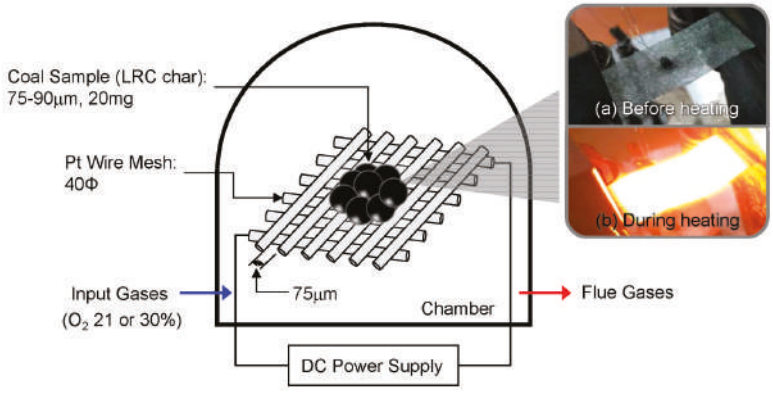

Figure 2. Schematic of the coal heating reactor. The photographs on the right show the system (**a**) before heating and (**b**) during heating.

2.3. Numerical Methods for Kinetics

In this study, a mathematical model was suggested for the calculation of the reaction kinetics of coal char combustion with an oxygen content of 21–30% after devolatilization. The carbon conversion ratio can be expressed as:

$$x = \frac{m_0 - m_t}{m_0 - m_{ash}} \tag{1}$$

where m_0 is the initial mass of the coal char, m_t is the mass of the coal char at time t, and m_{ash} is the mass of the ash content.

The apparent reaction rate (R_{app}) is expressed as:

$$R_{app} = \frac{dx}{dt} \tag{2}$$

where R_{app} is the change of carbon conversion over time.

The random pore model (RPM) is widely used to simulate changes in the micropore structure of coal char. However, when considering most low-rank coal or biomass, the random pore model does not fit well with observations. In order to achieve more accurate pore development modeling and reaction rate correlations, the Flexibility-Enhanced Random Pore Model (FERPM) proposed by Lisandy et al. was used in this study [22]. During the coal char oxidation reaction, the loss of coal char occurs rapidly. Thus, the micropore structure of the coal char also changes rapidly. In order to calculate the pore development (S_g), the RPM and FERPM were both used in this study, and they are shown below:

$$\frac{dx}{dt} = k_{RPM}(1-x)\sqrt{1 - \psi_{RPM}\mathrm{In}(1-x)} \tag{3}$$

$$\frac{dx}{dt} = k_{FERPM}\left[(1-x)^a\sqrt{1 - \psi_{FERPM}\mathrm{In}(1-x)}\tanh(cx) + (1-x)^b\right] \tag{4}$$

where k_{RPM} and k_{FERPM} are the initial reaction rates as a function of the temperature, and ψ_{RPM} and ψ_{FERPM} are the structural parameters. a, b and c are extra parameters for improving the accuracy of the prediction.

In order to determine the intrinsic reaction rate of the coal char oxidation (R_{in}, g/cm^2·s), an nth-order rate equation was used. The nth-order rate equation of the global reaction can be expressed in its Arrhenius form as:

$$R_{in} = A_{in}\exp\left(-\frac{E_{in}}{R_u T_p}\right)P_{O_2,\infty}^n \tag{5}$$

where A_{in} is the intrinsic pre-exponential factor, E_{in} is the intrinsic activation energy, R_u is the universal gas constant, T_p is the coal char particle temperature, $P_{O_2,\infty}$ is the partial pressure of oxygen in the ambient atmosphere, and n is the reaction order, which was derived from the experimental results. This equation is defined by the reaction order and two Arrhenius parameters, A_{in} and E_{in}.

In order to analyze the oxidation of the coal char, the effect of the internal and external effectiveness factors should be considered. The apparent reaction rate is then expressed as [28]:

$$R_{app} = \eta_{in}\eta_{ex}S_g R_{in} \tag{6}$$

The internal effectiveness factor can be defined by the Thiele modulus (ϕ), which was developed to determine the relationship between the diffusion and the reaction rate in a microporous structure [29,30]:

$$\eta_{in} = \frac{1}{\phi}\left(\frac{1}{\tanh(3\phi)} - \frac{1}{3\phi}\right) \tag{7}$$

$$\phi = \frac{d_p}{2}\sqrt{\frac{(n+1)\nu S_g \rho_p k_{in} R_u T_p P_{O_2,S}^{n-1}}{2D_{eff,O_2}}} \tag{8}$$

where d_p is the diameter of the coal char, ν is the stoichiometric coefficient (i.e., 0.0833 moles of O_2 consumed per gram of reacted carbon), ρ_p is the apparent density, and D_{eff,O_2} is the effective O_2 diffusion coefficient in the coal char surface.

D_{eff,O_2} is calculated as:

$$D_{eff,O_2} = \frac{\varepsilon}{\tau}D \tag{9}$$

where is the porosity, D is the diffusivity, and τ is the tortuosity coefficient of the coal char pore, and its value is assumed to 1.414 [31]. The diffusivity, D, is calcas:

$$D = \frac{1}{\frac{1}{D_{AB}} + \frac{1}{D_k}} \tag{10}$$

where D_{AB} is the binary diffusivity and D_k is the Knudsen diffusivity, which is the diffusion that occurs when the diameter of the pore is comparable to or smaller than the mean free path of the gas particles involved. These diffusivities are expressed as [29–31]:

$$D_k = 4580 d_{pore}\sqrt{\frac{T_p}{M_A}} \tag{11}$$

$$D_{AB} = \frac{0.02628T^{3/2}}{M_{AB}^{1/2}\sigma_{AB}^2\Omega_{AB}P} \tag{12}$$

where d_{pore} is the diameter of the coal char pore, M_A is the molar mass, M_{AB} is the mixed molar mass of A and B, σ_{AB} is the particle collision diameter, Ω_{AB} is the collision integral, and P is the total pressure of the system.

The external effectiveness factor (η_{ex}) is an expression of gas transport to the boundary layer, which is the ratio of the partial pressure of the particle surface to the ambient atmosphere surrounding the coal char particle, and is expressed as:

$$\eta_{ex} = \frac{P_{O_2,S}}{P_{O_2,\infty}} \tag{13}$$

The kinetic coefficients of the reaction can be considered by the linear regression method as follows:

$$R_{app} = \eta_{in}\eta_{ex}^{n} S_g A_{in} \exp(-\frac{E_{in}}{R_u T_p}) P_{O_2,\infty}^{n} \tag{14}$$

$$\ln(\frac{R_{app}}{\eta_{in}\eta_{ex}^{n} P_{O_2,\infty}^{n}}) = \ln A_{in} S_g - \frac{E_{in}}{R_u T_p} \tag{15}$$

$$\ln(R_{app}) = n \ln(\eta_{ex} P_{O_2,\infty}) + \ln\left\{\eta_{in} S_g A_{in} \exp\left(-\frac{E_{in}}{R_u T_p}\right)\right\} \tag{16}$$

3. Results and Discussion

3.1. Combustion Temperature and Reaction Time

Table 2 shows the variations in combustion temperature and reaction time for low-rank coal char and graphite when the oxygen content of the primary combustion air in the coal-heating reactor was increased from 21% to 30%. The experimental data are the mean value from 10 of replicate experiments and measurements. The setup temperature, or the combustion temperature during char oxidation, was set to four values. Most of the results shown in Table 2 show more significant reaction time reductions in the lower temperature region (e.g., a 35–38% reaction time reduction at a setup temperature of 1373 K, as compared to a 28–30% reduction at a setup temperature of 1673 K). These results suggest that improved reaction rates can be achieved at lower combustion temperatures.

Table 2. Combustion temperatures and reaction time variations for oxygen-enriched combustion.

Samples	Low-Rank Coal Char				Graphite			
	O_2 21% (N_2 Balance)		O_2 30% (N_2 Balance)		O_2 21% (N_2 Balance)		O_2 30% (N_2 Balance)	
Setup Temperature (K)	Maximum Temperature (K)	Reaction Time (s)	Maximum Temperature (K)	Reaction Time (s)	Maximum Temperature (K)	Reaction Time (s)	Maximum Temperature (K)	Reaction Time (s)
1373	1411.34	2.6	1420.37	1.6	1393.71	4.4	1415.30	2.88
1473	1514.68	1.98	1532.83	1.35	1525.65	2.5	1539.83	1.68
1573	1619.17	1.7	1658.47	1.15	1616.79	1.8	1654.08	1.25
1673	1721.69	1.43	1769.41	1	1705.29	1.37	1764.35	0.98

In the case of low-rank coal char at a setup temperature of 1373 K, the difference between the maximum temperatures for oxygen contents of 21% and 30% was 9 K. When the setup temperature was increased, this temperature difference tended to increase. The difference between the maximum temperatures was 47 K at a setup temperature of 1673 K.

In comparison, graphite exhibited an identical trend to that of the low-rank coal char. In the case of graphite at a setup temperature of 1373 K, the difference between the maximum temperatures for oxygen contents of 21% and 30% was 21 K. Additionally, it exhibited an increase in maximum temperature of 59.06 K at a setup temperature of 1673 K.

The results suggest that low-rank coal char developed a surface pore structure during the devolatilization process, and that this pore structure contributed to the combustion reaction by increasing the surface area. On the other hand, graphite, which has a carbon content of 99.21%, had a poor pore structure. It therefore exhibited a slow reaction at relatively low setup temperature. However, a higher environmental temperature resulted in a more effective surface for combustion, with the oxidation reaction occurring so rapidly at the particle surface that the oxidation gas could not diffuse through the pores. For this reason, the reaction time for graphite became similar to that of low-rank coal char at temperatures around 1673 K.

3.2. Reaction Kinetics

The surface area of coal char as calculated by RPM and FERPM can be expressed as follows:

$$S_{g,RPM} = S_0(1-x)\sqrt{1-\psi_{RPM}\ln(1-x)} \tag{17}$$

$$S_{g,FERPM} = S_0[(1-x)^a\sqrt{1-\psi_{FERPM}\ln(1-x)}\tanh(cx)+(1-x)^b] \tag{18}$$

An experiment was performed during thermogravimetric analysis (TGA) in order to define the structural parameters ψ_{RPM} and ψ_{FERPM}. Samples of 15 mg of coal char or graphite were heated to 1273 K at a ramp rate of 20 K/min under a N_2 atmosphere. After remaining isothermal at 1273 K for 10 min, the gas was changed to air and the samples were reacted isothermally at 1273 K for 30 min. The structural parameters ψ_{RPM} and ψ_{FERPM} were obtained by fitting the TGA analyses with the RPM and FERPM, as shown in Figures 3 and 4. As discussed previously, the surface areas S_g determined in Figures 3 and 4 shows that graphite had almost no microporous structure when compared to the low-rank coal char. Moreover, the FERPM was calculated using a correction function with the optimal values of the pore development model during coal combustion, including gasification. The correlation coefficient between the experimental and fitting results using the RPM was 0.6532 for low-rank coal char, while the value for graphite was 0.8376. The FERPM led to much higher correlation coefficients, with the value for low-rank coal char being 0.9956, and that for graphite being 0.9980. The improvement in the fitting correlation would be very helpful for modeling purposes as predictions that are more accurate can be made using the revised model. Table 3 summarizes the calculated structural parameters (ψ) and initial particle surface areas (S_0) of low-rank coal char and graphite. The structural parameter of low-rank coal char shows a good agreement with the prediction obtained by using the equation proposed by the literature [22], which predicts that the coal with a fixed carbon content of 42% should have a structural parameter about 0.46. However, the results for graphite, which has a carbon content of 98%, did not agree with the value provided by FERPM equation, which predicted a structural parameter of around 1. This may be due to the different fuel types used in the literature, which predicted structural changes for the thermal coal. This means that graphite was not considered in the range of fuel types used by the literature.

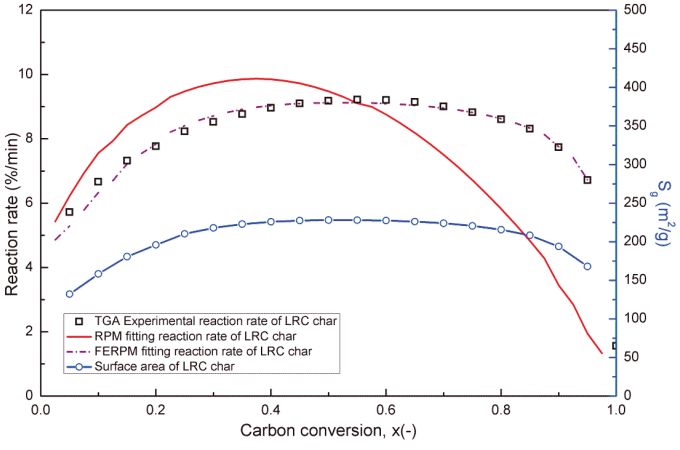

Figure 3. Char oxidation reaction rates and surface areas (S_g) for the carbon conversion of low-rank coal char as calculated by the random pore model (RPM) and Flexibility-Enhanced Random Pore Model (FERPM) using thermogravimetric analyzer (TGA) apparatus.

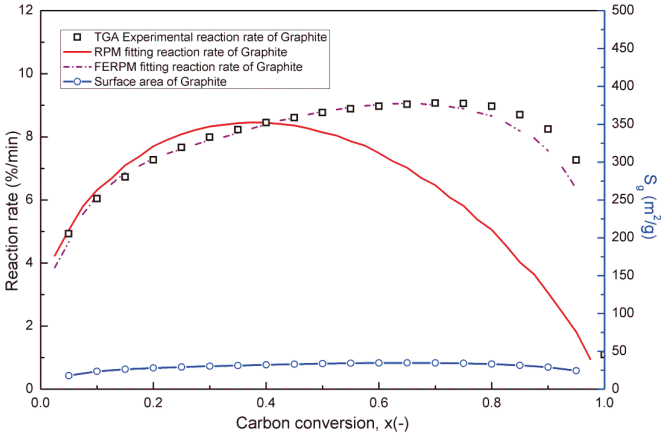

Figure 4. Oxidation reaction rates and surface areas (S_g) for the carbon conversion of graphite as calculated by the RPM and FERPM using TGA apparatus.

Table 3. Calculated structural parameters (ψ), FERPM parameters, and initial particle surface areas (S_0) of low-rank coal char and graphite.

Samples	Low-Rank Coal Char	Graphite
Structural parameter (ψ_{RPM})	23.63	32.99
Structural parameter (ψ_{FERPM})	6.81	17.43
FERPM parameter (a)	0.38	0.46
FERPM parameter (b)	2.40	6.63
FERPM parameter (c)	5.53	12.34
Initial particle surface area (S_0) (BET Ar adsorption, m^2/g)	113.4201	12.8004

The coal char surface area (S_g) was used to determine the intrinsic reaction rate, as discussed in Equation (5). The reaction order (n) can be calculated by linearly fitting the natural logarithm value of the $\eta_{ex} P_{O_2,\infty}$ and R_{app}, as described in Equation (16), with the calculated reaction order for low-rank coal char being 0.51 and the value for graphite being 0.73. The calculated reaction order results are presented in Figure 5.

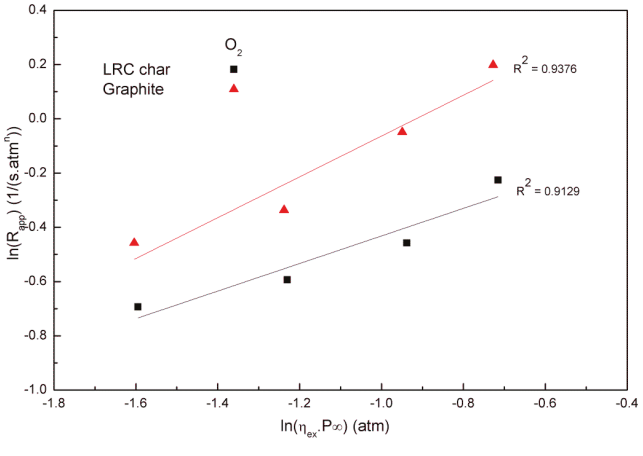

Figure 5. nth order Arrhenius plots for low-rank coal char and graphite.

In order to allow for a comparison of the reaction rate constants when considering oxygen diffusion, the apparent and intrinsic kinetics are shown in Figures 6 and 7, and Table 4, calculated by the linear regression method using Equation (15). From an Arrhenius plot, Ln k versus 1/T, a linear relationship is obtained and according to Equation (15), the activation energy and the pre-exponential factor can be calculated. The results imply that the intrinsic and apparent reaction kinetics considered both internal and external effectiveness factors at ambient oxygen concentrations of 21% and 30% as the temperature increased. Low-rank coal char and graphite both showed more significant differences between their intrinsic and apparent reaction kinetics at increased temperatures. Moreover, the results suggest that the samples were diffusion controlled, with the effectiveness factors shown in Figures 8 and 9 providing evidence to support this conclusion. To evaluate the effectiveness factors obtained from the intrinsic reaction rates at high a temperature, the external effectiveness factor decreased from 1 to 0.95, with graphite being slightly more affected by the external effectiveness factor. Meanwhile, the internal effectiveness factors decreased significantly as the temperature dropped. This implies that the reaction rates of the two samples were controlled by diffusion at high temperatures [6].

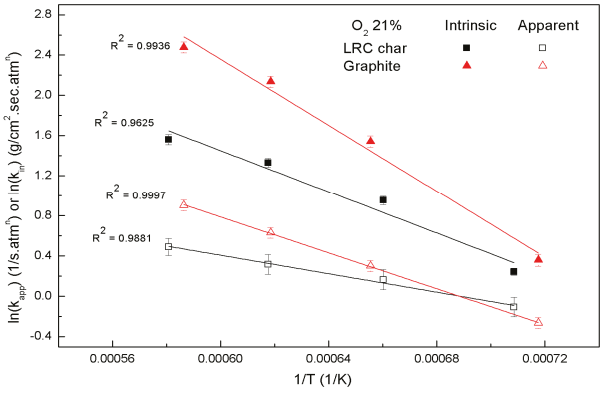

Figure 6. Comparison of reaction rate constants when considering oxygen diffusion at an ambient oxygen concentration of 21%.

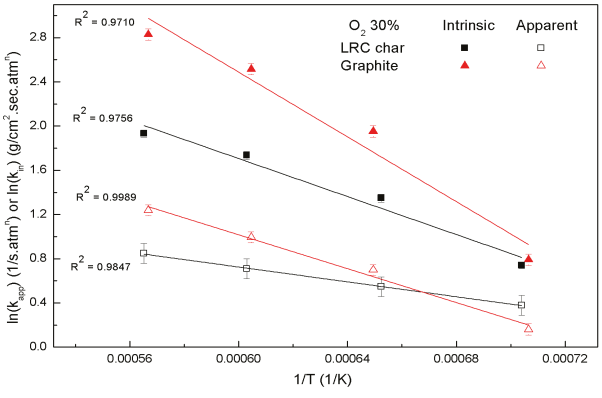

Figure 7. Comparison of reaction rate constants when considering oxygen diffusion at an ambient oxygen concentration of 30%.

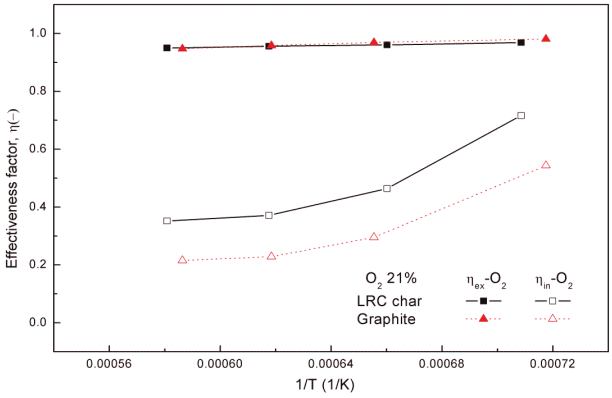

Figure 8. Effectiveness factors as a function of particle temperature at an ambient oxygen concentration of 21%.

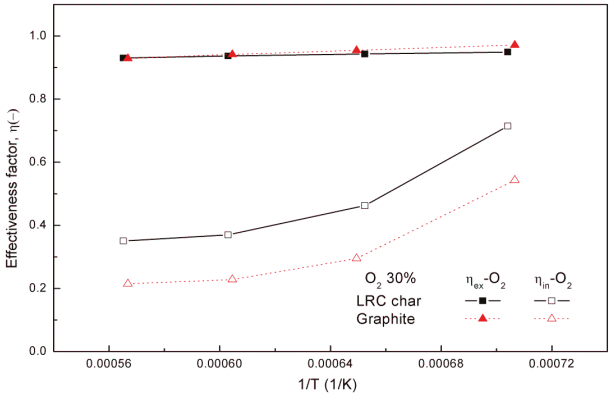

Figure 9. Effectiveness factors as a function of particle temperature at an ambient oxygen concentration of 30%.

Table 4. Linear regression results for the intrinsic reaction rates expressed as *n*th-order Arrhenius equations.

Samples		Low-Rank Coal Char		Graphite	
		O_2 21% (N_2 Balance)	**O_2 30% (N_2 Balance)**	**O_2 21% (N_2 Balance)**	**O_2 30% (N_2 Balance)**
Reaction order, (-)		0.5081		0.7295	
Apparent kinetics	E_a (kJ/mol)	38.1	27.9	74.1	63.7
	A ($1/s \cdot atm^n$)	1.031×10^{-5}	6.81×10^{-6}	1.363×10^{-3}	8.105×10^{-4}
Intrinsic kinetics	E_a (kJ/mol)	85.5	71.4	136.6	121.7
	A ($g/cm^2 \cdot s \cdot atm^n$)	8.956×10^{-4}	4.186×10^{-4}	5.954×10^{-1}	2.315×10^{-1}

It is apparent from the plots and the table that increasing the amount of oxygen in the atmosphere increased the burning rate in the char kinetics, in spite of the faster char combustion rates. The absolute values of the slopes of Figures 6 and 7 give the activation energies, E, and the intercepts with the y-axis provide the natural logarithms of the pre-exponential factors, A.

In order to define the intrinsic kinetics of the reaction, a mathematical model was used. The activation energy of the low-rank coal char sample reacted at an O_2 concentration of 21% was 85.5 kJ/mol, and the pre-exponential factor was 8.956×10^{-4} g/cm^2·s·atm^n, whereas the low-rank coal char sample reacted at an O_2 concentration of 30% had an activation energy of 71.4 kJ/mol and a pre-exponential factor of 4.186×10^{-4} g/cm^2·s·atm^n. Similarly, the activation energy of the graphite sample reacted at an O_2 concentration of 21% was 136.6 kJ/mol, and the pre-exponential factor was 5.954×10^{-1} g/cm^2·s·atm^n, whereas the graphite sample reacted at an O_2 concentration of 30% had an activation energy of 121.7 kJ/mol and a pre-exponential factor of 2.315×10^{-1} g/cm^2·s·atm^n. Based on these results, it can be seen that increasing the oxygen concentration in combustion promoted the char reaction rate and lowered the activation energy. The intrinsic kinetics derived from the mathematical model showed the same trend as the experimental results. As the oxygen content increased, the reaction rates of both the coal char and the graphite sample increased. Thus, oxygen-enriched combustion could help to enlarge fuel range utilization so that low-rank coal, which is hardly used in coal-fired boilers, can be used as a more common fuel.

4. Conclusions

A coal-heating reactor was utilized for oxygen-enriched combustion with oxygen concentrations of 21–30%. It consisted of a Pt wire mesh for generating heat from a DC power supply and a setup temperature controller. Low-rank coal char samples (75–90 μm) produced from pyrolysis of the raw coal were used as fuel for char oxidation, and the experimental results were compared with those obtained by using graphite with a carbon content of 99.12 wt %.

As the oxygen content in the reactor atmosphere was increased from 21% to 30%, the combustion temperature of the low-rank coal char increased by 47.72 K at a setup temperature of 1673 K, whereas the reaction time decreased by 30.22% at the same temperature. The graphite sample exhibited similar trends in combustion temperature and reaction time. This suggests that the difference between the temperature changes of the two samples at a low temperature was caused by the development of a microporous structure during the initial stage of combustion. A numerical model was chosen for calculating the reaction kinetics of the coal char in the presence of an oxygen content of 21–30%.

The structural parameters used in the fitting of the low-rank coal experiment result in a good agreement between the FERPM and predictions from previous work. However, in the case of graphite, a parameter outside of the predicted range was observed. This shows that the application of the prediction model proposed in the previous work to a wider range of fuel types is improper, despite the good agreement between the result and the model when using a prediction of the fitting parameter outside of the usual range.

The activation energy of the low-rank coal char sample when reacted in an atmosphere with an oxygen content of 21% was 85.5 kJ/mol, and the pre-exponential factor was 8.956×10^{-4} g/cm^2·s·atm^n. The low-rank coal char sample reacted at 30% oxygen content and had an activation energy of 71.4 kJ/mol and a pre-exponential factor of 4.186×10^{-4} g/cm^2·s·atm^n. The value of the activation energy was reduced at 30% oxygen content. Therefore, it is apparent that the reactivity of the low-rank coal char improved in a 30% oxygen atmosphere when compared to its reactivity in a 21% oxygen atmosphere. Furthermore, the graphite sample exhibited the same trend as was seen for the experimental results for the low-rank coal char.

Acknowledgments: This work was supported by the Power Generation & Electricity Delivery Core Technology Program of the Korea Institute of Energy Technology Evaluation and Planning (KETEP), and was granted financial resources from the Ministry of Trade, Industry & Energy, Korea (No. 20131010101810).

Author Contributions: C.-H.J., J.-P.K. and G.-M.K. conceived and designed the experiments; G.-M.K. and J.-P.K. performed the experiments; G.-M.K., J.-P.K. and K.Y.L. analyzed the data; G.-M.K., J.-P.K. and C.-H.J. wrote the paper.

Conflicts of Interest: The authors declare no conflict of interest.

Nomenclature

A_{int}	intrinsic pre-exponential factor (g/cm^2·s)
C	reaction rate constant (1/s)
D	diffusion constant (cm^2/s)
D_{AB}	molecular diffusion coefficient (cm^2/s)
$D_{eff,O2}$	effective O_2 diffusion coefficient (cm^2/s)
d_p	diameter (cm)
d_{pore}	pore diameter (cm)
E_{int}	intrinsic activation energy (kJ/mol)
k_{app}	apparent rate constant (1/s)
k_{int}	Intrinsic rate constant (g/cm^2·s·atm)
m	mass (g)
m_{ash}	ash mass (g)
m_0	initial mass of char (g)
m_t	mass of char at the time (g)
M	molecular mass (g/mol)
M_{AB}	mixed molar mass of A and B (g/mol)
n	Reaction order
P	pressure (atm)
$P_{O2,S}$	partial pressure of O_2 with at the external particle surface (atm)
$P_{O2,\infty}$	partial pressure of O_2 in the ambient atmosphere (atm)
R_{app}	apparent reaction rate (1/s)
R_{int}	intrinsic reaction rate (1/s)
R_u	gas constant (8.314×10^{-3} KJ/(mol·K) = 82.057 atm/(cm^3·mol·K))
S_g	surface area (cm^2/g)
T_p	particle temperature (K)
x	carbon conversion (g/g)

Greek Symbols

ε	char particle porosity
Φ	Thiele modulus
η_{ex}	external effectiveness factor for gas transport in the boundary layer
η_{in}	internal effectiveness factor
ν	stoichiometric coefficient
τ	tortuosity factor of the pore (=1.414)
ρ_p	apparent density (g/cm^3)

References

1. Tchapda, A.H.; Pisupati, S.V. A Review of Thermal Co-Conversion of Coal and Biomass/Waste. *Energies* **2014**, *7*, 1098–1148. [CrossRef]
2. Wang, P.; Means, N.; Shekhawat, D.; Berry, D.; Massoudi, M. Chemical-Looping Combustion and Gasification of Coals and Oxygen Carrier Development: A Brief Review. *Energies* **2015**, *8*, 10605–10635. [CrossRef]
3. Rao, Z.; Zhao, Y.; Huang, C.; Duan, C. Recent developments in drying and dewatering for low rank coals. *Prog. Energy Combust. Sci.* **2015**, *46*, 1–11. [CrossRef]
4. Hwang, M.; Song, E.; Song, J. One-Dimensional Modeling of an Entrained Coal Gasification Process Using Kinetic Parameters. *Energies* **2016**, *9*, 99. [CrossRef]
5. Wang, H.; Zhang, J.; Wang, G.; Zhao, D.; Guo, J.; Song, T. Research on the Combustion Characteristics and Kinetic Analysis of the Recycling Dust for a COREX Furnace. *Energies* **2017**, *10*, 255. [CrossRef]
6. Kim, R.G.; Jeon, C.H. Intrinsic reaction kinetics of coal char combustion by direct measurement of ignition temperature. *Appl. Therm. Eng.* **2014**, *63*, 565–576. [CrossRef]
7. Kim, R.G.; Hwang, C.W.; Jeon, C.H. Kinetics of coal char gasification with CO_2: Impact of internal/external diffusion at high temperature and elevated pressure. *Appl. Energy* **2014**, *129*, 299–307. [CrossRef]

8. Zhang, D.K.; Poeze, A. Variation of sodium forms and char reactivity during gasification of a South Australian low-rank coal. *Proc. Combust. Inst.* **2000**, *28*, 2337–2344. [CrossRef]
9. Yin, C.; Yan, J. Oxy-fuel combustion of pulverized fuels: Combustion fundamentals and modeling. *Appl. Energy* **2016**, *162*, 742–762. [CrossRef]
10. Kim, D.H.; Choi, S.M.; Shaddix, C.R.; Geier, M. Effect of CO_2 gasification reaction on char particle combustion in oxy-fuel conditions. *Fuel* **2014**, *120*, 130–140. [CrossRef]
11. Daood, S.S.; Javed, M.T.; Gibbs, B.M.; Nimmo, W. NO_x control in coal combustion by combining biomass co-firing, oxygen enrichment and SNCR. *Fuel* **2013**, *105*, 283–292. [CrossRef]
12. Boushaki, T.; Merlo, N.; Chauveau, C.; Gökalp, I. Study of pollutant emissions and dynamics of non-premixed turbulent oxygen enriched flames from a swirl burner. *Prog. Combust. Inst.* **2017**, *36*, 3959–3968. [CrossRef]
13. Aziz, M.; Budianto, D.; Oda, T. Computational Fluid Dynamic Analysis of Co-Firing of Palm Kernel Shell and Coal. *Energies* **2016**, *9*, 137. [CrossRef]
14. Li, J.; Huang, H.; Huhetaoli; Osaka, Y.; Bai, Y.; Kobayashi, N.; Chen, Y. Combustion and Heat Release Characteristics of Biogas under Hydrogen- and Oxygen-Enriched Condition. *Energies* **2017**, *10*, 1200. [CrossRef]
15. Murphy, J.J.; Shaddix, C.R. Combustion kinetics of coal chars in oxygen-enriched environments. *Combust. Flame* **2006**, *144*, 710–729. [CrossRef]
16. Wu, K.K.; Chang, Y.C.; Chen, C.H.; Chen, Y.D. High-efficiency combustion of natural gas with 21–30% oxygen-enriched air. *Fuel* **2010**, *89*, 2455–2462. [CrossRef]
17. Thornock, J.; Tovar, D.; Tree, D.R.; Xue, Y.; Tsiava, R. Radiative intensity, no emissions, and burnout for oxygen enriched biomass combustion. *Proc. Combust. Inst.* **2015**, *35*, 2777–2784. [CrossRef]
18. Pawlak-Kruczek, H.; Ostrycharczyk, M.; Czerep, M.; Baranowski, M.; Zgora, J. Examinations of the process of hard coal and biomass blend combustion in OEA (oxygen enriched atmosphere). *Energy* **2015**, *92*, 40–46. [CrossRef]
19. Gavalas, G.R. A random capillary model with application to char gasification at chemically controlled rates. *AIChE J.* **1980**, *26*, 577–585. [CrossRef]
20. Bhatia, S.K.; Perlmutter, D.D. A random pore model for fluid-solid reactions: I. Isothermal, kinetic control. *AIChE J.* **1980**, *26*, 379–386. [CrossRef]
21. Bhatia, S.K.; Perlmutter, D.D. A random pore model for fluid-solid reactions: II. Diffusion and transport effects. *AIChE J.* **1981**, *27*, 247–254. [CrossRef]
22. Lisandy, K.Y.; Kim, G.M.; Kim, J.H.; Kim, G.B.; Jeon, C.H. Enhanced Accuracy of the Reaction Rate Prediction Model for Carbonaceous Solid Fuel Combustion. *Energy Fuels* **2017**, *31*, 5135–5144. [CrossRef]
23. Lisandy, K.Y.; Kim, J.W.; Lim, H.; Kim, S.M.; Jeon, C.H. Prediction of unburned carbon and NO formation from low-rank coal during pulverized coal combustion: Experiments and numerical simulation. *Fuel* **2016**, *185*, 478–490. [CrossRef]
24. Lisandy, K.Y.; Kim, R.G.; Hwang, C.W.; Jeon, C.H. Sensitivity test of low rank Indonesian coal utilization using steady state and dynamic simulations of entrained-type gasifier. *Appl. Therm. Eng.* **2016**, *102*, 1433–1450. [CrossRef]
25. Smoot, L.D.; Smith, P.J. *Coal Combustion and Gasification*; Plenum Press: New York, NY, USA, 1979.
26. Guizani, C.; Jeguirim, M.; Valin, S.; Limousy, L.; Salvador, S. Biomass Chars: The Effects of Pyrolysis Conditions on Their Morphology, Structure, Chemical Properties and Reactivity. *Energies* **2017**, *10*, 796. [CrossRef]
27. Anthony, D.B.; Howard, J.B.; Hottel, H.C.; Meissner, H.P. Rapid devolatilization of pulverized coal. *Symp. Int. Combust. Proc.* **1975**, *15*, 1303–1317. [CrossRef]
28. Song, J.H.; Jeon, C.H.; Boehman, A.L. Impacts of Oxygen Diffusion on the Combustion Rate of In-Bed Soot Particles. *Energy Fuels* **2010**, *24*, 2418–2428. [CrossRef]
29. Liu, G.; Wu, H.; Gupta, R.P.; Lucas, J.A.; Tate, A.G.; Wall, T.F. Modeling the fragmentation of non-uniform porous char particles during pulverized coal combustion. *Fuel* **2000**, *79*, 627–633. [CrossRef]

30. Kajitani, S.; Suzuki, N.; Ashizawa, M.; Hara, S. CO_2 gasification rate analysis of coal char in entrained flow coal gasifier. *Fuel* **2006**, *85*, 163–169. [CrossRef]
31. Laurendeau, N.M. Heterogeneous kinetics of coal char gasification and combustion. *Prog. Energy Combust. Sci.* **1978**, *4*, 221–270. [CrossRef]

© 2017 by the authors. Licensee MDPI, Basel, Switzerland. This article is an open access article distributed under the terms and conditions of the Creative Commons Attribution (CC BY) license (http://creativecommons.org/licenses/by/4.0/).

energies

MDPI

Article

Biomass Production from Crops Residues: Ranking of Agro-Energy Regions

Christina Moulogianni and Thomas Bournaris *

Department of Agricultural Economics, Aristotle University of Thessaloniki, Thessaloniki 541 24, Greece; kristin@agro.auth.gr

* Correspondence: tbournar@agro.auth.gr; Tel.: +30-231-0998423

Academic Editor: Mejdi Jeguirim

Received: 4 July 2017; Accepted: 20 July 2017; Published: 22 July 2017

Abstract: The aim of the paper is to rank the agro-energy regions according to their potentials of biomass production in the Region of Central Macedonia (RCM). For this reason, a model of Multi-Criteria Analysis (MCDA) is developed with the ELimination and Et Choix Traduisant la REalite (ELECTRE) III method, with the construction of outranking relations. The aim is to compare in a comprehensive way each pair of action, in our case the agro-energy regions of the RCM, in order to satisfy the main goal which is to rank the seven regions as regards their biomass production. The final goal is to select the optimal crop plan as a pilot case for biomass production in the region. In the case of ELECTRE III multicriteria model, we used several conflicting criteria such as the farm income, the biomass production from crop residues, the variable costs, and the production of thermal energy and electrical energy. Alongside a technical and economic analysis of the study area is conducted for the existent crop plans of each agro-energy region. The results show that agro-energy regions with cereals and arable crops have better results than regions with fruit trees and other crops.

Keywords: biomass production; multicriteria model; ELECTRE III

1. Introduction

The E.U. Common Agricultural Policy (CAP) has set a series of environmental measures known as Agrienvironmental Schemes .Farmers must meet the conditions set by these measures in order to be eligible for subsidies for their cultivated crops. The new CAP framework for the 2014–2020 programming period reinforces the environmental conservation agenda [1]. According to Vlontzos et al. [1] these policy interventions impact both the energy and environmental efficiency of the primary sectors of E.U. member states. Also, one of the main objectives of the Horizon 2020 program is the creation of competitive industries based on sustainable technologies [2]. The contribution of biomass utilization industries from agricultural residues and in particular in Southern Europe has been presented in several research papers [3,4]. In this way farmers have an incentive to keep agricultural residues, a new form of bio-energy and agro-energy regions grow, diminishing the effects of climate change and creating a sustainable economic model [5].

According to the E.U. Biomass Policy and Action Plan [6] "biomass is essential for environmental and competitiveness reasons". On the other hand the European Parliament has adopted the statement that "biomass has many advantages over conventional energy sources, as well as over some other renewable energy forms". These advantages can be summarized, in the "low costs, less dependence on short-term weather changes, promotion of regional economic structures and provision of alternative sources of income for farmers". For these reasons Rosillo-Calle argues that biomass production is of high importance for rural areas and especially for overall rural development [7].

According to Best [8] "agro-energy refers to the energy function of agriculture, which can make significant contributions to achieving social and environmental sustainability at local, national, regional and global levels". This goal can be achieved by using agricultural and livestock resources worldwide and many new technologies in order to transform the traditional uses of these resources into modern forms of energy [8].

Based on the European energy policy axis [9] and the late development of renewable energy sources in Greece, the region of Macedonia is the best example to examine the creation of agro-energy regions. It is assumed that the exploitation of agricultural and forest residues has only positive impact in terms of jobs creation and the generated thermal and electrical energy [10]. Also, the utilization of energy crops and the production of biofuels, has an overall positive impact worldwide [11]. Greece depends heavily on imported forms of fossil fuels, but has high renewable energy production capacity and has set high goals. The objectives of Greece for producing final energy from renewable sources (any form) amount to 20% of total production by 2020 [12].

The main goal of this paper is to rank the agro-energy regions of the Region of Central Macedonia in Northern Greece. This can be achieved by calculating a number of indicators for biomass and bio-energy production from agricultural residues. By implementing an ELECTRE III multicriteria model, we will rank the seven agro-energy regions (Thessaloniki, Imathia, Kilkis, Pella, Pieria, Serres and Chalkidiki) with a set of criteria regarding economic and environmental aspects. In the next steps, ELECTRE III multicriteria model will compare in a comprehensive way each pair of indicators and will rank them with the use of the conflicting criteria. The three of them are economic criteria (gross margin, income and variable cost) and the rest are environmental criteria (biomass production, production of thermal energy, production of electrical energy). The final result will be the ranking of the seven agro-energy regions according to their potential production of biomass from agricultural crop residues.

First, the methodology of the ELECTRE III multicriteria model is presented with all the necessary mathematical equations. The section also includes the presentation of the case study area and the calculation of the main environmental and economic indicators that will be used as criteria for ranking the agro-energy regions of the Central Macedonia. The following section presents the results of the analysis from the implementation of the ELECTRE III multicriteria model. The final section contains the concluding remarks.

2. Methodology

2.1. Multicriteria Methods for Biomass Production

Many mathematical programming models of the decision-making process of farmers have been applied in several studies found in the literature. Examples are the multicriteria model for the assessment of rural development plans in Greece [13], the model for rural households to measure the effects of the Common Agricultural Policy (CAP) in three Southern European countries [14], and similar examples are the work of Xu et al. [15], Valiakos and Siskos [16] and Prišenk et al. [17]. The use of multicriteria models for ranking regions is also very common in the literature [18,19]. On the other hand, many methodologies have been successfully applied for the biomass production in farm level such as Haas et al. [20], Brentrup et al. [21], Pulighe et al. [22], Neri et al. [23], Blengini and Busto [24], Yu and Tao [25], Castillo-Villar et al. [26] and Fedele et al. [27].

This study will develop an ELECTRE III mathematical programming model for ranking the agro-energy regions of the region of Central Macedonia. The ELECTRE III multicriteria model will be used for the first time for ranking agro-energy regions focusing on biomass production. The great advantage of the methodology is that the results are presented clearly, facilitating the rational discussion of the results and the policy makers. The existent crop plans play a vital role in policy for biomass exploitation, especially in a sensitive environmental area since a large part of Central Macedonia consists of the Network areas Natura 2000. Therefore, this methodology is the most appropriate supportive tool for the ranking of the potentials of agro-energy regions and their combinations. Also,

the ELECTRE III multicriteria model has not been implemented anywhere in Greece for the analysis of biomass production.

2.2. The ELimination and Et Choix Traduisant la REalite (ELECTRE III) Multicriteria Method

ELECTRE III is a well-known multicriteria method widely chosen in the international literature [28,29]. This method requires the determination of prices of three thresholds of the criteria which are used as the indifference threshold, preference threshold and the veto threshold [30]. These allow the uncertainties of the evaluation criteria, be integrated into a decision-making process [31]. The ELECTRE III multicriteria model is used in solving multi-criteria decision-making problems in order to determine the best alternative to a given problem using the multi-criteria analysis [32]. The only reason that this method could be meaningless is the lack of available weights of the criteria and/or the accurate and complete information in minimum preference limits [31]. In this study a number of g_j, criteria (indicators in our case), where $j = 1, 2, \ldots$ r and a group of alternative scenarios (agro-energy regions in our case) are considered. Between the two scenarios a and b there is a possibility to have the following relationships and opposite [30]:

- a**P**b: The a is strongly preferred to b, where $g(a) - g(b) > p$
- a**Q**b: The a is meager preferred to b, where $q < g(a) - g(b) \leq p$
- a**I**b: Indifference between a and b, when $|g(a) - g(b)| \leq q$

where p is the preference threshold and q the indifference threshold. The prices for p and q are set by the decision makers [30].

For the implementation of the ELECTRE III multicriteria model we introduce the relation with IPS = a**S**b symbolism, indicating that scenario a, is at least as good as b. In order to examine the a**S**b statement introduces the following principles according to Buchaman et al. [33]:

- Agreement Principle: Applies a**S**b for the majority of the criteria.
- Principle of non-discrepancy: From all the criteria under which it accepted the statement contains no criterion on which this statement is strongly rejected.

The a**S**jb symbol indicates that scenario a is at least as good as b relative to the j criterion. In order the criterion j to be considered in accordance with the a**S**b statement should apply a**S**jb, i.e., $g_j(a) \geq g_j(b) - q_j$. Respectively the criterion j is in disagreement with the statement a**S**b when applicable b$\mathbf{P}_j$a, i.e., $g_j(b) \geq g_j(a) - p_j$.

In general, the purpose of the method is defined as the ranking of alternative scenarios considering [34]:

- The indifference and preference thresholds for each criterion.
- The criteria weights.
- The difficulties that may arise from comparing two scenarios, the first is significantly better than the second relative to a subset of criteria but inferior compared with the total evaluation.

Multicriteria evaluation of the potentials of biomass production of the agro-energy regions of Central Macedonia consists a problem which is formulated by using a set of alternatives (a, b, c, d, e, f, g) and a set of criteria (c1, c2, c3, c4, c5, c6). The evaluation of criterion j for alternative A is described as c_j(A). The approach adopted in the framework of this analysis uses a ranking scheme following ELECTRE III principles, based on binary outranking relations in two major concepts; "Concordance" (c_j) when alternative a outranks alternative b if a sufficient majority of criteria are in favour of alternative a and "Non-Discordance" (d_j) when the concordance condition holds, none of the criteria in the minority should be opposed too strongly to the outranking of b by a. The assertion that a outranks b is characterized by a credibility index which permits knowing the true degree of this assertion [35]. To compare a pair of alternatives (a,b) for each criterion, the assertion "a outranks b" is

evaluated with the help of pseudo-criteria. As already discussed, the pseudo-criterion is built with two thresholds, namely indifference (q_j) and preference (p_j), for which the following apply [30]:

- When $c_j(a) - c_j(b) \leq q_j$, the non-difference between alternatives a and b for the specific criterion j under study is identified. In this case $c_j(a,b) = 0$.
- When $c_j(a) - V_j(b) > p_j$, then a is strictly preferred to b for criterion j. In this case $c_j(a,b) = 1$.

For a criterion j and a pair of alternatives (a,b), the concordance index is defined as follows [30]:

$$c_j(a,b) = \begin{cases} 1 & g_j(b) - g_j(a) \leq q_j \\ 0 & g_j(b) - g_j(a) \geq p_j \\ \frac{p_j + g_j(a) - g_j(b)}{p_j - q_j} & q_j \leq g_j(b) - g_j(a) \leq p_j \end{cases}$$

A global concordance index $C_{a,b}$ for each pair of alternatives (a,b), is computed with the concordance index c_j (A, B) of each criterion j [30]:

$$c(a,b) = \frac{1}{\sum_{j=1}^{r} k_j} \sum_{j=1}^{r} k_j c_j(a,b)$$

where k_j is the weight of criterion j.

As already mentioned, a discordance index $d_j(a,b)$ is also taken into consideration for all pairs of alternatives and each criterion j. Discordance index (d_j) is evaluated with the help of pseudo-criteria with a veto threshold (v_j), which represents the maximum difference $c_j(a) - c_j(b)$ acceptable to not reject the assertion "a outranks b", as follows [30]:

$$d_j(a,b) = \begin{cases} 0 & g_j(b) - g_j(a) \leq p_j \\ 1 & g_j(b) - g_j(a) \geq v_j \\ \frac{g_j(b) - g_j(a) - p_j}{v_j - p_j} & p_j \leq g_j(b) - g_j(a) \leq v_j \end{cases}$$

The index of credibility $S(a,b)$ of the assertion "a outranks b" is defined as follows [30]:

$$S(a,b) = \begin{cases} C(a,b) & d_j(a,b) \leq C(a,b) \\ & \forall j \\ & d_j(a,b) \geq C(a,b) \\ C(a,b) \cdot \prod_{j \in J(a,b)} \frac{1 - d_j(a,b)}{1 - C(a,b)} & J(a,b) : d_j(a,b) > C(a,b) \end{cases}$$

In the case that a veto threshold is exceeded for at least one of the selected criteria, the credibility index is null. In other words, the assertion "a outranks b" is rejected. As regards the ranking procedure of all available location alternatives A_j, two complete pre-orders are constructed through a descending and an ascending distillation procedure [30]. In a nutshell, descending distillation refers to the ranking from the best available alternative to the worst, while ascending distillation refers to the ranking from the worst available alternative to the best [36,37]. As a last step of the developed methodology, sensitivity analysis is available, since parameter values in real life applications originate from estimations which are sometimes more or less reliable (weighting factors, thresholds, criteria qualitative values etc.) [30].

The next step is to rank the scenarios according to the reliability table. Originally there are formed two rankings Z1 and Z2, one ascending and one descending preference respectively and from their combination we end up in the final standings Z = Z1 ∩ Z2 [30].

At this point the constant λ is inserted, which is the highest reliability panel λ = max $S(a,b)$ and is defined as s reliability value (λ), such as to remain only the values $S(a,b)$ gene is greater than $\lambda - s(\lambda)$.The reliability value, like boundaries p_j, q_j, v_j above, determined by the decision-maker. We then apply [30]:

$$T(a,b) = \left\{ \begin{array}{ll} 1 & S(a,b) > \lambda - s(\lambda) \\ 0 & S(a.b) < \lambda - s(\lambda) \end{array} \right\}$$

From the implementation of the last function derived the final scoreboard under which rankings will be achieved. For the implementation of the ELECTRE III multicriteria model, the "demo" version of the software developed by the French university "LAMSADE Paris-Dauphine" was used [38]

2.3. Case Study Area and Criteria

2.3.1. Case Study Area

The case study area in this study is the Region of Central Macedonia (RCM). The RCM is divided into seven regional units, namely Chalkidiki, Imathia, Kilkis, Pella, Pieria, Serres and Thessaloniki. These regional units are considered as the agro-energy regions of the study. According to the biomass potential maps of the National Information System for Energy, the region of Central Macedonia has the largest reserves of biomass from agricultural residues of all Greece. All the appropriate technical and economic data of the total number of the agricultural holdings, collected from the General Directorate of Rural Economy and Veterinary and the Hellenic Statistical Authority. The data refers to the year of 2013. Crop plans of the agro-energy regions of the RCM are presented in Table 1.

Table 1. Crop plans of the agro-energy regions of the RCM.

Crops	Chalkidiki	Imathia	Kilkis	Pella	Pieria	Serres	Thessaloniki
Alfalfa		5548	4408.7	5518.7	3394.6	10,175.7	
Apples		2614					
Apricots				1628.7			
Barley	4265.8	1493.5	3549.8	4064	2425.4	7825	5324.8
Cherries				7825.1			
Cotton		16,354.4	6814.1	11,204.8	4614.8	14,816.2	10,348.6
Hard Wheat	16,218	4842	38,247.8	5933.5	9498.7	33,527	30,848.1
Kiwi					3218.4		
Maize		5998.3	3394.9	8498.7	1754.5	24,135	2994.8
Nectarines		3914		2948.5			
Oats	3214.2						
Olive Trees	30,847				3214.8	4623	2418.7
Peaches		18,235.7		15,898.7			
Rapeseed						2145	
Rice		1624			987.5	3104.5	17,994.5
Set Aside	11,922.9	2778.4	9909.9	4998.3	4358.4	8245.8	8494.5
Soft Wheat	3654.1	1598.4	22,246.3	4134.8	7914.8	11,924.5	21,911.2
Sunflower	1658.1		2158.9			10,748.5	5284.5
Tobacco					4888.8	2245	
Vetch	2549.1						
Total	30,847	65,000.7	90,730.4	72,653.8	46,270.7	133,515.2	105,619.7

2.3.2. Criteria

The selected criteria for the implementation of the ranking methodolody were three economic criteria (gross margin, income and variable cost) and three environmental criteria (biomass production, production of thermal energy, production of electrical energy). The criteria are calculated by multiplying the total land (ha) of each crop in the agro-energy district with the values of each indicator separately. A short description of the criteria is presented below.

Gross Margin

Gross margin is calculated by subtracting from income the variable cost of each crop of the agro energy region.

Income

It was computed by the simple combination of yields (kg/ha), and prices (€/ha), plus subsidies where applicable for each crop of the agro-energy region.

Variable Cost

In order to calculate variable cost all the agricultural inputs are summarized (seeds, fertilizers, chemicals, machinery, labour and the cost of water etc. (€/ha)).

Biomass Production

Based on the literature and taking into account newer research efforts [39] in the same direction [5] the agricultural residues from larger crops per area and yield in tons per hectare are calculated and are presented in Table 2.

Table 2. Biomass production (tn/ha) from crops residues for the main crops of the Region of Central Macedonia.

Crops	Residues Type	Output of Residues (tn/ha)	Humidity %	Biomass (tn/ha)
Alfalfa	Straw	3	0.15	2.6
Apples	Pruning	2.4	0.40	1.4
Apricots	Pruning	1.6	0.40	1
Barley	Straw	2.7	0.15	2.3
Cherries	Pruning	2.5	0.40	1.5
Cotton	Straw and shell (overground)	4.2	0.40	2.5
Cotton	Straw and shell (root)	1.3	0.56	0.6
Hard Wheat	Straw	1.6	0.15	1.4
Kiwi	Pruning	1.6	0.35	1
Maize	Stalks and cobs	10.5	0.55	4.7
Nectarines	Pruning	2.9	0.40	1.7
Olive Trees	Pruning	1.7	0.50	0.9
Peaches	Pruning	2.9	0.40	1.7
Rapeseed	Straw	4	0.53	1.9
Rice	Straw	3.8	0.25	2.9
Set Aside	Not applied			
Soft Wheat	Straw	2.5	0.15	2.1
Sunflower	Stalks	4	0.40	2.4
Tobacco	Stalks	2.2	0.85	0.3

Production of Thermal and Electrical Energy

In order to calculate the production of thermal and electrical energy for crops, the Lower Heating Values (LHV) were considered [40,41]. In the final stage of calculating the production of thermal and electrical energy using the following formulas respectively:

$$\text{Production of Thermal energy (MJ): } 0.9 \times \text{Biomass (kg)} \times \text{LHV(MJ/kg)}$$

$$\text{Production of Electrical energy (MJ): } 0.2 \times \text{Biomass (kg)} \times \text{LHV(MJ/kg)}$$

3. Results and Discussion

The following section includes the calculation of the indicators which are used as criteria in the ELECTRE III model (Table 3). It also includes the ranking of the seven agro-energy regions of the Central Macedonia after the implementation of the ELECTRE III multicriteria model.

Table 3. Calculation of the six criteria for ELECTRE III model.

Alternatives Agro-Energy Regions	Criteria					
	Gross Margin (€)	Income (€)	Variable Cost (€)	Biomass Production	Production of Thermal Energy (MJ)	Production of Electrical Energy (MJ)
Imathia	82,639,292.18	210,811,094.64	128,171,802.46	153,941.88	2,565,940,026.60	570,208,894.80
Thessaloniki	54,904,658.03	119,336,134.20	64,431,476.17	213,695.21	3,140,541,839.70	697,898,186.60
Kilkis	48,153,421.10	87,650,548.66	39,497,127.56	160,925.00	2,383,266,261.96	529,614,724.88
Pella	174,610,011.65	317,328,408.48	142,718,396.83	161,579.45	2,686,299,186.15	596,955,374.70
Pieria	50,209,550.87	104,365,027.78	54,155,476.91	77,115.67	1,175,256,301.05	261,168,066.90
Serres	80,164,854.89	178,619,541.72	98,454,686.83	318,397.21	4,837,020,975.00	1,074,893,550.00
Chalkidiki	56,526,005.64	135,930,670.10	79,404,664.46	77,969.21	1,275,268,402.80	283,392,978.40

From Table 3 we can conclude that Serres agro-energy region has the highest potential values for biomass production. The second region is Thessaloniki, followed by Pella, Kilkis and Imathia. The agro-energy regions of Chalkidiki and Pieria are the two with the lowest biomass production potentials. The crop plans of Serres and Thessaloniki mainly include arable crops and cereals which have mainly straw as output residues and high biomass values. The crop plans of Pella and Imathia include mainly fruit trees which produce high pruning values but with low output residues. Finally, the regions of Chalkidiki and Pieria have mixed crop plans with olive trees and arable crops. From these results we can conclude that the variety of crops in the existent crop plans is one of the most important factors as regards the biomass production potentials. Thus, agro-energy units with crops with high agricultural output residues have better results as regards the biomass production and in the production of thermal and electrical energy. As regards the comparison between the economic indicators and the biomass production potential we can conclude that biomass production hasn't any relation to the economic results. Agro-energy regions with high values of gross margin such as Pella and Imathia present the lowest biomass production potentials in comparison with the agro-energy regions of Serres and Thessaloniki.

Ranking

The ranking of the agro-energy regions of the Region of Central Macedonia was performed using the ELECTRE III multicriteria model. The criteria (gross margin, income and variable cost, biomass production, production of thermal energy, production of electrical energy) were used to describe the characteristics of each agro-energy region of the Region of Central Macedonia as regards the economic and environmental aspects. Some of these criteria are conflicting, which is important for the implementation of the ELECTRE III model.

For the implementation of the ELECTRE III multicriteria model, it is necessary a set of weights for every criterion in our research. For this reason, a group of experts (including policy makers from the Ministry of Rural Development and Food, the General Directorate of Rural and Veterinary Economy, farmers and researchers) were interviewed. For the definition of the criterias' weights, a questionnaire administered through personal meetings was used. The results of the questions as regards the weights of each criterion are presented in Table 4.

Table 4. Weights of each criterion.

Criteria	Weights (%)
Gross Margin (€)	7.70
Income (€)	7.70
Variable Cost (€)	7.70
Biomass Production	35.10
Production of Thermal Energy (MJ)	22.20
Production of Electrical Energy (MJ)	19.60
Total	100

The ELECTRE III multicriteria model was implemented using the "demo" version of a software developed by the French university "LAMSADE Paris-Dauphine" [38]. Each agro-energy region of the region of Central Macedonia was assigned a unique alphanumeric code for software use. The alphanumeric codes were:

A0001: Agro-energy Region of Imathia
A0002: Agro-energy Region of Thessaloniki
A0003: Agro-energy Region of Kilkis
A0004: Agro-energy Region of Pella
A0005: Agro-energy Region of Pieria
A0006: Agro-energy Region of Serres
A0007: Agro-energy Region of Chalkidiki

The credibility matrix of the ELECTRE III multicriteria models for the agro-energy regions was (Table 5):

Table 5. Credibility Matrix.

Codes	A0001	A0002	A0003	A0004	A0005	A0006	A0007
A0001	1	0.15	0.92	0.85	0.92	0.15	0.92
A0002	0.85	1	0.92	0.85	0.95	0.077	0.98
A0003	0.81	0.15	1	0.67	0.98	0.077	0.9
A0004	0.92	0.22	0.92	1	0.92	0.15	0.92
A0005	0.077	0.21	0.15	0.077	1	0.077	0.92
A0006	0.92	0.92	0.92	0.85	0.92	1	0.92
A0007	0.077	0.15	0.15	0.077	0.92	0.077	1

The concordance matrix of the ELECTRE III multicriteria models for the agro-energy regions was (Table 6):

Table 6. Concordance Matrix.

Codes	A0001	A0002	A0003	A0004	A0005	A0006	A0007
A0001	1	0.15	0.92	0.85	0.92	0.15	0.92
A0002	0.85	1	0.92	0.85	0.95	0.077	0.98
A0003	0.81	0.15	1	0.67	0.98	0.077	0.9
A0004	0.92	0.22	0.92	1	0.92	0.15	0.92
A0005	0.077	0.21	0.15	0.077	1	0.077	0.92
A0006	0.92	0.92	0.92	0.85	0.92	1	0.92
A0007	0.077	0.15	0.15	0.077	0.92	0.077	1

After the implementation of the ELECTRE III multicriteria model, the following ranking emerged for the agro-energy regions of the Region of Central Macedonia where:

$$A0006 > A0002 > A0004 > A0001 > A0003 > A0005 \text{ and } A0007$$

The final ranking of the alternatives (agro-energy regions) presented in the next table (Table 7):

Table 7. Final ranking of the seven agro-energy regions of the RCM.

Ranking	Code	Agro-Energy Region
1	A0006	Serres
2	A0002	Thessaloniki
3	A0004	Pella
4	A0001	Imathia
5	A0003	Kilkis
6	A0005 and A0007	Pieria and Chalkidiki

From the table above, we can observe that as regards the biomass production potentials in the Central Macedonia region, the agro-energy region of Serres has the first position, followed by the agro-energy region of Thessaloniki. The third position is held by the agro-energy region of Pella, followed by the agro-energy region of Imathia. In fifth position we have the agro-energy region of Kilkis. The agro-energy regions of Pieria and Chalkidiki share the final position.

From the results we can conclude that the size of the agro-energy region was an important factor. The crop plan of the agro-energy region of Serres seems to have the best mix of crops that produce biomass. The crop plan includes mainly arable crops and cereals as described in the previous section. The second crop plan, of Thessaloniki, seems to have a similar crop mix as the agro-energy region of Serres. The following crop plans of Pella and Imathia mainly comprise fruit trees.

The next figure (Figure 1) shows the ascending and descending distillations of the optimal agro-energy region which in our case is Serres, for biomass production.

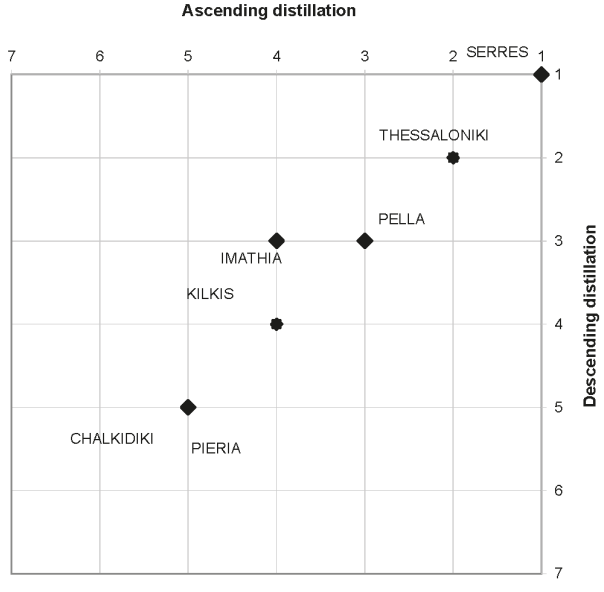

Figure 1. Ascending and descending distillations of the optimal agro-energy region for the biomass production.

4. Conclusions

The main aim of this research was to rank the agro-energy regions in Central Macedonia as regards their potential for biomass production from agricultural residues. For this purpose six main indicators were calculated (gross margin (€), farm income (€), variable costs (€), biomass production (tn), production of thermal energy (mj), production of electrical energy (mj),) for the seven agro-energy regions of the region. These indicators were used as criteria in a multicriteria analysis model. The multicriteria analysis model was developed using the ELECTRE III method. This model was used to rank the crop plans of the seven agro-energy regions under the eight criteria that we have selected. The research also examined the thermal and electrical energy in MWh produced by the biomass from agricultural residues. The results showed that the agro-energy region of Serres had the optimal crop plan for biomass production in the region, followed by the agro-energy region of Thessaloniki. These agro-energy regions had crop plans that included cereals (hard and soft wheat), maize, cotton and rice which are crops that produce high levels of biomass. The next crop plans were the crop plans from the agro-energy regions of Pella and Imathia. These crop plans included fruit

trees crops such as peaches and cherries which can produce high levels of residues from their pruning. From the above we can conclude that the biomass production in the region of Central Macedonia can be increased if the farmers were to turn to crop plans that include cultivation options like those of the agro-energy regions of Serres and Thessaloniki. Also, in the multicriteria ELECTRE III model we used criteria such as gross margin and variable costs that are basic criteria in the farmers' decision-making process when they select the crops that they will cultivate. On the other hand, as we know, their decisions do not include the biomass production. The multicriteria analysis managed to include these conflicting selection criteria in the model and the results of the ELECTRE III ranking proposed the optimal crop plans that the farmers can use and the policy makers can suggest.

The main policy message from this study is that the creation of agro-energy districts with the use of the proposed crop plans can lead to an increase in farm income and promote sustainable development for rural areas using agricultural residues for biomass production both for economic and environmental reasons. The proposed crop plans could be an important tool for the local and regional authorities, since they integrate the farmers' desire for profits and the social concerns about environmental issues. The ELECTRE III multicriteria model could be further improved in order to include more economic, environmental and social criteria that affect the biomass production. We postulate that in the future biomass production from agricultural residues will be one of the main criteria for farmers in their crop selection decision-making process. We can suggest that policy makers should encourage public and private investments in the production of energy from biomass and the creation of agro-energy districts in order to achieve better income for farmers and more sustainable development for rural areas.

Acknowledgments: Christina Moulogianni is supported by the State Scholarships Foundation (IKY) "IKY Fellowships of Excellence for Postgraduate Studies in Greece-Siemens Program".

Author Contributions: The paper was a collaborative effort between the authors. The authors contributed collectively to the theoretical analysis and manuscript preparation.

Conflicts of Interest: The authors declare no conflict of interest.

References

1. Vlontzos, G.; Niavis, S.; Manos, B. A DEA approach for estimating the agricultural energy and environmental efficiency of EU countries. *Renew. Sustain. Energy Rev.* **2014**, *40*, 91–96. [CrossRef]
2. European Commision. *Horizon 2020. Work Programme 2016–2017. 9. Food Security, Sustainable Agriculture and Forestry, Marine and Maritime and Inland Water Research and the Bioeconomy*; European Commision: Brussels, Belgium, 2015.
3. Fantozzi, F.; Bartocci, P.; D'Alessandro, B.; Arampatzis, S.; Manos, B. Public-private partnerships value in bioenergy projects: Economic feasibility analysis based on two case studies. *Biomass Bioenergy* **2014**, *66*, 387–397. [CrossRef]
4. Manos, B.; Partalidou, M.; Fantozzi, F.; Arampatzis, S.; Papadopoulou, O. Agro-energy districts contributing to environmental and social sustainability in rural areas: Evaluation of a local public-private partnership scheme in Greece. *Renew. Sustain. Energy Rev.* **2014**, *29*, 85–95. [CrossRef]
5. Tziolas, E.; Manos, B.; Bournaris, T. Planning of agro-energy districts for optimum farm income and biomass energy from crops residues. *Oper. Res.* **2017**, *17*, 535–546. [CrossRef]
6. European Commission (EC). *Biomass Action Plan*; European Commission: Brussels, Belgium, 2005.
7. Rosillo-Calle, F. The Role of Biomass Energy in Rural Development. Available online: http://www.proceedings.scielo.br/scielo.php?pid=msc0000000022000000100028&script=sci_arttext (accessed on 10 Feburary 2017).
8. Best, G. *Agro-Energy: A New Function of Agriculture*; Latin America Thematic Network on Bioenergy (LAMNET): Morelia, Mexico, 2003.
9. European Commission (EC). *A Strategy for Competitive, Sustainable and Secure Energy*; Energy 2020; European Commission: Brussels, Belgium, 2010.
10. Nishiguchi, S.; Tabata, T. Assessment of social, economic, and environmental aspects of woody biomass energy utilization: Direct burning and wood pellets. *Renew. Sustain. Energy Rev.* **2016**, *57*, 1279–1286. [CrossRef]

11. Bassegio, D.; Zanotto, M.D.; Santos, R.F.; Werncke, I.; Dias, P.P.; Olivo, M. Oilseed crop crambe as a source of renewable energy in Brazil. *Renew. Sustain. Energy Rev.* **2016**, *66*, 311–321. [CrossRef]
12. REN21. *Renewable Energy Policy Network for the 21st Century*; REN21: Paris, France, 2016.
13. Bournaris, T.; Moulogianni, C.; Manos, B. A multicriteria model for the assessment of rural development plans in Greece. *Land Use Policy* **2014**, *38*, 1–8. [CrossRef]
14. Manos, B.; Bournaris, T.; Chatzinikolaou, P.; Berbel, J.; Nikolov, D. Effects of CAP policy on farm household behaviour and social sustainability. *Land Use Policy* **2013**, *31*, 166–181. [CrossRef]
15. Xu, J.; Chang, S.; Yuan, Z.; Jiang, Y.; Liu, S.; Li, W.; Ma, L. Regionalized Techno-Economic Assessment and Policy Analysis for Biomass Molded Fuel in China. *Energies* **2015**, *8*, 13846–13863. [CrossRef]
16. Valiakos, A.; Siskos, Y. Multicriteria decision support for the evaluation of agricultural units in Greece. *Oper. Res.* **2015**, *15*, 379–393. [CrossRef]
17. Prišenk, J.; Turk, J.; Rozman, Č.; Borec, A.; Zrakić, M.; Pažek, K. Advantages of combining linear programming and weighted goal programming for agriculture application. *Oper. Res.* **2014**, *14*, 253–260. [CrossRef]
18. Koutroumanidis, T.; Papathanasiou, J.; Manos, B. A multicriteria analysis of productivity of agricultural regions of Greece. *Oper. Res.* **2002**, *2*, 339–346. [CrossRef]
19. Chatzinikolaou, P.; Bournaris, T.; Kiomourtzi, F.; Moulogianni, C.; Manos, B. Classification and ranking rural areas in Greece based on technical, economic and social indicators of the agricultural holdings. *Int. J. Bus. Innov. Res.* **2015**, *9*, 455–469. [CrossRef]
20. Haas, G.; Wetterich, F.; Geier, U. Life Cycle Assessment Framework in Agriculture on the Farm Level. *Int. J. Life Cycle Assess.* **2000**, *5*, 345–348. [CrossRef]
21. Brentrup, F.; Kusters, J.; Kuhlmann, H.; Lammel, J. Application of the Life Cycle Assessment methodology to agricultural production: an example of sugar beet production with different forms of nitrogen fertilisers. *Eur. J. Agron.* **2001**, *14*, 221–233. [CrossRef]
22. Pulighe, G.; Bonati, G.; Fabiani, S.; Barsali, T.; Lupia, F.; Vanino, S.; Nino, P.; Arca, P.; Roggero, P. Assessment of the Agronomic Feasibility of Bioenergy Crop Cultivation on Marginal and Polluted Land: A GIS-Based Suitability Study from the Sulcis Area, Italy. *Energies* **2016**, *9*. [CrossRef]
23. Neri, E.; Cespi, D.; Setti, L.; Gombi, E.; Bernardi, E.; Vassura, I.; Passarini, F. Biomass Residues to Renewable Energy: A Life Cycle Perspective Applied at a Local Scale. *Energies* **2016**, *9*. [CrossRef]
24. Blengini, G.A.; Busto, M. The life cycle of rice: LCA of alternative agri-food chain management systems in Vercelli (Italy). *J. Environ. Manag.* **2009**, *90*, 1512–1522. [CrossRef] [PubMed]
25. Yu, S.; Tao, J. Economic, energy and environmental evaluations of biomass-based fuel ethanol projects based on life cycle assessment and simulation. *Appl. Energy* **2009**, *86* (Suppl. S1), S178–S188. [CrossRef]
26. Castillo-Villar, K.; Minor-Popocatl, H.; Webb, E. Quantifying the Impact of Feedstock Quality on the Design of Bioenergy Supply Chain Networks. *Energies* **2016**, *9*. [CrossRef]
27. Fedele, A.; Mazzi, A.; Niero, M.; Zuliani, F.; Scipioni, A. Can the Life Cycle Assessment methodology be adopted to support a single farm on its environmental impacts forecast evaluation between conventional and organic production? An Italian case study. *J. Clean. Prod.* **2014**, *69*, 49–59. [CrossRef]
28. Fagioli, F.F.; Rocchi, L.; Paolotti, L.; Słowiński, R.; Boggia, A. From the farm to the agri-food system: A multiple criteria framework to evaluate extended multi-functional value. *Ecol. Indic.* **2017**, *79*, 91–102. [CrossRef]
29. Micale, R.; Giallanza, A.; Russo, G.; La Scalia, G. Selection of a sustainable functional pasta enriched with Opuntia using ELECTRE III methodology. *Sustainability* **2017**, *9*. [CrossRef]
30. Banias, G.; Achillas, C.; Vlachokostas, C.; Moussiopoulos, N.; Tarsenis, S. Assessing multiple criteria for the optimal location of a construction and demolition waste management facility. *Build. Environ.* **2010**, *45*, 2317–2326. [CrossRef]
31. Banias, G. Development of a System for the Optimal Construction and Demolition Waste Management. Ph.D. Thesis, Aristotle University of Thessaloniki, Thessaloniki, Greece, 2009.
32. Wang, X.; Triantaphyllou, E. Ranking irregularities when evaluating alternatives by using some ELECTRE methods. *Omega* **2008**, *36*, 45–63. [CrossRef]
33. Buchanan, J.T.; Sheppard, P.J.; Vanderpooten, D. *Project Ranking Using ELECTRE III*; Department of Management Systems, University of Waikato: Hamilton, New Zealand, 1999.

34. Roy, B.; Présent, M.; Silhol, D. A programming method for determining which Paris metro stations should be renovated. *Eur. J. Oper. Res.* **1986**, *24*, 318–334. [CrossRef]
35. Roussat, N.; Dujet, C.; Méhu, J. Choosing a sustainable demolition waste management strategy using multicriteria decision analysis. *Waste Manag.* **2009**, *29*, 12–20. [CrossRef] [PubMed]
36. Roy, B.; Bouyssou, D. *Aide Multicriterea la Decision: Methods et Cas*; Economica: Paris, France, 1993.
37. Maystre, L.Y.; Pictet, J.; Simos, J.; Roy, B. *Méthodes Multicritères ELECTRE: Description, Conseils Pratiques et cas D'application à la Gestion Environnementale*; Presses Polytechniques et Universitaires Romandes: Lausanne, Switzerland, 1994.
38. LAMSADE ELECTRE III e IV Software Official Webpage. Available online: https://www.lamsade.dauphine.fr/spip.php?rubrique64&lang=en (accessed on 15 December 2016).
39. Zambon, I.; Colosimo, F.; Monarca, D.; Cecchini, M.; Gallucci, F.; Proto, A.; Lord, R.; Colantoni, A. An Innovative Agro-Forestry Supply Chain for Residual Biomass: Physicochemical Characterisation of Biochar from Olive and Hazelnut Pellets. *Energies* **2016**, *9*. [CrossRef]
40. Di Blasi, C.; Tanzi, V.; Lanzetta, M. A study on the production of agricultural residues in Italy. *Biomass Bioenergy* **1997**, *12*, 321–331. [CrossRef]
41. Menconi, M.E.; Chiappini, M.; Grohmann, D. Implementation of a genetic algorithm for energy design optimization of livestock housing using a dynamic thermal simulator. *J. Agric. Eng.* **2013**, *44*, 191–196. [CrossRef]

© 2017 by the authors. Licensee MDPI, Basel, Switzerland. This article is an open access article distributed under the terms and conditions of the Creative Commons Attribution (CC BY) license (http://creativecommons.org/licenses/by/4.0/).

MDPI
St. Alban-Anlage 66
4052 Basel
Switzerland
Tel. +41 61 683 77 34
Fax +41 61 302 89 18
www.mdpi.com

Energies Editorial Office
E-mail: energies@mdpi.com
www.mdpi.com/journal/energies

MDPI
St. Alban-Anlage 66
4052 Basel
Switzerland

Tel: +41 61 683 77 34
Fax: +41 61 302 89 18

www.mdpi.com

ISBN 978-3-03921-663-5